Validation and benchmark of modelling tools for light assessment using ray-tracing and GPU-based method

Symbiosyst

Horizon Europe EU project
Grant Agreement No. 101096352

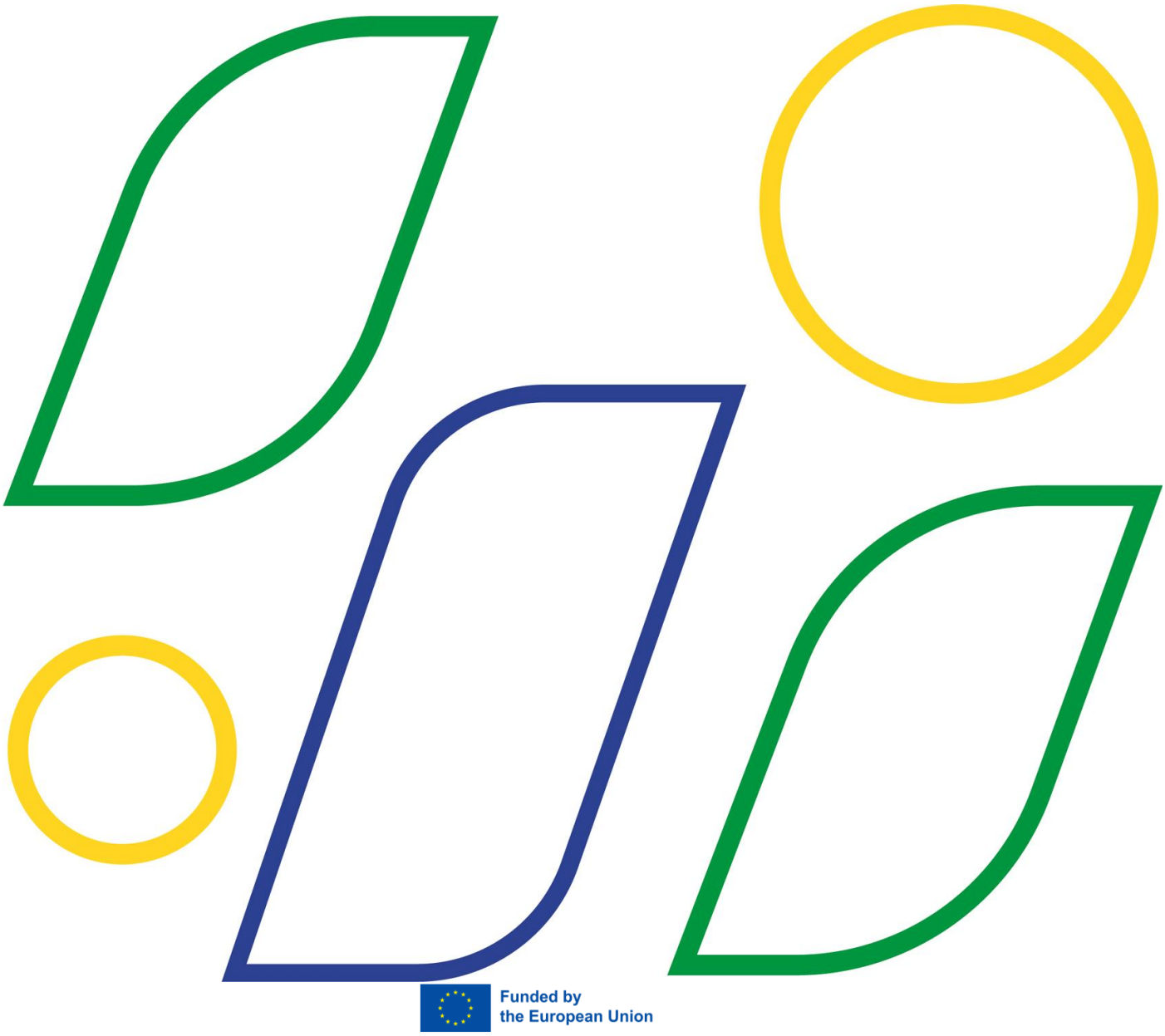

DOCUMENT CONTROL SHEET

Project	**SYMBIOSYST – Create a Symbiosis where PV and agriculture can have a mutually beneficial relationship**
Topic identifier	HORIZON-CL5-2022-D3-01-06
Grant Agreement N°	101096352
Coordinator	ACCADEMIA EUROPEA DI BOLZANO
Duration	01/01/2023 – 31/12/2026
Work package N°	2
Work package title	Robust and replicable design of novel and sustainable Agri-PV solutions
Work package leader	LuciSun
Task n°	T2.2: Modelling of advanced concepts for light assessment and control
Task leader	LuciSun
Document title	D2.2: Validation and benchmark of modelling tools for light assessment using ray-tracing and GPU-based method
Lead Beneficiary	LuciSun
Dissemination level	Public
Authors	S Prithivi Rajan, Shu-Ngwa Asaa, Alexandros Katsikogiannis, Jesús Robledo, Jonathan Leloux, Ismail Kaaya, Giacomo Bosco
Contributors	
Reviewer(s)	David Moser, Giovanni Borz
Issue date	30/12/2024

History of versions

Version	Date	Author - Beneficiary	Comments
v1.0	26/12/2024	Jonathan Leloux - LuciSun	Final Draft
v1.1	30/12/2024	David Moser - EURAC	Final Review

Dissemination Level [PUBLIC]

ACKNOWLEDGEMENTS

The work described in this publication has received funding from the European Union Horizon Europe research and innovation programme under grant agreement Nº 101096352.

DISCLAIMER

EXECUTIVE SUMMARY

This work, carried out within the SYMBIOSYST project, focuses on the development, validation, and benchmarking of advanced modelling tools for agrivoltaic systems. These systems integrate photovoltaic modules with agricultural activities, presenting unique challenges due to the complex interactions of light, shading, and crop growth. The study aims to evaluate the performance of various modelling tools, ensure methodological consistency, and derive insights to guide the design and optimisation of efficient agrivoltaic systems.

The study uses three advanced modelling tools. LuSim by LuciSun is a GPU-accelerated 3D simulation platform. Imec employs a ray-tracing framework, and TUD applies a Radiance-based approach. Fotoniq contributes essential expertise in characterising photovoltaic module materials and optical properties, which informs the modelling processes. The validation framework combines simple analytical test cases with realistic scenarios, such as the Bolzano demonstrator in Italy. This dual approach ensures accuracy for basic configurations while addressing the complexities of real-world agrivoltaic systems, including shading, albedo, and light redistribution.

The findings demonstrate significant progress in understanding light interactions in agrivoltaic systems. At lower module heights, the study identifies minor discrepancies between the tools, mainly due to differences in shading and ground reflectance modelling. As module height increases, these discrepancies diminish, with results converging at heights such as 50 meters. This consistency highlights the robustness of the tools for applications where shading is less critical. The study also provides valuable insights into the role of greenhouse glass, which reduces overall irradiance while significantly improving light uniformity, especially on clear-sky days. This smoothing effect minimises sharp transitions between shaded and illuminated areas, which benefits crop performance.

The benchmarking exercise shows that tools relying on similar ray tracing methodologies, such as Imec and TUD, produce closely aligned results. LuSim, with its innovative GPU-based 3D view-factor approach, performs strongly and demonstrates its flexibility in addressing unique modelling requirements. Additionally, Fotoniq's characterisation of photovoltaic materials enhances the accuracy of the simulations, particularly in scenarios involving semi-transparent modules and light diffusion.

This work establishes a comprehensive foundation for comparing and validating agrivoltaic modelling tools, contributing to the broader adoption of these systems. By addressing key challenges in light distribution, shading, and module transparency, the findings support the refinement of design methodologies and the optimisation of agrivoltaic installations. While certain aspects, such as dynamic crop growth and environmental variability, remain areas for future exploration, this study underscores the potential of advanced modelling to drive innovation in sustainable energy and agriculture.

TABLE OF CONTENTS

ACRONYMS AND ABBREVIATIONS

Table 1: Acronyms and Abbreviations list.

Abbreviation	Meaning
1P	PV layout with 1 row of PV modules installed in Portrait mode
AC	Alternating Current
Agri-PV/ AV	Agrivoltaics
BEG	Bifacial energy gain
BRDF	Bidirectional Reflectance Distribution Function
BTI	Direct (Beam) Tilted Irradiance
DC	Direct current
DHI	Diffused horizontal irradiance
DLI	Daily light integral
DNI	Direct normal irradiance
E-W	East-West
EOT	Electrical, optical and thermal
FS	Full sun
GAV	Global irradiance for the agrivoltaic system
GCR	Ground cover ratio
GHI	Global horizontal irradiance
GPU	Graphics Processing Unit
G_{ref}	Global irradiance for the reference system
GTI	Global tilted irradiance
HSAT	Horizontal Single-Axis Tracker
kWh/m^2	Kilowatt-hour per square metre
MWh/m^2	Megawatt-hour per square metre
MBD	Mean Bias Deviation
N-S	North-South
PAR	Photosynthetically active radiation
PD	Percentage difference
POA	Plane of array
PV	Photovoltaics
RMSD	Root Mean Square Deviation
Ta	Air temperature
W/m^2	Watts per meter square
Wp	Watt peak
Ws	Wind speed

1. INTRODUCTION

Agrivoltaics, the integration of photovoltaic (PV) systems with agricultural activities, represents an innovative solution to simultaneously address the growing demand for renewable energy and the need for sustainable food production. By enabling dual land use, agrivoltaic systems offer the potential to optimise energy generation while supporting agricultural productivity. However, their design and implementation require a detailed understanding of the complex interactions between light, PV modules, and crops in various configurations.

This deliverable presents the outcomes of Task 2.2 of the SYMBIOSYST project, which focuses on the advanced modelling of light transmittance, reflectance, and blockage in agrivoltaic systems. By leveraging innovative methodologies such as GPU-based simulations and spectrally resolved ray tracing, the work addresses the challenges of light assessment and optimisation for both open and closed agrivoltaic configurations.

Lucisun's tool, LuSim, is a GPU-based 3D simulation framework designed to provide high-resolution assessments of irradiance distribution across complex environments, including the ground, crop canopies, and PV modules. It uses advanced evaluation libraries to model light interactions with high spatial and temporal resolution, ensuring detailed analyses of shading and bifacial effects. In the context of the SYMBIOSYST project, LuSim was adapted to evaluate light transmittance in greenhouses, considering typical materials such as glass and EVA, as well as the effects of light diffuser coatings. The modelling focused on generating isotropic irradiance profiles and analysing spectral modifications of transmitted light, providing insights into light availability and distribution within controlled agricultural environments. Additionally, LuSim was employed to characterise light reflection using Bidirectional Reflectance Distribution Functions (BRDFs), enabling a detailed assessment of reflected and blocked light across system components.

Imec's spectrally resolved ray-tracing framework offers a physics-based approach to simulate light interactions with high accuracy. By incorporating advanced optical models, the tool can evaluate the effects of spectral variations and inhomogeneous light distribution on PV modules and crops. For the SYMBIOSYST project, Imec applied this framework to model agrivoltaic systems with enhanced spectral resolution. Specific developments included the simulation of PV module designs featuring UV-to-PAR coatings developed by Fotoniq, aimed at enhancing Photosynthetically Active Radiation (PAR) for crops. Imec also conducted comparative analyses of their ray-tracing approach against LuSim's GPU-based models, benchmarking computational efficiency and accuracy to provide complementary insights.

TUD's modelling framework focuses on optimising light distribution and semi-transparency in agrivoltaic systems. It offers a structural approach to simulate different geometrical features and panel arrangements, enabling the analysis of light uniformity beneath PV arrays. For this project, TUD advanced the tool to address the challenges of both open and closed agrivoltaic systems. Their work emphasised the optimisation of semi-transparent PV systems to balance crop productivity and energy yield. By simulating various configurations, TUD contributed valuable insights into design strategies that maximise light-sharing benefits and system performance.

The document begins with an overview of the validation and benchmarking efforts that ensure the reliability and robustness of the modelling approaches. These efforts compare the computational efficiency and accuracy of GPU-based simulations and spectrally resolved ray-tracing methods, highlighting their respective advantages and limitations. The validation includes quantitative comparisons of light modelling under controlled conditions.

Following the validation, the document explores the application of these tools to various agrivoltaic configurations, including open Agri-PV and closed Agri-PV. This includes the optimisation of semi-transparent PV systems for open and closed environments, the assessment of light transmittance in greenhouses, and the evaluation of PV module designs with advanced coatings such as those developed by Fotoniq. The results of these simulations are presented, emphasising their implications for system design, light-sharing benefits, and agricultural productivity. Finally, the document concludes by summarising the main findings and outlining future perspectives for advancing agrivoltaic modelling and deployment.

2. MODELLING TOOLS OVERVIEW

This section provides a comprehensive overview of the modelling tools used in the SYMBIOSYST project for simulating agrivoltaic systems. These tools were developed to address the unique challenges of accurately assessing light distribution, shading, and energy yield in complex agrivoltaic environments. Each tool brings distinct capabilities, tailored to specific modelling needs, such as evaluating the impact of light interactions on crop canopies, PV modules, and surrounding structures.

The tools covered in this section include LuSim from LuciSun, a GPU-based 3D simulation framework designed for high-resolution evaluations of light distribution and shading in agricultural settings, the spectrally resolved ray-tracing model from Imec, which provides precise insights into spectral variations and their effects on energy yield and crop productivity, and TUD's structural modelling framework, which focuses on optimising semi-transparent PV configurations and light-sharing designs. Alongside these tools, Fotoniq developed advanced UV-to-PAR coatings for PV modules, aimed at enhancing Photosynthetically Active Radiation (PAR) transmission for crops.

In the context of the SYMBIOSYST project, these tools and developments were tailored to address the specific requirements of agrivoltaics. LuSim was adapted to simulate light transmittance in greenhouses, incorporating material properties such as glass and EVA with light diffuser coatings. Imec extended its ray-tracing framework to include spectral optimisation and the evaluation of PV module designs with UV-to-PAR coatings developed by Fotoniq. These coatings were designed to improve the spectral quality of light for crops while maintaining energy yield. TUD advanced its framework to simulate semi-transparency and optimise light-sharing benefits in open and closed agrivoltaic systems. Fotoniq’s optical characterisations of their coatings were integrated into the modelling frameworks, enabling a detailed evaluation of their impact on crop productivity and PV performance.

The descriptions of these tools highlight their key features and functionalities, detailing their contributions to advancing the modelling of agrivoltaic systems. By leveraging innovative approaches, such as GPU acceleration, advanced optical modelling, and novel material developments, these tools form the backbone of the project’s efforts to optimise agrivoltaic designs for both energy and agricultural outputs. The subsequent sections delve into the specific methodologies, applications, and validation efforts associated with each tool.

2.1. LuSim (LuciSun)

Simulating the energy produced by bifacial photovoltaic (PV) modules in agrivoltaic (Agri-PV) systems is challenging because of the complex interactions between light, PV modules, and crops. These systems often involve a variety of factors, such as uneven ground, shading from crops or nearby objects, and the movement of tracking systems. To accurately estimate bifacial energy gain (BEG) in these configurations, advanced methods are needed to handle these complexities while considering both energy production and the availability of light for crops.

LuSim is a 3D simulation tool designed to meet these needs. It uses the power of Graphics Processing Units (GPUs) to model how light interacts with PV modules, crops, and the ground. LuSim provides detailed simulations with high spatial accuracy and frequent time intervals, making it well-suited for studying Agri-PV systems. The tool can be applied to scenarios like vertical bifacial PV systems in greenhouses, systems designed for sharing light in orchards or vineyards, and PV installations combined with protective net structures. LuSim also calculates detailed light patterns, such as the amount of light reaching individual leaves or PV cells. These results are then used in energy models that account for conversion losses, based on well-established tools like pvlib [1] or findings from scientific studies.

Traditional methods for simulating bifacial PV systems generally fall into two groups. One group uses analytical methods to estimate light on the backside of PV modules. These methods are efficient but less accurate. The other group uses ray tracing, which can provide very detailed results by tracing the paths of light but requires significant computing power. LuSim offers a middle ground by combining high accuracy with lower computing requirements, making it practical for designs that require multiple simulations.

In Agri-PV systems, LuSim helps analyse how PV modules and crops interact. It can study the effects of semi-transparent PV modules on crop growth and find the best way to adjust trackers to balance energy production and light for crops. It also evaluates how shading, both direct and reflected, affects different parts of the system. Each system is modelled as a 3D environment, allowing for precise analysis of how light is shared and its impact on both energy production and crop growth.

LuSim's previous applications are described in earlier studies [2-6]. Figure 1 provides examples of its use in different settings. These examples highlight its ability to model complex interactions between light and PV systems and to assess their performance in a range of PV or Agri-PV configurations.

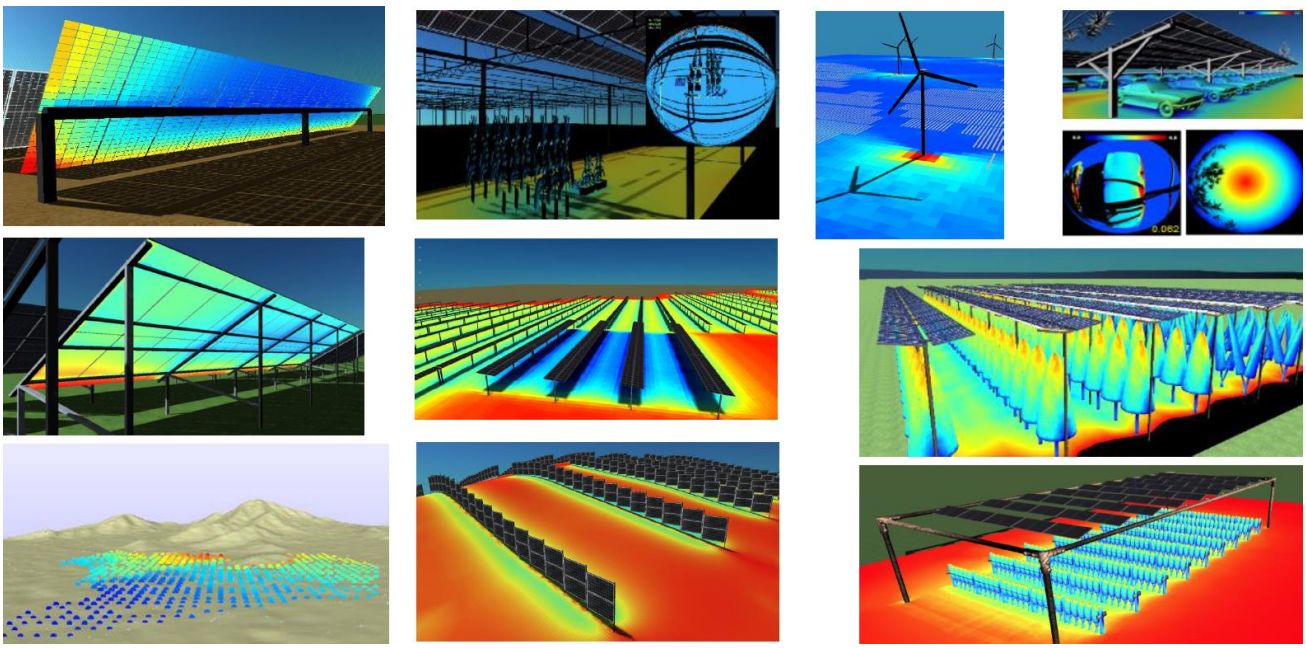

Figure 1: Previous PV or Agri-PV simulations carried out with the LuSim modelling framework.

2.2. Imec

Imec's simulation framework [7] is a rigorous, patented, bottom-up physics-based approach that applies advanced ray-tracing techniques to model the path of light through PV modules, crop canopies, and other components of agrivoltaic systems. This framework provides a detailed understanding of light interactions by incorporating physical models for light scattering, reflection, transmission, and ground-reflected irradiance (albedo). It supports the simulation of various PV configurations, including mono- and bifacial modules, fixed-tilt and tracked systems, and integrated designs such as BIPV and floating PV systems.

The framework's ray-tracing capabilities accurately resolve the effects of partial shading caused by surrounding objects and allow for the calculation of incident irradiance on both the front and rear sides of bifacial modules. Components within the agrivoltaic scene, such as PV module surfaces, the ground, and vegetation, are defined in Radiance by assigning material properties, including reflectivity, transmissivity, and emissivity. This granular approach enables the analysis of different PV module materials and configurations, including semi-transparent modules, by capturing their impact on energy yield and light availability for crops. The framework can also account for the complex optical properties of plant surfaces, making it highly adaptable to diverse agrivoltaics scenarios Figure 2 summarises the Imec modelling framework as applied to agrivoltaic systems.

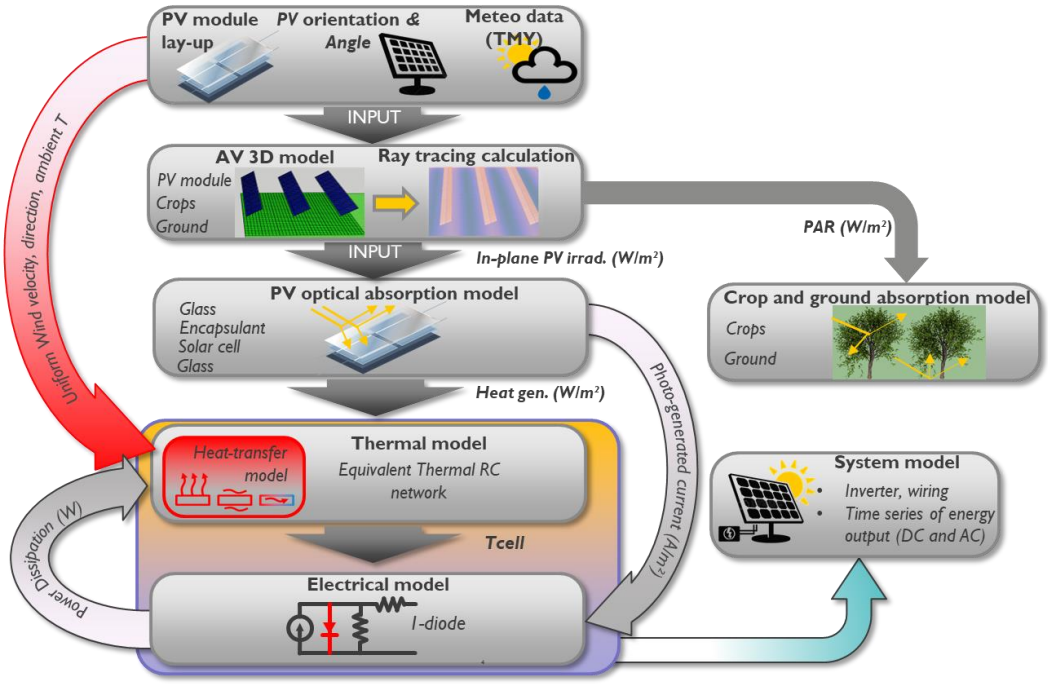

Figure 2: Imec's ray tracing based simulation framework.

2.3. TUD

The irradiation model used by TU Delft (TUD), is based on Radiance, a robust, open-source light simulation software comprising a suite of Unix-based tools. To integrate Radiance into Windows, TUD developed a special adapter, inspired by bifacial_radiance [8]. This adapter not only employs advanced Radiance tools but also supports multiprocessing through the Windows Subsystem for Linux (WSL). This enhancement significantly reduces computational time, especially in complex scenarios like those encountered in Agri-PV systems with tall crop canopies. Moreover, the model has been upgraded to include spectral skies based on local weather conditions and atmospheric data, along with 3D porous and transient tree canopies. Additional helper functions have been developed to streamline various stages of light simulation, facilitating smooth optimization workflows.

When performing light simulations using Radiance, a modeller needs to go through several steps, as illustrated in Figure 3. These steps can be broadly categorized into three main processes: setting the scene, compiling the octree, and raytracing. Since these processes have been thoroughly documented elsewhere, gravity will be put on specific advanced features of Radiance, particularly the extensions developed by TUD that enhance compatibility with Agri-PV settings. Scene setup is the most time-consuming phase, involving the generation of sky and ground, geometries, and application of optical properties. These data are organized into an octree, a specialized data structure that allows Radiance to efficiently determine light interactions with each surface. Raytracing is initiated by specifying the temporal, spatial, and spectral aspects of irradiance sampling, which includes the timestep, sensor distribution, and number of wavebands.

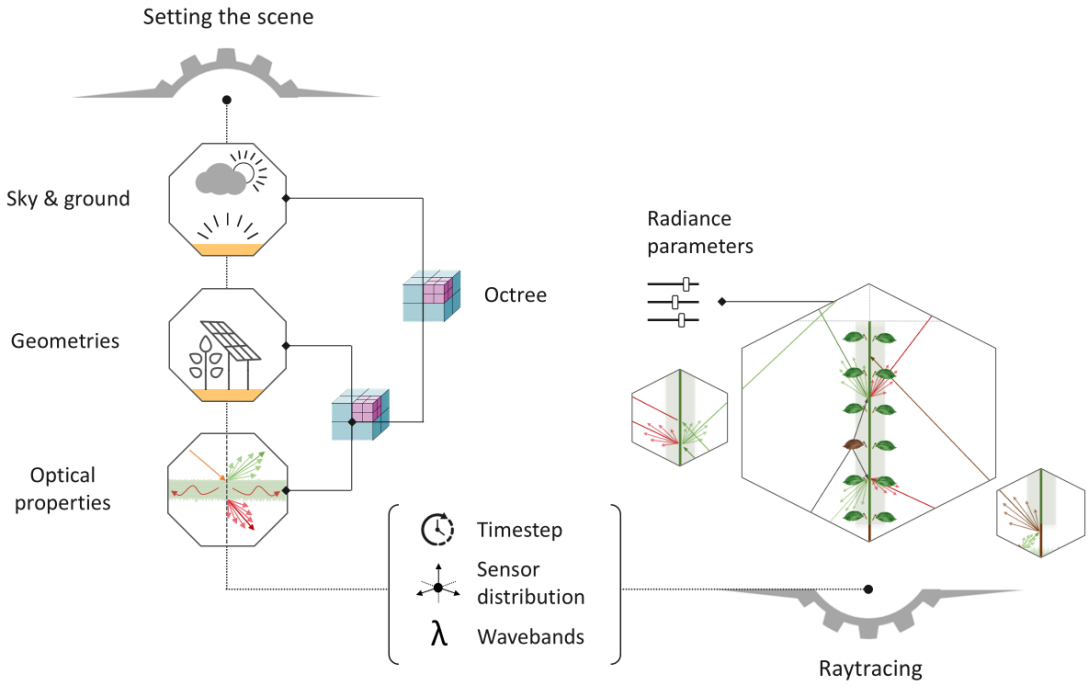

Figure 3: Overview of TU Delft's irradiation model utilizing the raytracing algorithm from Radiance.

3. SPECIFIC AGRI-PV MODELLING DEVELOPMENTS

3.1. 3D modelling of crops

The modelling of crop shapes is a key element in simulating light interactions within agrivoltaic systems. The way crops are represented has a direct impact on the accuracy of light distribution and shading analyses, making it important to select the right approach for the specific application. During the SYMBIOSYST project, various methods for representing crops were considered, balancing computational efficiency with the level of detail required. These methods range from simple geometric shapes to highly detailed models, with a compromise solution using external envelopes and parameterised models offering flexibility for diverse scenarios.

The simplest method involves using basic geometric shapes, such as parallelepipeds, spheres, or cones, to approximate the overall structure of crops. This approach significantly reduces computational demands by limiting the number of points where irradiance calculations need to be performed. As a result, it is particularly useful for large-scale simulations or initial evaluations, where computational efficiency is a priority. Simple shapes are effective for general assessments of light distribution and shading, especially in comparative studies of different PV system configurations. However, this method may oversimplify the representation of the canopy, potentially leading to inaccuracies in predicting photosynthetic activity and shading effects.

At the other end of the spectrum, complex shapes aim to replicate the precise geometry of crops, including individual leaves, stems, and branches. This approach provides a highly accurate representation of light interactions, capturing the detailed scattering, transmission, and penetration of light through the canopy. By modelling the optical porosity and varying density of the crop structure, this method allows for an in-depth understanding of light behaviour within the plant. However, the detailed nature of this approach requires significant computational resources due to the high spatial resolution and the number of irradiance calculation points. Additionally, it is less compatible with simpler agronomic models that rely on approximations of light distribution at the canopy level. For these reasons, complex shapes are generally reserved for specialised studies focused on micro-scale interactions, rather than for large-scale or comparative analyses. Figure 4 illustrates examples of crop modelling using complex shapes.

Figure 4: Modelling of crops using complex shapes. Left: Lettuce. Right: Tomatoes.

As a middle ground, the combined approach using external envelopes with parameterised models was developed to balance accuracy and computational efficiency. External envelopes define the overall boundaries of the crop canopy, capturing its size and shape with a greater degree of realism than simple geometric shapes. Parameterised models are attached to these envelopes to simulate the optical properties of the crop, such as effective light porosity, reflectivity, and transmission. For instance, the envelope can be represented by simplified polygons or polyhedra, while the optical properties are embedded in the materials or textures applied to these shapes. This method allows for a more realistic representation of light penetration and scattering within the canopy without the computational burden of fully replicating every leaf and stem. By combining geometric envelopes with parameterised properties, this approach provides a flexible and efficient way to simulate light interactions in diverse agrivoltaic scenarios. Figure 5 shows examples of crop modelling using external envelopes in an Agri-PV project combining lettuce and tomatoes.

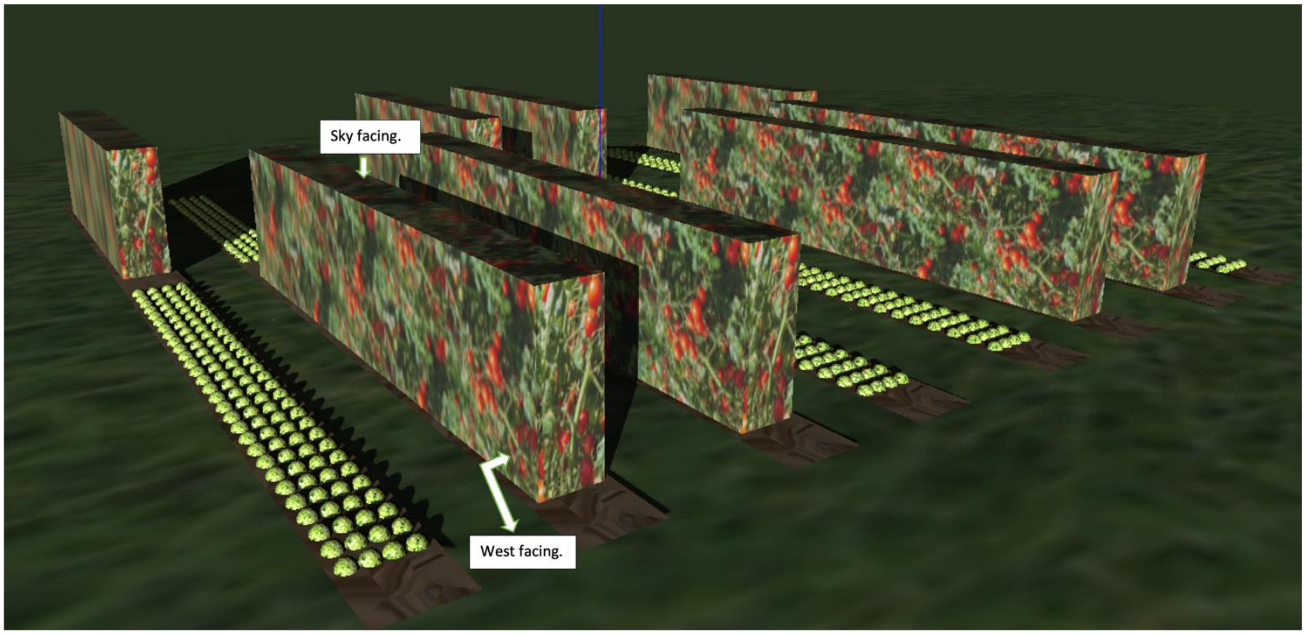

Figure 5: Crop modelling of the external envelope using simple shapes for lettuce and tomatoes.

This progression from simple shapes to complex models, with the compromise offered by external envelopes, reflects the variety of approaches available to address the challenges of crop modelling in agrivoltaics. Each method offers distinct advantages and is suited to different applications, depending on the desired balance between computational cost and the level of detail required.

3.2. Spectral resolved ray tracing

Quantifying or simulating energy gains or losses in PV energy yield due to spectral irradiance variations remains a significant challenge in the PV industry, primarily because solar spectral irradiance data is scarce. Furthermore, most commercial simulation tools are designed to incorporate only broad-band irradiance in energy yield simulations. In the case of Agri-PV, where it is crucial to account for the effects of crop reflectance and estimate Photosynthetically Active Radiation (PAR) within the visible light spectrum—critical for plant growth and development—spectral-resolved simulation becomes increasingly important. The irradiance estimation and ray tracing model used in Imec's simulation framework has been extended to incorporate the capability for spectrally resolved ray tracing. This enhancement involves several steps:

Initially, we assessed the additional inputs necessary beyond those used in the conventional normal or broadband ray tracing approach. Spectrally resolved ray tracing demands a comprehensive understanding of optical properties spanning the solar spectrum. Key parameters encompass spectral response and transmittance of the cell, as well as refractive index and absorptance of front/backsheets. Next, one needs to have spectral resolved irradiance data or convert the broadband irradiance parameters into spectral irradiance. This requires applying the AM1.5 spectrum, transforming beam irradiance into direct normal irradiance and sky diffuse irradiance into diffuse horizontal irradiance.

Subsequently, the method requires to run ray tracing for all spectral bands considering the specific optical properties for each band. This iterative approach facilitates the estimation of irradiance converted into photocurrent by leveraging the cell's spectral response. Simultaneously, it evaluates the irradiance transmitted through the module by considering the cell's transmittance alongside the optical properties of the front/backsheets. Finally, we estimated the total photocurrent and total transmitted irradiance by aggregating the values derived from the sequence of ray tracing iterations.

3.2.1. Evaluating the Optimal Distribution of Spectral Bands

Since the iteration process used in spectral resolved ray tracing approach could be computationally expensive especially when dealing with high resolution and longer timeseries, we evaluated what would be the optimal spectral bands depending on the PV cell technology under investigation. To do this, we used spectral and global horizontal irradiance data from a partner project. External quantum efficiency (EQE) data of a bifacial PERC module, obtained from Imec, and grass reflectance data from NASA are utilized to characterize the surfaces involved in the study. A systematic approach is employed to determine the possible combinations of spectral bands in intervals of 20 nm for each considered number of bands ranging from 2 to 5 as shown in Figure 6.

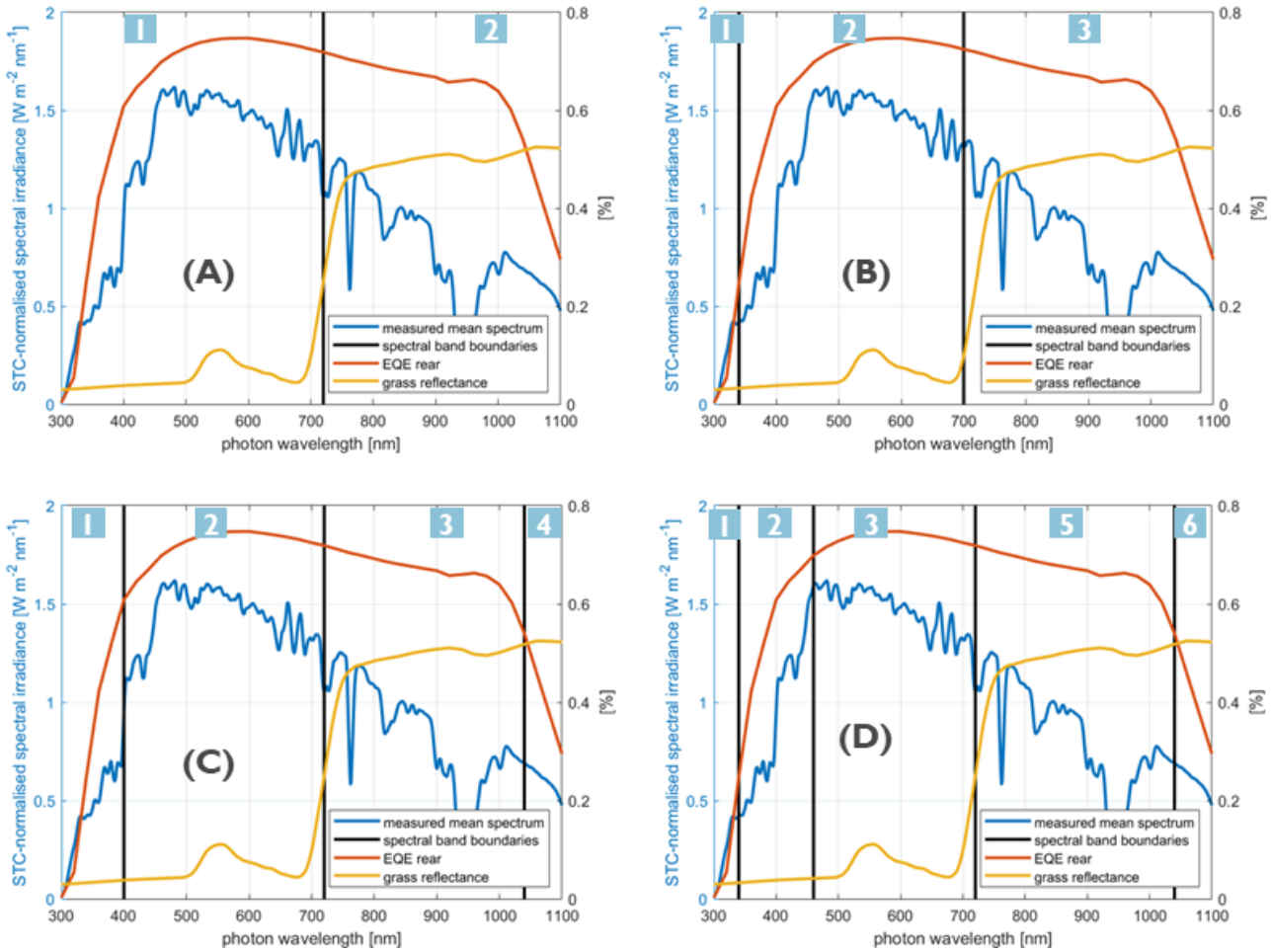

Figure 6: Selection of spectral band boundaries based on EQE and grass reflectance for bifacial modules. From A through D, the numbers show the band boundaries.

For each combination of spectral bands: (i) Band-specific irradiance levels are calculated based on the collected data, (ii) front and rear EQE along with grass reflectance are calculated for each spectral band considering the standard spectrum and (iii) broadband photocurrent density (J_{ph}) time series are derived by summing up the band-specific photocurrents.

To select the optimal band, for each considered number of bands, the optimal combination of spectral bands is determined by minimizing the Root Mean Square Error (RMSE) of J_{ph} estimates compared to the J_{ph} calculated based on high-resolution data as shown in Figure 7.

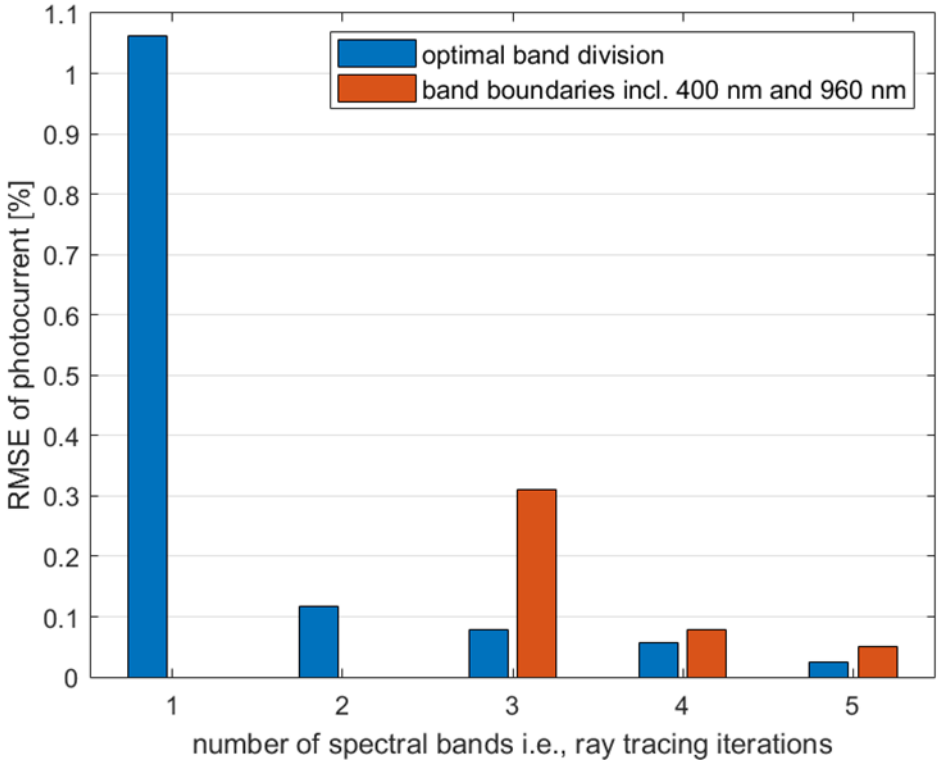

Figure 7: Number of ray tracing iterations vs RMSE of photocurrent for bifacial modules.

In the analysis conducted at the specified location, employing the standard spectrum yields RMSE of 2.0%, with an associated MBE of +0.9%. This outcome demonstrates that for bifacial installations on grass (Agri-PV), upscaling spectral data into a single band introduces notable uncertainty. Therefore, the implementation of spectrally resolved ray tracing proves advantageous. It is observed that employing two spectral bands (equivalent to two ray tracing iterations) is adequate for accurately estimating energy yield, while reducing the computation costs. The determination of optimal band boundaries tends to align with wavelengths where the slope of spectral properties (such as EQE and grass reflectance) is most pronounced. This optimization contributes to improved accuracy in energy yield estimation.

3.2.2. Broadband vs spectral resolved ray tracing for estimating bifacial rear irradiance

In this report, we present two scenarios showcasing the application of spectrally resolved ray tracing in Agri-PV:

a. Evaluating deviations in rear irradiance on bifacial modules caused by variations in grass reflectance.
b. Comparing the relative deviations in PAR estimation when using a simple percentage of broadband data versus spectrally resolved data.

Here we analyse the discrepancies in rear irradiance between spectral resolved and broadband ray tracing methods. For the spectral resolved simulation, spectral data from Genk, Belgium was used. The optimal band boundaries were selected based on the measured EQE for PERC and grass reflectance as shown in the Figure

8. As indicated in the figure for green grass two bands are used and for brown grass three bands are used. For broadband simulation, an average reflectance of 0.313 and 0.296 for brown and green grass are used respectively.

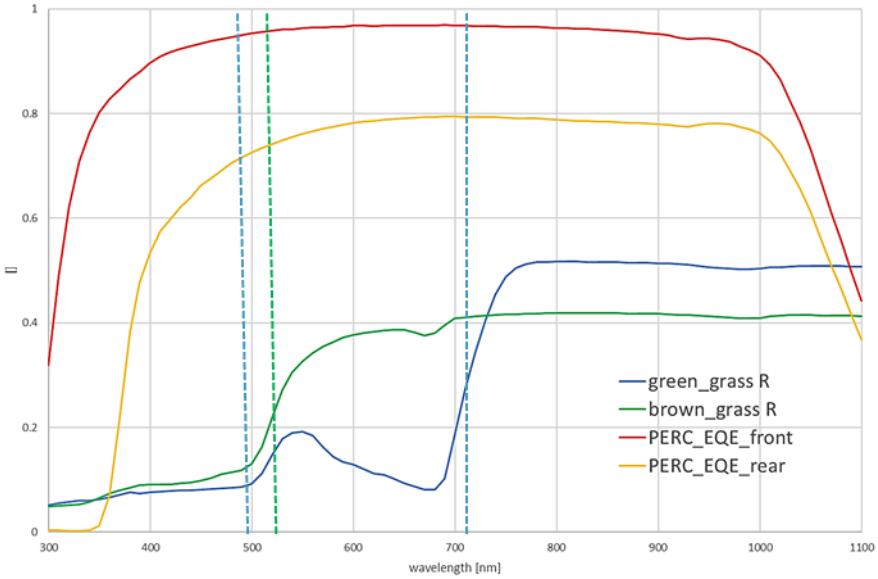

Figure 8: Measure external quantum efficiency (EQE) for PERC module and reflectance (R) for green and brown grass.

Figure 9-A illustrates the simulated rear irradiance for brown grass using spectrally resolved and broadband ray tracing methods. The figure highlights that the variations depend significantly on the season, with higher differences exceeding 25 W/m² observed during the summer months. Figure 9-B presents the relative deviation (in percentage) between broadband and spectrally resolved simulations for green and brown grass reflectance. These deviations vary based on the season and time of day, with deviations exceeding 15% being more pronounced for brown grass. It is important to note that these deviations are specific to the simulated location and may vary significantly with changes in geographic and environmental conditions.

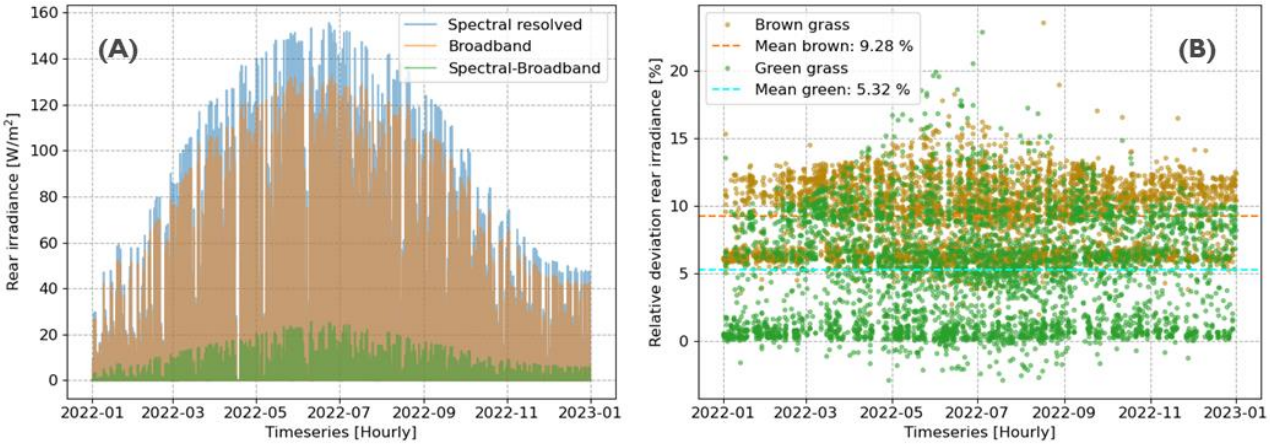

Figure 9: (A) Simulated rear irradiance using spectral resolved and broadband ray tracing using brown grass and (B) Relative deviation in rear irradiance between spectral and broadband ray tracing using brown and green grass.

3.2.3. Broadband vs spectral resolved ray tracing for PAR estimation

Photosynthetically Active Radiation (PAR) refers to the portion of sunlight (wavelengths between 400 and 700 nm) that plants use for photosynthesis. It is a critical parameter in agriculture, as it directly influences plant growth and productivity. PAR is commonly estimated from broadband irradiance by applying a fixed fraction, typically around 45–50% of the total incoming solar radiation [9], based on empirical relationships. While this approach is straightforward, it assumes a consistent spectral distribution of sunlight, which can lead to inaccuracies under varying atmospheric and environmental conditions, such as changes in cloud cover or ground reflectance. Accurate PAR estimations are needed for modelling plant productivity and biomass production. For greater precision, spectrally resolved data can be used to directly calculate the PAR, accounting for these variations. Here we evaluate the discrepancies of PAR estimation by applying a fixed fraction of 45 % and using spectrally resolved ray tracing data Figure 10-A demonstrates the simulated irradiance on the crop canopy using a full spectrum and with PAR-range spectrally resolved simulations. The PAR ratio is shown in Figure 10-B. According to the time of the day the PAR ratio of the simulated location range approximately from 0.39 to 0.47 (39 % to 0.47 %) neglecting outliers. The mean PAR ratio is approximately 0.43 a little bit lower than the reported ranges of 0.45 to 0.50 in literature. Since the ratio is location and time dependent, the discrepancy can be within the uncertainty range. Figure 10-C shows a scenario where the simulation of irradiance on the crops is done by using a 45 % PAR approximation of the full spectrum and using PAR range spectrally resolved irradiance. It is visible that there are some discrepancies between the two approaches within the range of -5 % to 13 % as shown in Figure 10-D. The mean deviation for the entire year is about 3.65 % , indicating over-estimation of PAR when using a 45 % approximation for this specific location.

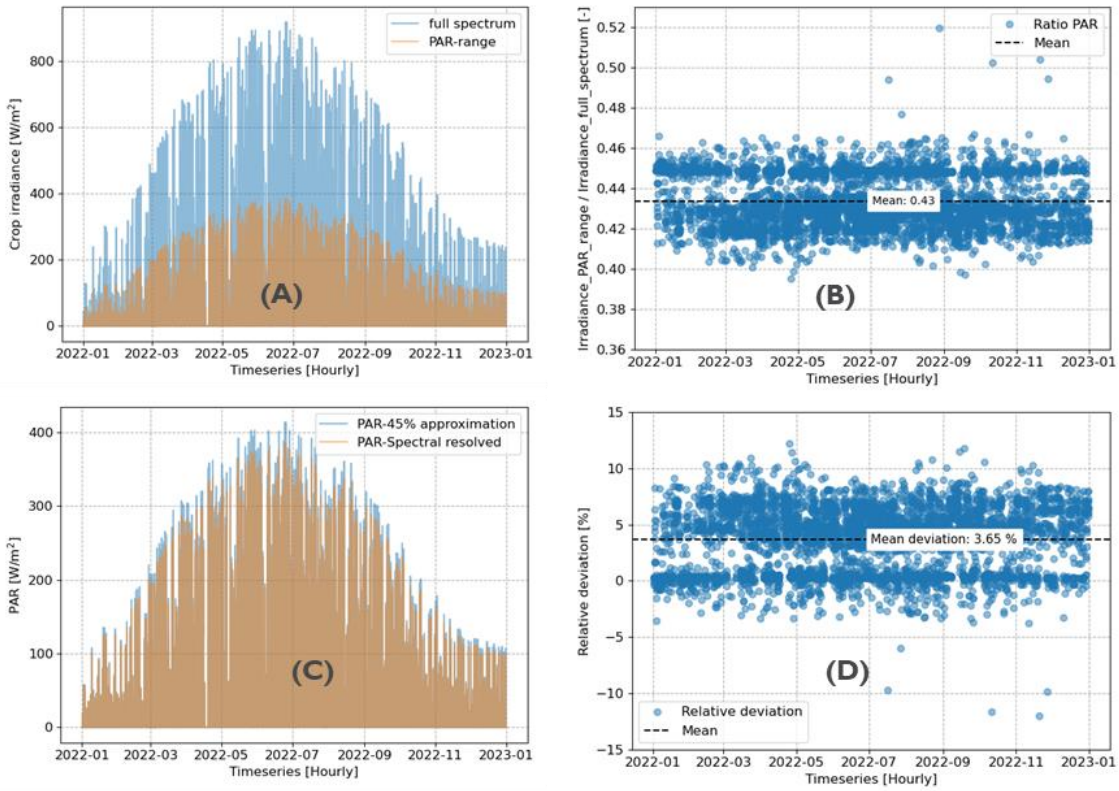

Figure 10: (A) Simulated irradiance on crop canopy using full spectrum (broadband) and PAR-range (spectrally resolved). (B) PAR ratio (irradiance PAR-range / irradiance full spectrum). (C) PAR estimated as 45% of full spectrum simulation and PAR on crop canopy estimated using PAR-range. (D) Relative deviation between PAR estimated using 45 % approximation and using PAR-range simulation.

Conclusively, the integration of spectrally resolved ray tracing into the simulation framework allows us to analyse discrepancies in irradiance between spectral resolved and broadband methods. However, a significant challenge lies in the scarcity of spectral data for thorough validation of the methodology, which requires further work.

3.3. Modelling of Bidirectional Reflectance Distribution Function (BRDF)

LuSim has developed the capacity to include advancements in reflection modelling that have been proposed through the integration of Bidirectional Reflectance Distribution Function (BRDF) modelling. The proposed methodology for defining a Bidirectional Reflectance Distribution Function (BRDF) by LuciSun utilises the Sasktran Python library, designed for simulating the reflectance characteristics of different materials [10]. This library offers a comprehensive selection of material properties and broadband reflectance simulations, with a detailed reference to the methodologies employed in each case. The BRDF, in general terms, is characterized for various materials and broadbands using three specific angles, as illustrated in Figure 11, to accurately model the interactions of light with surfaces.

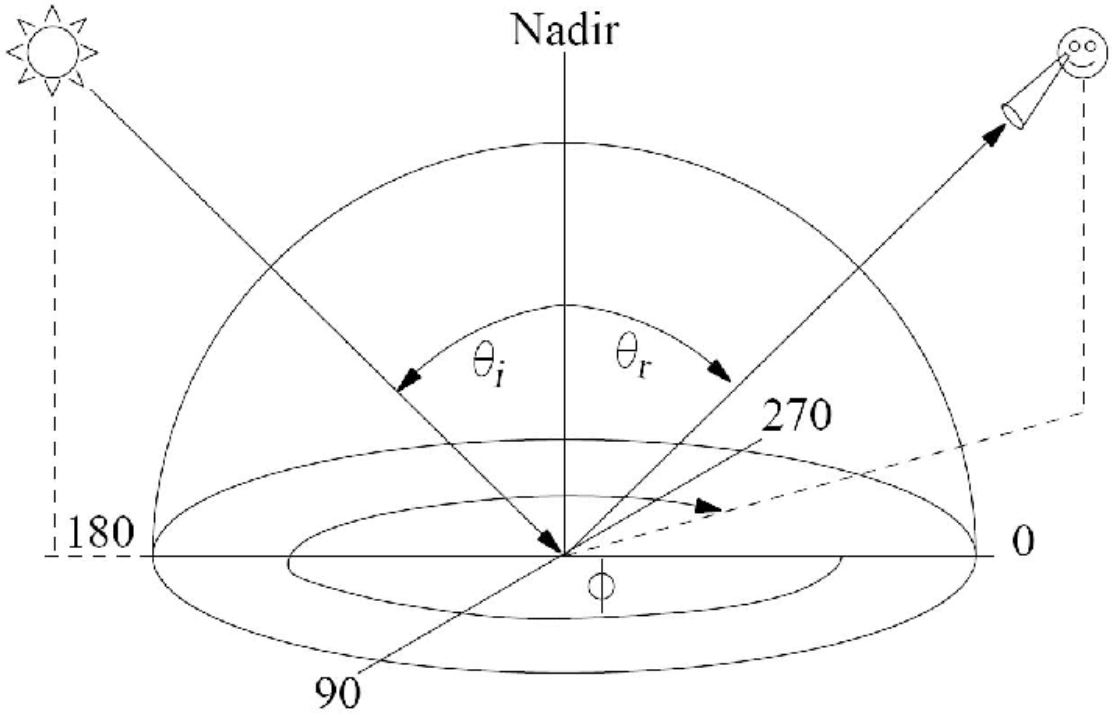

Figure 11: Angles definition involved in the BRDF methodology.

In the context of BRDF modelling, the light source (in this case, the sun) defines a plane using the surface's local normal and the incident light direction. Within this plane, the incident vector forms an incident angle, denoted as θ_i, with the surface normal. This represents the first of the three defining angles.

The reflected direction is determined by the vector connecting the reflection point on the surface to the observer's position. This vector is expressed in spherical coordinates using two angles: ϕ and θ_r, as depicted in the Figure 11 above. These angles represent the other two defining angles in the BRDF formulation.

This methodology assumes isotropy in the material configuration concerning azimuthal direction. Consequently, the reflection remains unaffected by the incident azimuth direction, a valid assumption for most materials of interest in agrivoltaic applications.

An alternative to using the functions defined in the Sasktran library, particularly when working with pre-existing models, involves using a table of reflectance values corresponding to the three aforementioned angles for specific materials and broadband ranges. The resolution of the angles can be adjusted based on the requirements of each software tool.

For instance, considering a resolution of 5 degrees for both azimuth and zenith reflection directions, the number of reflectance directions for a single incident angle would be (360/5) times (90/5), resulting in 1296 values. If the incident angle is also considered at a 5 degrees resolution, the resulting table would require (90/5) times 1296, that's equal to 23,328 lines. With a 10 degrees resolution for all angles, the table size would

reduce to approximately 2916 lines, with linear interpolation used for values between the defined table entries.

As an example, using the 'Grass Lawn' surface option in the Sasktran BRDF library based on the Roujean methodology within the visible light broadband, the shape of the BRDFs for two different incident angles (0 degrees on the left and 45 degrees on the right) at a 5 degrees resolution is depicted in Figure 12.

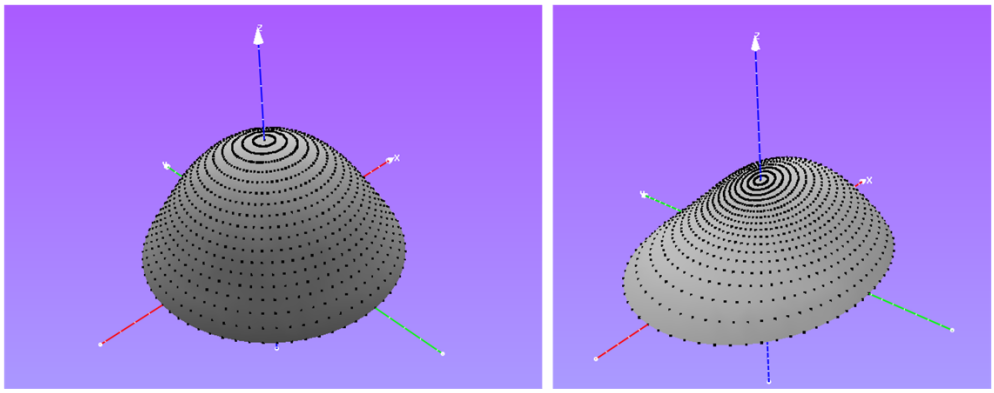

Figure 12: BRDF for "Grass Lawn" surface at 0° (left) and 45° (right) incident angles, with 5° resolution.

The BRDF values for incident angles ranging from 0 to 90 degrees, at 5 degrees intervals, can be compiled into a table containing 25,992 lines. For the agrivoltaics example, the "Grass Lawn" model is proposed for the ground material in the visible broadband, while Lambertian materials are used for other elements within the scenario.

A triangular mesh, corresponding to these textures, defines the spatial resolution for irradiance modelling. The resulting mesh vertices can be interpreted as virtual 'sensors' for ray-tracing-based tools.

Once the 3D mesh model of the agrivoltaics system is finalized, irradiance simulations are conducted for each time step and for all radiation components, including direct, isotropic sky diffuse, circumsolar sky diffuse, and reflected radiation from surrounding 3D elements. The irradiance values are subsequently aggregated into specific areas of interest, such as objects or zones, within the 3D scenario. These integrations are further evaluated over relevant time periods (e.g., daily, monthly, or yearly), depending on the crop type and its corresponding growth and harvest cycles. This methodology establishes a foundational basis for advancing and extending the project by integrating detailed material properties, precise BRDF modelling, and high-resolution irradiance simulations. It provides a framework for future developments, enabling more accurate assessments and optimizations tailored to specific agrivoltaics systems and scenarios.

3.4. Characterization of optical properties of materials for greenhouses

To aid the modellers into simulating the light transport on the greenhouse demonstration site, Fotoniq has collaborated by characterizing samples of Fotoniq's PAR+ coating but also on PV module structural materials such as the glass, encapsulants and the transparent backsheet.

Imec has carried out haze measurements and calculating Hortiscatter values (in collaboration with Fotoniq) of commercial PV module materials including different encapsulants (EVA, TPO and EVA), glass and transparent backsheets. As the modules in agrivoltaics greenhouses could be semi-transparent, this research is aimed at assessing the scattering or distribution of the transmitted light. This is aimed at enhancing the uniformity and distribution of the light at the crop canopy. The values obtained from the optical characterizations are currently being used as input for Imec's simulations in the implementations of diffusers in agrivoltaic greenhouses.

3.4.1. PV material sample fabrication and haze measurement

To enhance the light availability at the crop canopy in agrivoltaic greenhouses, semi-transparent and high light diffusing materials are desired.

Haze is mathematically defined as:

$$Haze = [Ts - Te]/Tt$$

The structural layout of the transparent (inactive) region of a semi-transparent c-Si PV module consists of glass/encapsulant/encapsulant/glass (or transparent backsheet). To investigate the scattering of the light incident on such regions, samples of size 5x5 cm with nine different encapsulants including ethylene vinyl acetate (EVA), thermoplastic polyolefin (TPO) and polyolefin elastomers (POEs) in between a front glass and a rear glass (or transparent backsheet) were manufactured using a PV module laminator. Figure 13 shows an example of the sample stack based, along with the structural layers.

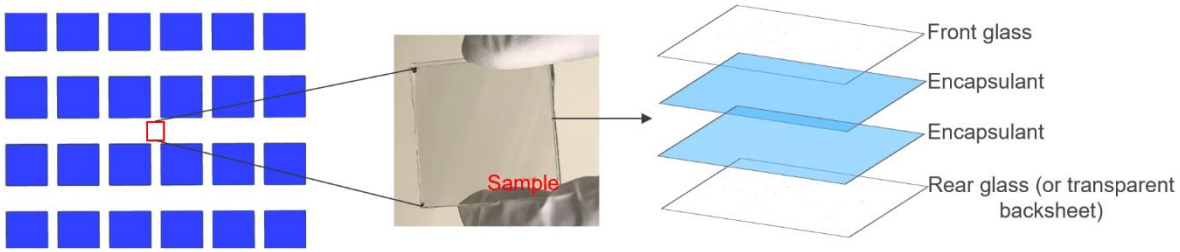

Figure 13: Schematic view of the structural layers of the samples used in haze measurements. Each sample represents the transparent region of a semi-transparent c-Si PV module.

Each sample stack was laminated and tested with the different encapsulants for both glass-glass (GG) and glass-transparent backsheet (GTB).

The haze measurements for each sample were carried out using an integrating sphere according to the ASTM D1003 standard and based on the three measurement steps shown in Figure 14 and similarly described by [17]. In Figure 14 A, the sample is placed at the entrance of the integrating sphere while a white reflecting plate at the rear ensures that the total sample transmitted light (T_t) is recorded by the sensor. In Figure 14 B, the exit of the integrating sphere is opened such that only the light scattered by the sample (T_s) at the entrance is recorded. In Figure 14 C, the light scattered by the equipment (T_e) is measured, which is subtracted from

the calculation of haze as shown in equation (1). The reflected light at the sample surface is neglected in this work. This study is focused on the diffusivity of light covering the PAR spectrum (400 -700 nm). The haze measurements were therefore carried out in 5 nm wavelength steps for light in the UV-VIS/NIR spectrum of 375 -800 nm. After the haze measurements, accelerated UV preconditioning tests based on the IEC 61215 standard were carried out to characterize the impact of potential optical degradation on the light scattering properties of the samples.

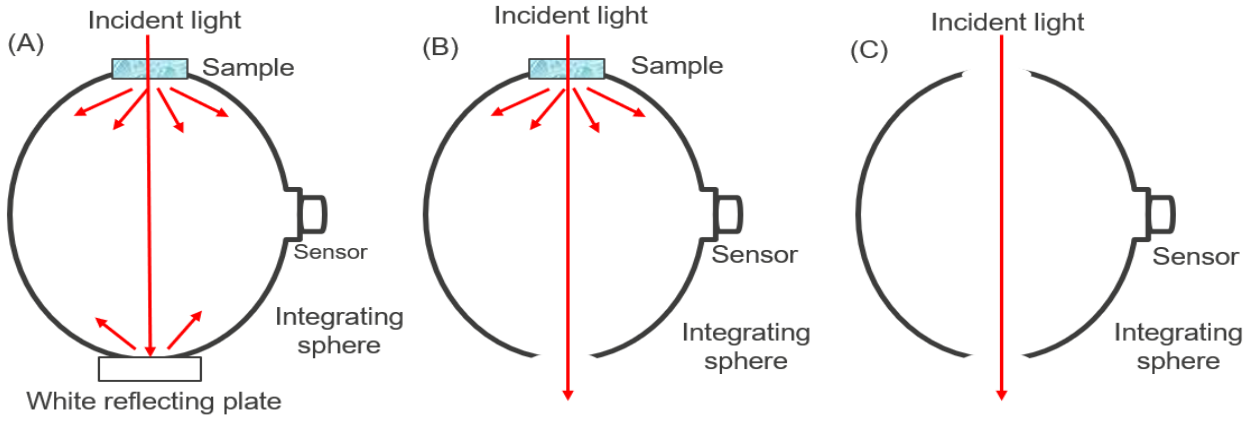

Figure 14: Illustration of different configurations used to measure the haziness of the PV material samples. (A) Shows the measurement of total sample transmittance, (B) measurement of sample diffuse transmittance and (C) measurement of the equipment diffuse transmittance.

3.4.2. Concept of Hortiscatter

The concept of haze has been established in horticulture to indicate the percentage of light scattered by 2.5°. However, haze measurements give no information on the angular dependence of the scattered light. To determine the angular light profile of the sample in transmission, reflection or both, bidirectional scattering distribution function (BSDF) measurements are needed. BSDF measurements can be separated into reflected and transmitted components respectively known as bidirectional reflectance distribution (BRDF) and bidirectional transmittance distribution (BTDF) measurements. BRDF and BTDF measurements represent how light is angularly reflected or transmitted respectively by a sample for a given wavelength and light angle of incidence (AOI).

In the Netherlands, BTDF information is used as input to compute what is known as Hortiscatter (HS). HS describes how evenly the incoming light is distributed in all directions. That is, how close the distribution of the transmitted light is to perfect light scattering. The NEN2675+C1:2018 standard describes the Hortiscatter of materials and is being used to characterize the light transmittance and scatter of the covering materials, screens and coatings of greenhouses.

The BTDF was obtained via an image-based scattering measurement approach using the Mini-Diff V2 from Synopsys. The Mini-Diff V2 measures the forward scatter diffuse materials. The method is based on measuring the lateral distribution of transmitted luminance using an imaging detector with 640×480 pixels to convert the

observed point-spread function to a surface's BTDF at an AOI of 0°. The detector has a dynamic range of 5 orders of magnitude and allows measurements in the visible range by using, as light sources, monochromatic LEDs with emission centres at 465, 525, and 630 nm. Figure 15 shows a picture and a schematic of its working principle alongside a description of its most relevant components. The BTDF data collected at 0° AOI is converted to Hortiscatter (HS) following the steps described by the norm NEN2675+C1 from 2018 where specific data normalization procedures are described.

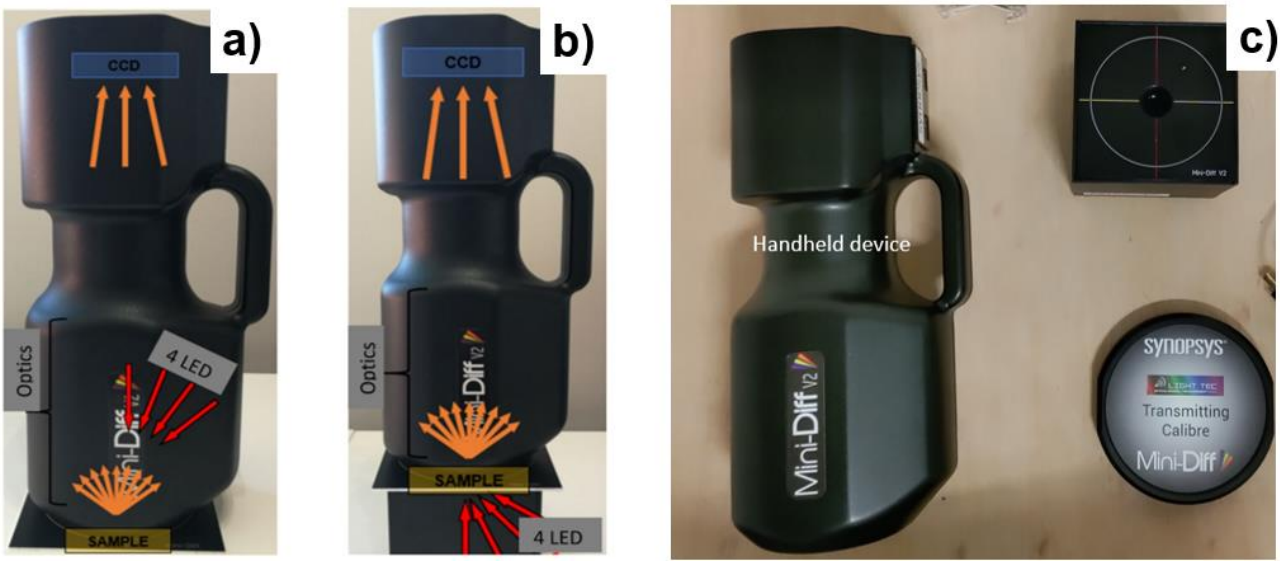

Figure 15: a) and b) Operating principle of the Mini-Diff V2 form Synopsys and c) its components. The handheld device has 4 LEDs, one for each AOI, namely 0°, 20°, 40°, and 60°. Each LED emits at three different wavelengths (465, 525, and 630 nm) and is focused on the lower part of it. The diffusely reflected light of the probed surface at its bottom is collected and detected by a camera situated on top allowing for BRDF measurements. For transmission measurements, a transmission module with other 4 LEDs allow the camera to capture the BTDF for the same configuration as with the handheld device.

3.4.3. Haze values

The haze values for the different samples are shown in Figure 16. The results show that the GTB samples (dash lines) offered higher light diffusivity compared to the GG ones. The backsheet was the main contributor to the haziness. Also, samples with the cross-linking encapsulants (POE and EVA) were less hazy compared to TPO. The UV ageing on average reduced the haziness of the GG PV samples. For the GTB samples, there was an observed discoloration of the polymer backsheet. Although no clear trend can be observed, most of the samples showed an initial and continuous decrease in haze with UV exposure, except for TPO-1 and TPO-3 samples which had an increase in haze from 40-65 kWh/m^2.

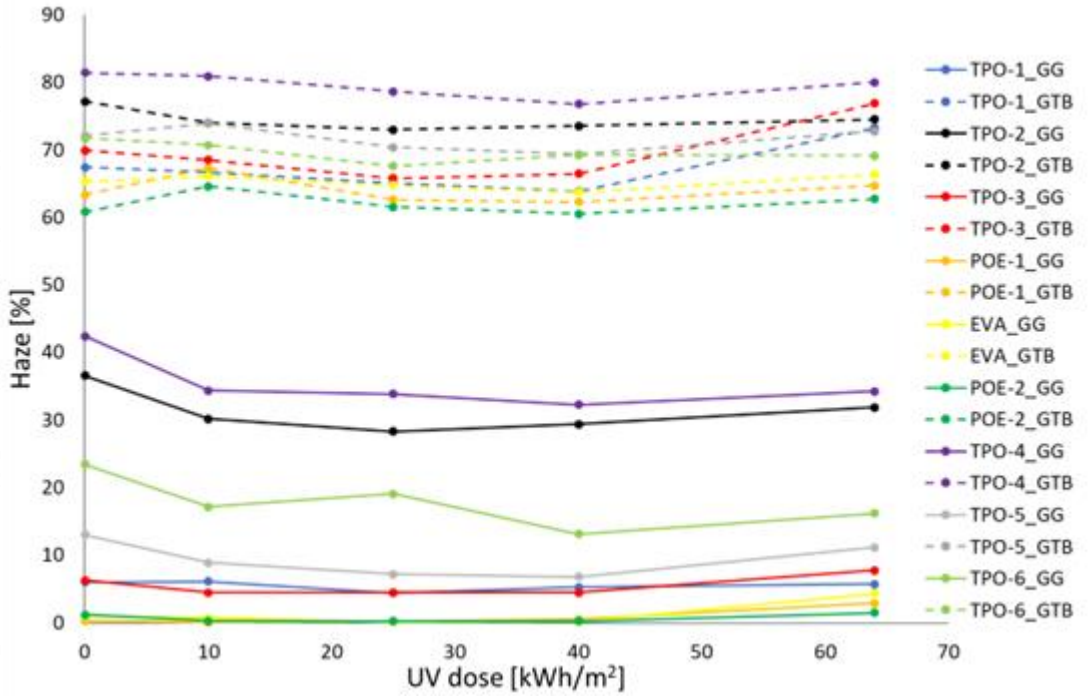

Figure 16: Haze values of the different samples after UV degradation.

3.4.4. Hortiscatter values

The haziest samples were further analysed in the BTDF measurements to get the HS values. Figure 17 shows the BTDF plots for the haziest GG and GTB samples. For the GG sample, (Figure 17-C), the BTDF behaviour is similar for all three wavelengths and is mostly specular, while the GTB sample shows an increase in light diffusivity with decreasing wavelength as seen in Figure 17-F. During the measurement by the Mini-Diff at each of the three wavelengths, a distribution function of the sample is obtained for each wavelength and for 0° AOI.

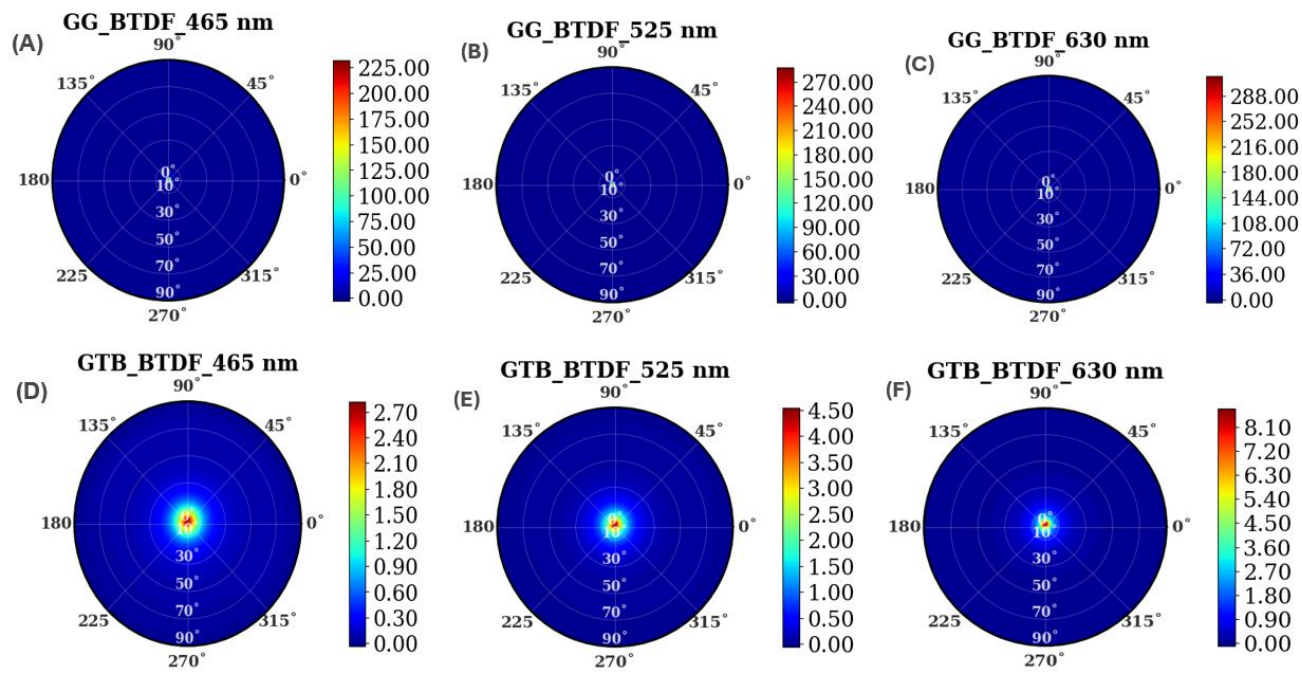

Figure 17: BTDF polar plots for the GG (A to C) and GTB (D to F) sample at 0° AOI for 3 wavelengths of 465, 525 and 630 nm. The BTDF data is used to calculate the HS for the two samples based on the NEN2675+C1:2018 standard.

Figure 18 shows the linear plot of the transmittance distribution function for the selected GG (Figure 18-A) and GTB (Figure 18-B) samples at 630 nm wavelength. The distribution function of the sample is plotted against that of a perfectly diffusing material; Lambertian light scattering and the light distribution of the measurement equipment. By averaging the HS at each of the three wavelengths of 465, 525 and 630 nm, HS values of 27.27% and 83.83% were obtained for the GG and GTB sample respectively.

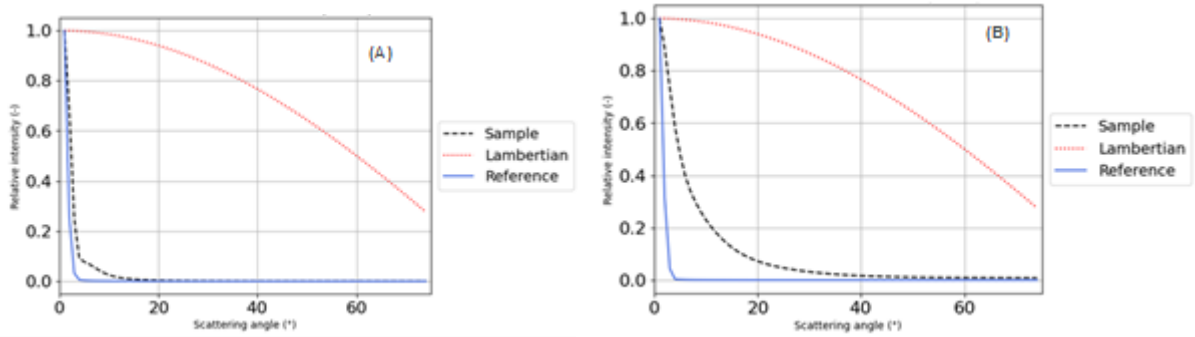

Figure 18: Linear plot of the distribution function of the (A) GG and (B) GTB sample as measured by the Mini-Diff V2 at 630 nm. The azimuth average transmission distribution function at 0° of incidence of the instrument, IR(θ)IR(θ), in blue. The same for the sample in black dashed line, IS(θ)IS(θ) as measured at 630

nm. The dotted line in red represents the cosine distribution of a Lambertian emitter. The HS values in the blue boxes represent that for the 630 nm wavelength and not the total average across all three wavelengths.

The HS value is not a direct conversion of the haze value. In general, a haze value can be used as guide to determine the Hortiscatter of a material. Hence, materials with the higher haze values are expected to have a higher HS. The haze and HS values presented in this work are comparable for the two samples measured. A comparison of the Haze and HS values for these two samples is plotted in Figure 19.

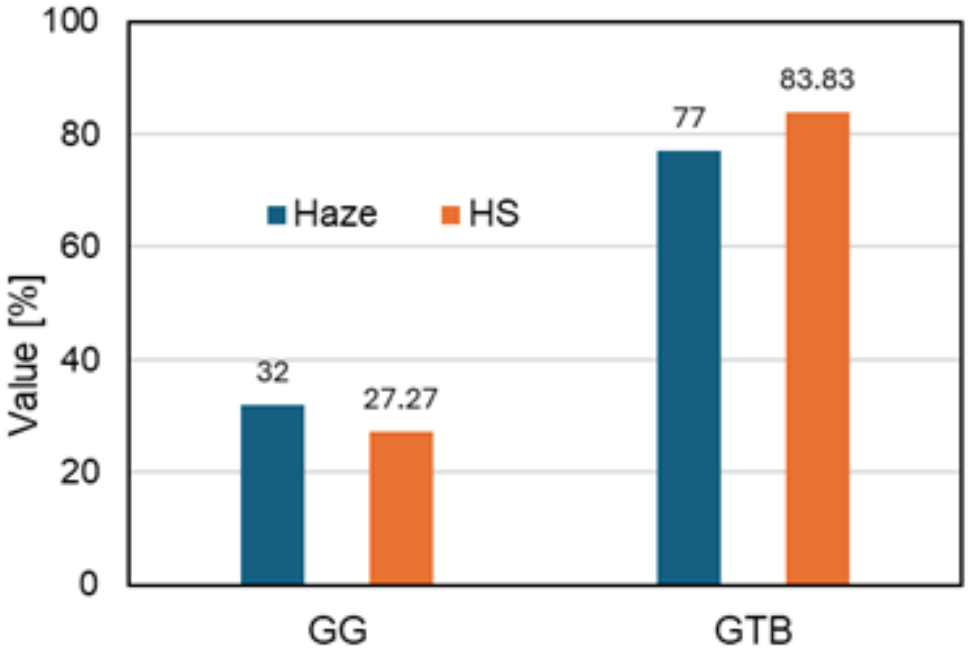

Figure 19: Summary of the highest haze and HS values for the best GG and GTB samples in this work. The encapsulant in each sample is TPO.

3.4.5. BSDF data of PAR+ coating on Optiwhite™ glass

Figure 20 shows BRDF and BTDF profiles of PAR+ coating over clear glass. The data is in a format that can be directly used as input for modellers when calculating the light transport in the greenhouse demo.

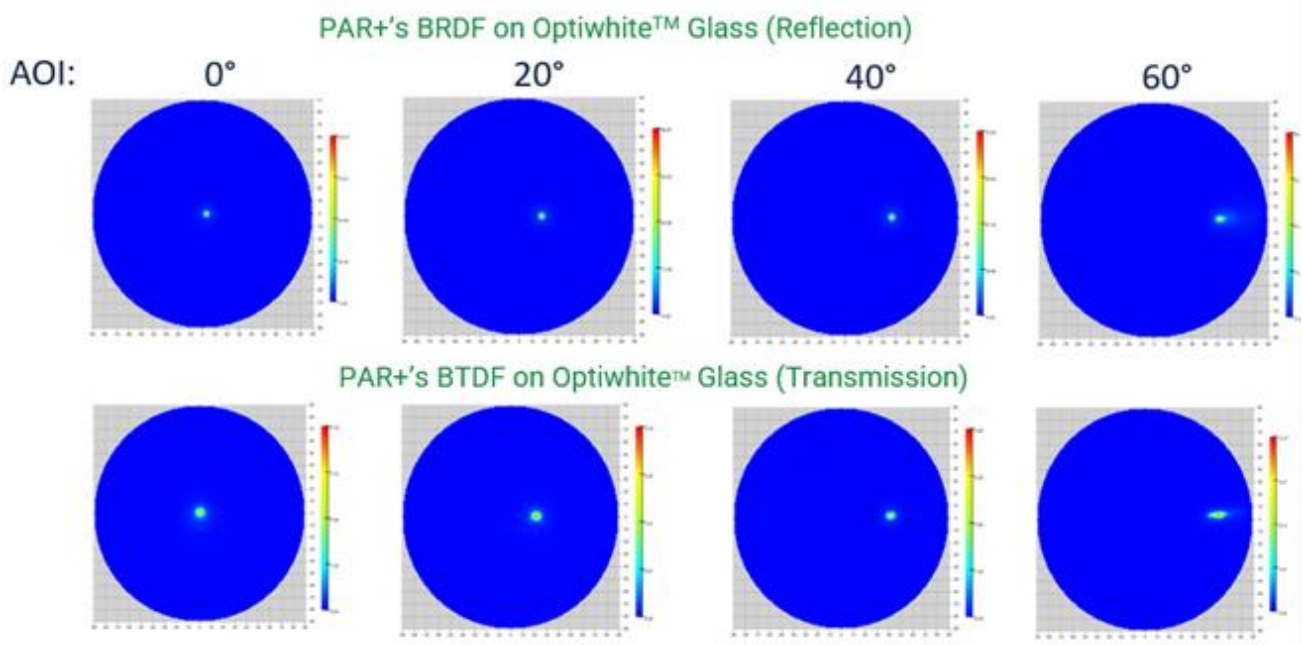

Figure 20: BRDF and BTDF profiles of PAR+ coating over clear glass. Data format can be used as input for modellers when calculating the light transport in the greenhouse demo.

The results from this work indicate that semi-transparent c-Si modules with a TPO encapsulant and a transparent backsheet could be suitable for increasing the light diffusivity in agrivoltaic greenhouses and open horticultural systems. The haze and Hortiscatter data from this work is being implemented as input for the modelling and simulation of irradiance distribution at crop canopies and for predicting potential increase in the crop yields in agrivoltaic greenhouses.

3.5. Light transmittance modelling for agrivoltaic greenhouses

To simulate light transmission through glass or other materials commonly used in agrivoltaic greenhouses, LuSim employs a methodology that separately models the diffuse and direct contributions of irradiance. This approach relies on dividing the irradiance into a set of view factors that are determined by the geometrical and material properties of the system. These view factors are then multiplied by an irradiance value, split into its diffuse and direct components.

3.5.1. Diffuse irradiance

The diffuse irradiance is modelled using a transmissivity factor (τ), which quantifies the proportion of light transmitted through greenhouse glazing materials, such as glass, EVA, plastic, or coatings. This factor is applied to each direction accounted for in the view factor calculations. The attenuation caused by the transmissivity factor is illustrated in Figure 21, which depicts the visibility of the sky as observed from the upper section of the crops. In this scenario, where glass is used as the glazing material, the areas covered by the glass act as a uniform filter with a transmissivity value (τ) applied to the diffuse irradiance coming from the sky. Areas

obstructed by solid objects, such as PV panels, completely block the contribution of diffuse irradiance. The view factor at each observation point, multiplied by the diffuse isotropic component, determines the diffuse irradiance contribution to the overall light distribution.

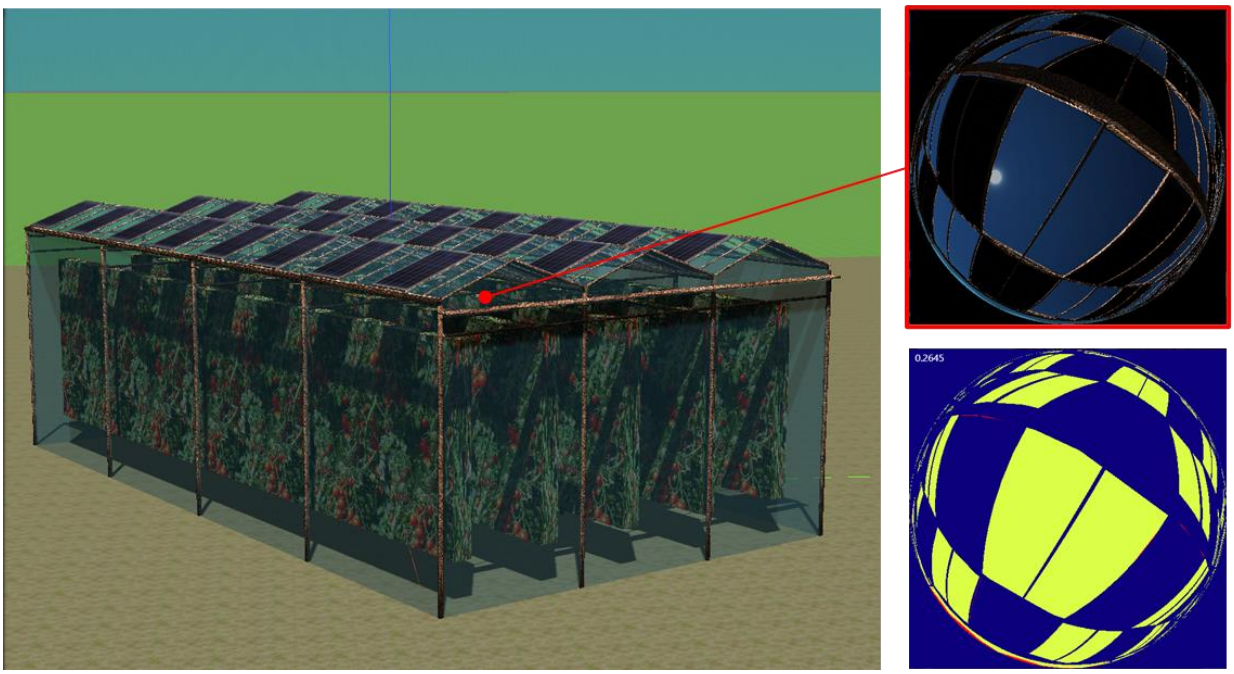

Figure 21: Effective view factor for the diffuse component of the irradiance as seen by the top of the crops.

3.5.2. Direct irradiance

For the direct irradiance, the simulation is more complex, as it includes a diffusion factor over the irradiance that comes from the sun direction that considers three angles, as shown in Figure 22:

- Incident angle of the sun (θ_i)
- Transmitted azimuth (ψ_t)
- Transmitted zenith (θ_t)

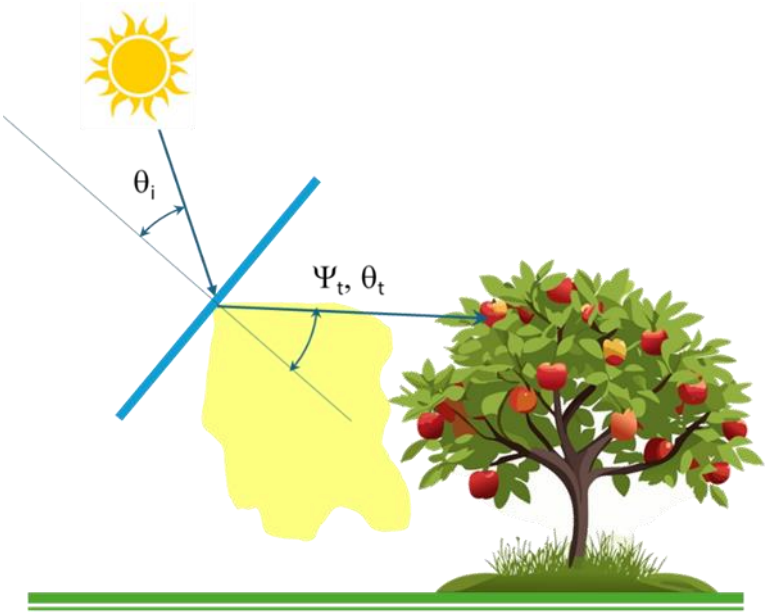

Figure 22: Generic implementation of a diffusion factor for the direct component of the irradiance.

Several models can be applied to determine the diffusion factor applied to directional irradiance, each introducing variations in how the overall irradiance contribution is calculated. Regardless of the model used, the spherical rendering of the view factor from the observer's perspective differs in the contribution to the overall irradiance, as illustrated in Figure 23. In this example, for visualisation purposes only, a function is applied that introduces an attenuation factor based on the angular separation from the sun's direction.

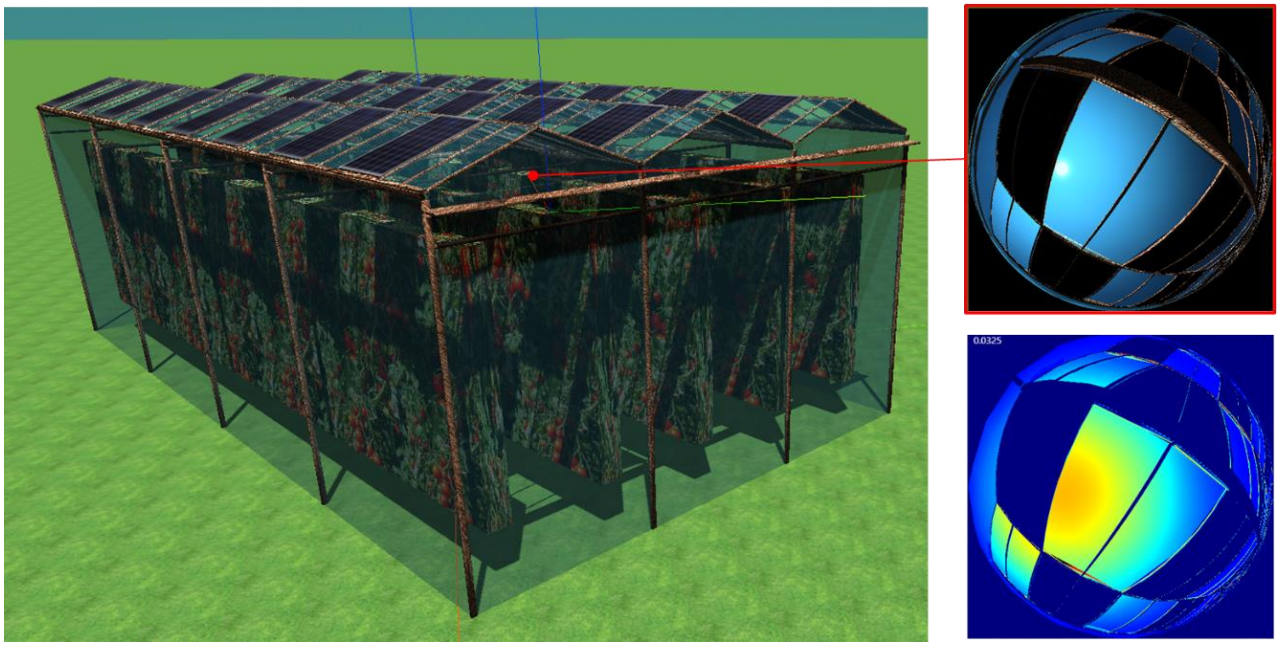

Figure 23: Example of attenuation of the diffusion factor when separating from sun direction.

For most practical agrivoltaic applications, the general light-diffusing model can be simplified to reduce computational demands and enhance its practicality for use with the types of inputs typically available in commercial agrivoltaic engineering projects. The simplified model is illustrated in Figure 24.

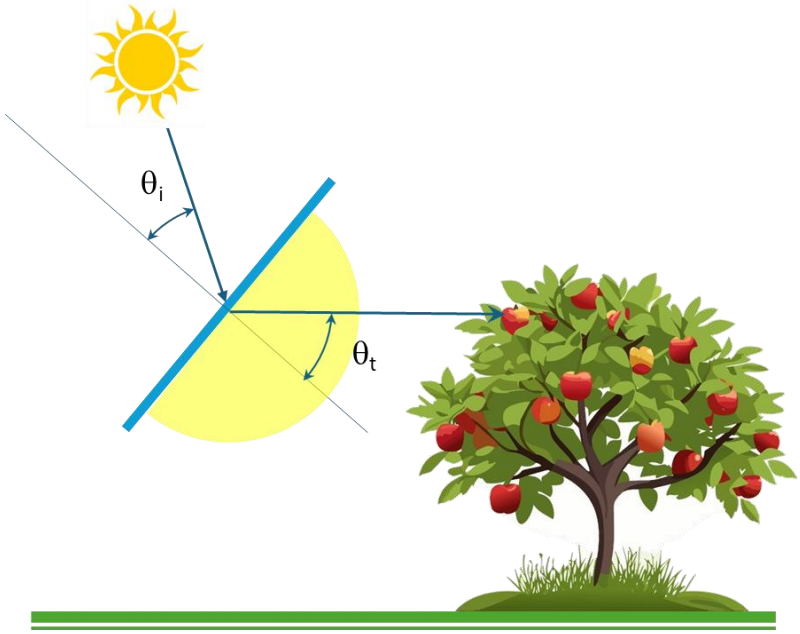

Figure 24: Homogeneous diffusion factor considered for the simulation of the greenhouse.

In this case, the Bidirectional Transmissivity Diffusion Factor (BTDF) is considered to depend solely on the incident angle of the sun relative to the normal of the glass surface. This factor can be expressed as:

$$BTDF = \frac{\tau cos\theta_i}{\pi}$$

where τ is the transmissivity of the glass.

The rationale behind this expression is to ensure energy conservation across all directions within the hemisphere of diffusion. When applied to the simulated render from an observer located at the top of the crops, the areas covered by the glass exhibit a uniform appearance. This uniformity is determined by the local incident angle of the sun with respect to each glass normal, as shown in Figure 25.

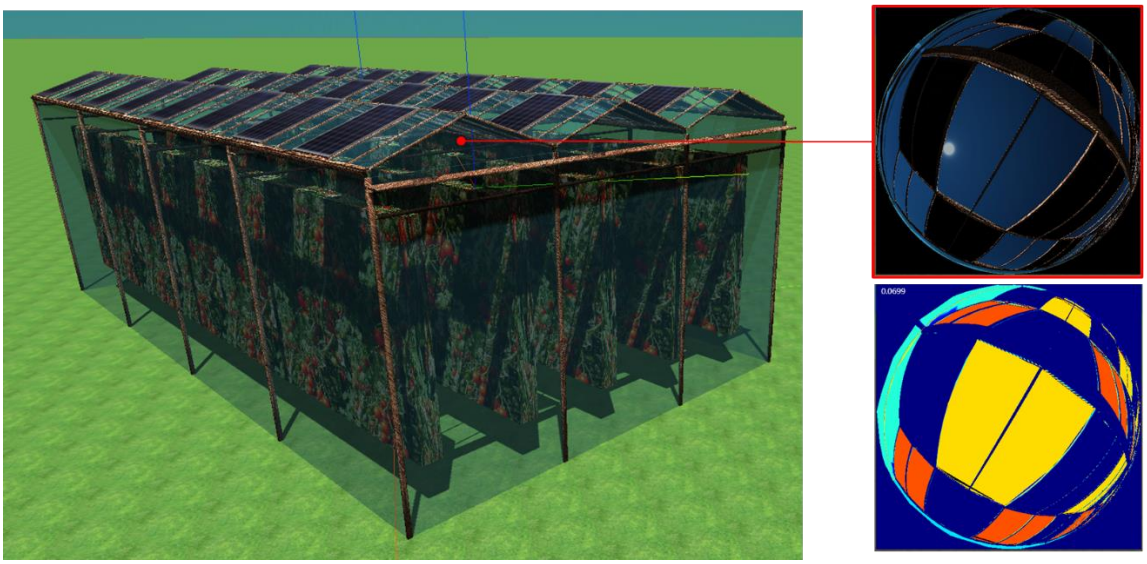

Figure 25: Example of attenuation of the diffusion factor when separating using a Lambertian model.

For the application of light-diffusion modelling to the greenhouse considered in this work, LuSim uses a transmissivity factor τ of 0.6 for the various glass elements of the greenhouse. This value is typical for glass with a diffusing coating of this kind.

The Hay-Davis [11] transposition model is implemented in LuSim to separate the diffuse irradiance into two components: an isotropic component and a circumsolar component. The circumsolar component, representing a directional element of the diffuse irradiance, is treated similarly to the direct irradiance in this simplified approach. The product of the effective view factor, the direct irradiance, and the circumsolar component is used to calculate the contribution of the directional part of the irradiance.

4. TOOLS VALIDATION AND BENCHMARKING

4.1. Methodology overview

Validation and benchmarking of modelling tools is critical to ensure their reliability and applicability to agrivoltaic systems. The tools developed by the different project partners in the SYMBIOSYST project use varied approaches, each with its own advantages and limitations. These tools are capable of simulating different features and aspects of light modelling. To provide a fair and meaningful evaluation, a common ground is needed for their validation and benchmarking. This exercise allows us to compare their performance across a shared set of scenarios, ensuring consistency in the evaluation process.

When validating a PV modelling tool, multiple approaches can be considered, each with its pros and cons. A commonly used method involves comparing model outputs to light measurements obtained from real-world scenarios. While this approach has been widely applied in research, it poses significant challenges in the context of agrivoltaics. Agrivoltaic systems involve highly complex 3D environments, where accurately defining the exact 3D scene is challenging. Furthermore, the nature of the 3D environment evolves over time, influenced by crop growth, system modifications, and other dynamic factors. These challenges are compounded when the system is a demonstrator, as it must first be constructed before sensors can be installed. Once installed, these sensors require careful calibration and ongoing maintenance. The precise location and characteristics of the sensors, as well as the quality of the measurements, often become a subject of investigation themselves, which is the focus of another task within the SYMBIOSYST project.

Given these complexities, light measurements often lack the accuracy needed to serve as a reliable reference for benchmarking modelling tools. In many cases, measurement uncertainties are comparable to or exceed the modelling uncertainties, making it difficult to draw definitive conclusions about the tools' performance based solely on measured data.

To address these challenges, this validation and benchmarking exercise uses a set of carefully designed test cases. These test cases represent a combination of simple and progressively more complex scenarios. The simpler cases allow for validation against analytical solutions, which can be reliably calculated for specific reference points and conditions. The more complex cases introduce challenges typically encountered in light modelling, such as reflectance modelling, spatial and temporal resolution, and the trade-offs between accuracy and computational resources. These cases are designed to evaluate the modelling tools' ability to handle these difficulties while providing a structured framework for comparison.

As an initial step, a simple scenario is considered where the irradiance on both sides of a single PV module is computed. This scenario provides a controlled environment for calibrating the methodologies and comparing the tools. In this setup, the module is positioned horizontally, resulting in distinct irradiance contributions for each side.

For the upper side of the module, irradiance is composed of the direct and circumsolar components from the sun's direction and the diffuse contribution from the sky, with no contribution from ground reflections due to

the module's horizontal orientation. In contrast, the rear side of the module receives no direct or diffuse contribution from the sky; instead, it is entirely dependent on reflections from the ground. This controlled setup allows for an analytical solution for reference points, serving as a foundation for validating and benchmarking the tools.

This approach, which combines simple and analytically solvable cases with more complex scenarios, ensures that the tools are validated comprehensively. It allows the strengths and limitations of different methods to be assessed while addressing the practical challenges of modelling in agrivoltaic systems. This framework forms the basis for reliable comparisons and supports the continued improvement of modelling tools for agrivoltaic applications.

4.2. Cases studied

The system under evaluation consists of a simple square PV module with dimensions of 1 m x 1 m, positioned horizontally above a flat terrain at varying heights. The module is arbitrarily located at geographical coordinates near the LuciSun office in Brussels (50.8384°N, 4.37643°E). The studied 3D scenario includes an inner ground area measuring 100 m x 100 m, surrounded by an outer ground area extending to 1 km x 1 km. The entire setup is defined within a Cartesian coordinate system, where the centre of the scenario aligns with the origin (0, 0, 0). The PV module, with a total surface area of 1 m² and negligible thickness, is positioned horizontally at the centre of the scenario.

The objective of this case study is to compare the modelled total global tilted irradiance (GTI) or total global incident irradiance reaching the middle of the back and front side of the PV module. This includes evaluating the total incident irradiance/irradiation at various temporal resolutions. The analysis aims to assess the total incident irradiance reaching the front and back side of the PV module and compare the results across different modelers.

Both ‘studied ground’ and the ground area encompassing that, called ‘external ground’ area has an albedo of 20 % (0.2) with a simple Lambertian reflection, while the PV cells are assigned an albedo value of 0.05. In some cases, an alternative approach is used for the terrain, including a chessboard pattern of alternating tiles of 10 x 10 cm with different albedos of 0.3 and 0.1, which is still equivalent to a 0.2 albedo overall. A view of that configuration can be seen in Figure 26.

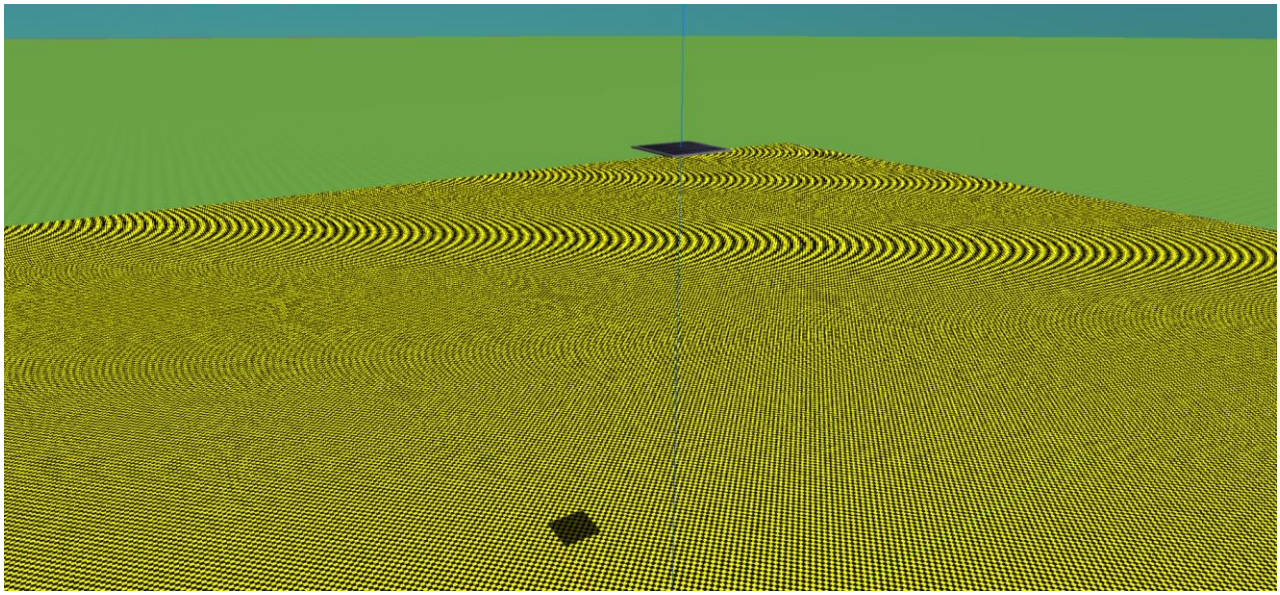

Figure 26: 3D scene with a chessboard albedo pattern over the ground.

The **main parameters** varied to evaluate their influence are as follows:

- **Distance between the module and the ground**: When the module is positioned very close to the ground, it blocks a significant portion of the irradiance that would otherwise reach and reflect off the ground. Conversely, when the module is placed further from the ground, its effect on ground irradiance becomes negligible, minimising its impact on reflections.
- **Albedo material of the ground**: To assess the resolution capabilities of the different simulation models, various ground materials and shapes are considered for the 100 m x 100 m inner ground section. These variations help capture the sensitivity of the models to changes in reflectance properties.
- **Presence of obstacles between the module and the ground**: The influence of obstacles is evaluated to understand their impact on the interaction of light between the module and the ground.

Three different cases were considered:

- **Case 1:** In this case three different heights for the location of the PV module are considered: 0.5 m, 2 m and 50 m. The terrain used was a uniform ground albedo of 0.2.
- **Case 2:** The height of the PV module is fixed to 10 m over the ground, and an alternate pattern of high albedo (0.3) and low albedo (0.1) patches of 10 cm x 10 cm is used on the inner ground.
- **Case 3:** The inner ground considered in Case 1 is used, with the module at a height of 10 m as in Case 2, but an obstacle in the shape of an opaque mask, with albedo 0, made of a checkerboard-patterned net of 10 x 10 x 2.5 cm blocks is included at an intermediate height of 5m between the module and the ground, as shown in Figure 27.

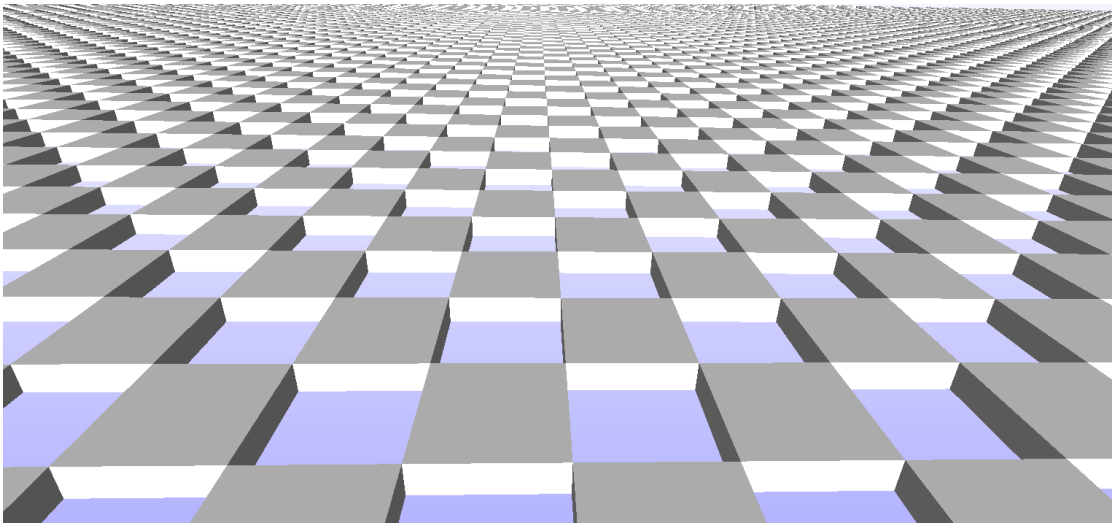

Figure 27: Details of chessboard pattern the net used in Case 3.

4.3. Solar resource

The solar resource data is derived from the hourly TMY dataset provided by PVGIS/SARAH2 [12] for the geographical coordinates 50.8384, 4.37643. For sky irradiance modelling each partner uses their preferred methods. TUD and Imec utilize the Perez All-Weather sky model [13], while LuciSun employs the Erbs model for decomposition combined with the Hay-Davis transposition model. The horizon profile is excluded from this study, ensuring a uniform focus on the selected models for evaluating irradiance.

4.4. Metrics used

The comparisons are based on metrics such as Root Mean Square Deviation (RMSD) and Mean Bias Deviation (MBD) to check for consistency and accuracy across outcomes from different modelers. The metrics used are:

- Mean absolute deviation (MAD): Measures the average absolute difference between the outputs of two software programs as:

$$MAD = \frac{\sum_{i=1}^{n} |S_{1i} - S_{2i}|}{n}$$

- Root mean square deviation (RMSD): Focuses on differences between software outputs.

$$RMSD = \sqrt{\frac{\sum_{i=1}^{n} (S_{1i} - S_{2i})^2}{n}}$$

4.5. General approach followed by the partners

4.5.1. LuSim (LuciSun)

LuSim, a software tool developed by LuciSun, calculates irradiance at various points within a scene by multiplying the different irradiance components (diffuse and direct) by a set of precomputed 3D view factors. These view factors are generated using GPU (Graphics Processing Unit) computing capabilities and account for the scene's geometrical characteristics and material properties, such as directional albedo. The computation of these view factors requires representing the scene using triangular meshes to enable proper rendering within the GPU engine. The resolution of the mesh significantly influences both the accuracy of the results and the computation time. To achieve an optimal balance between mesh size and accuracy, several analyses were conducted, and the findings were applied in this study.

The following view factors are considered:

- **View factor for isotropic diffuse irradiance**:

  This factor accounts for all geometrical considerations for a specific position and orientation of a local observer. When multiplied by the horizontal isotropic diffuse component, it quantifies the contribution of irradiance reaching the observer point directly from the sky. Figure 28 illustrates this view factor as perceived by an observer at a point on the ground. The shading effect caused by the plate reduces the field of view from an initial value of 1.0 to 0.7789. Consequently, when this view factor is applied to the horizontal isotropic diffuse irradiance, it indicates that approximately 22.1% of the irradiance is obstructed and does not reach the point.

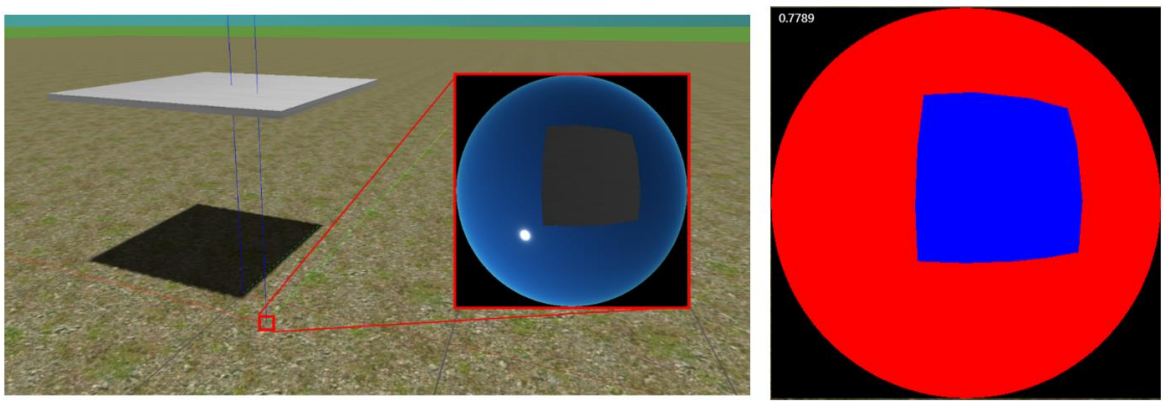

Figure 28: View factor for isotropic diffuse irradiance for a point located on the ground.

- **View factor for "effective" albedo on isotropic diffuse irradiance**:

  This factor accounts for the geometrical and reflective properties of elements in the scene that reflect photons originating from the sky. When multiplied by the horizontal isotropic diffuse component, it represents the portion of isotropic diffuse irradiance reflected by the scene's objects that reaches the observer point.

The view factor considers all effects influencing isotropic diffuse irradiance originating from the sky and subsequently reflected by various objects. Two key factors are involved in this process. First, the objects reflecting the irradiance have a specific diffuse albedo, which depends on their material properties. Second, partial shading reduces the amount of irradiance from the sky that reaches the reflective surfaces at any given point. This shading effect is represented by the previously discussed view factor for isotropic diffuse irradiance. Consequently, the evaluation of this view factor involves two phases.

In the first phase, the sky view factor is computed at different locations on the reflective surface (such as the ground or other objects). The required resolution for these calculations was determined through a trade-off analysis to balance accuracy and computational efficiency. Figure 29 illustrates this process, showing view factor values computed on the ground at various distances from the shading influence area. For example, the view factors at these points are 0.7558, 0.8353, and 0.9174, demonstrating how the shading impact diminishes as the distance from the shading source increases.

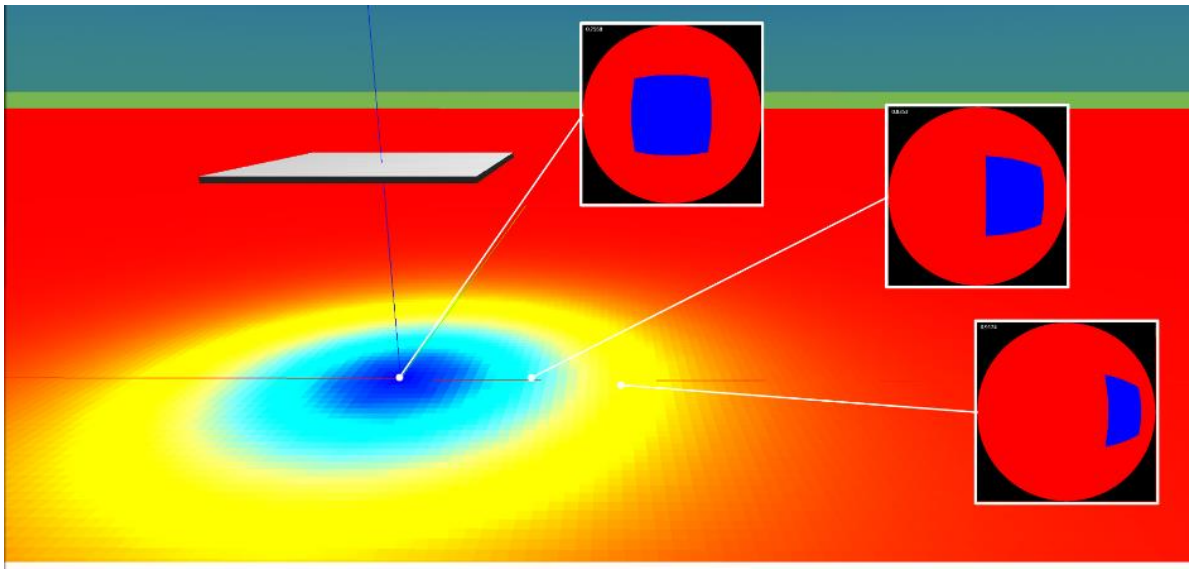

Figure 29: View factor for isotropic diffuse irradiance on ground at various distances from shading influence.

In the second phase, the shading information computed in the first phase is applied to the reflective albedo of the ground and other reflective objects. The scene is then rendered again from the observer's point of view at the final destination. For instance, if the reflective object (in this case, the ground) has a diffuse albedo of 0.2, the points shown in Figure 29 exhibit "effective" albedo values of 0.1512, 0.1671, and 0.1835. These values progressively approach 0.2 as the distance from the shaded influence area increases, reflecting the reduced shading effect. This effectively reduces the observed view factors by a factor of 0.2, corresponding to the albedo of the ground.

This phenomenon is further illustrated in Figure 30, which shows the "effective albedo" view factor as observed from a point located on the back of the plate. The overall value for the entire projection, considering this specific position of the plate (or PV module), is calculated to be 0.1795.

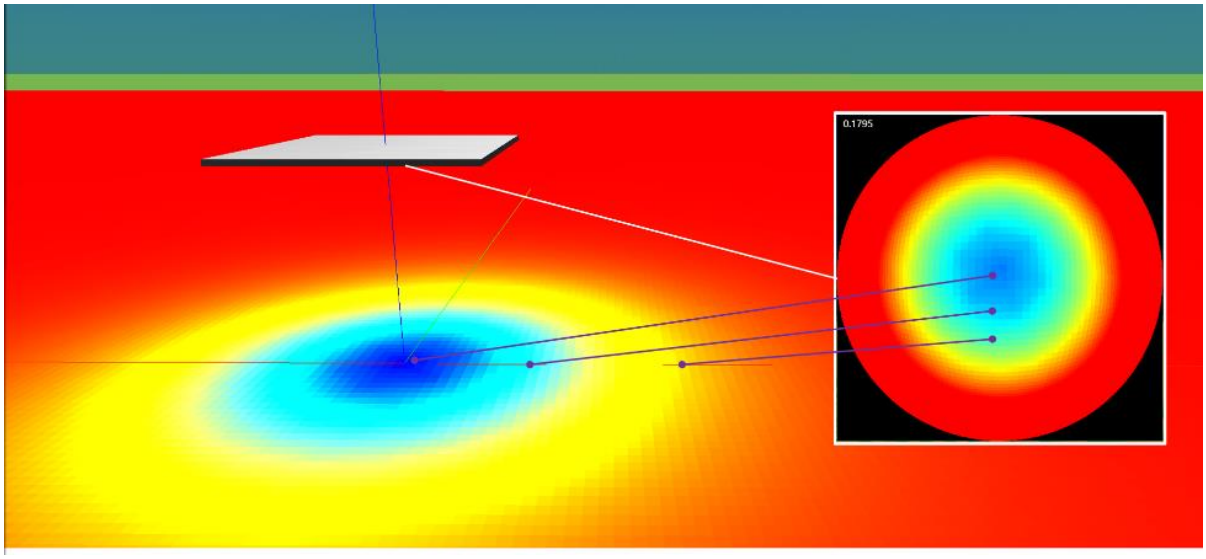

Figure 30: View factor for “effective” albedo on isotropic diffuse irradiance seen from bottom of plate.

- **View factor for “effective” albedo on directional irradiance (direct and circumsolar diffuse)**:

  This factor considers the geometrical and reflective properties, along with shading and directionality, of irradiance originating from the sun's direction. It represents the contribution of directional irradiance (direct and circumsolar) that reflects off various surfaces in the scene and reaches the observer point. The irradiance reflected from the ground or other objects can be modelled using different approaches. A Lambertian reflectance model, which assumes uniform scattering, is a practical approximation for most agrivoltaic engineering applications. Alternatively, a Bidirectional Reflection Distribution Function (BRDF) can be used for higher accuracy when needed.

  This view factor also accounts for the sun's elevation and the shading patterns present in the scene, as observed from the specified point. For example, Figure 31 demonstrates this factor for two different sun positions during the summer solstice, equinox, and winter solstice. The shadow cast by the PV module itself is clearly visible in these examples.

  When applied to the direct and diffuse circumsolar irradiance, this view factor incorporates key parameters, including the observer's position and orientation, material properties, shading effects, and the sun's position relative to the scene.

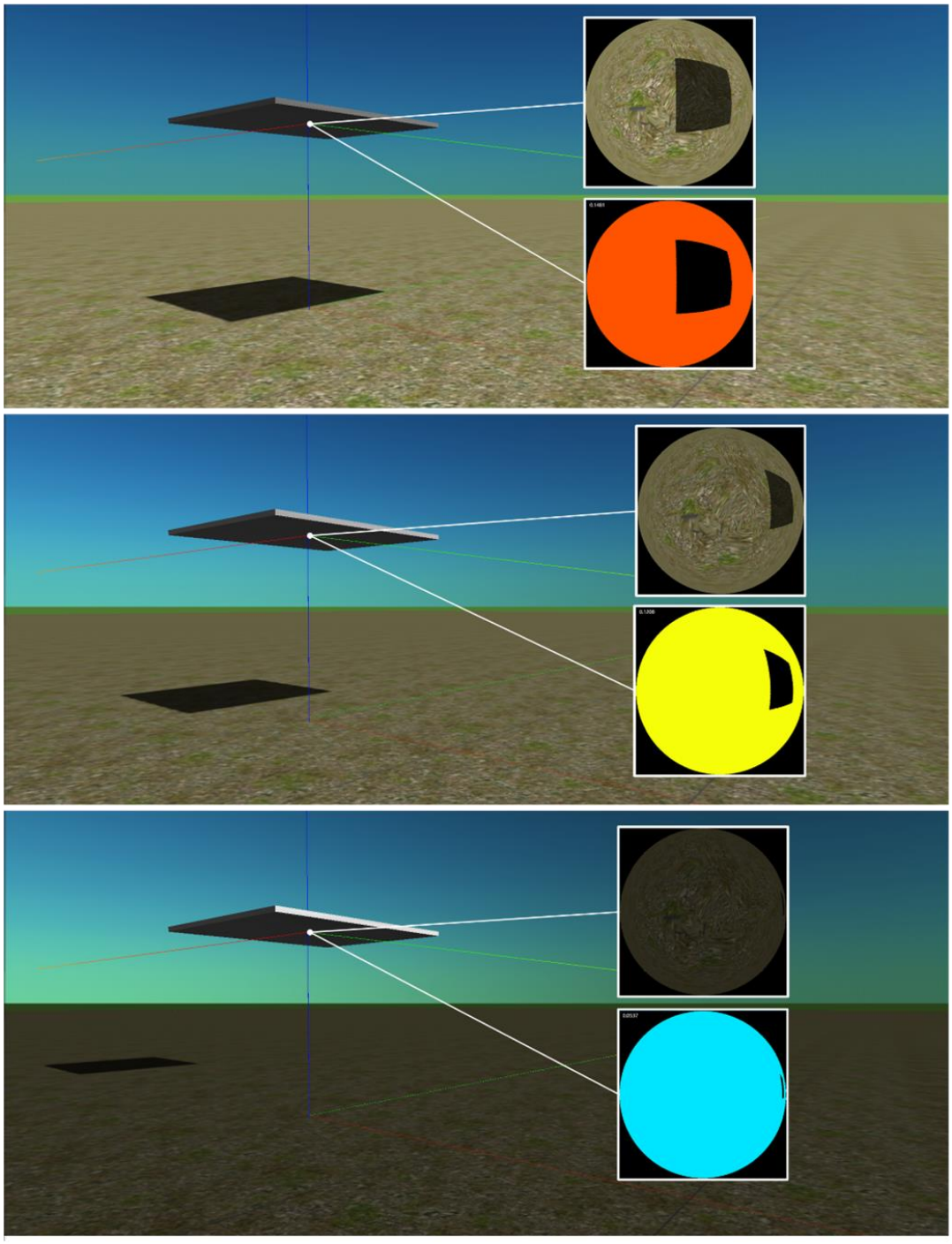

Figure 31: View factor for “effective” albedo on directional irradiance (direct and circumsolar diffuse) for different sun positions (Solar noon, up – June 21st, centre – Sep 21st, bottom – Dec 21st).

4.5.2. TUD

In our efforts to eliminate various sources of uncertainty, we formulated multiple “ideal” case studies, two of which are illustrated in Figure 32. These simplified scenes allow the isolation of error. For this reason, certain aspects of the tool, such as the number of wavebands, previously described in Figure 3, were neglected.

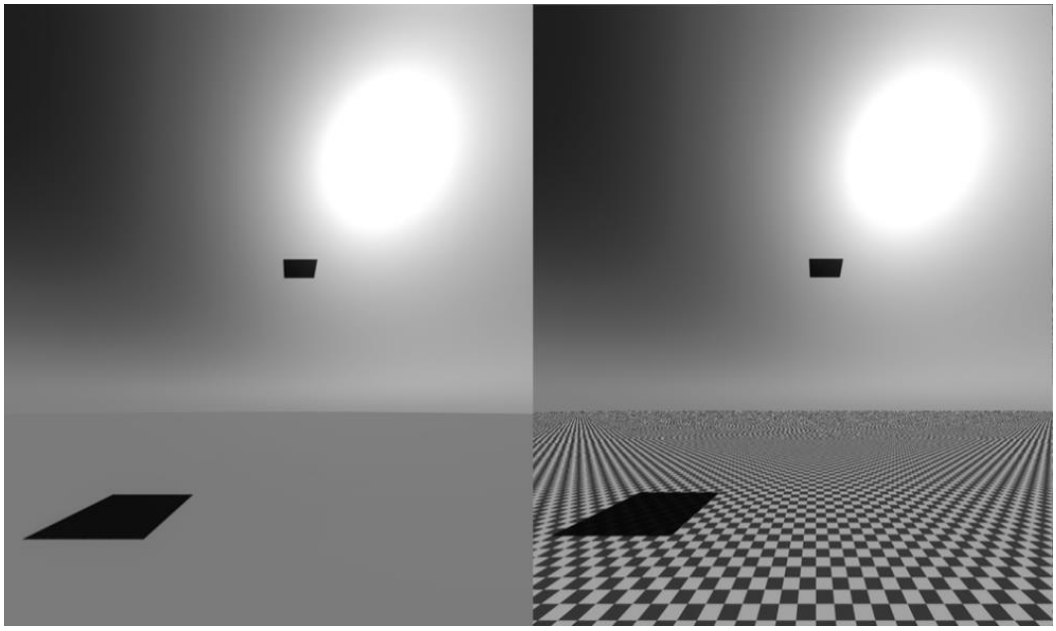

Figure 32: Rendering of the scene in Case 1 (left) with the PV module above homogeneous ground, and in Case 2 (right) with non-homogeneous ground featuring a chessboard pattern.

4.5.3. Imec

The 3D scene of Case 1 was set up according to the inputs described in the input section. The setup involves positioning the PV module and the ground at the centre of the scene:

- Internal Ground: A 100 x 100-unit area representing the internal evaluation region.
- PV Module: A module with dimensions of 1 m x 1 m, positioned horizontally at various heights above the ground as mentioned above in the inputs.

The 3D scene was created using the design tool SketchUp Pro 2023. The radiance files from the scene were then imported into the simulation framework for ray tracing. Figure 33 below shows the 3D scene generated. In this ray tracing approach, the irradiance is computed by placing sensors at specific points of interest. For case 1, the sensors are placed at the front and rear of the PV module, to assess the irradiance on these specific regions. The amount of light reaching the rear of the PV modules is dependent on the ground albedo and the reflectance properties of any other materials present in the scene. As the irradiance on the ground is not being assessed in this case, the ground is given a Lambertian reflectance value (albedo of 20 %).

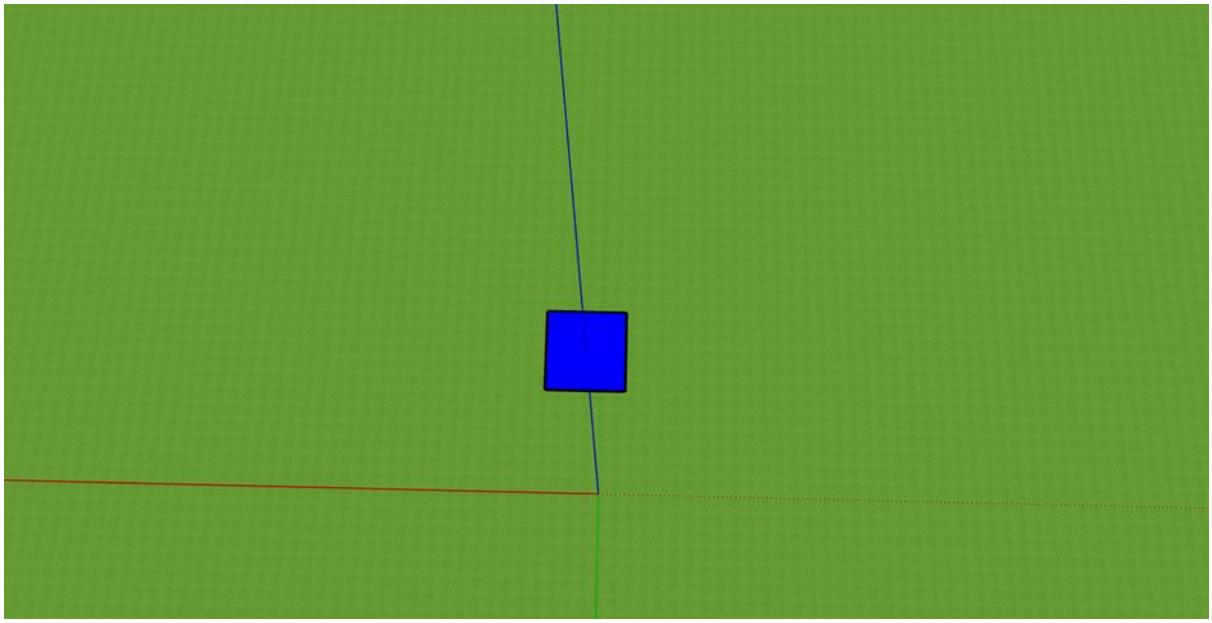

Figure 33: Imec's 3D scene generated from SketchUp Pro 2023 for Case 1. Scene shows the PV module at the centre of the grassland (field).

4.6. Comparison of results

4.6.1. Case 0: Reference case with analytical solutions

The benchmarking and comparisons between the different modelling tools were conducted using a square plate of 1 m x 1 m as the light receiver. This setup provides a practical and straightforward case that is easily manageable across all simulation tools. However, from a theoretical perspective, obtaining an analytical reference solution is more straightforward with a disk rather than a square. This is particularly true for points located directly beneath the disk, along its vertical axis, as shown in Figure 34, due to the axisymmetric properties of the disk.

To address this, a preliminary step in the validation exercise involved first obtaining an analytical reference solution for the disk. The results were then compared to those for a square plate of the same area (1 m²) to determine whether the two cases could be practically assimilated under certain conditions. This preliminary validation included a comparison of the analytical results obtained for the disk with the 3D view factor approach implemented in LuSim.

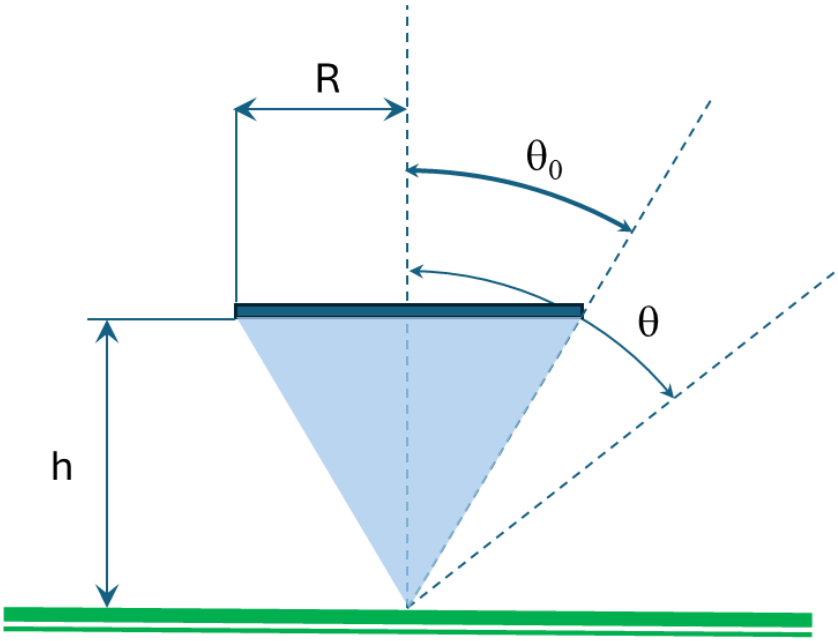

Figure 34: Sky fraction covered by a disk of radius R at a height h.

In this specific case, the fraction of isotropic diffuse irradiance received at the point directly beneath the disk can be calculated using the following mathematical expression:

$$f = \frac{1}{\pi}\int_{\theta_0}^{0}\int_{0}^{2\pi} cos\theta sin\theta d\varphi d\theta = 1 - sin^2\theta_0$$

where φ is the azimuthal angle of the differential solid angle (constant as we consider an axisymmetric case with a disk) and the angle θ_0 is derived from the relationship between the disk radius R and the height h, given by:

$$tan\theta_0 = \frac{R}{h}$$

As this fraction corresponds to the definition of the sky view factor on isotropic diffuse irradiance in LuSim, a specific simulation using the setup shown in Figure 35 was used.

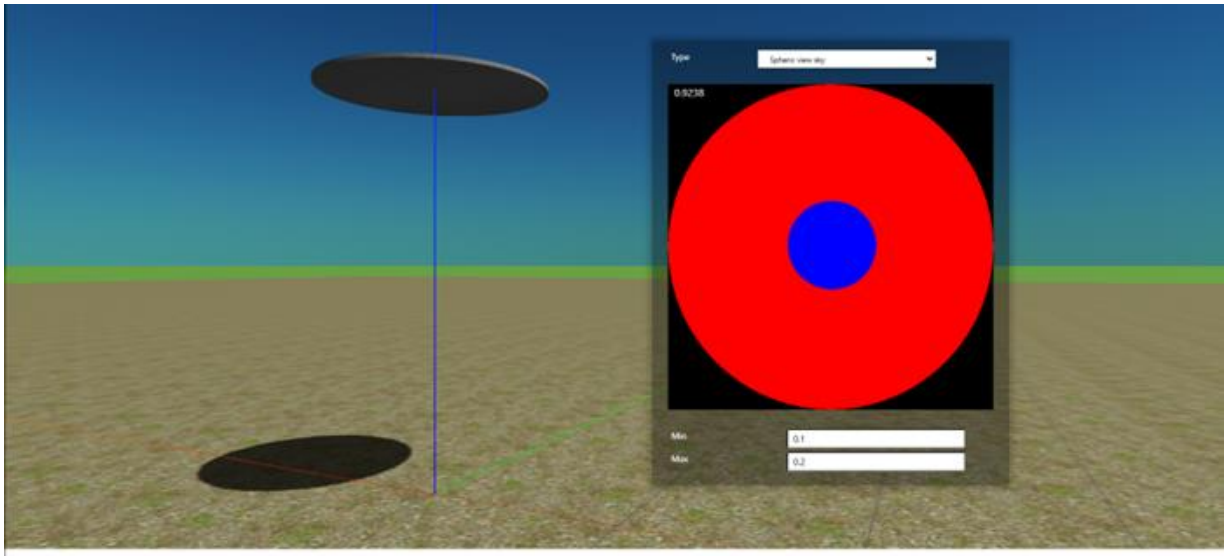

Figure 35: View factor for isotropic diffuse irradiance on the ground with the disk as an obstruction.

The evolution of this view factor with the distance between the disk and the ground, as modelled using LuSim, demonstrates values that closely align with those predicted by the analytical model, as shown in Figure 36. In this setup, a disk with a radius of 0.564 m was used, providing the same blockage area as the 1 m² square under consideration.

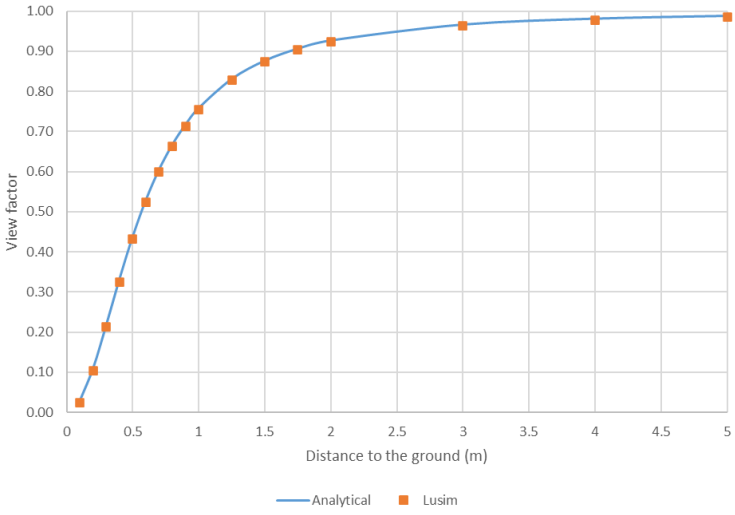

r	0.564			
h	theta	f analytical	f computed	Difference
0.1	79.95	0.0305	0.0248	18.6%
0.2	70.48	0.1116	0.1033	7.5%
0.3	62.00	0.2204	0.2133	3.2%
0.4	54.66	0.3345	0.3255	2.7%
0.5	48.45	0.4399	0.4317	1.9%
0.6	43.24	0.5307	0.5234	1.4%
0.7	38.87	0.6062	0.5998	1.1%
0.8	35.19	0.6678	0.6623	0.8%
0.9	32.08	0.7179	0.7129	0.7%
1	29.43	0.7585	0.7541	0.6%
1.25	24.29	0.8308	0.827	0.5%
1.5	20.61	0.8761	0.8728	0.4%
1.75	17.87	0.9058	0.9027	0.3%
2	15.75	0.9263	0.9233	0.3%
3	10.65	0.9658	0.9633	0.3%
4	8.03	0.9805	0.9778	0.3%
5	6.44	0.9874	0.9848	0.3%

Figure 36: Comparison of view factor on isotropic diffusion irradiance with LuSim or analytical solution.

To assess the differences between using a disk (which can be validated analytically) and a square (used in the test cases) with the same area, simulations were performed for both geometries. The results, shown in Figure **37**, illustrate the expected behaviour of view factors when transitioning from a disk to a square. The most significant differences occur when the plate is positioned close to the ground, where the shape has a

pronounced effect on the view factor. However, as the plate is elevated, the influence of the shape diminishes rapidly, and height becomes the dominant factor affecting the results.

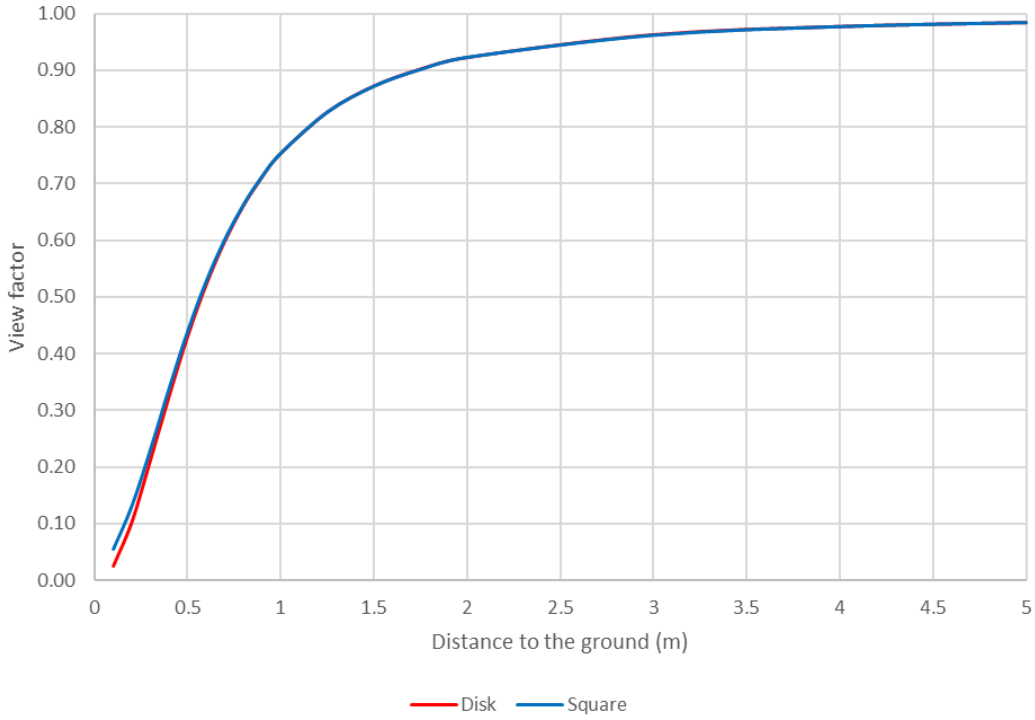

Figure 37: Comparison of view factors for isotropic diffuse irradiance with a disk (computed analytically) and a square plate (computed with LuSim).

The similarity between the cases of the square and the disk at a reasonable distance from the ground justifies the use of the square as a proxy for subsequent validations, comparing the results of the modelling tools with the analytical reference. For instance, in the case of the view factor used by LuSim for the albedo on isotropic diffuse irradiance, the factor approaches the diffuse albedo of the ground (0.2 in this example) as the plate is elevated further above the ground. Conversely, it trends towards 0 as the plate is positioned closer to the ground.

A preliminary validation can be performed by evaluating this factor at various heights, confirming that it approaches 0 near the ground and converges to 0.2 at higher elevations. This trend is depicted in Figure 38.

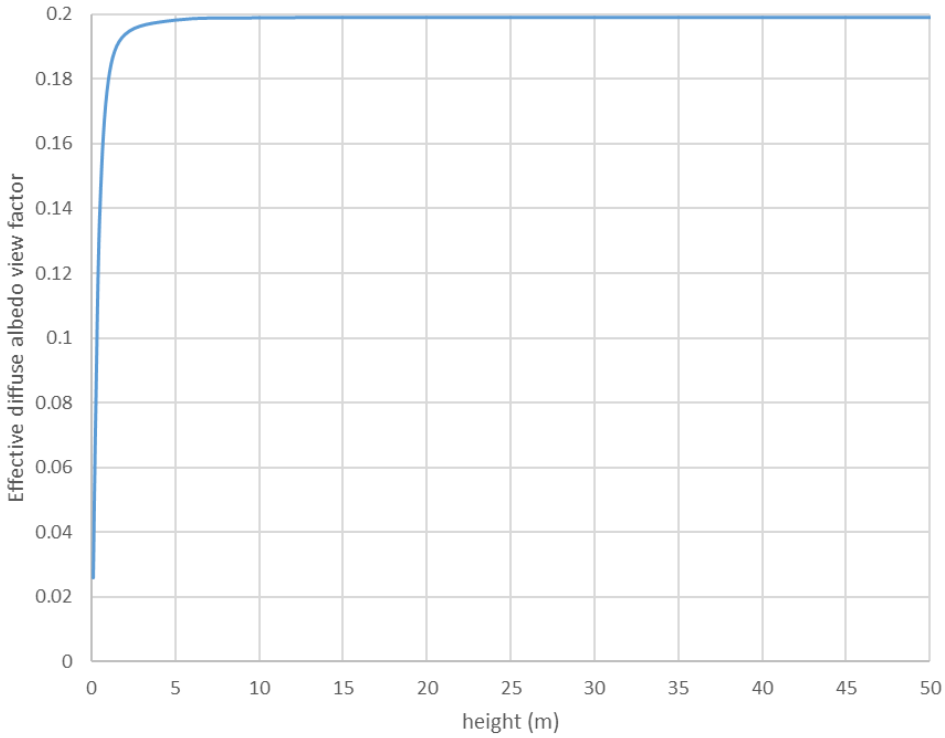

Figure 38: View factor for effective albedo on isotropic diffuse irradiance vs height from the ground.

Similarly, for the view factor that accounts for the "effective" albedo on directional irradiance (direct and circumsolar diffuse), an exact analytical solution is not readily available. This is primarily due to the complexity of evaluating shadows on the ground within spherical projections. However, basic validations can still be performed. For example, at higher module positions, where shading has minimal influence, the view factor converges to the cosine of the sun's incident angle multiplied by the Lambertian albedo. This behaviour is illustrated in Figure 39.

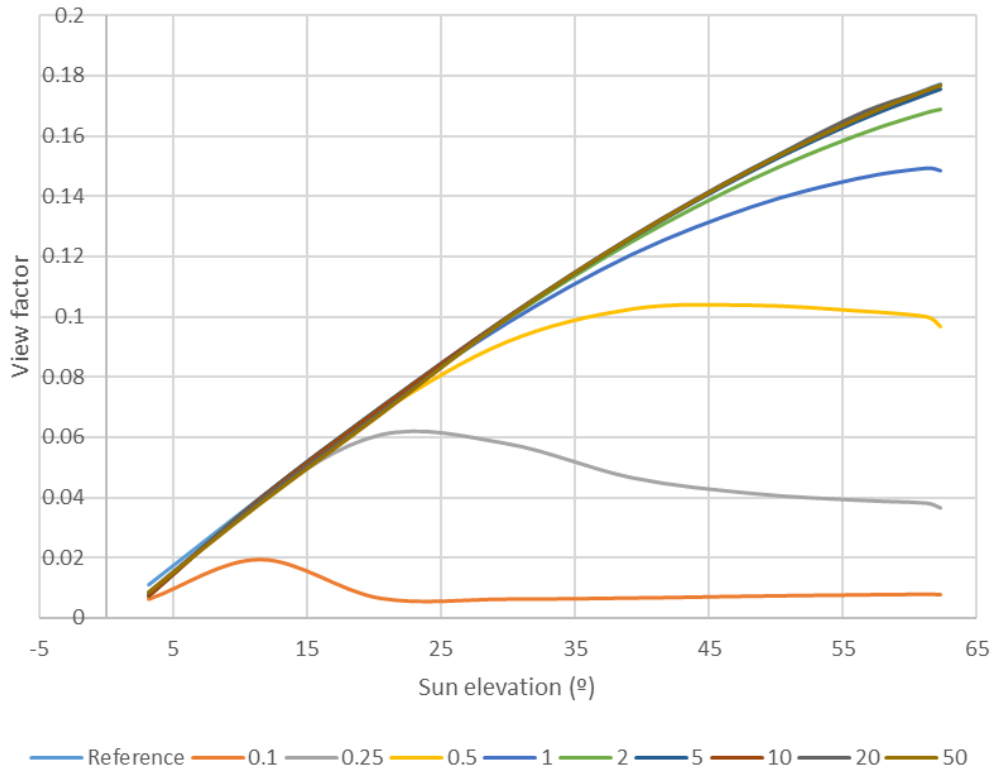

Figure 39: View factor for effective directional irradiance vs height from the ground.

4.6.2. Case 1: Horizontal square plate above uniform ground albedo

A simulation was conducted by the three modelling partners of SYMBIOSYST: LuciSun, Imec, and TUD. The simulation covered a full year with a time resolution of one hour. The irradiance received on both the front and rear sides of the square plate, assimilated to be a PV module, was calculated, allowing the bifacial gain to be determined.

These results served as a preliminary checkpoint. For a horizontal module, it is expected that at sufficient heights, where shading effects near the ground are minimal, the irradiance gain from the rear side should approximate the albedo of the ground. Additional checks were conducted for scenarios where the module was closer to the ground, where shading effects are more pronounced.

The simulation also provided information on the overall irradiance received on the rear side of the module. This analysis included different days of the year with varying sun elevations and clear sky conditions.

Front side irradiance

The global irradiance values on the front side of the PV module were highly consistent across the results obtained by the different partners, as shown in Figure 40, which includes data for a series of clear and cloudy days during spring. The results are presented for a plate positioned at an elevation of 50 m. Similar trends were observed at other heights, but only this case is shown for clarity.

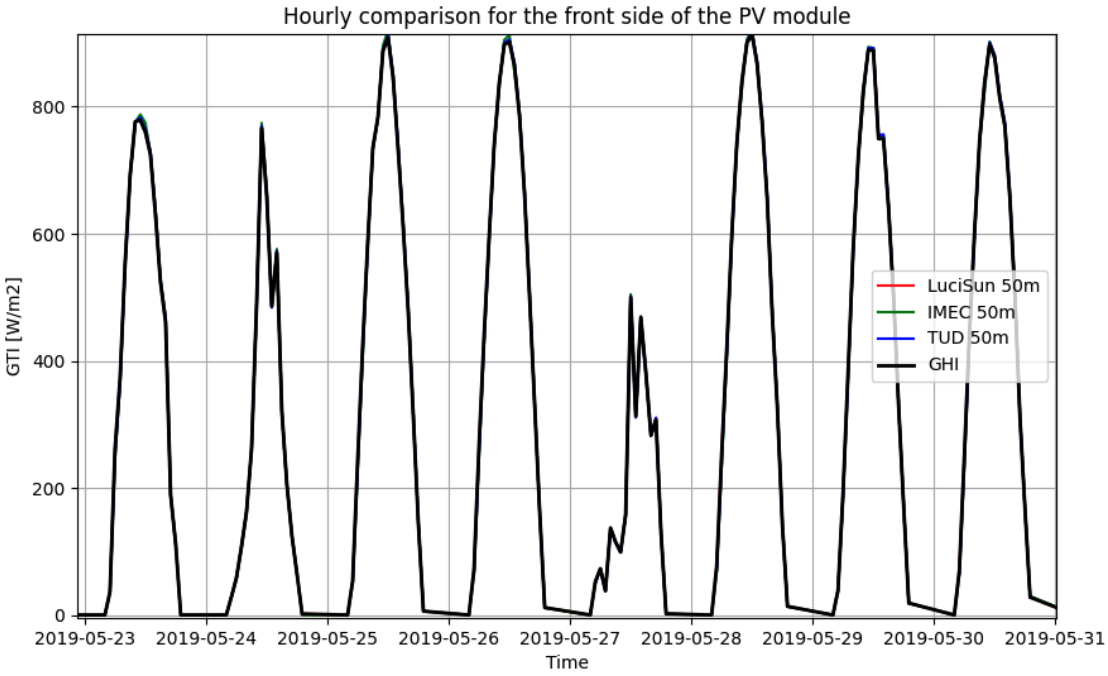

Figure 40: Global irradiance received on the front side of the module – Simulation by each partner.

Bifacial irradiance gain

The bifacial irradiance gain, defined as the ratio between the irradiance received on the rear side and the front side, demonstrates the expected behaviour of approaching the overall ground albedo (20%) as the height of the square plate increases. This trend is illustrated in Figure 41 for a spring day with a time resolution of one hour. For clarity, the heights of 0.5 meters and 2.0 meters are presented separately from the 50-meter height, as different scales were used.

The most significant deviations occur when the plate is positioned close to the ground, where shading effects become more pronounced. The small oscillations around the expected 20% gain value are likely due to numerical approximations applied by the different partners at each time step.

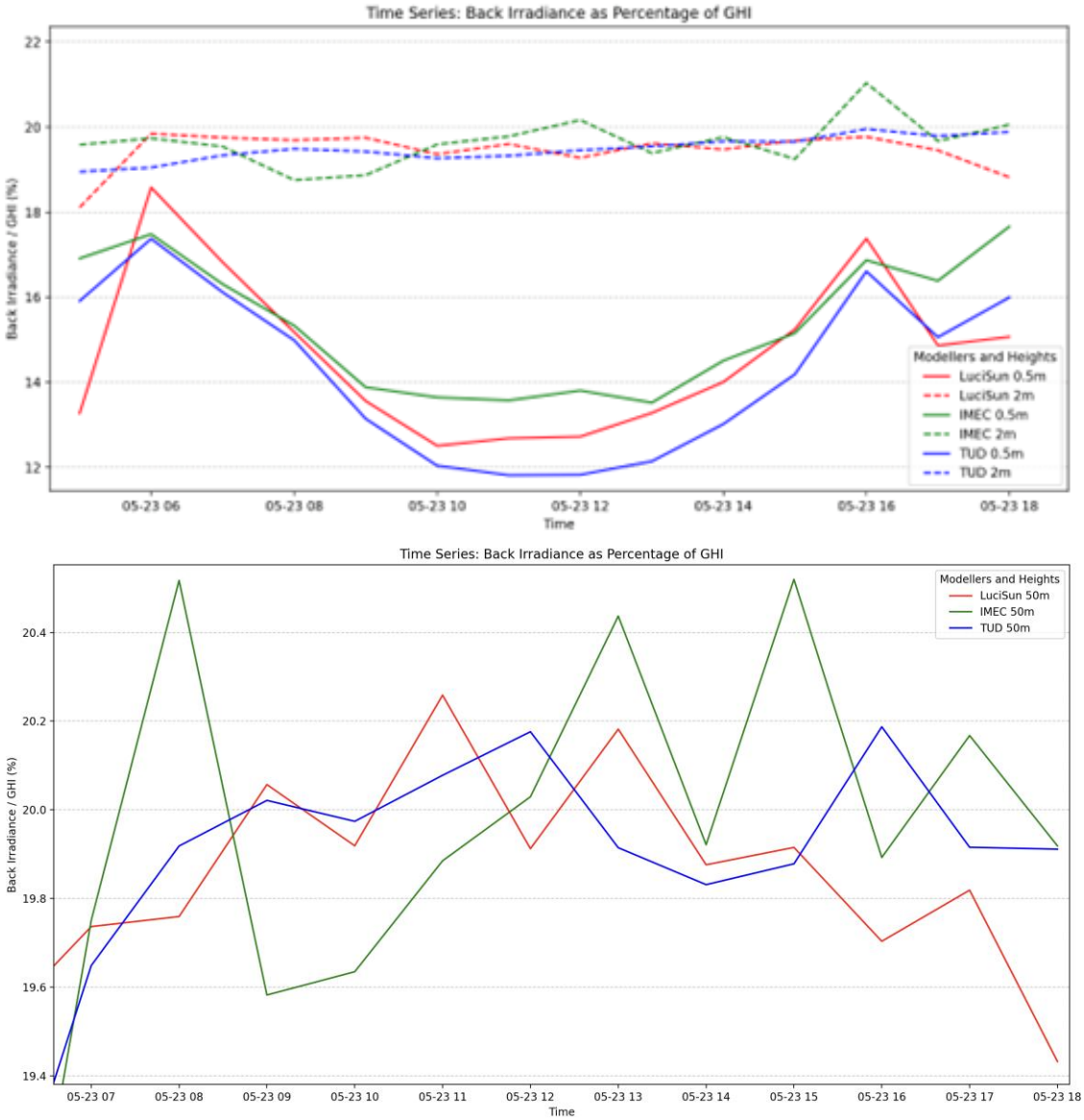

Figure 41: Bifacial gain on May 23rd (TMY) at different heights (0.5 and 2 m top, 50 m bottom).

In order to analyse with higher detail those differences, the rest of this section focuses on the comparison of the irradiance received on the back side of the modules.

Rear side irradiance

The rear side irradiance forms the central focus of the discussion in this section, as evaluating this contribution poses the greatest challenges and reveals the most significant differences in the methodologies used by the different partners. The analysis is presented sequentially, examining variations across days, time resolutions, and module heights as reported by each partner. The analysis is presented for hourly, monthly and yearly time integration periods.

Hourly time integration

This initial step involves conducting hourly checks for specific days under varying conditions, ranging from clear skies to cloudy weather, across both winter and summer months. The primary objective is to identify the causes of similarities and differences among the results produced by the different models. Additionally, the study examines potential time shifts that may arise from variations in the physical models used by the partners.

To ensure clear visualization, not all heights from the three modelling tools are presented in the same plot. Figure 42 illustrates the hourly comparison of global incident irradiance at the midpoint of the rear side of the PV module for heights of 0.5 meters, 2 meters, and 50 meters.

The analysis begins with clear-sky days, as the primary contribution to the rear side irradiance originates from the reflection of the direct component, which depends on the sun's position. Days were selected near the solstices and equinoxes with near-clear-sky conditions, specifically June 20th, September 23rd, and December 25th.

The observed tendencies align with expectations: as the module height increases, the simulations among the partners show greater consistency due to the reduced significance of shading effects on the ground. The largest differences occur when the module is positioned close to the ground, particularly near the summer solstice. During this period, the module's shadow falls almost directly beneath it, highlighting discrepancies in the modelling approaches used by the partners. Near the winter solstice, the module's shadow has less impact because the sun is lower in the sky, and the shadow extends far to the north.

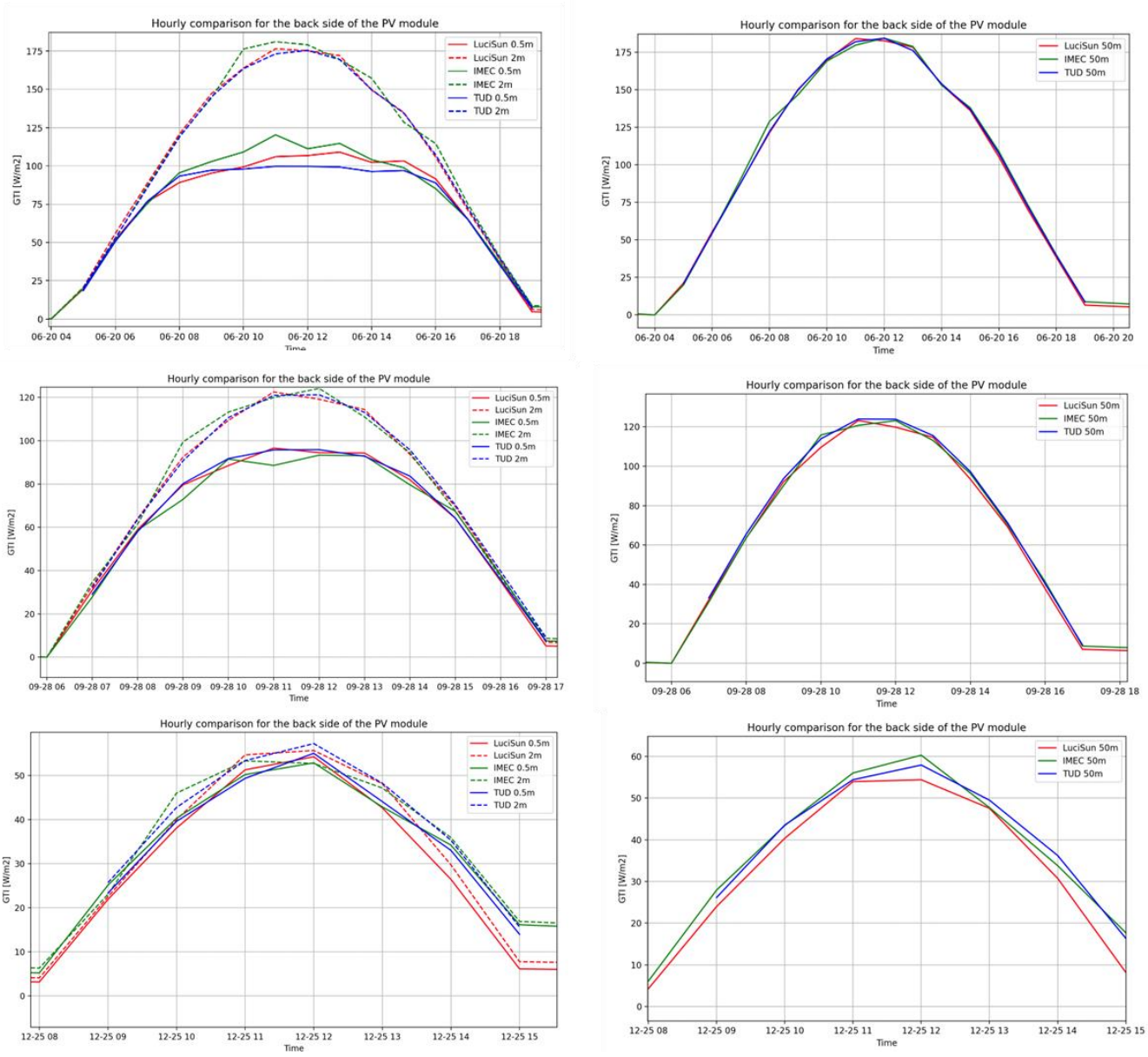

Figure 42: Comparison of hourly back irradiance simulations for clear-sky days close to solstices and equinoxes for different module heights.

While analysing the trends of direct irradiance on clear-sky days, it is equally important to evaluate the behaviour of the diffuse isotropic component. Under cloudy conditions, where the contribution of the direct component to global tilted irradiance (GTI) diminishes, the diffuse isotropic component becomes dominant.

In these scenarios, the sun's position is less relevant, so several random cloudy days were selected for analysis. Figure 43 presents the hourly comparison for a cloudy day on 31st March, showing results for heights of 0.5 meters and 2 meters, followed by the comparison for a height of 50 meters.

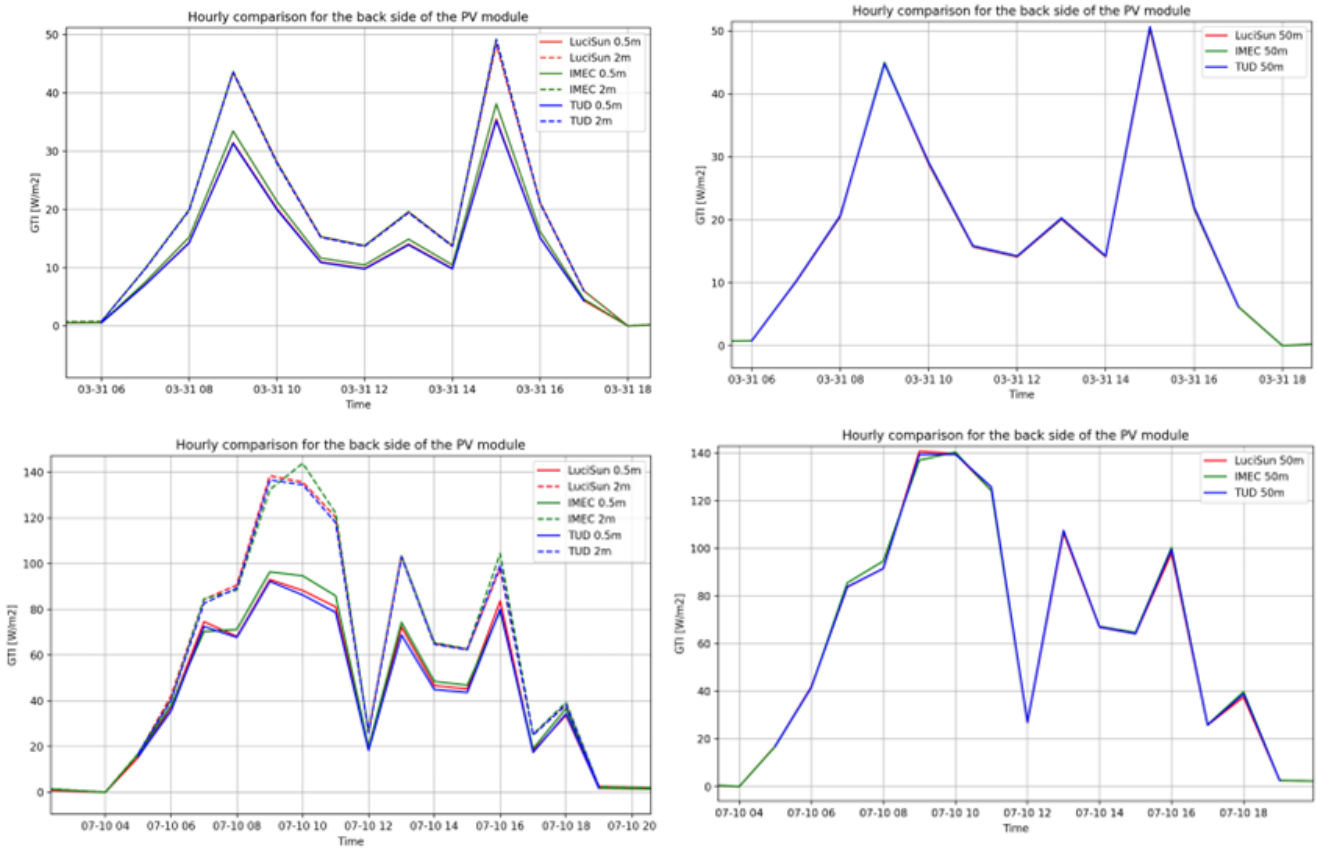

Figure 43: Comparison of hourly back irradiance simulations for cloudy days for different module heights.

Similar to the previous results, as the module height increases, the agreement between the simulation tools improves. At a height of 50 meters, the differences between the tools are negligible. However, when the module is closer to the ground, small discrepancies are observed.

With an understanding of the seasonal variations across different heights and conditions, it becomes important to assess how these differences accumulate on a monthly and yearly basis when the modelled irradiances are summed. This analysis provides insight into the broader impact of these deviations over extended periods.

Monthly time integration

The monthly comparison presented in Figure 44 provides a clear visualization of the aggregated Global Tilted Irradiation (GTI) results for the back side of the PV module at various heights. The top graph compares the results for heights of 0.5 m and 2 m across the modellers LuciSun, Imec, and TUD, while the bottom graph isolates the comparison for the height of 50 m.

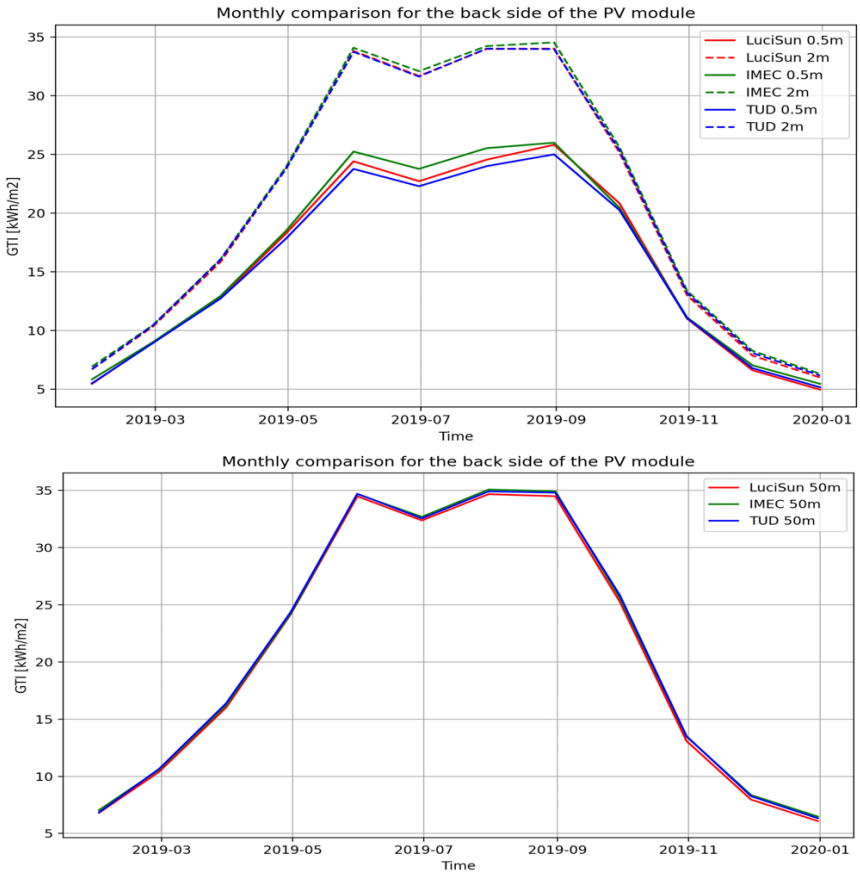

Figure 44: Monthly comparison for GTI at midpoint of backside of PV module for heights 0.5 m and 2 m (top), and 50 m (bottom).

At a height of 0.5 meters, Imec slightly overestimates irradiance compared to LuciSun and TUD during the summer months, while LuciSun marginally overestimates relative to TUD. This behaviour aligns with observations from the hourly analysis, which indicate that discrepancies at smaller heights, such as 0.5 meters, are likely due to partial shading caused by the PV module and the spatial distribution of ground points. During summer months, when the sun's elevation is higher, shading becomes more prominent, creating scenarios where points under the module experience partial shading. This highlights the critical role of the spatial arrangement of these points at smaller heights, as the ratio of shaded to illuminated points directly influences the reflected irradiance, leading to variations in the results among the modellers.

In contrast, at greater heights, such as 2 meters and 50 meters, the effects of partial shading and the spatial distribution of points become less significant. At 2 meters, the shadow cast by the module is more diffuse and skewed, resulting in a more uniform illumination or shading of the points under the module. This minimises the impact of spatial variability on reflected irradiance, leading to consistent results across the modellers. At 50 meters, where the module's influence on sky visibility and reflected irradiance effectively disappears, the results align closely across all modellers, as the effects of shading and ground point variability are negligible.

The monthly comparison thus provides a comprehensive summary of the trends identified in the hourly analysis. At smaller heights, partial shading and the spatial distribution of ground points play a significant role, particularly during the summer months when shading is more pronounced under the PV module. At greater heights, such as 2 meters and 50 meters, the more uniform illumination or shading of ground points reduces the impact of spatial variability, resulting in greater consistency among the modellers.

Yearly time integration

Figure 45 provides the aggregated yearly bar plot comparison for the Global Tilted Irradiance (GTI) at the midpoint of the backside of the PV module for different heights: 0.5 m, 2 m, and 50 m.

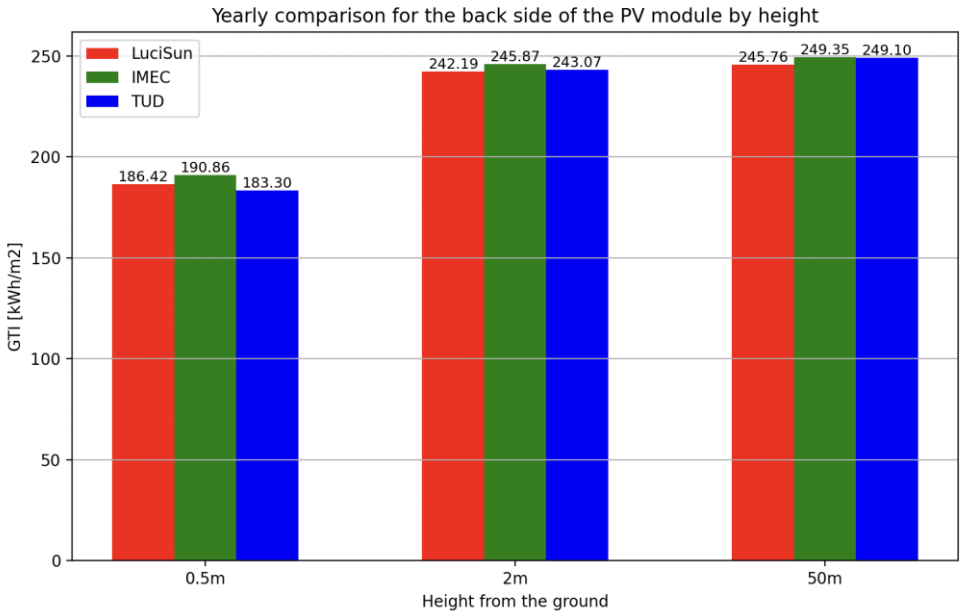

Figure 45: Yearly comparison for GTI at midpoint of backside of PV module for heights 0.5 m, 2 m and 50 m.

The monthly trends observed earlier extend consistently to the yearly results, showcasing the cumulative effects of discrepancies influenced by partial shading are smaller. These factors vary with seasons and sky conditions, leading to the observed differences among the models. The slightly lower values from LuSim at 50 m are assumed to be due to the scenario rendered, particularly for the outer ground, where the overall size is 1 km x 1 km, resulting in a finite surface contributing to the irradiance reflection.

The next section focuses on the comparative statistical metrics between the modellers, offering a more detailed quantitative evaluation of their performance.

Deviation evaluation

Figure 46 presents a heatmap visualization of the statistical comparative analysis of the yearly results, using Mean Bias Deviation (MBD), Root Mean Square Deviation (RMSD), and percentage differences across the three module heights (0.5 m, 2 m, and 50 m) for all modellers.

The main conclusion is that the greatest differences among the modellers occur at the lowest height of 0.5 meters. At this height, Imec estimates 2.35% more than LuSim, TUD estimates 1.69% less than LuSim, and Imec estimates 4.04% more than TUD. These differences are primarily attributed to variations in how shading effects near the ground are modelled.

As the module height increases, these differences become smaller. At 2.0 meters, Imec estimates 1.51% more than LuSim, TUD estimates 0.36% more than LuSim, and Imec estimates 1.15% more than TUD. At 50 meters, the differences are minimal, with Imec estimating 1.45% more than LuSim, TUD estimating 1.35% more than LuSim, and Imec estimating only 0.1% more than TUD. The small discrepancy observed for LuSim at this height is likely due to the limited size of the ground scenario considered (1 km x 1 km), which reduces the surface available for reflection, as previously discussed.

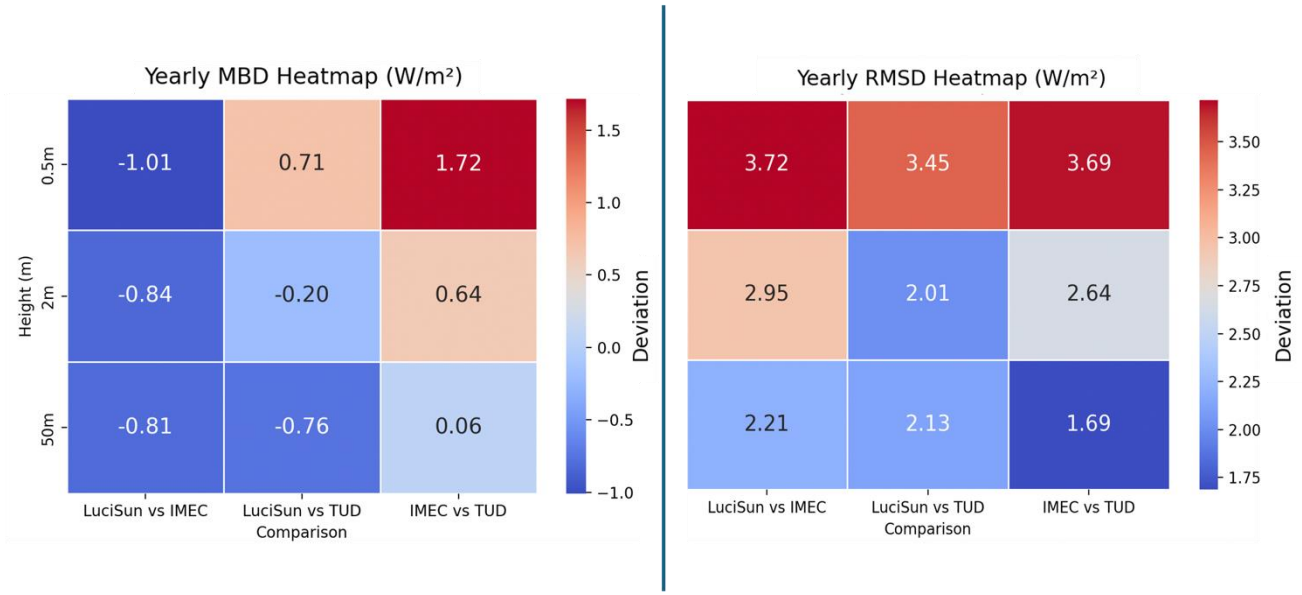

Figure 46: Yearly MBD and RMSD comparison heatmap for GTI at midpoint of backside of module.

The monthly MBD and RMSD heatmap in Figure 47 provides a detailed statistical comparison of the backside irradiance of the PV module at a height of 2 meters throughout the year. It highlights monthly trends in deviations among the three modellers, LuciSun, Imec, and TUD, and examines whether the previously observed discrepancies and trends persist on a monthly scale for MBE.

The heatmap reveals only slight differences between summer and winter months, which are likely influenced by variations in sun elevation and the resulting shading effects of the module on the ground.

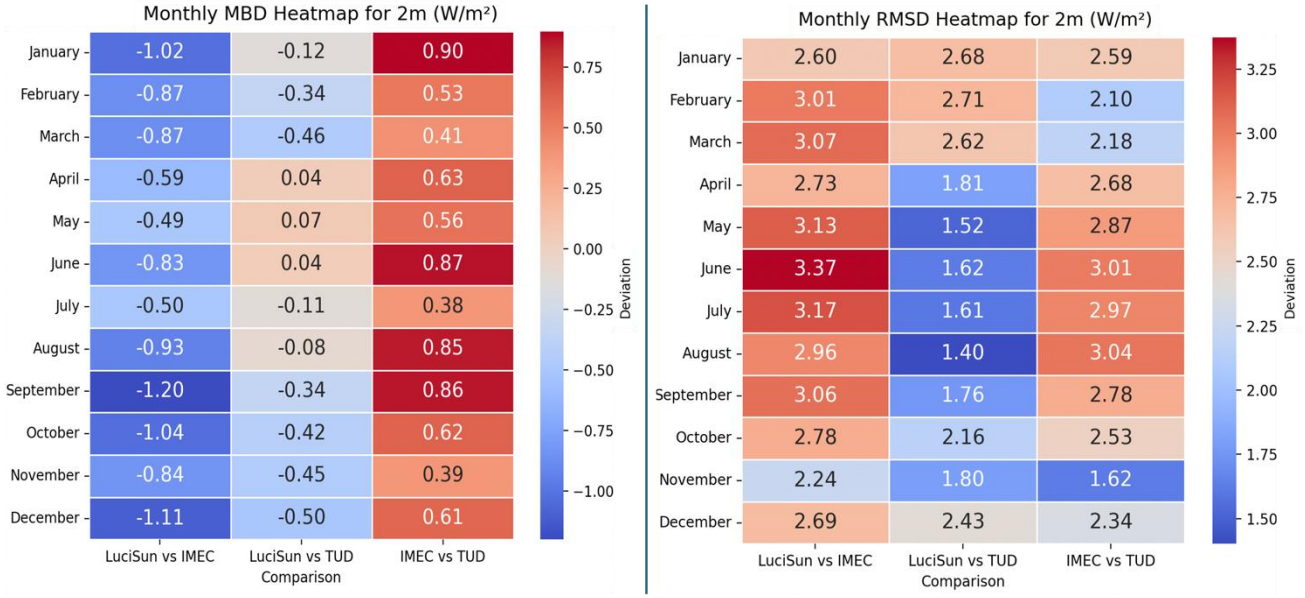

Figure 47: Monthly MBE and RMSD heatmap for GTI at midpoint of backside of PV module for height of 2 m.

Since three different tools are involved in the comparisons, it can sometimes be more practical to select one as the reference for certain exercises. In theory, the results from Imec and TUD would be expected to align more closely, as both use Radiance as their ray tracing core engine. In contrast, LuciSun employs a different methodology, relying on high-resolution 3D view factors. For the following visualisations, LuSim has been chosen as the reference.

When evaluating frontside irradiance throughout the year, all tools closely align across all heights, as expected. For illustrative purposes, a module height of 0.5 meters was selected (see Figure 48). The relative deviation between Radiance-based tools and LuciSun's remains within 5% for zenith angles lower than 60°, and within 10% for zenith angles lower than 80°, so they agree relatively well expect for very low solar elevation angles. This deviation is reasonable given that Imec and TUD use the Perez sky model, while LuciSun utilises the Hay and Davies model. The main difference between the two models is that the Perez model includes an additional diffuse irradiance component close to the horizon.

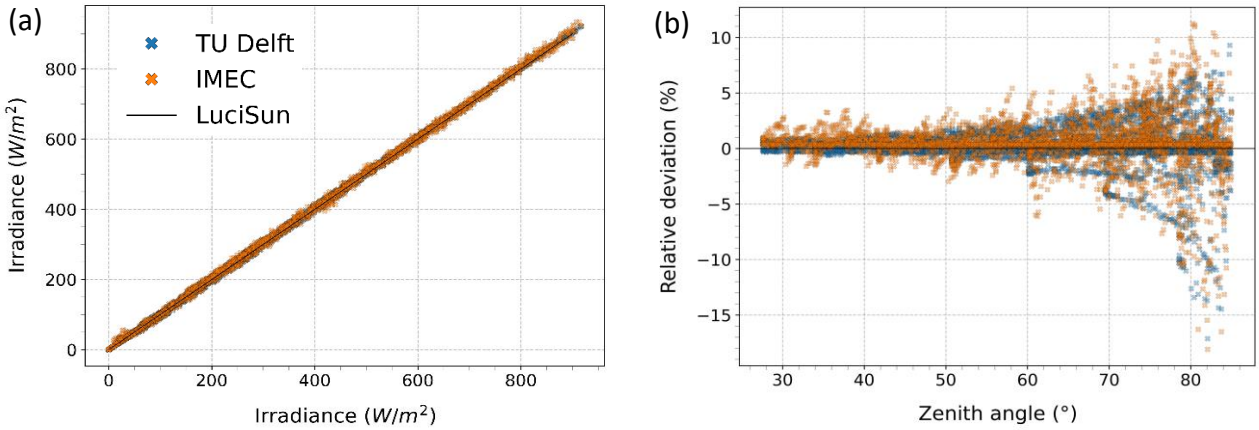

Figure 48: Frontside irradiance comparison between tools at 0.5 meters module height. Graph (a) displays the simulated irradiance from TUD's and IMEC's tools on the y-axis and LuciSun's on the x-axis. Graph (b) shows the relative irradiance deviation of TUD's and IMEC's against LuciSun's on the y-axis, with the solar zenith angle on the x-axis.

When evaluating backside irradiance, height plays a significant role. At 0.5 meters, as illustrated in Figure 49 (a), a discrepancy between the two Radiance-based tools was observed. Imec's and TUD's simulated irradiance exhibit a negative and positive bias, respectively, compared to LuciSun's. This bias is likely due to variations in Radiance simulation parameters that govern ambient light calculation. This effect was more pronounced under overcast skies (high diffuse fraction), as shown in Figure 49 (b). Conversely, at elevated heights (2 and 50 meters), such biases were not identified. To avoid redundancy, the 50-meter height was selected (see Figure 49 (c) and (d).

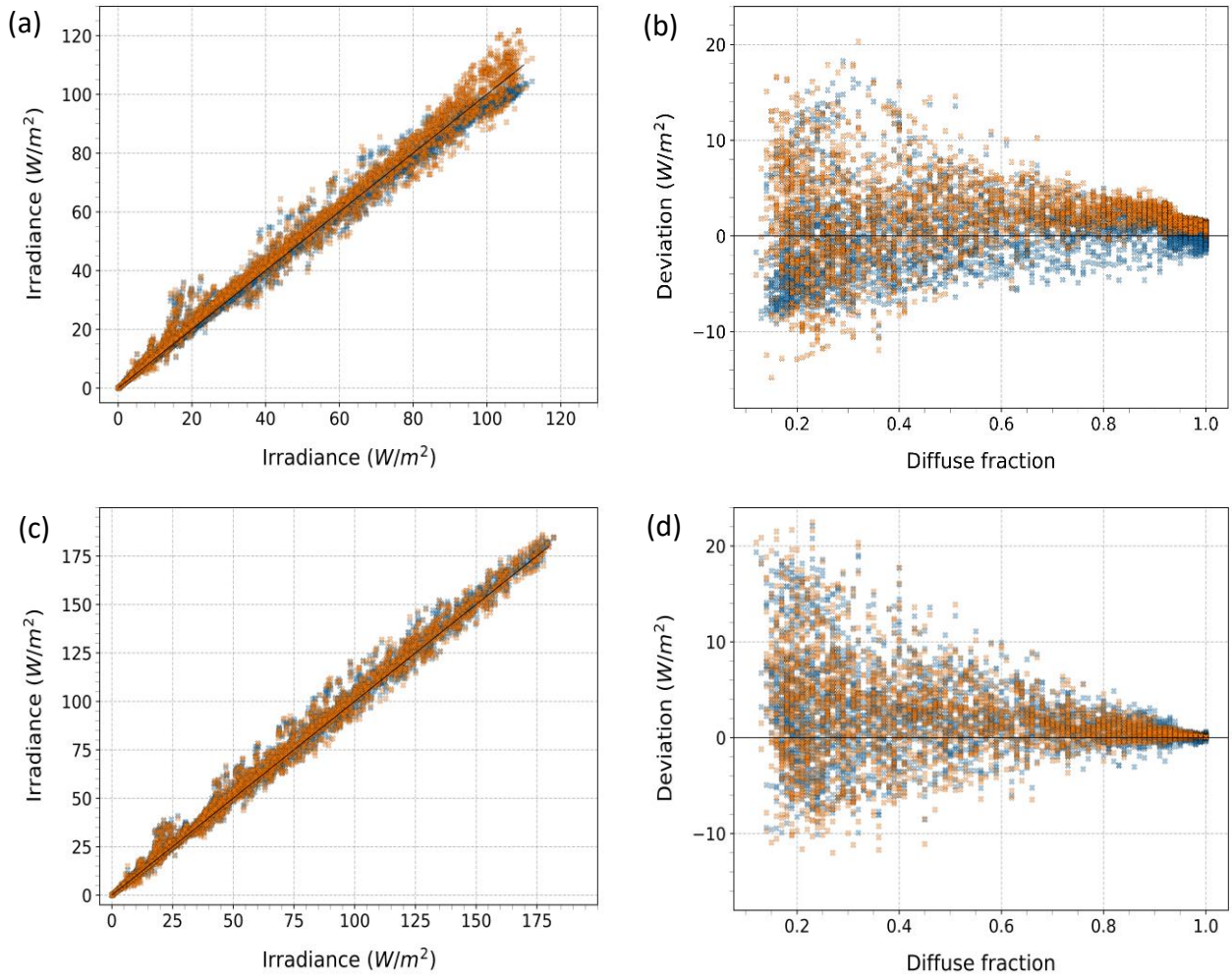

Figure 49: Backside irradiance comparison between tools at 0.5 meters (top) and 50 meters (bottom) module height. Graphs (a) and (c) display simulated irradiance from TUD's and IMEC's tools on the y-axis and LuciSun's on the x-axis. Graphs (b) and (d) show simulated irradiance deviation from TUD's and IMEC's tools against LuciSun's on the y-axis, with diffuse fraction on the x-axis.

4.6.3. Case 2: Checkerboard-patterned ground with two alternating albedo values

This case maintains the same setup as in Case 1, with modifications to the ground surface properties. The ground is designed with a checkerboard pattern, consisting of alternating 10 cm x 10 cm squares cantered around the origin. Half of these squares have an albedo of 10%, while the other half have an albedo of 30%. On average, the ground still has an albedo of 20 % at the macro level. All other inputs, including the PV module setup and solar resource, remain the same as in Case 1.

The following sections outline the specific adaptations in the methodology for each partner (LuciSun, Imec, and TUD) and conclude with a comparison of the modelled outputs.

LuciSun

The methodology employed for this case mirrors that used in Case 1, with the key difference being the modelling of the internal ground. As outlined in the system setup, the 100 m x 100m internal ground is designed to exhibit a checkerboard pattern, consisting of alternating squares with distinct albedo values (10 % and 30 %). This configuration aims to capture the effects of spatial albedo variation on the irradiance calculations. On the other hand, the module is high enough to neglect the shading effects of the effective diffuse albedo over the ground.

Figure 50 illustrates the top-down view of the modelled ground in LuSim, with the PV module positioned at 10 m above the ground. The alternating checkerboard pattern for the ground is depicted with yellow and black squares, representing albedo values of 30% and 10% respectively.

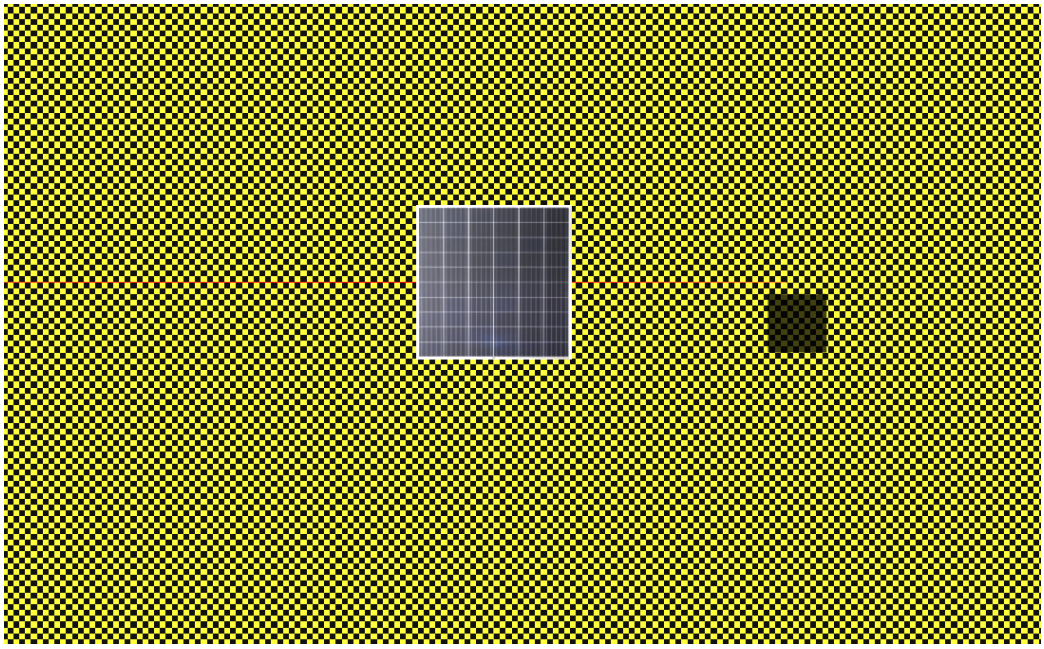

Figure 50: Top view of Case 2 illustrating the checkerboard-patterned ground and the PV module positioned 10 m above the ground.

As evaluating the light reaching the midpoint of the backside of the PV module is of prime importance, the view factors observed from this point are analysed first. The view factors for the diffuse and direct component at 12:00 PM (UTC) on June 10th (TMY), as seen from the mid-point of the rear side of the module, are presented in Figure 51.

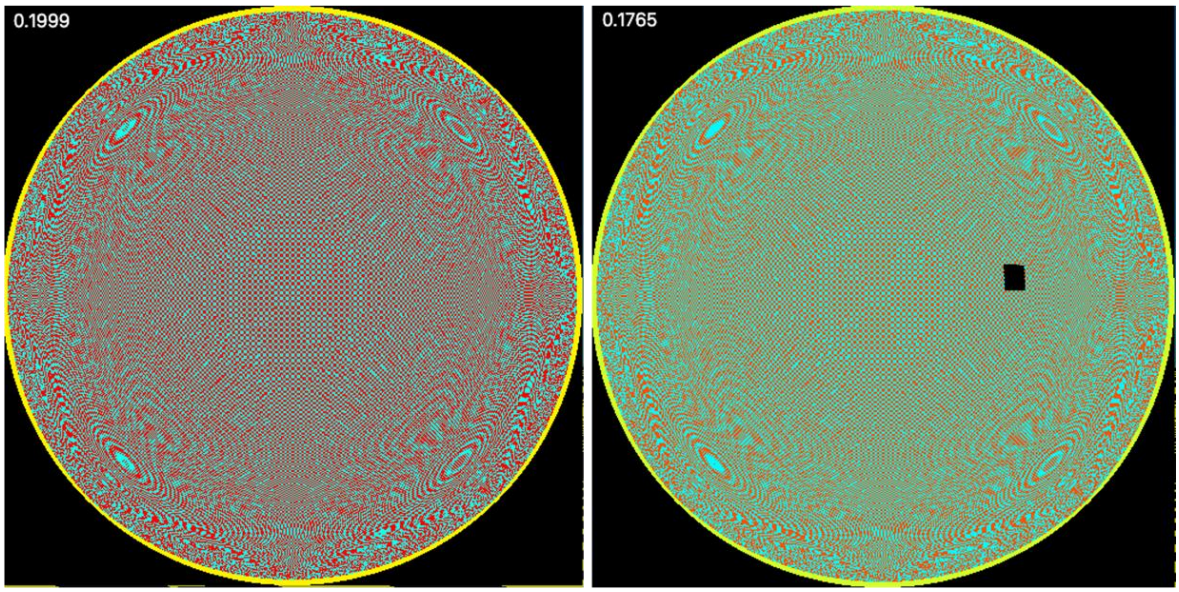

Figure 51: View factor on diffuse (left) and direct (right) irradiance at 12:00 PM on June 10th (UTC) as seen from the midpoint of the PV module.

In Figure 51, the colour scale is adjusted between 0 and 0.3, effectively highlighting the albedo differences across the checkerboard pattern. The external border, shown in yellow, corresponds to areas with an albedo of 0.2 for the outer ground. Red points within the pattern indicate squares with an albedo of 0.3, while blue points signify squares with an albedo of 0.1. Some visual artifacts are visible in the display due to pixel resolution limitations. As the view moves further from the centre, more squares fall into a single pixel.

The view factor for the effective albedo on isotropic diffuse irradiance is approximately 0.1999, aligning closely with the expected average of 0.2 (the midpoint between 0.1 and 0.3). This alignment confirms the model's accuracy in representing varied albedo values in a complex pattern and with high spatial resolution requirements. On the other hand, the reflected contribution from the ground due to direct irradiance is influenced by the sun's position. The comparison of the view factor for the effective albedo on direct irradiance as calculated by LuSim with the theoretical value $\rho \cdot cos\theta s$ is presented in Figure 52 for December 13th, March 15th, and June 10th.

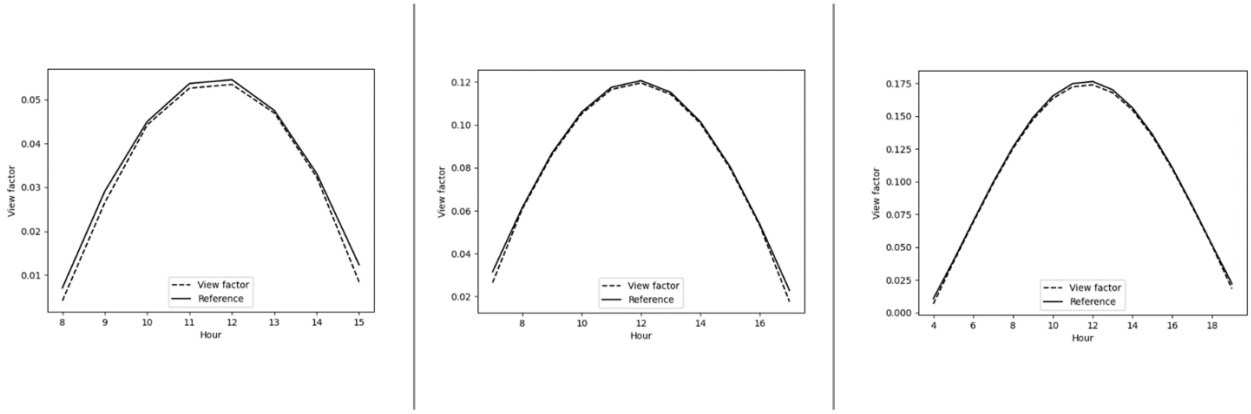

Figure 52: Hourly direct albedo view factor comparison for December 13th (left) , March 15th (middle), and June 10th (right).

Imec

The methodology in Case 2 is similar to that of case 1. The 3D scene was similarly created with SketchUp Pro 2023 and the Radiance files are used as input for the ray tracing. Similar to Case 1, the sensors are placed at the front and rear of the PV module, to assess the irradiance on these specific regions. Figure 53 shows the 3D scene created. The irradiance on the rear side of the PV module is mainly composed of the diffuse and ground reflected irradiance (dependent on the combined albedo values of the checkerboard ground).

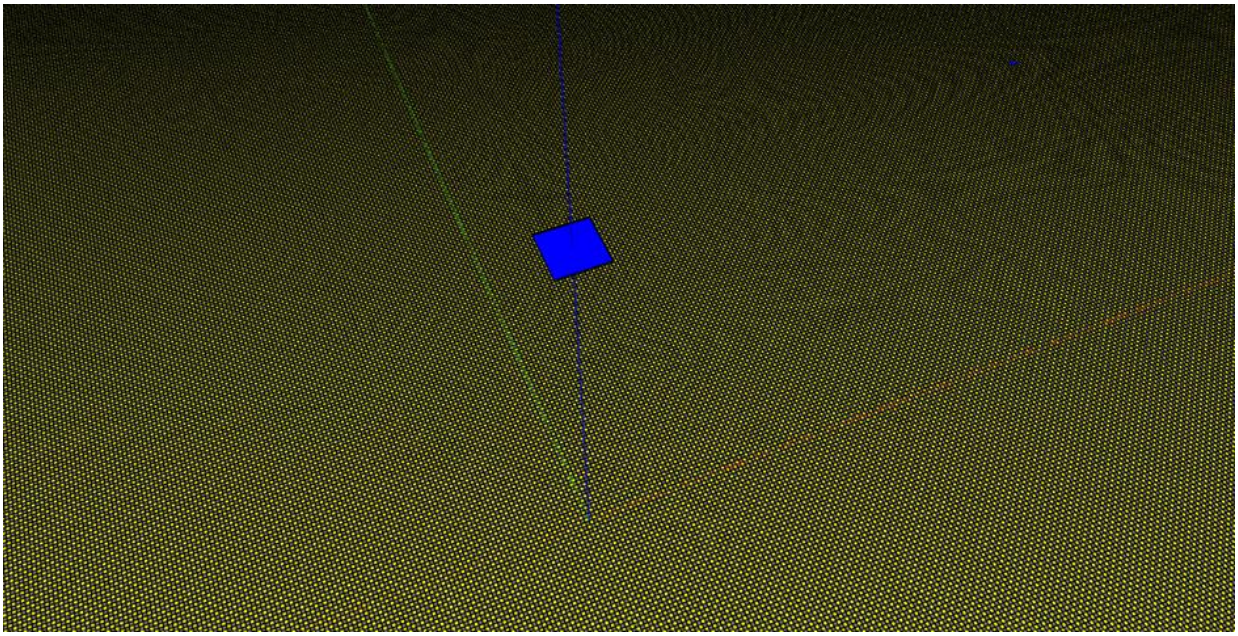

Figure 53: Imec's 3D scene generated from SketchUp Pro 2023 for Case 2. The scene shows the PV module at the centre of the checkerboard ground.

Comparison

Similar to Case 1, the primary focus for Case 2 is on analysing the midpoint of the back side of the PV module, which is placed 10 m above the checkerboard-patterned ground with alternating albedo values of 10% and 30%, respectively. As presented in the previous section, at that module height, not many differences are expected between the modellers, that now could be due to the different capabilities to capture the details of the new ground. Consequently, less situations are included in the analysis for this section. The analysis begins with an hourly comparison to identify seasonal trends and pinpoint recurring behavioural patterns across the models. The aim is to investigate the root causes for any observed discrepancies, which are expected to align with the trends and explanations identified in Case 1. This is followed by a monthly and yearly analysis to evaluate the aggregated effects of the identified causes and trends.

Hourly time integration

Figure 54 presents the hourly comparison of the GTI results for three consecutive clear-sky days; April 21st, 22nd, and 23rd. These days are selected to provide a detailed view of the day-to-day variability and recurring behaviour across the models for this specific scenario. The results from the three modelers, LuciSun, Imec, and TUD, show good alignment throughout the day, particularly around 12:00 PM UTC. This complements the reasoning that the shadow effect on the ground contributing to the reflected irradiance for the back side diminishes significantly with increasing height. At this height, the spatial arrangement and resolution of the ground points contributing to the reflected light play a minimal role, leading to closer alignment among the modelers.

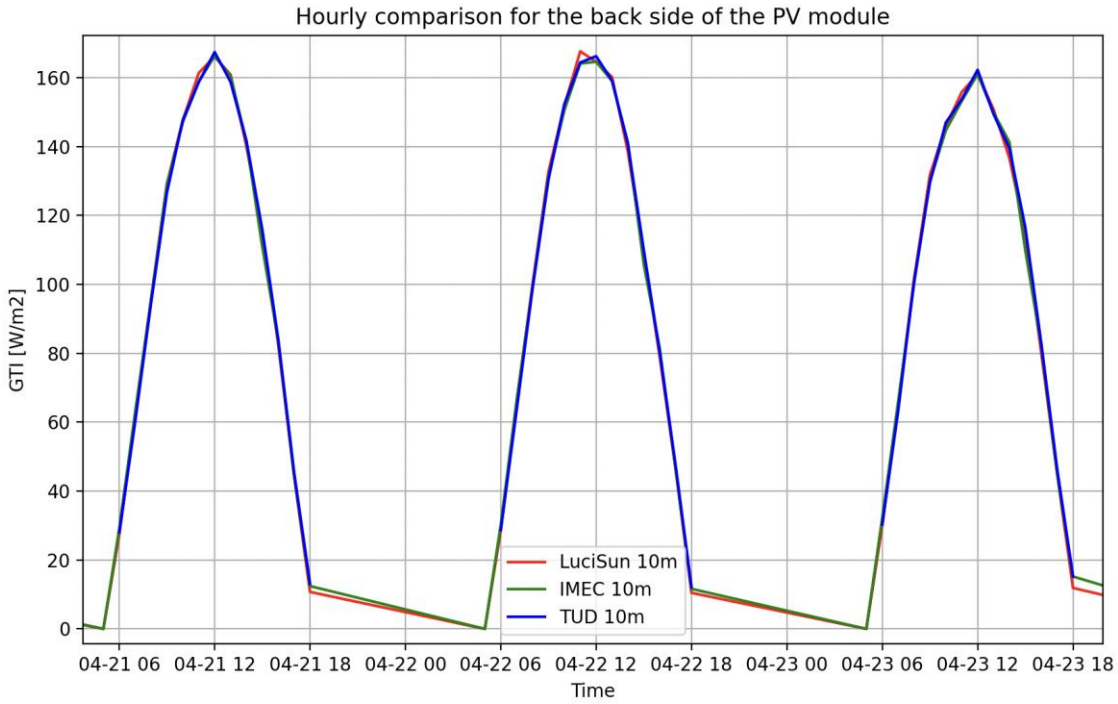

Figure 54: Hourly comparison for three consecutive clear-sky days of 21st, 22nd and 23rd April (UTC).

To further validate and understand this behaviour across varying sky conditions, additional consecutive summer days were analysed, encompassing both clear-sky and cloudy days. Figure 55 presents the GTI comparison for the consecutive days spanning 2nd May to 8th May. The first three days represent clear-sky conditions, the next two days are characterized by cloudy conditions, and the final two days again depict clear-sky behaviour.

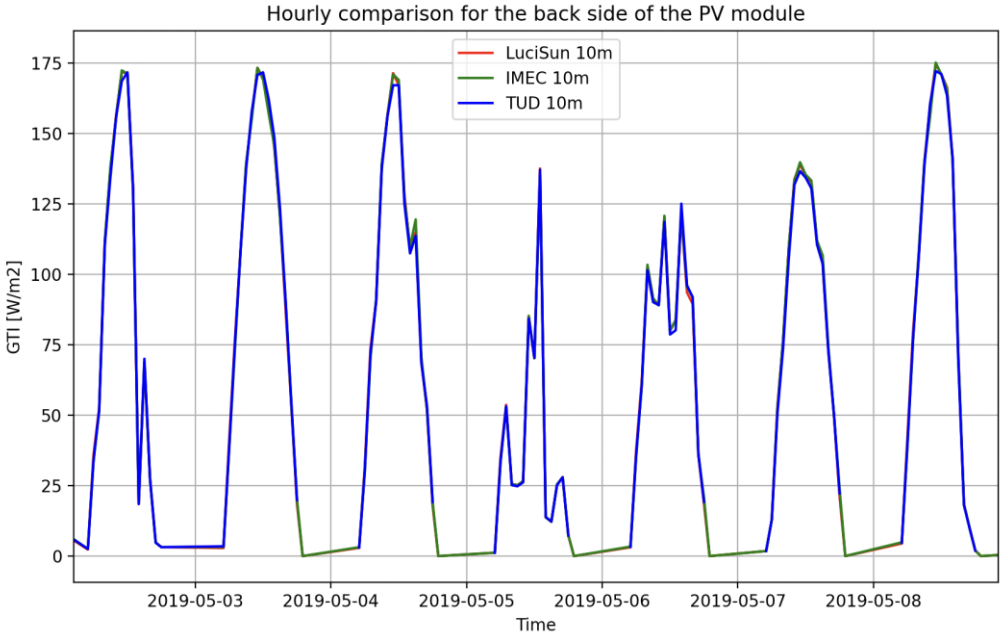

Figure 55: Hourly comparison of GTI for the consecutive days spanning from 2nd May till 8th May (UTC), encompassing both clear-sky and cloudy days.

There is good alignment among all three modelers, LuciSun, Imec, and TUD, across all days analysed. The clear-sky days (2nd, 3rd, and 4th May) demonstrate consistent alignment in trend and magnitude, reinforcing the behaviour observed in the earlier analysis. Similarly, for the cloudy days (5th and 6th May), the alignment among the modelers remains strong, supporting the conclusion that diffuse-dominated conditions reduce discrepancies. The subsequent clear-sky days (7th and 8th May) also show consistent agreement, confirming the robustness of the models under varying sky conditions. This consistency across both clear and cloudy days underscores the reliability of the models in capturing the irradiance behaviour at this height, from a ground composed of several albedo values.

Monthly time integration

To better understand the seasonal impact of these variations, the monthly trends are visualized to examine the aggregated effects. Figure 56 below provides the monthly comparison for the same analysis. LuciSun tends to very marginally underestimates the irradiance compared to Imec and TUD during the colder months, while Imec marginally overestimates compared to TUD and LuciSun during the summer months. This behaviour aligns with the seasonal patterns observed in Case 1.

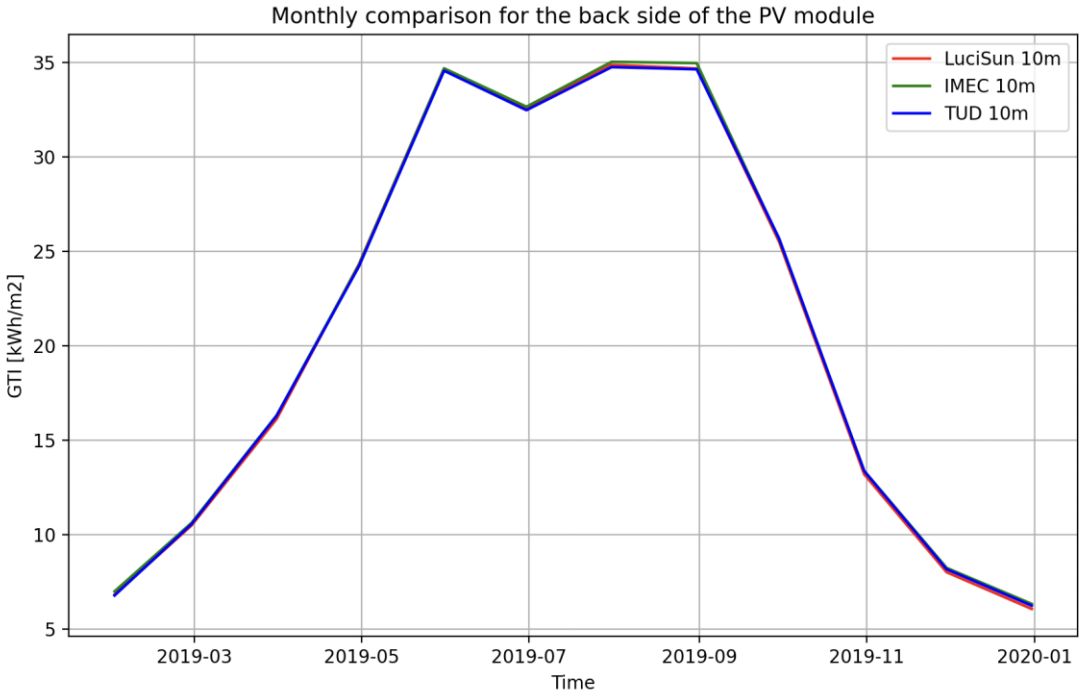

Figure 56: Monthly comparison for the GTI at the midpoint of backside of the PV.

Yearly time integration

The variations observed in the hourly and monthly analyses are further aggregated and visualised in the yearly comparison shown in Figure 57. The bar plot provides a clear representation of the yearly Global Tilted Irradiance (GTI) for the back side of the PV module at the midpoint, as modelled by LuSim, Imec, and TUD. The yearly results show a close agreement among the modellers, with Imec slightly overestimating by approximately 0.7% compared to TUD and LuciSun, which are in closer alignment with each other, differing by only 0.2%.

These results are consequently consistent with the results obtained in the previous example and the main conclusion is that the complexity included in the ground was properly captured by all the modellers.

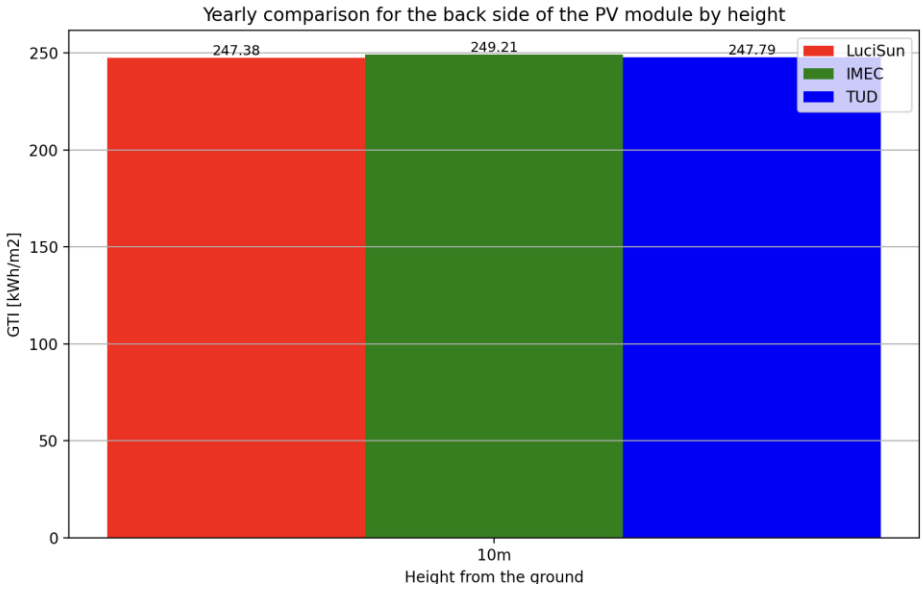

Figure 57: Yearly comparison for the GTI at the midpoint of backside of the PV.

Deviation evaluation

The yearly and monthly deviations observed earlier are quantified in the statistical comparative section below, where MBD and RMSD metrics summarize the differences between the modellers. Results are very similar to the ones obtained in the previous case, so only a summary is provided.

Yearly MBD and RMSD

Table 2 provides the yearly MBD and RMSD for the modelled GTI at the midpoint of the back side of the PV module placed 10 m above the checkerboard-patterned ground. The statistics highlight the comparative deviations between the three modellers. LuciSun generally shows a slight underestimation compared to Imec and TUD, reflected by the negative MBE values, while Imec tends to marginally overestimate relative to TUD. The RMSD values remain low overall, indicating strong alignment among the modellers, with the smallest deviations observed between TUD and Imec.

Table 2: Yearly MBD and RMSD for a height of 10 m.

	LuciSun vs Imec	**LuciSun vs TUD**	**Imec vs TUD**
MBD (W/m2)	-0.41	-0.09	0.32
RMSD (W/m2)	2.15	2.10	1.77

To verify the seasonal trend observed in the monthly comparison, the monthly MBD heatmap across the modellers is shown in Figure 58. LuciSun slightly underestimates overall compared to Imec. While compared with TUD, LuciSun marginally overestimates for the summer month and underestimates for the winter month.

Imec, on the other hand, slightly overestimates during the summer months but also marginally overall compared to TUD.

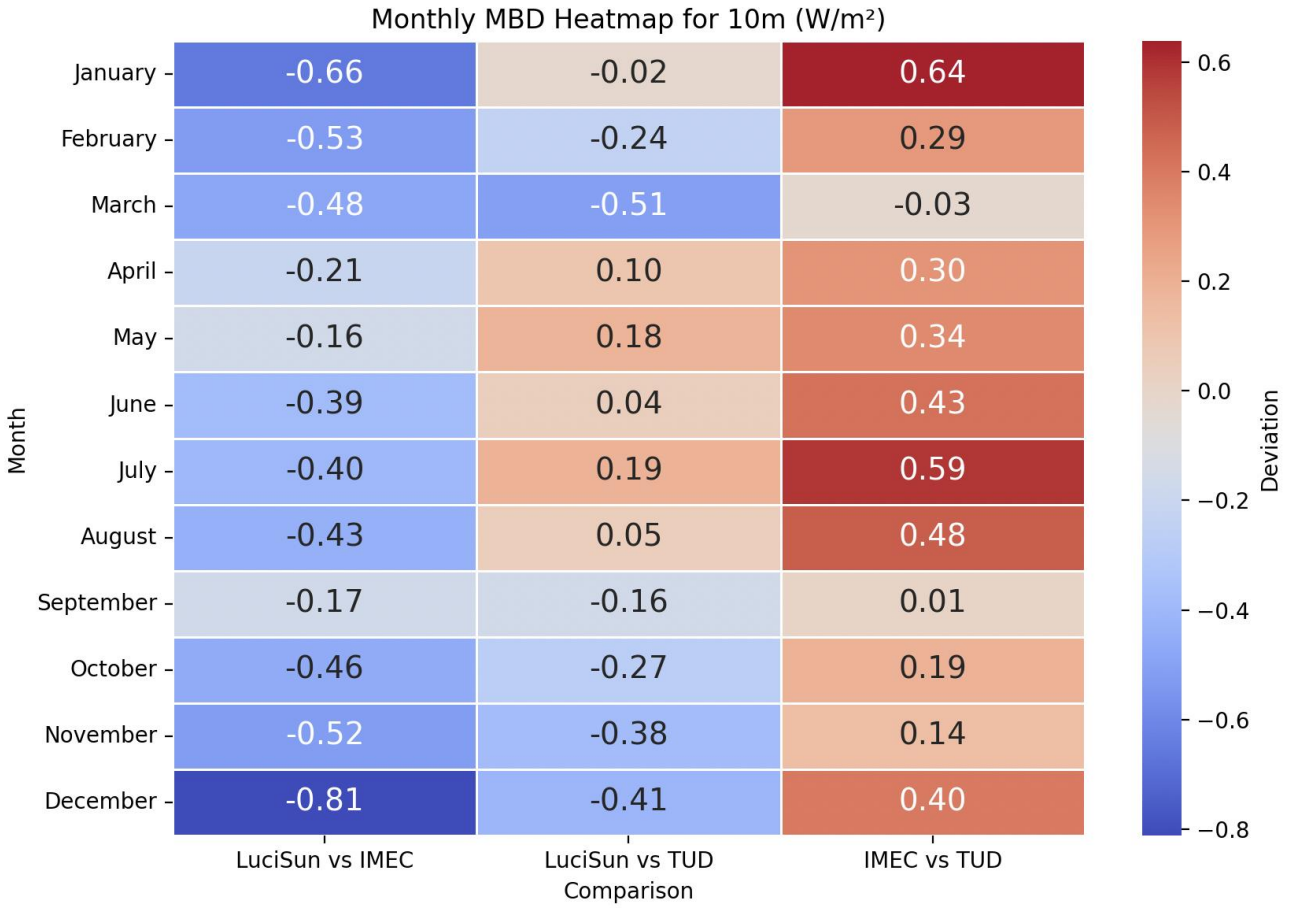

Figure 58: Monthly MBE comparison heatmap for GTI at midpoint of backside of PV module for height 10 m.

Finally, the seasonal trends observed across all modellers in the monthly MBE heatmap are consistent with the findings in Figure 59.

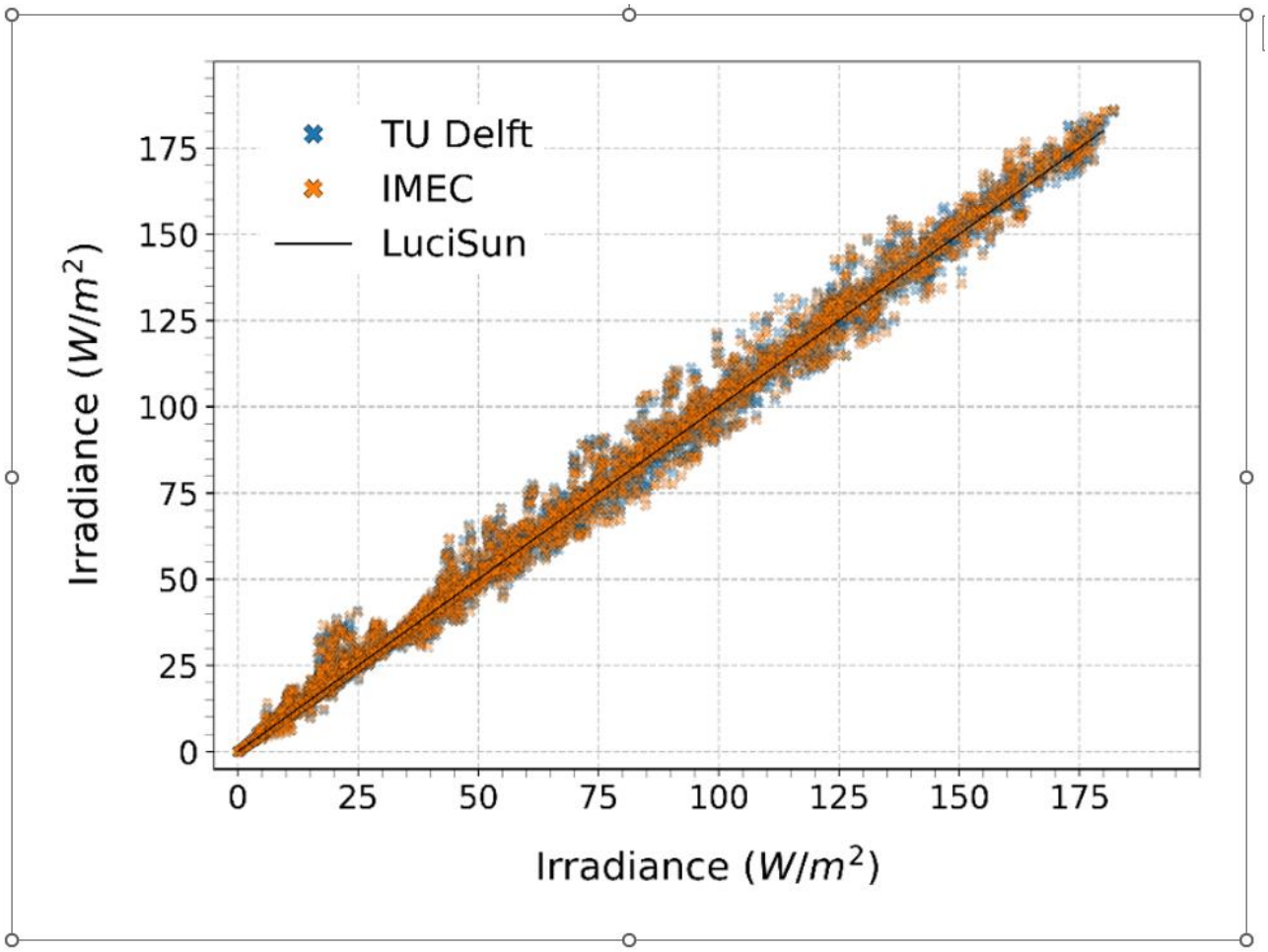

Figure 59: Backside irradiance comparison between tools at 10 meters module height. The y-axis displays the simulated irradiance from Imec's and TUD's tools, while the x-axis from LuciSun's.

4.6.4. Case 3: Checkerboard-patterned mask between ground and module

LuciSun

The setup is identical to Case 1, with the addition of a checkerboard-patterned surface located 5 meters above the ground, spanning an area of 100 m x 100 m. This surface consists of 10 cm x 10 cm squares, with half being opaque and half transparent, and has a thickness of 2.5 cm. The PV module remains positioned at a height of 10 m, while the new surface acts as a mask, covering the same 100 m x 100 m area as the active ground in Case 1.

Solar irradiance is evaluated on a 10 m x 10 m section of the ground at the centre of the scenario, using a detailed spatial resolution. Table 3 presents the coordinates of two points on the internal ground where the incident irradiance is analysed. As described above, the system is constructed with the origin (0, 0, 0) as the centre in a Cartesian coordinate system.

Table 3: Coordinates of the 'internal ground' where the irradiance has been evaluated'.

Position	Coordinates (x, y, z)
'Edge'	4.97, 4.94, 0
'Origin'	0, 0, 0

Furthermore, the mask surface has an albedo of 0, serving exclusively to block 50% of the incoming light without contributing to reflectance. All other inputs, including material properties, solar resource, and simulation parameters, remain unchanged.

The following sections detail the methodology and results for each partner (LuciSun, Imec, and TUD), followed by a comprehensive comparison of the modelled outputs.

The methodology used in this case is consistent with that of Case 1, with the primary difference being the addition of an internal ground area for evaluation and a net positioned 5 meters above the ground, with a thickness of 2.5 cm. The PV module remains fixed at a height of 10 meters, and the additional internal ground area measures 10 m x 10 m. Figure 60 provides several views of the modelled scenario in LuSim with the PV module marked in white to provide a contrast against the thick black net for better visibility.

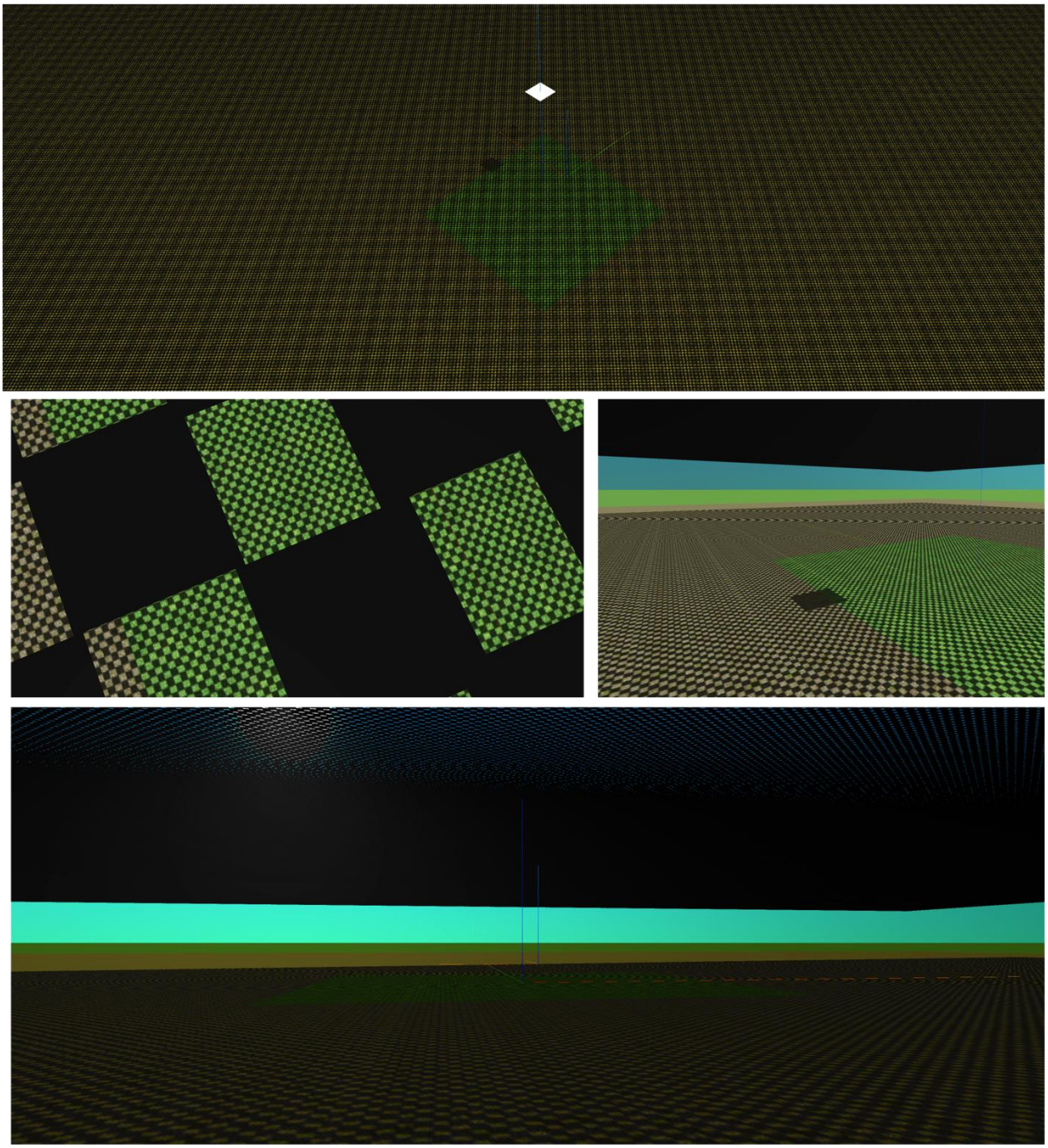

Figure 60: Case 3 modelled in LuSim featuring the net between the ground and PV module marked in white, and the additional internal ground of 10 m x 10 m.

The impact of adding a net with increased thickness is first analysed to ensure the effect on the ground is accurately captured. Figure 61 presents heatmaps of sky visibility view factors for a 100 m x 100 m area. The heatmap on the left represents the scenario without net thickness, while the one on the right incorporates a

2.5 cm net thickness, as specified for this setup. Each scenario includes both a top-down view (top) and a side view (bottom), providing a clear visualisation of the changes introduced by the net's thickness and effectively highlighting its impact.

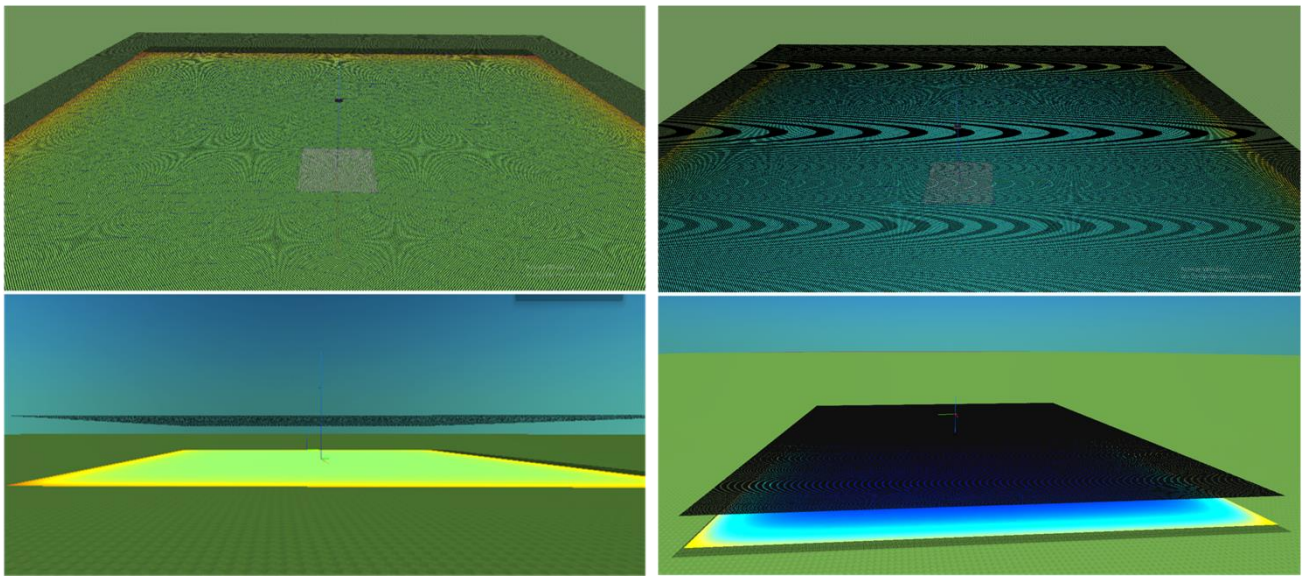

Figure 61: Top view (top) and side view (bottom) of the sky view factor heatmap on the internal ground, showing the comparison between no net thickness (left) and a net thickness of 2.5 cm (right).

When comparing the scenarios without and with net thickness in the heatmap, it becomes evident that the thicker net further restricts the sky view, thereby reducing the amount of irradiance reaching the ground. This is particularly noticeable in the heatmap, where the ground in the right image (representing the scenario with added thickness) is predominantly dark blue. As outlined in the previous section, the diffuse irradiance values at an instant are normalized on a scale from 0 to 1, aligning with the conventional approach used in view factor mapping. Here, a value of 1, represented by hot red, signifies maximum sky visibility and the highest levels of diffuse irradiance, while a value of 0, represented by cold blue, indicates areas with minimal sky visibility, receiving the lowest levels of diffuse irradiance.

This reduction in sky visibility directly impacts the sky view factor seen from the midpoint of the rear side of the PV module. As illustrated in Figure 62, the view factors are compared for the scenario without thickness (left) and with thickness (right).

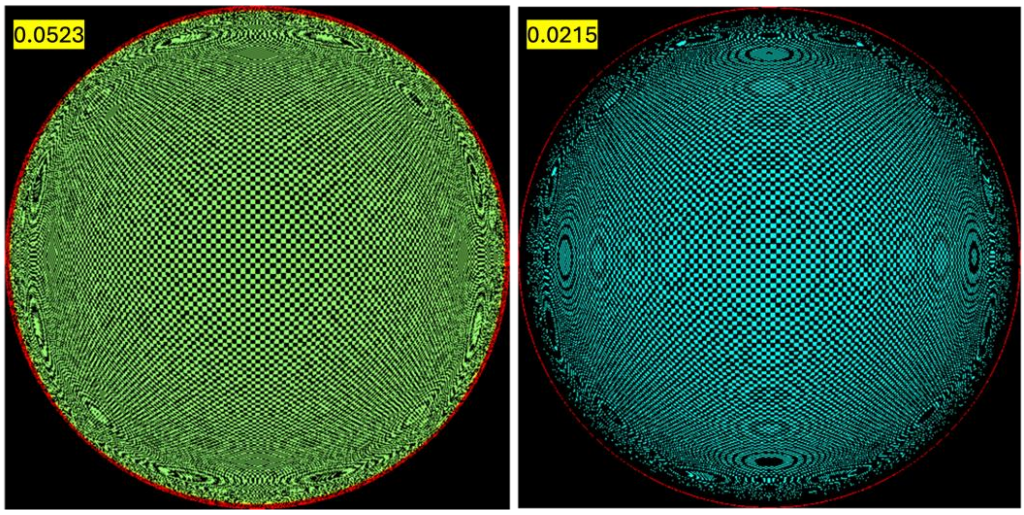

Figure 62: View factor for effective albedo on isotropic diffusive irradiance. Comparison for the scenario with no net thickness (left) and with net thickness of 2.5 cm (right).

When comparing the effective view factor for isotropic diffuse irradiance, the value decreases significantly in the case with added net thickness, dropping to approximately 0.0215, less than half of the 0.0523 observed for the scenario without thickness. This substantial reduction is attributed to the sky obstruction caused by the net's thickness, which limits sky visibility from the ground. Consequently, the reduced visibility from the module's perspective diminishes the reflected irradiance reaching the back side of the PV module.

The effect of the net's thickness on the diffuse albedo view factor at the midpoint of the PV module's back side was previously analysed. A similar methodology is now applied to assess its impact on the direct albedo view factor. Figure 63 compares the time-dependent effective view factor for direct irradiance computed by LuSim with the analytical solution, expressed as $\rho \cdot \cos\theta s$, for December 13th, March 15th, and June 10th. The results are presented for two scenarios: one without net thickness (top) and another with a net thickness of 2.5 cm (bottom).

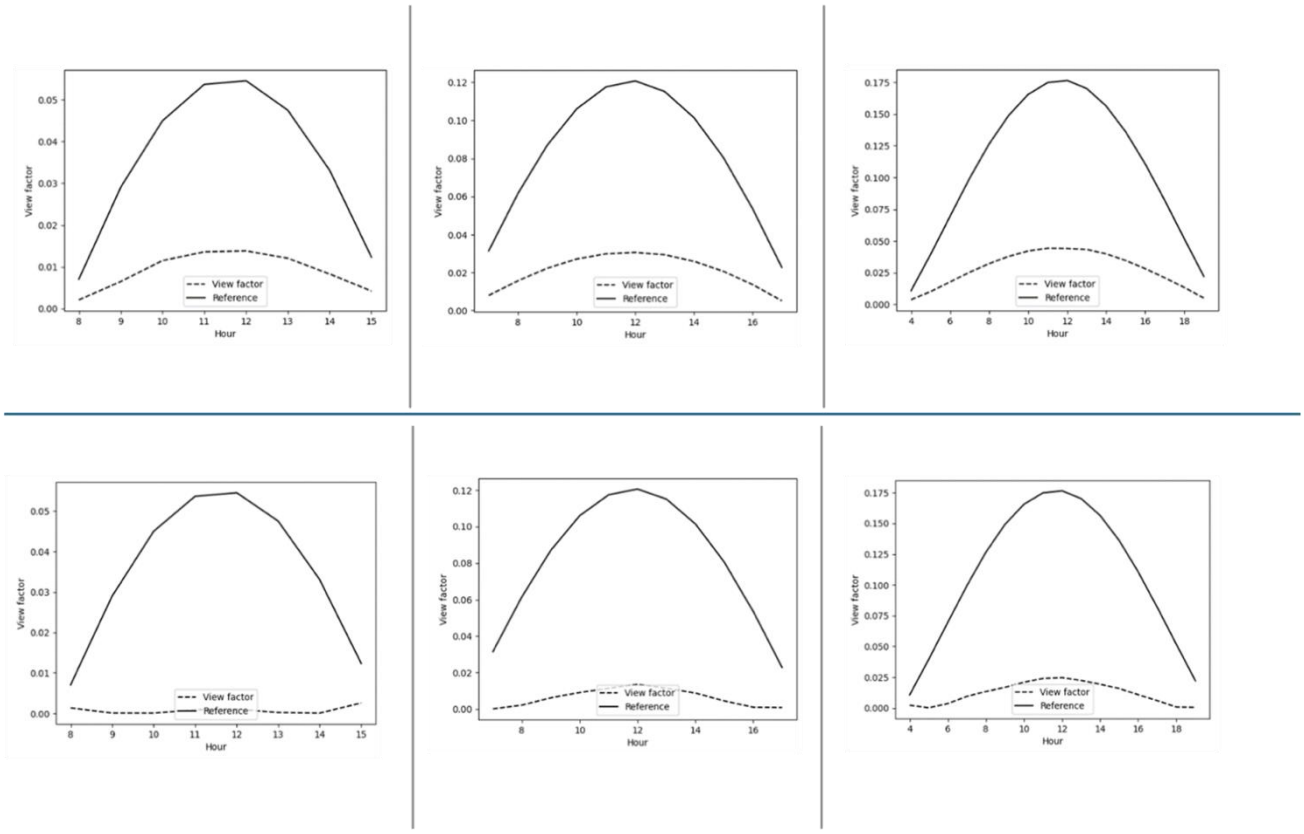

Figure 63: Comparison of the view factor for effective albedo on direct irradiance from the midpoint of the back side of the PV module for the days 13th December, 15th March, and 10th June, for the case with no net thickness (top) and the case with a net thickness of 2.5 cm (bottom).

The top plots (net with no thickness) illustrate that the observed view factor from the midpoint of the back side of the PV module is approximately 0.25 times the theoretical value. This result aligns with expectations, as the presence of the net reduces the ground's exposure to light by half, and only half of the light reaching the ground is reflected to the back of the PV module. Thus, the computed direct albedo view factor is about 0.25 of the theoretical value.

However, for the case with the net containing thickness (bottom plots), the view factor shows smaller values than those observed for the case with no thickness. This occurs because, from the midpoint of the back side of the PV module, fewer points on the ground are visible compared to the case with no thickness. The added thickness of the net directly obstructs more of the ground, and any areas not completely blocked are still partially shaded. This combination of direct obstruction and shading further reduces the effective irradiance reaching the back side of the PV module, underscoring how the physical thickness of the net influences both view factors and irradiance distribution.

The behaviour of light reaching the midpoint of the back side of the PV module is further explored in the comparison section, where the modelled incident light is compared with outputs from other modelers.

In addition to evaluating light at the rear side of PV module's midpoint, this case also focuses on analysing the light reaching specific coordinates on the ground. This section examines the behaviour of the modelled light on the ground due to the net placed 5 m above the surface, with a thickness of 2.5 cm, which casts a prominent shadow and further blocks the light reaching the ground.

To visualise and validate the shading effect, a realistic rendering of shading in LuSim's interface is provided in Figure 64, alongside an hourly plot for a clear-sky day on 28th May. The three snapshots show the ground encompassing the Cartesian coordinate (4.97, 4.94, 0) at 10:00, 11:00, and 13:00 as indicated on the snapshots respectively. These timestamps are also marked in the graph with red circles to highlight key peaks and depths in the modelled BTI_shaded (direct beam tilted irradiance with shading).

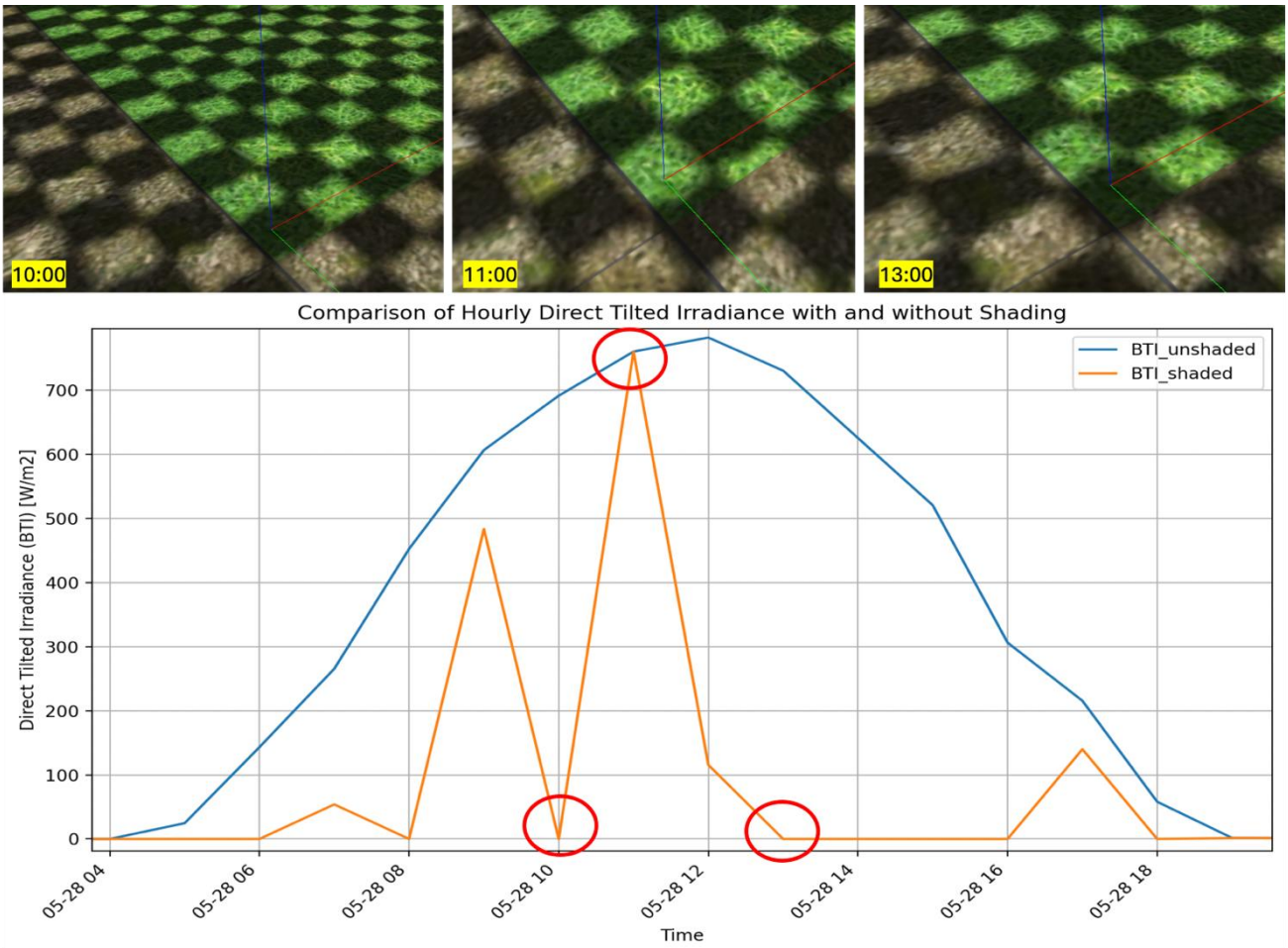

Figure 64: Shading profile at the 'Edge' of the internal ground with realistic snapshots of shading in 3D for the clear-sky day of 28th May.

The alternating shading pattern observed, caused by the sun's movement and the presence of the net, is clear. The points marked with circles on the plot correspond to snapshots placed above, showcasing the realistic rendering of the 3D scene along with the shading. At 10:00 and 13:00, the shading effect can be visualised in

the respective snapshots, which display the ground at the Cartesian coordinate (4.97, 4.94, 0), marked by the tricolored axis. These snapshots highlight the prominent shading patterns at those specific instances. Notably, the peak observed in the plot at 11:00 results from the absence of shading at this point, with the location being illuminated.

For reference, the 'BTI_unshaded' (direct beam tilted irradiance without shading effects) is also plotted, providing a direct comparison to the 'BTI_shaded' values. This comparison highlights the impact of shading caused by the net on the direct irradiance reaching the specified coordinate. This basic visual check has been conducted for the 'Edge' of the internal ground.

It is equally relevant to analyse the behaviour of the second point at the coordinate (0, 0, 0), referred to as the 'Origin.' Following the same methodology, Figure 65 presents 'BTI_shaded_origin' alongside 'BTI_shaded_edge' and 'BTI_unshaded' for reference, for the same clear-sky day of 28th May. Timestamps 10:00 and 14:00 are specifically marked to highlight two key differences between the 'Edge' and 'Origin' points. Snapshots of the realistic shading rendering from LuSim's 3D interface, corresponding to the marked times on the plot, are also provided. These snapshots enable a direct visual comparison of the shading effects at these critical instances, offering further insight into the spatial and temporal variations in shading caused by the net.

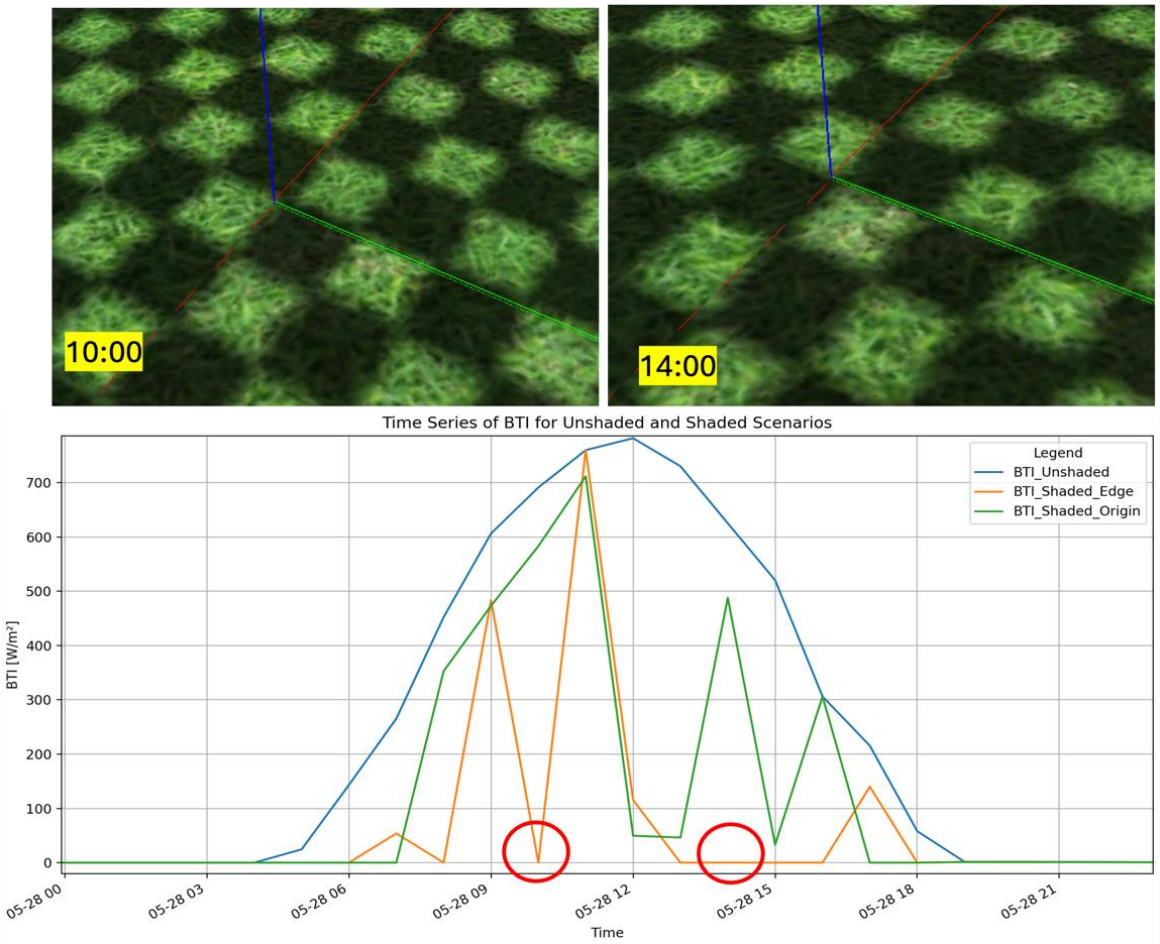

Figure 65: Shading profile comparison for the 'Edge' and 'Origin' of the internal ground with realistic snapshots of shading in 3D for the clear-sky day of 28th May.

The shading profiles for the two selected points; 'Edge' and 'Origin' are distinct. This highlights the importance of selecting diverse points for analysis to better understand and compare the behaviour across different modellers. The observed differences in behaviour are expected due to the alternating net pattern, which casts varying levels of shading at different points on the ground over time.

Two notable differences are marked on the plot for 'BTI_shaded_edge', where, for the corresponding timestamps, the behaviour of 'BTI_shaded_origin' is opposite. Specifically, at these instances, the Origin point does not undergo complete shading but rather remains under partial shading, as evidenced by its comparison with 'BTI_unshaded' at the same timestamps. This behaviour is further verified through the realistic 3D renderings of the shading, presented at the top of the 2D line plot. These renderings provide a clear visual confirmation of the shading differences, reinforcing the alternating shading effect caused by the net's pattern and the sun's movement throughout the day.

With this preliminary check confirming that the obtained modelled time series for the ground aligns well with the 3D shading rendered, visually validated through snapshots, it becomes particularly relevant to analyse

how the point at (4.97, 4.94, 0), referred to as the 'Edge', compares to the point at (0, 0, 0), referred to as the 'Origin', in terms of yearly shading losses. This comparison is not intended to identify any specific pattern in the differences between the two points, as they are randomly selected with an understanding that they will inherently behave differently. This difference is driven by their unique positions relative to the alternating shading pattern created by the mask with added thickness. The primary purpose of this analysis is to observe and compare how these two points perform among different modellers, rather than to draw any conclusive comparisons within the points themselves, beyond the expectation that their behaviour will differ.

Figure 66 provides a visual comparison of the yearly shading losses for the two points; 'Edge' and 'Origin'. Where, the Edge represents the periphery of the analysed 10m x 10m ground and the Origin corresponds to its centre.

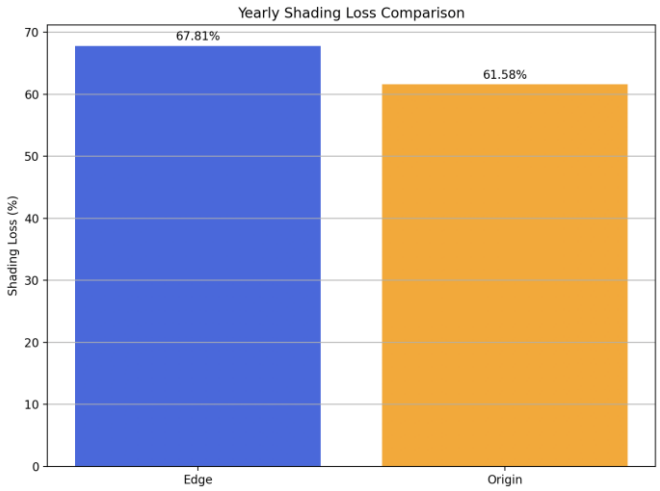

Figure 66: Yearly shading loss comparison between the two selected points on the internal ground.

As expected, the comparison highlights the difference in shading behaviour between the edge and the centre of the ground. This can be purely attributed to the specific locations of these points and the shading patterns they are subjected to, caused by the checkerboard-patterned mask with an added thickness of 2.5 cm. The variation observed across these two points demonstrates the impact of different shading conditions on the internal ground of 10 m x 10 m, which is placed centrally beneath a 100 m x 100 m net, elevated 5 m above the ground.

5. MODELLING OF OPEN AGRI-PV SYSTEMS

5.1. Introduction

For the modelling of open agrivoltaic systems, the Bolzano demonstrator in Italy (located in the municipality of Ora) is used as the case study. The top view of the demonstrator, presented in Figure 67, highlights both the "existing" plant and the "new" plant. This study focuses on the "new section" of the demonstrator, with the methodology and simulation results provided by each partner in their respective sections.

The new section differs from the existing one in two key aspects:

- The spacing between the rows of trees.
- The transparency of the photovoltaic modules.

In the new plant, photovoltaic modules are mounted on horizontal single-axis trackers (HSAT) aligned along the NNE-SSW axis, commonly referred to as roll trackers. These trackers are equipped with a backtracking algorithm to optimise sunlight interception and reduce shading losses.

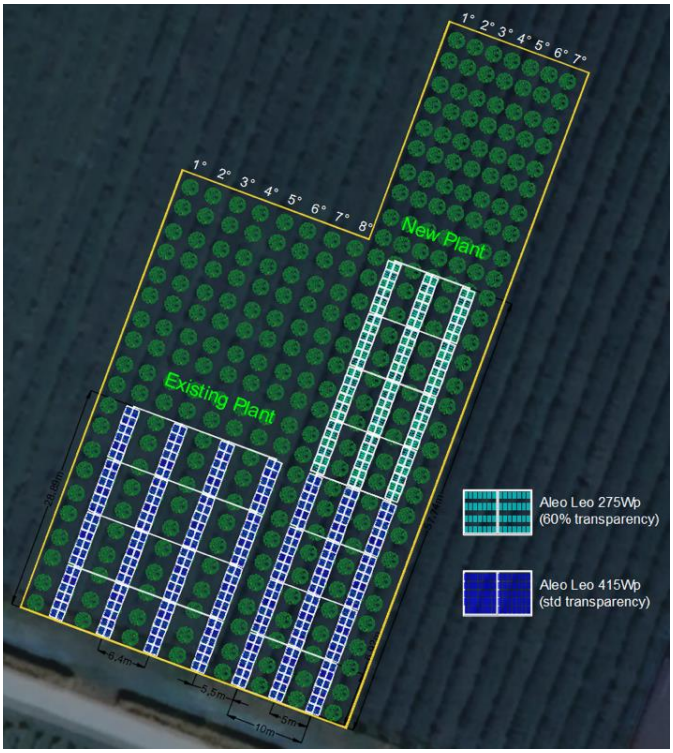

Figure 67: Top view of open Agri-PV system of Bolzano, Italy, including existing and new plant.

The objective of this study is to compare the modelled total global tilted irradiance (GTI) or total global incident irradiance reaching the surface of the crop's envelope. This includes evaluating the total incident irradiance/irradiation at various spatial resolutions, i.e., at various places on the crop, and temporal

resolutions, along with the corresponding percentage shading losses caused by the PV system, support structures, and inter-row shading from the crops.

5.2. Input Data

5.2.1. Modelling Environment

From a modelling perspective, the Agri-PV plant is segmented into three components:

- The PV modules support structure
- The crops
- The PV system

The entire system is modelled with the field azimuth set to a 20.3˚ deviation clockwise from south, ensuring accurate alignment of the plant's components with the surrounding environment.

5.2.2. PV Modules Support Structure

The PV module support structure is based on a fundamental gantry system, as shown in Figure 68. This system consists of a grid-like frame supported by four vertical poles, forming the basic structural unit of the frame system. The beams in the y-direction (aligned along the east-west axis, indicated by the green line) supports grouping of PV modules, whose layout is detailed in the PV modules section. The beams in the x-direction (aligned along the north-south axis, indicated by the red line) provide additional structural stability. This structural unit is designed to be modular and can be replicated, as explained in the layout section.

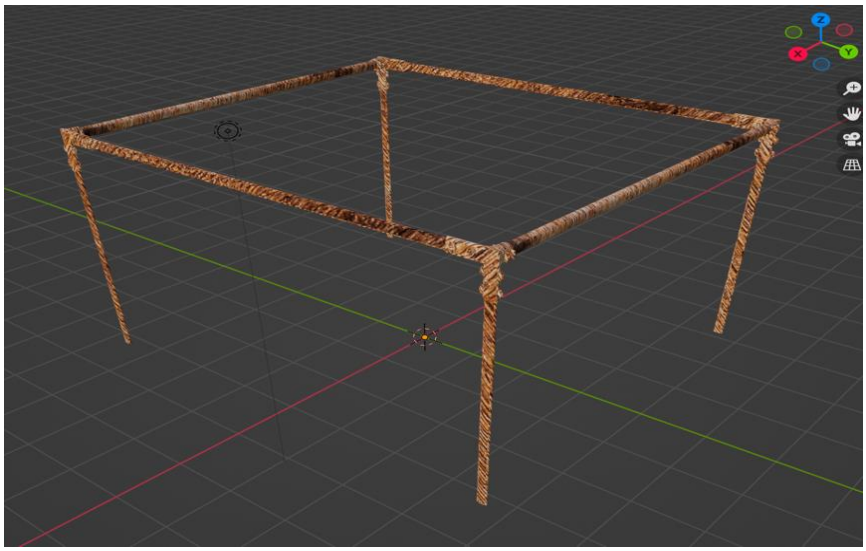

Figure 68: Frame design for the Agri-PV plant in Bolzano.

The PV module support structure features beams in the x-direction (north-south) with a length of 7.225 m. The beams are spaced 5 m apart in the y-direction (east-west), creating a consistent and organized layout. The

beams themselves represent a shape of cylindrical tube with a radius of 0.1 m. The total height of the frame in the z-direction is 4.7 m.

As shown in Figure 69, the PV module support structure consists of a total of three frames in the east-west direction and four frames in the north-south direction, forming a grid-like arrangement. The downward side corresponds to south, while the rightward side corresponds to east.

This layout represents the new plant. The arrangement is modelled to scale, accurately reflecting the dimensions and proportions of the plant for precise analysis and simulation.

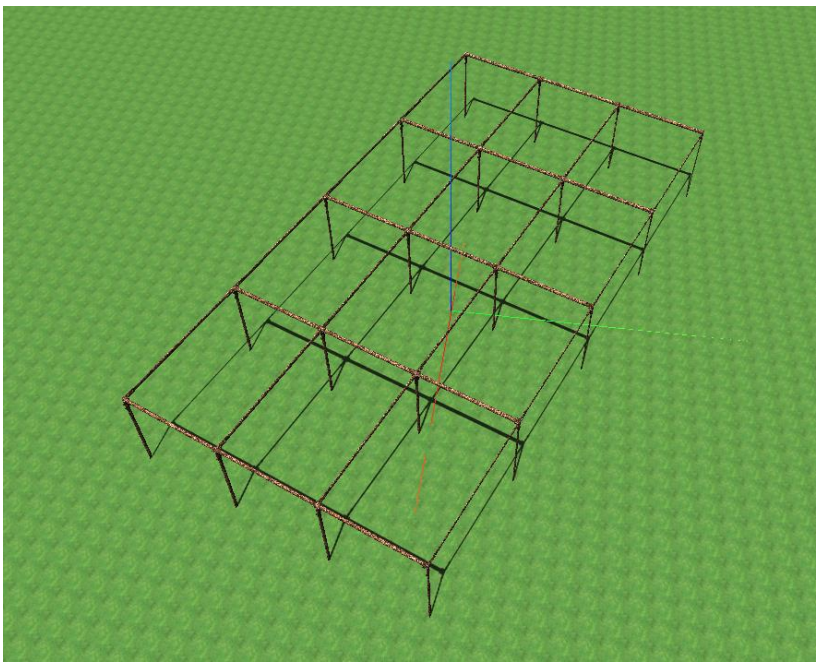

Figure 69: Layout of frame for the open Agri-PV system.

5.2.3. Crops Modelling

The current focus is on modelling apple orchards, encompassing both the planting and harvesting phases. The investigation is focused on the 'New Plant', with particular attention to the illumination reaching the surface of the 3D-modeled envelope of the apple crop and the corresponding percentage of shading loss caused by the PV system.

In the context of 3D modelling, the choice of crop representation plays a key role in achieving a balance between realistic detail, computational feasibility, and the utilization of crop yield models developed by agronomists. Two broad approaches can be considered:

- **Complex geometries:** Complex geometries aim to replicate the detailed structure of plant organs and leaves. This approach is advantageous for utilizing advanced models to evaluate crop photosynthesis and to estimate the 3D optical porosity of the canopy with high accuracy. However, this method demands significantly higher computational resources, as it increases the number of points where

irradiance must be calculated. It also poses challenges for modelers to couple the simulated irradiance with the crop yield models that uses simpler agronomic models that rely on irradiance incident on the external envelope of the crop. Figure 70 illustrates a complex geometry model of the Existing Plant within the Agri-PV demonstrator in LuSim.

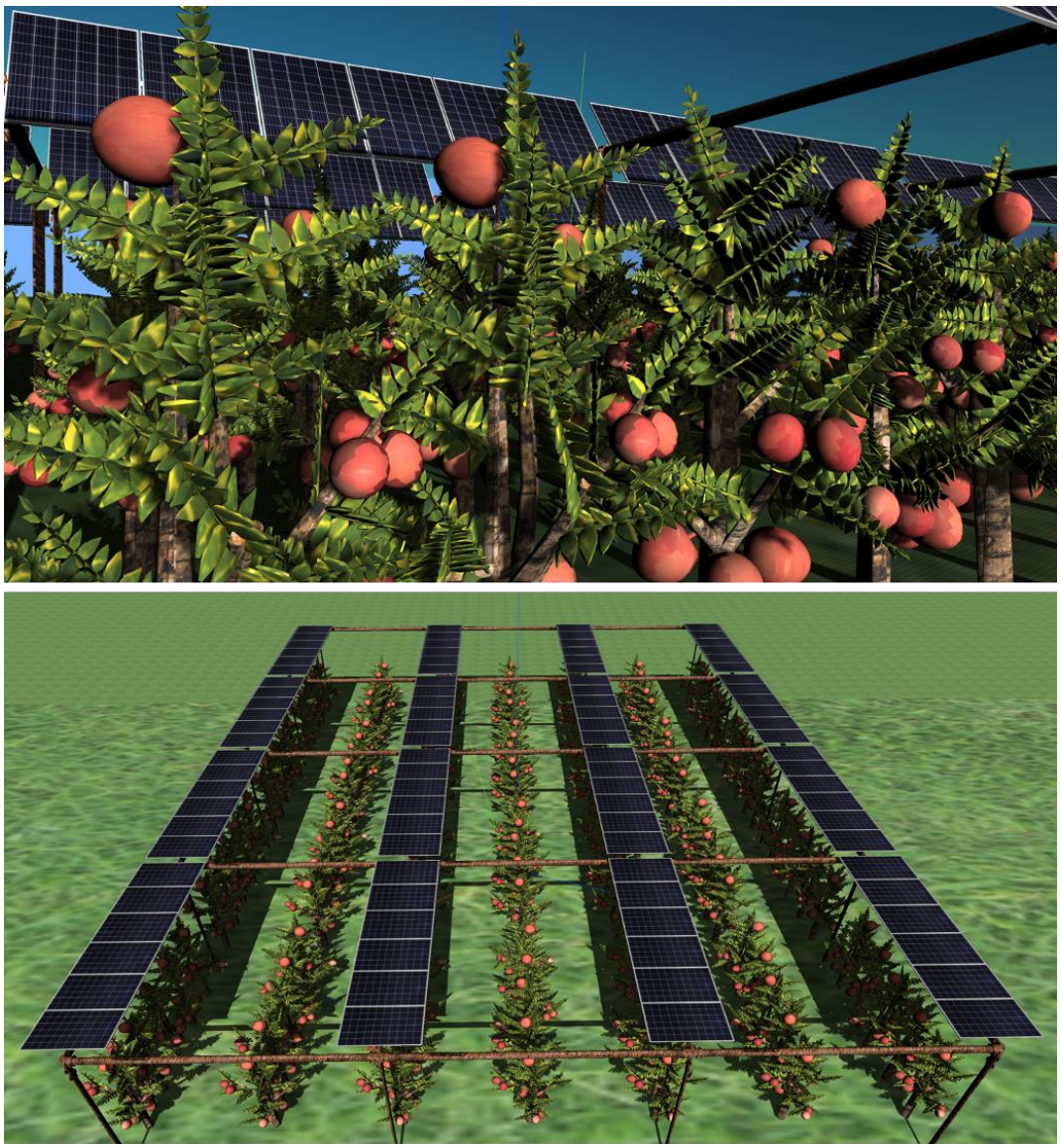

Figure 70: Complex shaped crops featured in the open Agri-PV system in LuSim.

- **Simplified shapes:** Using basic geometric shapes to approximate the outer envelope of crops reduces computational complexity while facilitating the use of parametric models for crop yield. This approach limits the uncertainty introduced by varying tool capacities for modelling intricate shapes, thus, particularly suitable for comparing results among modelers.

Given the trade-offs, the simplified geometric approach is adopted at this stage to balance precision and computational efficiency. This approach ensures consistency in modelling outcomes and enables the evaluation of solar irradiance on the apple orchard's external canopy. A parallelepiped is used to represent two apple trees or one-fourth of the complete orchard row. This object has an assumed width of 0.4 meters in the east-west direction, a length of 6.8 meters in the north-south direction, and a vertical height of 3.0 meters for the canopy. Additionally, the canopy maintains a ground clearance of 0.5 meters. The dimensions are marked accordingly in Figure 71 representing the canopy of the apple crop.

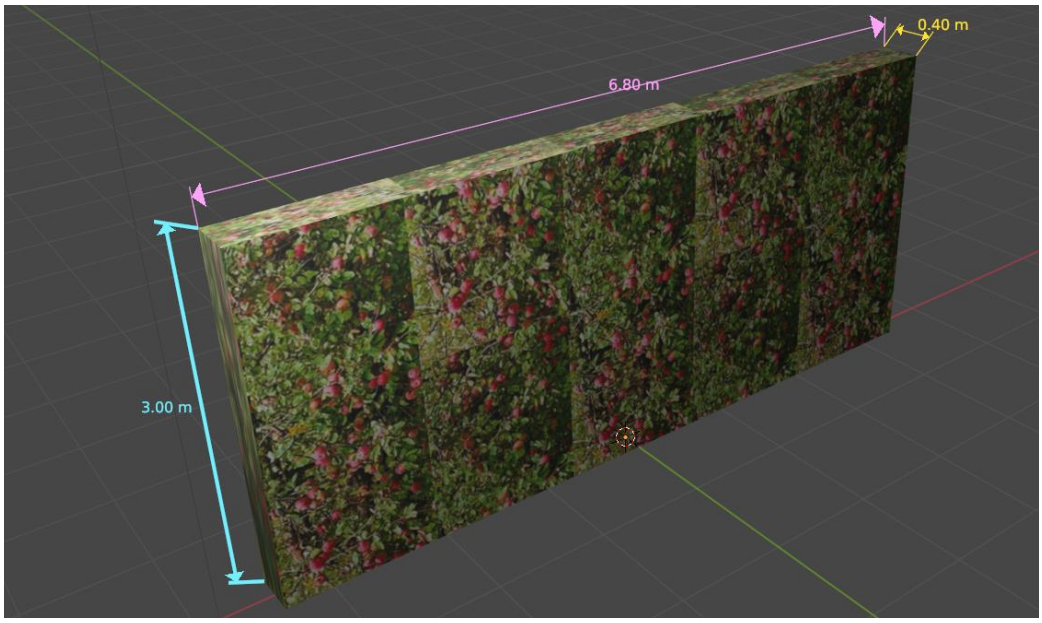

Figure 71: Dimensions of the orchard crop parallelepiped used in the simulations.

Figure 72 shows the front view as seen from the west. It can be observed that there are four blocks of parallelepiped along the north-south direction, with one block positioned within each frame. These crops are centrally aligned along the length of the frame in the north-south direction.

Figure 72: View from the west show casing the crop layout.

The side view from the south, in Figure 73, illustrates the distribution of the rows of crops that are aligned north-south along the east-west direction, with a pitch of 2.5 meters between two rows of orchard blocks.

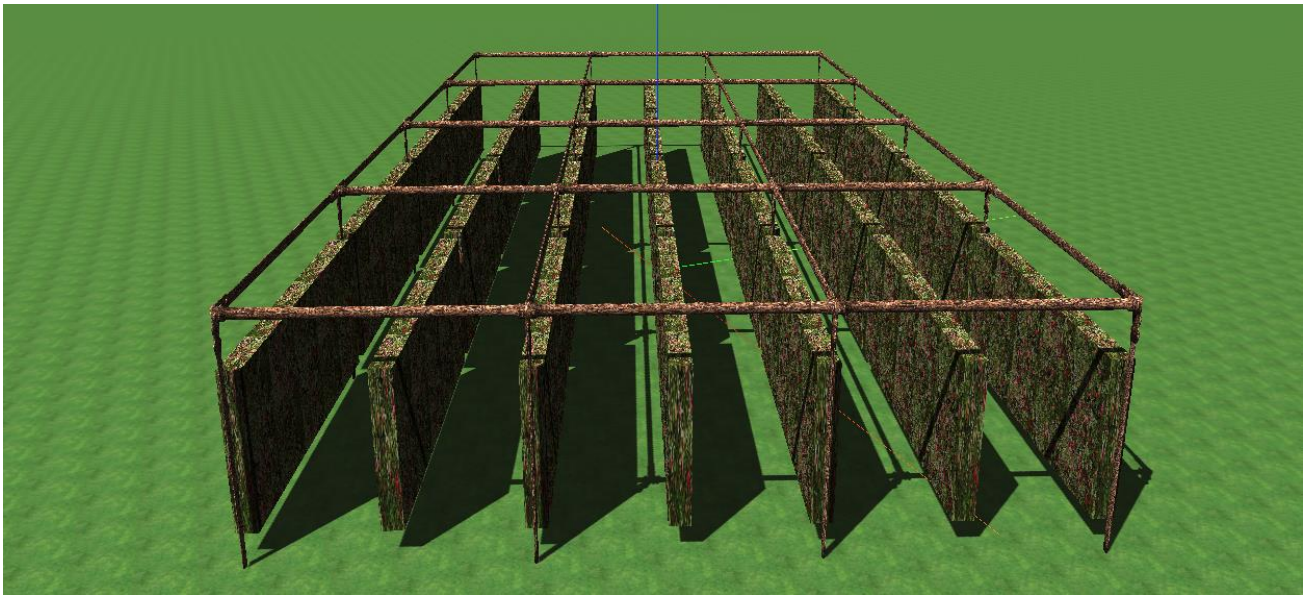

Figure 73: View from the south showcasing the crop's pitch in east-west and layout.

5.2.4. PV Array

The PV system in the new plant features the Aleo 275 Wp bifacial semi-transparent module with an estimated 40 % transparency, integrated with a tracking and back-tracking system.

Each PV module has a length of 1.752 meters, a width of 1.144 meters, and a thickness of 0.04 meters. The total number of cells per module is 72. The layout of the PV module is shown in Figure 74.

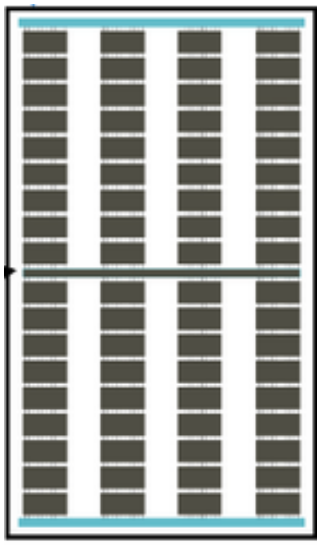

Figure 74: Cell layout in the module with 40% transparency.

For this study, torque-tube specifications related to the tracking system are not considered in the modelling. Consequently, their dimensions are deemed redundant and are excluded from the scope of this analysis.

Each tracker in the PV system is designed to accommodate 24 PV modules, spanning a single row along the north-south direction. The modules are arranged into 4 groups of 6 modules each, with each group separated by a gap of 0.15 meters. The arrangement spans 4 frames, with each frame along its length corresponding to a span. The pitch of the system, defined by the east-west frame width, is set at 5 meters. The modules are mounted on a horizontal single-axis tracker, allowing a maximum rotation of ±55°, with the rotation axis positioned at an elevation of 4.7 meters. The modules are configured in a 1P arrangement (portrait orientation with one PV module in height) and the layout is visually represented in Figure 75, showcasing the complete open Agri-PV system.

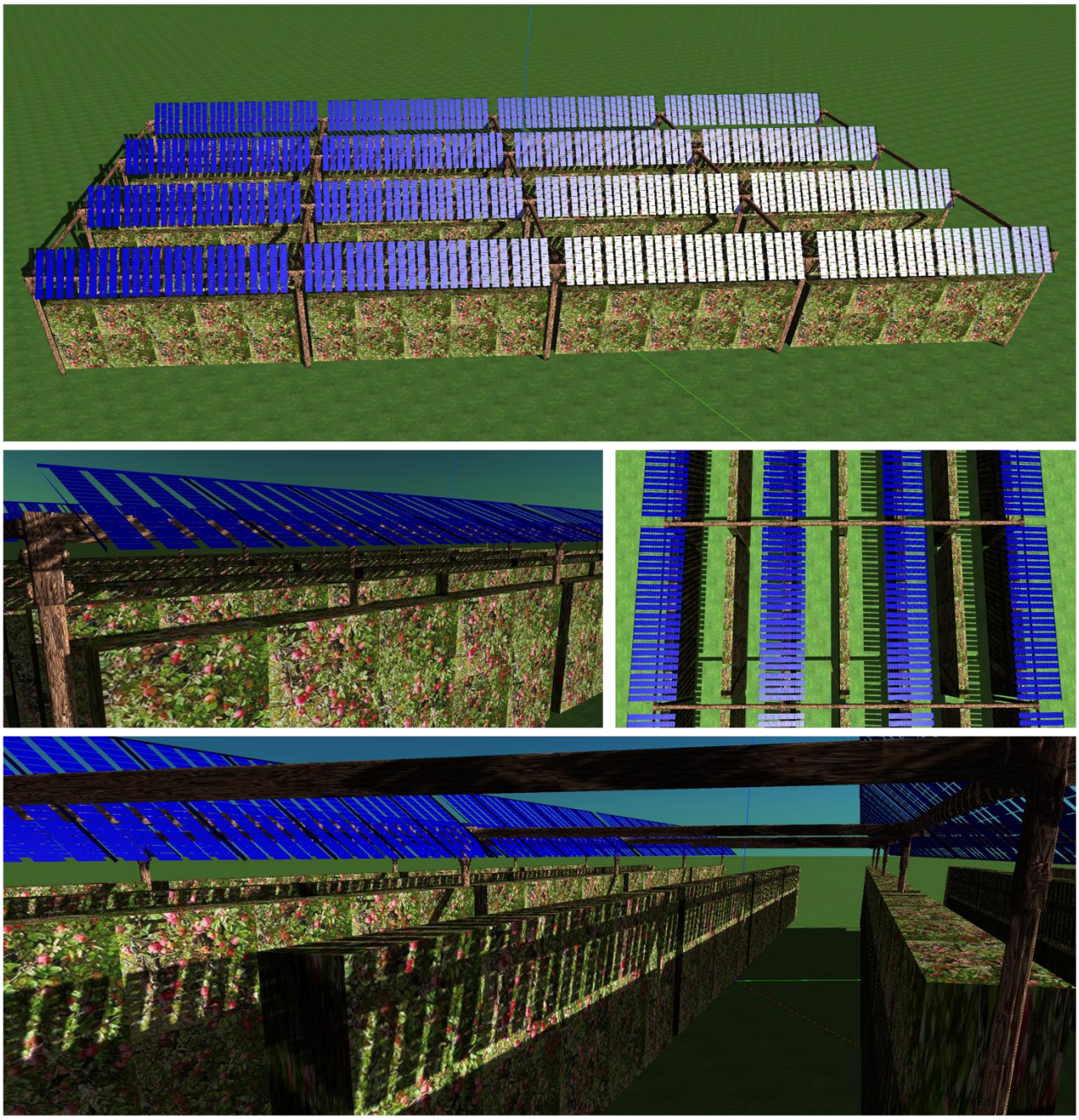

Figure 75: Agri-PV system layout featuring crops and PV modules with standard transparency.

5.2.5. Material Properties

The optical properties of all surfaces in the model are defined with a focus on consistency and simplicity. Lambertian reflectance is assumed as the default for all reflecting surfaces, including the ground, crops, wooden frames, PV cells, and the support structure. The glass transmittance is modelled as specular by Imec and TUD, while LuciSun assumes no diffusion with a transmittance value of 85 %. The albedo value is set to 0.2 for the ground, crops, and the frame, while the PV cells are assigned an albedo value of 0.05. The canopy reflectance is also modelled as Lambertian, with a transmittance of 0 % (fully opaque).

5.2.6. Solar Resource

For consistency among modelers and to reduce uncertainties in benchmarking the tools, the same time series file for the solar resource is used with the different tracker positions. This ensures a unified dataset across simulations. Table 4 shows a monthly summary of the solar resource data used in the modelling.

Table 4: Monthly summary of the solar resource and weather data used in the light evaluation.

Month	GHI [kWh/m²]	DNI [kWh/m²]	DHI [kWh/m²]
Jan.	41.13	61.27	19.34
Feb.	70.63	102.64	26.13
Mar.	105.55	110.36	42.83
Apr.	147.60	139.65	56.60
May	151.84	109.44	73.45
June	199.08	169.32	72.76
July	189.43	167.62	64.99
Aug.	166.28	159.56	56.99
Sep.	133.67	156.61	39.31
Oct.	77.35	89.59	31.96
Nov.	48.25	76.43	20.16
Dec.	32.86	55.06	15.45
Year	1363.67	1397.55	519.97

The input solar resource for modelling is based on a local weather file provided by EURAC for the coordinates 46.3807 (latitude) and 11.2870 (longitude). As the file consists of global horizontal irradiance (GHI) values based on pyranometer measurements, a decomposition algorithm was utilized to extract the direct and

diffuse irradiance components. This methodology, part of TUD's developments, is elaborated further in section 5.6.1 Modelling refinements. This file was adopted by all partners, which was fed into the sky model. Imec and TUD utilise the Perez All-Weather sky model [13], while LuciSun employs the Hay and Davies model [11]. The horizon profile is excluded from this study.

5.3. Methodology

This study aims to compare the modelled irradiance results across different tools. Ensuring consistency in inputs, simulation parameters, and output formats is crucial to minimize uncertainties and facilitate meaningful comparisons. Aligning all modelling tools with the same inputs, as outlined in the input section, and providing outputs under similar conditions will help reduce variability and focus on key deviations arising from differences in methodology, limitations, or models adopted during various stages of the modelling process.

Beyond the standardised inputs and simulation parameters, any additional assumptions, specific methodologies, or variations in the overall modelling flow are detailed in the methodology sections specific to each partner, which also includes the respective inputs. These sections provide an overview of the modelling approaches while emphasising the unique capabilities, functionalities, and limitations of each tool or method. This ensures a thorough understanding of how the partners apply their respective tools to model agrivoltaic systems.

This section emphasises the use of the input parameters mentioned earlier in the overall modelling process, detailing how these parameters are integrated to generate outputs. It also discusses the nature of outputs to be produced, and the methods employed to ensure they are comparable across tools, enabling an accurate and insightful comparison of results.

5.3.1. Irradiance evaluation on crop envelopes: targets, zone and sensor creation

One of the primary objectives of this study is to evaluate the light reaching the crop's envelope. A key question arises: how should the irradiance be calculated for comparison? This includes determining which crop in the entire 3D scene should be analysed and selecting crops that effectively represent the overall behaviour of all crops in the scene. Additionally, for the selected crops, consideration must be given to how the modelled light is spatially represented, whether the time series data should represent the entire crop's behaviour or focus on specific zones or selective areas of the crop that are known to behave differently or are prone to receiving varying levels of light. This focus aligns with agronomists' interests in understanding light distribution patterns at a granular level, as such information is often essential for optimising crop yield and management strategies.

For the purposes of modelling, whether at the zone level or the complete object level, the process involves computing irradiance at specific points on the surfaces of interest. These points may represent a zone, a surface, or the complete crop, and their values are averaged to depict the overall behaviour.

Two distinct modelling approaches are employed by the partners involved, each with its own methodology for computing irradiance:

- GPU-based 3D view factor approach in LuSim (LuciSun)
- Ray-tracing approach (Imec and TUD)

LuSim computes irradiance using triangular meshes, with irradiance calculated at the vertices of the mesh. Reducing the mesh size for a specific region increases the number of points where irradiance is evaluated, thereby improving accuracy.

In ray tracing, irradiance is computed by placing sensors at specific points, where rays are cast and projected to evaluate light. Increasing the number of points in this approach requires adding more sensors, thereby increasing the number of rays traced.

To compare results across these approaches, it is crucial to maintain consistency in the number of evaluation points for a specific region, object, or crop. This poses an additional challenge, as mesh resolution in LuSim and sensor point density in raytracing differ inherently in their representation and computation. The specific methodologies employed by each partner are explained in greater detail in their respective sections.

Although the study's primary aim is not to analyse light distribution across zones but rather to compare results between modelers under various crop conditions, focusing on specific points ensures consistency. By evaluating light incident at a single representative point, such as the midpoint of a selected zone or crop, the uncertainties associated with maintaining uniform spatial resolution are minimized. This point acts as a proxy for the zone, just as selected objects represent similar objects within the scene.

The selected point for comparison will be identified using its 3D coordinates. Since all modelers utilise a 3D origin coordinate system for their scenes, the location of the point can be defined precisely within the coordinate system. LuSim can simulate and export results for this point, while Imec and TUD can place sensors at the corresponding 3D location.

To ensure accurate comparisons, the entire system must be constructed with its centre aligned to the origin of the 3D coordinate system, adhering to the same layout and dimensions. This alignment ensures that the selected coordinates representing the point for evaluating irradiance will remain consistent across all modelling platforms. However, this approach introduces certain challenges due to differences in modelling methodologies.

The following sections in the methodology detail which crops are selected, how zones are allocated, and in what format results are exported to facilitate meaningful comparisons across different modelling tools.

Target Objects

To determine or obtain the coordinates for specific zones of the selected crop, the first step involves selecting a target object that is representative of similar objects within the 3D scene. In this study, the target object is the outer envelope of the apple crop, as specified in the 'Inputs' section. It is essential to choose specific envelopes that accurately represent the behaviour of other crop envelopes in the scene.

Two target objects are selected, each representing different conditions of crop placement with respect to their surroundings in the 3D environment:

- **Under-PV crop:** The envelope located directly under the PV modules.
- **Free crop:** The envelope positioned in the free space without PV modules or between two rows of PV modules.

Figure 76 showcases the Agri-PV system with the two target objects highlighted in white and marked in the 3D scene.

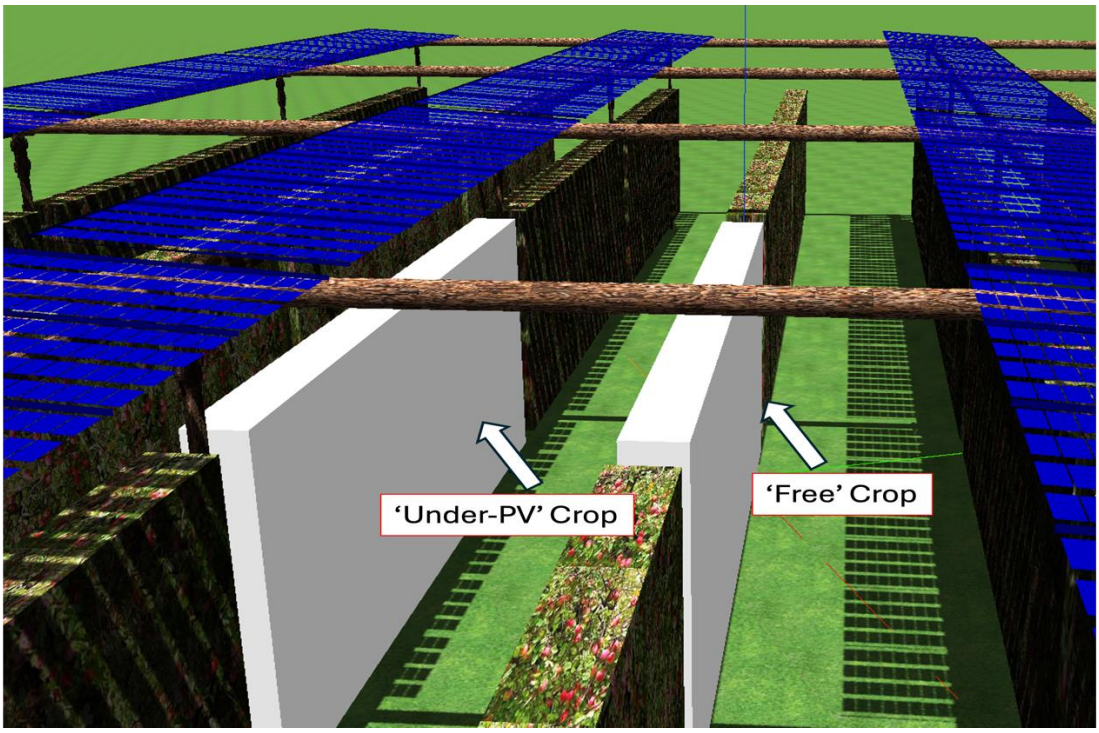

Figure 76: Bolzano's new Agri-PV plant, with crops indicated as target objects for simulations.

Zone Creation

When assessing the light reaching the crops and the corresponding shading loss percentage, the vertical surfaces of the modelled crop's envelope are of primary importance. These vertical surfaces play a significant role in photosynthesis due to their greater effective surface area for converting sunlight compared to the top of the canopy.

The vertical sides of the crop are divided into three equal zones based on their height:

- Bottom: Segment spanning from 0 to 1 meters
- Middle: Segment spanning from 1 meters to 2 meters
- Top: Segment spanning from 2 meters to 3 meters

The vertical faces are evenly divided into these three zones, while the top horizontal surface represents an additional zone for sky-facing light evaluation. Figure 77 illustrates this zone separation, with the west-facing and sky-facing sides indicated.

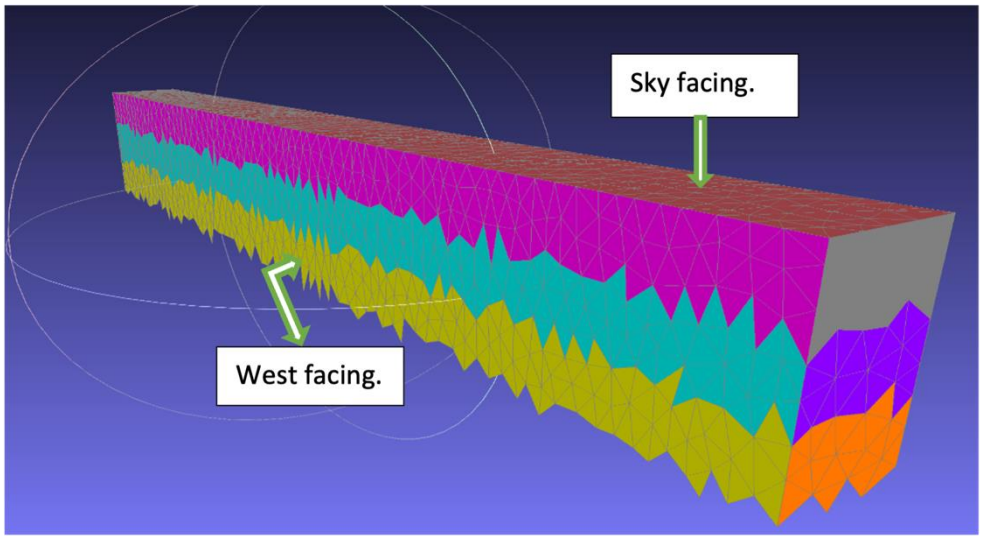

Figure 77: Zone separation for the apple crops as seen from the east side.

Thus, there are 3 zones on the eastern side and 3 zones on the western side. In addition, there is a top horizontal zone, which represents the light incident on the upper surface of the crop canopy. This configuration results in a total of 7 distinct zones for evaluating solar irradiance on the crops.

The southern and northern sides of the crop are not evaluated, as the length of the crop rows is considered long enough for the impact of these zones to be negligible.

Subsequently, each crop envelope is assigned a texture that contains its optical properties, as outlined in the input section. These properties ensure accurate simulation of the interaction of light with the crop surfaces and their corresponding zones.

Point Selection

As stated in the section on evaluating irradiance on crop envelopes and comparison strategy across the three modelling tools, roughly midpoints are selected as representative points for each zone. These midpoints serve as the basis for calculating irradiance and shading loss, ensuring consistency across modelling tools. Table 5 provides the 3D coordinates of the selected midpoints for each zone and each crop type (Under-PV and Free).

In this table:

- The Zone column describes the position of the zone, the corresponding number to identify it, and the direction it faces (east, west, or sky-facing).
- The Under-PV (X, Y, Z) column represents the 3D coordinates of the points on the crop envelope located directly beneath the PV modules.
- The Free (X, Y, Z) column represents the 3D coordinates of the points on the crop envelope located in the open space, without PV modules or between two rows of PV modules.

Table 5: Coordinates corresponding to selected zones of targeted crop for light analysis on respective point.

Zone	Under-PV (x, y, z)	Free (x, y, z)
1-bottom-east	2.96, -3.64, 0.78	2.8, -0.93, 0.95
2-middle-east	2.94, -3.64, 1.91	3.25, -1.12, 2.44
3-top-east	2.88, -3.61, 3.01	3.48, -1.21, 3.17
4-bottom-west	2.75, -3.99, 1.09	2.55, -1.26, 1.11
5-middle-west	2.74, -3.99, 1.86	2.9, -1.41, 1.91
6-top-west	2.76, -4.00, 3.11	3.29, -1.57, 3.04
7-sky-facing	2.85, -3.81, 3.5	3.46, -1.42, 3.5

These zones and their associated midpoints are designed to capture the variations in light distribution across the crop envelope. The coordinates ensure consistent representation of each zone and facilitate accurate placement within the 3D modelling environment for meaningful comparisons across tools.

5.3.2. Irradiance evaluation on the PV modules

In addition to the crop evaluation, irradiance is also evaluated at one point on the front and back sides of the PV module, following the layout and other inputs. A roughly central PV module has been selected for this purpose. Table 6 provides the 3D coordinates of the selected points on the front and back sides of the PV module.

Table 6: Coordinates corresponding to the front and rear side of the targeted PV module for the light analysis on the respective point.

Side	Coordinates (x, y, z)
Front	-4.64, - 0.71,4.80
Back	-4.64, - 0.71,4.80

Simulations are performed on the complete timeseries dataset described in the input section. The GTI values from each modeler for the selected points (on the crop and PV module) is generated over the entire timeseries in hourly intervals.

The following section on statistical parameters and error metrics elaborates on how the comparison results will be calculated, presented, and analysed. This ensures consistency in evaluation and provides insights into model performance across different tools.

The hourly irradiance is analysed across the modelling tools (LuciSun, and Imec and TUD) for different zones and selected points, under both clear-sky and cloudy-day conditions. This analysis aims to identify trends in irradiance behaviour and check for any potential time shifts between the tools.

Following the hourly analysis, the monthly irradiation trends and annual cumulative irradiation are compared across the tools. This step highlights longer-term behaviour, assessing the consistency in modelled outputs over extended periods.

5.4. LuciSun (LuSim)

For the targeted crops and the PV module, the incident irradiance components and the shading loss percentage are calculated. Figure 78 illustrates the meshing applied to the targeted crops, with zones and regions indicated accordingly for clarity.

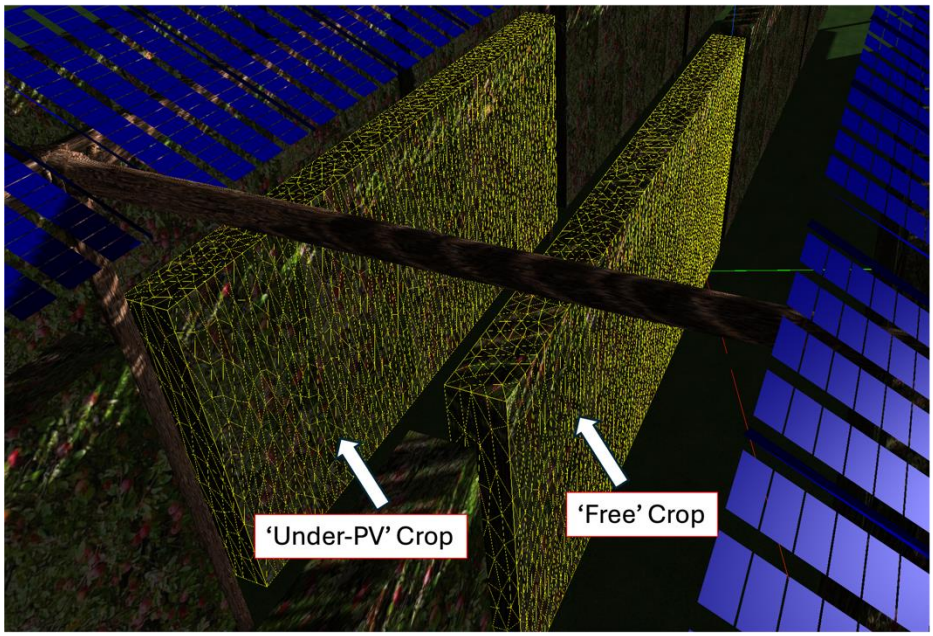

Figure 78: Meshing applied to the target objects.

The shading loss percentage is defined as the difference in light reaching specific target objects between the configuration with no PV system or greenhouse structure (reference case) and the configuration with the closed agrivoltaic system or greenhouse (test case), divided by the reference case. Maintaining consistency between the test case and the reference case is critical to ensure that the same parameters are considered in the modelling across different tools. This consistency allows results to be compared not only within this study but also in broader contexts, ensuring that the shading effects assessed by each tool stem from the same cause.

In LuSim, shading losses are computed without requiring the creation of a separate reference model or system. Instead, a single simulation of the "test" case is sufficient, as shading losses due to each additional 3D object capable of casting shadows are evaluated directly. Rather than focusing on the shading losses caused by

individual 3D objects, LuSim calculates the overall shading losses on selected crop points due to the complete 3D environment or the PV system. This approach aligns with the practical objective of determining the total shading impact.

Analysing shading losses from individual 3D objects is often valuable for projects where the system layout is still being optimised. However, in the case of a demonstrator with fixed parameters, such as the open agrivoltaic system in Bolzano, the focus shifts to understanding the total shading losses within the established configuration. For visualisation and clarity, the 'reference' case is shown in Figure 79.

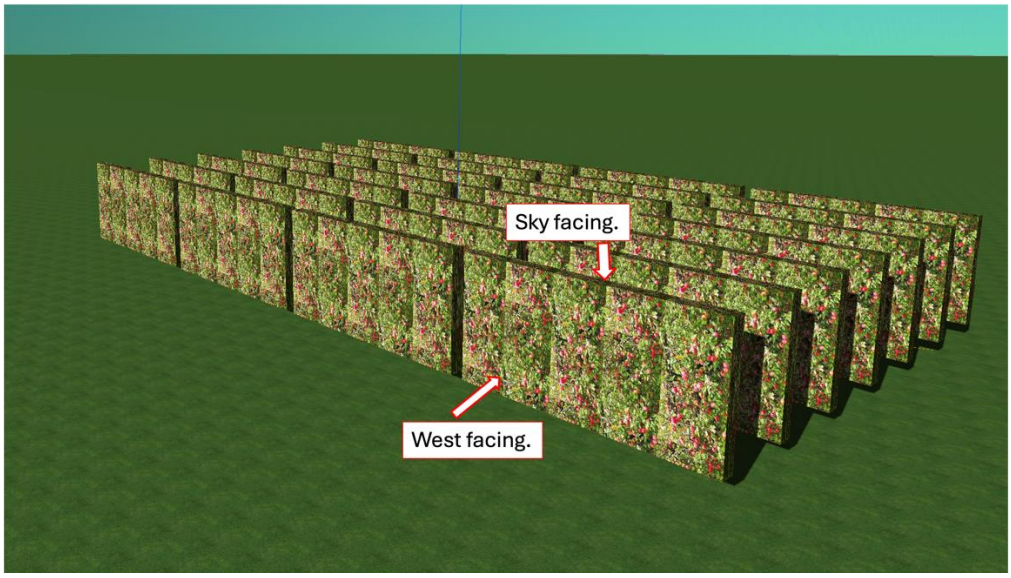

Figure 79: Reference case for Bolzano's existing section of the Agri-PV systems.

Within the context of this study, several key developments have been undertaken and implemented to complement the work carried out in Deliverable 5.1 of SYMBIOSYST [14]. While Deliverable 5.1 primarily focuses on modelling Global Tilted Irradiance (GTI) without incorporating reflected irradiance, as near shading losses were the primary concern for assessment, this deliverable extends the methodology by including the contribution of reflected irradiance as a function of various environmental factors, such as the ground, wooden frames, PV modules, and neighbouring crops. This represents a crucial enhancement as reflected irradiance contributes significantly to the GTI for any specific point on the crops. The material properties for these elements are detailed in the inputs section above.

A key development introduced in this work allows to model irradiance on any selected point on the 3D model, corresponding to any mesh vertex, for example, on the crop surface, as visualized in Figure 78 showcasing the meshing structure. This modelled irradiance can be exported or visualized in the LuSim interface, utilizing 2D plots that complement the 3D heatmaps. These visualisations provide enhanced granularity and precision, enabling GTI to be modelled and analysed for any specific location on the crop object. This surpasses the zone-aggregated approach of Deliverable 5.1, offering deeper insights into the irradiance distribution.

Another significant advancement pertains to the ability to model and export GTI at the cell level for both standard transparent and semi-transparent PV modules. To illustrate this, Figure 80 provides a top view highlighting the selected module in white (top) and a close-up view of the selected module (bottom) with the selected cell highlighted in red. The irradiance is analysed specifically at the coordinates mentioned in Table 5. The modelled irradiance includes both the front and back side contributions for that specific cell, visualised with the aid of a tri-coloured axis indicating the local coordinate system.

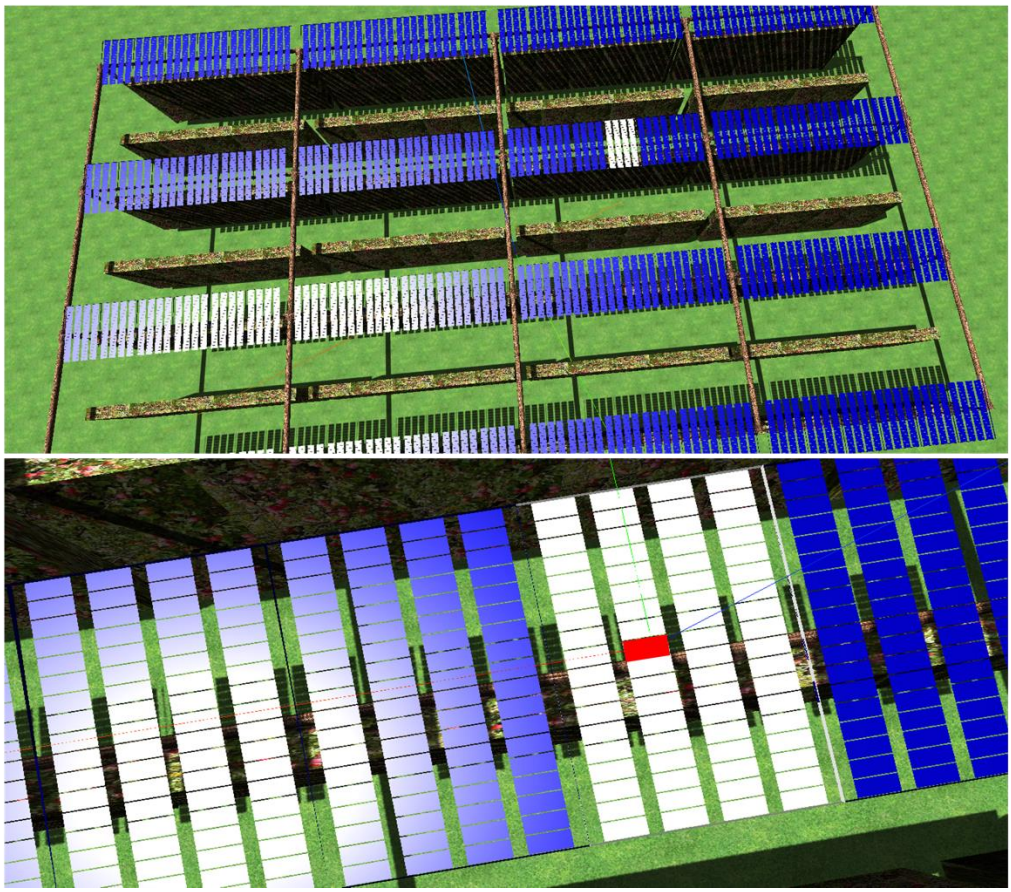

Figure 80: Top view highlighting selected PV module (white) and close-up view showing analysed cell (red).

Beginning with the analysis for the crop, it is crucial to evaluate how different zones behave compared to each other within a specific crop, followed by comparisons across different crops. This involves analysing zones within a crop and across crops for various irradiance components under varying sky and temporal conditions, which collectively contribute to the Global Tilted Irradiance (GTI in W/m²).

5.4.1. Direct Irradiance

In practice, LuSim applies the same view factors to both the direct irradiance and the circumsolar diffuse irradiance, as both components are directional. Throughout this section, any mention of direct irradiance should be understood to include both direct and circumsolar diffuse components. The extensive behaviour of

direct irradiance across all zones for the selected crops has been comprehensively detailed within the framework of SYMBIOSYST Deliverable D5.1 [14]. This section, however, focuses on validating the obtained time series to ensure they align with the shading profiles observed in the 3D environment. This is achieved through 2D plots and snapshots of realistic 3D shading renderings along with their corresponding heatmap counterparts from the LuSim 3D environment.

For this analysis, sky-facing zones from the two targeted crops are selected. The investigation begins with an hourly comparison for a clear sky day in summer, specifically on the 26th of May, 2023. The time series comparison in Figure 81 shows that the curve for the free space sky-facing zone is smoother, reflecting the characteristic of a clear-sky day with minimal interruptions. In contrast, the sky-facing zone under the PV crop experiences constant variations with peaks and depths, indicative of partial shading throughout the day. This behaviour is aligned with the presence of semi-transparent PV modules placed above, causing periodic shading and allowing only portions of light to pass through. These fluctuations in the under-PV zone are logical, given its placement beneath the PV modules.

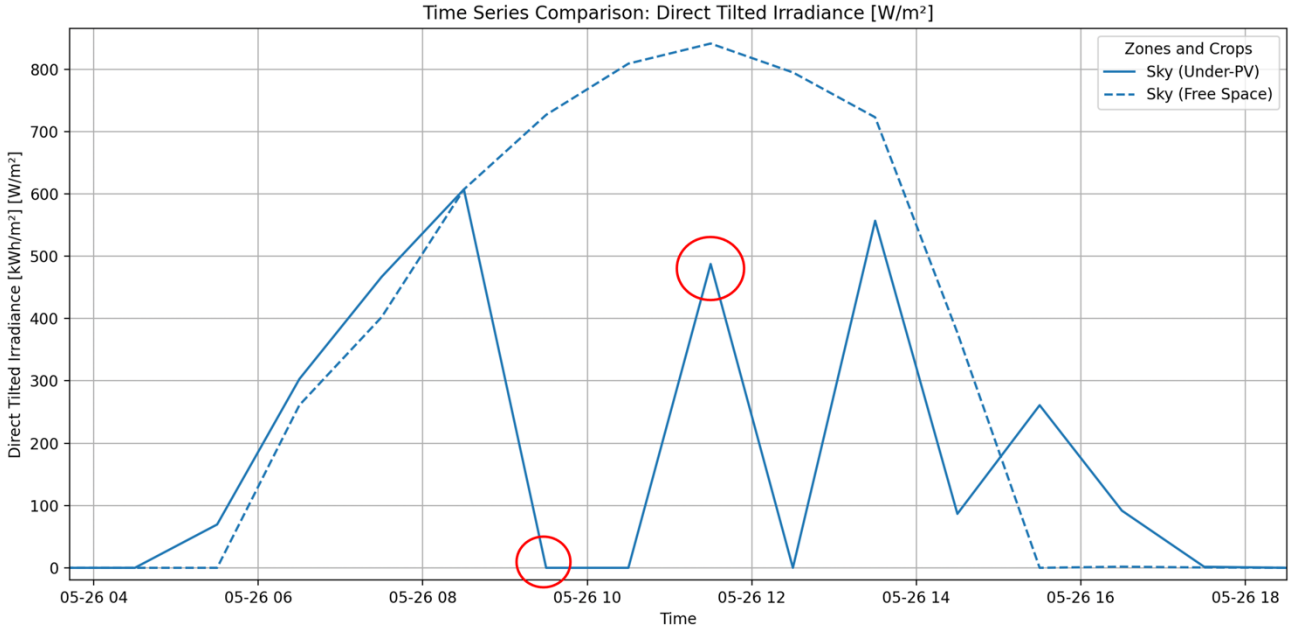

Figure 81: Hourly direct irradiance reaching for the sky facing zone of 'Free-Space' crop and 'Under-PV' crop.

To validate this observed behaviour, a 3D visualisation of the shading profile for the targeted points in the sky-facing zones for both crops is displayed. Figure 82 below shows the heatmaps corresponding to the times of 9:30 (left) and 11:30 (right), as marked in the plot above with red circles. These points serve as examples where distinctly different behaviour is observed for both curves. Additionally, within these two timestamps, variations in behaviour for the crop under PV can also be observed. This analysis, performed for the same clear sky day of 26th May, provides insight into how the PV modules affect the direct irradiance received by the zones. In the heatmap, two snapshots are presented for specific moments: 9:30 (left) and 11:30 (right), with

respective legends below them displaying irradiance values in W/m² derived from the input used for modelling the incident irradiance, along with the corresponding colour scale.

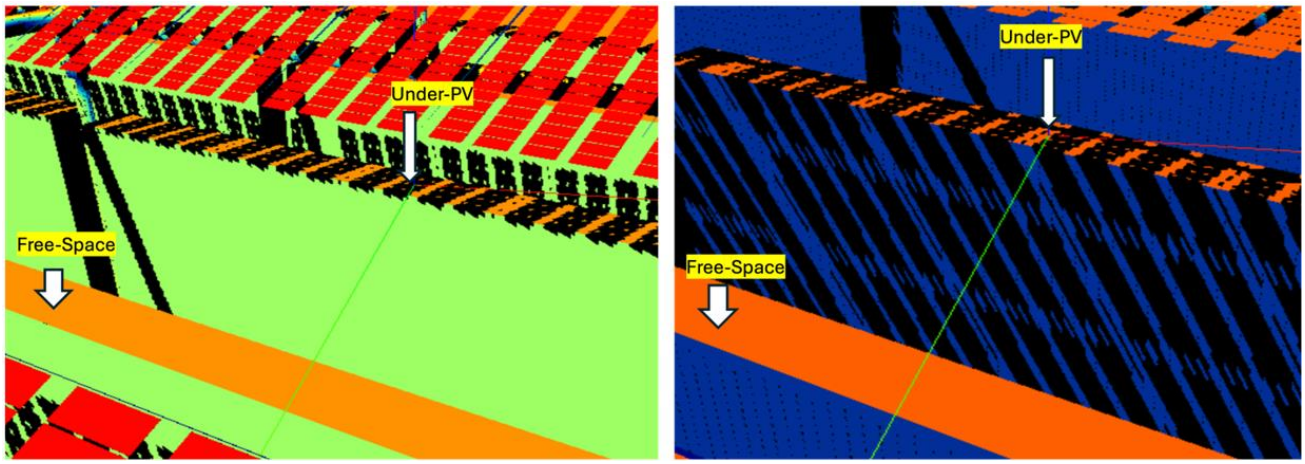

Figure 82: Direct tilted irradiance for 9:30 (left) and 11:30 (right) on the clear-sky day of 26th May, 2023.

It is immediately evident that the free-space sky-facing zone remains entirely unshaded throughout, aligning perfectly with the smooth trend observed in the hourly plot in Figure 81. On the other hand, the under-PV sky-facing zone exhibits shading cast by the semi-transparent PV modules placed above, as visualised in the heatmaps. This shading pattern explains the consistent peaks and depths observed in the under-PV plot in Figure 81.

To provide clarity, the exact coordinate analysed for the under-PV zone, indicated in Table 5, is highlighted with an arrow labelled “Under-PV” in the heatmaps. Additionally, a tri-coloured axis is placed on this specific point. Observing this point in both heatmaps reveals that at 9:30, the point is under complete shade, which aligns with the plot in Figure 81 showing direct irradiance at 0 W/m². By 11:30, the shading has shifted, and this point now receives direct light while still being subjected to partial shading. The visualisations in Figure 82 help confirm the shading effects caused by the semi-transparent PV modules and their impact on irradiance distribution, reinforcing the interplay between the shading and the resulting irradiance trends observed in the timeseries plot above.

With an understanding that the zones, depending on their placement with respect to the module positioned above, experience compounded effects of shading and irradiance distribution, a yearly comparison of shading loss across all zones provides a comprehensive perspective. This comparison between the crops under PV and in free space is visualized in Figure 83, highlighting how each zone is impacted on an annual scale by its specific environment and proximity to reflective or obstructive surfaces. The bar plot provides a comprehensive view of yearly shading losses across zones for the ‘Under-PV’ and ‘Free Space’ crops.

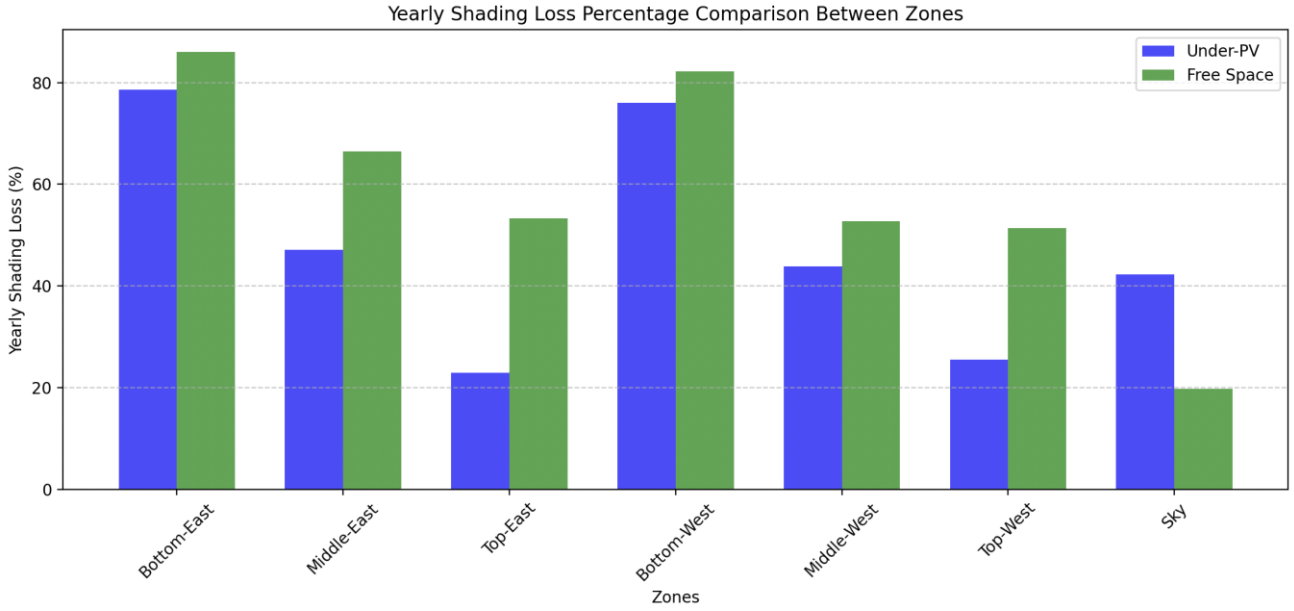

Figure 83: Yearly shading losses comparison for all zones between crop in 'Free-Space' and crop 'Under-PV'.

A clear trend emerges where, for both crops, the bottom-most zones experience the highest shading losses due to their proximity to the ground and the increased shading caused by surrounding crops. This is followed by the middle zones and then the top zones, with the sky-facing zones undergoing the least shading due to their unobstructed exposure to the sky. This behaviour aligns with expectations, as zones closer to the ground are more susceptible to intercrop shading and have reduced exposure to direct sunlight compared to the upper zones. Interestingly, when comparing across crops, contrary to expectations, crops under PV modules experience overall less shading than crops in free space. This counterintuitive result can be explained by the influence of sun movement and the use of trackers. These factors skew the shadow cast by the PV modules to the sides for most parts of the day, thereby shading the vertical faces of the crop in free space more than those directly beneath the modules. Benefiting the vertical sides under PV, which are crucial for light absorption and photosynthesis, these zones undergo less shading compared to free-space crops. However, when considering specific surfaces, the horizontal, sky-facing sides of crops benefit from being in free space, where they are exposed to uninterrupted sunlight without shading from PV modules. For crops where the vertical sides are pivotal for light absorption and photosynthesis, placement under PV modules proves beneficial. However, when the sky-facing horizontal surfaces are of primary interest, free-space crops demonstrate superior outcomes due to the absence of module-induced shading. Despite the sky-facing surfaces receiving more light in free-space crops, the vertical sides play a far more significant role in photosynthesis due to their larger light-collecting surface area. This underscores the practical importance of designing systems where crops are placed under PV modules, not only for optimized light exposure but also for protection against environmental factors such as hail, rain, and freezing conditions. To verify the seasonal impact on shading losses, the monthly shading losses for all zones are analysed for one such crop.

The results for the crop in free space are shown in Figure 84, providing insights into how shading effects vary across seasons and zones. The heatmap illustrates the monthly shading loss trends for the crop in 'Free-Space.' As expected, the sky-facing zone consistently receives the least shading loss, with the lowest values observed during the summer months due to the sun's higher elevation, minimizing shading effects. Conversely, during winter, the sun's lower elevation leads to PV modules from neighbouring rows casting shadows, increasing shading losses.

The bottom-most zones, particularly the west and east-facing zones, experience the highest shading losses. The bottom-west zone receives the most shading loss during the summer due to the system's south-east orientation and the sun's higher elevation. In contrast, the bottom-east zone incurs higher shading losses during the winter as the sun rises in the south-east with a low elevation, keeping this zone in shadow for longer durations.

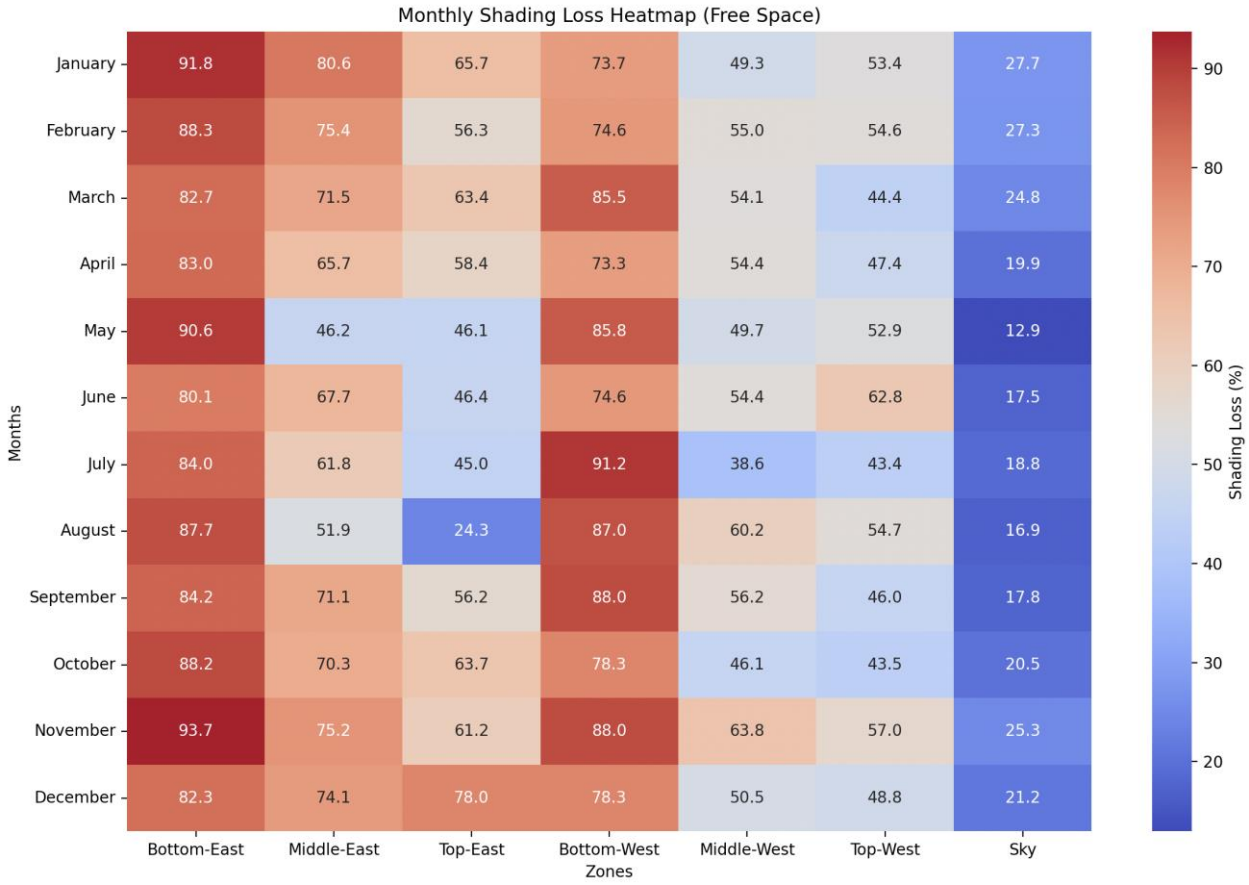

Figure 84: Monthly shading loss for all the zones of the crop in 'Free Space'.

For the middle-east and top-east zones, shading losses are lower in summer compared to winter. This is because, during summer, the sun's high elevation concentrates shadows towards the bottom regions of the vertical sides, resulting in reduced shading for the top-east zone. The middle-west and top-west zones experience relatively lower shading losses compared to their east-facing counterparts. During winter, with the

system's south-east alignment and the sun's low elevation, these zones receive partial illumination in the latter half of the day, whereas the east-facing zones remain more shaded. However, during summer, shading losses for the west middle and top zones increase as the sun rises from the east and stays higher in the sky, leading to more shadows on these zones in the latter part of the day compared to winter. The observed trends may not fully represent the entire zone's behaviour for a season, as the analysis is based on points randomly selected from the middle of each zone. These points may not capture all nuances of shading within the zone.

5.4.2. Diffuse Irradiance

The heatmap in Figure 85 illustrates the distribution of isotropic diffuse irradiance across the complete terrain, capturing the effects of sky visibility through view factors projected from each vertex of the triangular mesh, where the example of the mesh applied to targeted crops has been shown above in the methodology section. The diffuse irradiance values at an instant are normalized on a scale from 0 to 1. This normalization aligns with the standard approach when mapping with view factors, where a value of 1 (depicted in hot red) represents maximum sky visibility and the highest levels of diffuse irradiance, while a value of 0 (depicted in cold blue) indicates minimal sky visibility, corresponding to the lowest levels of diffuse irradiance.

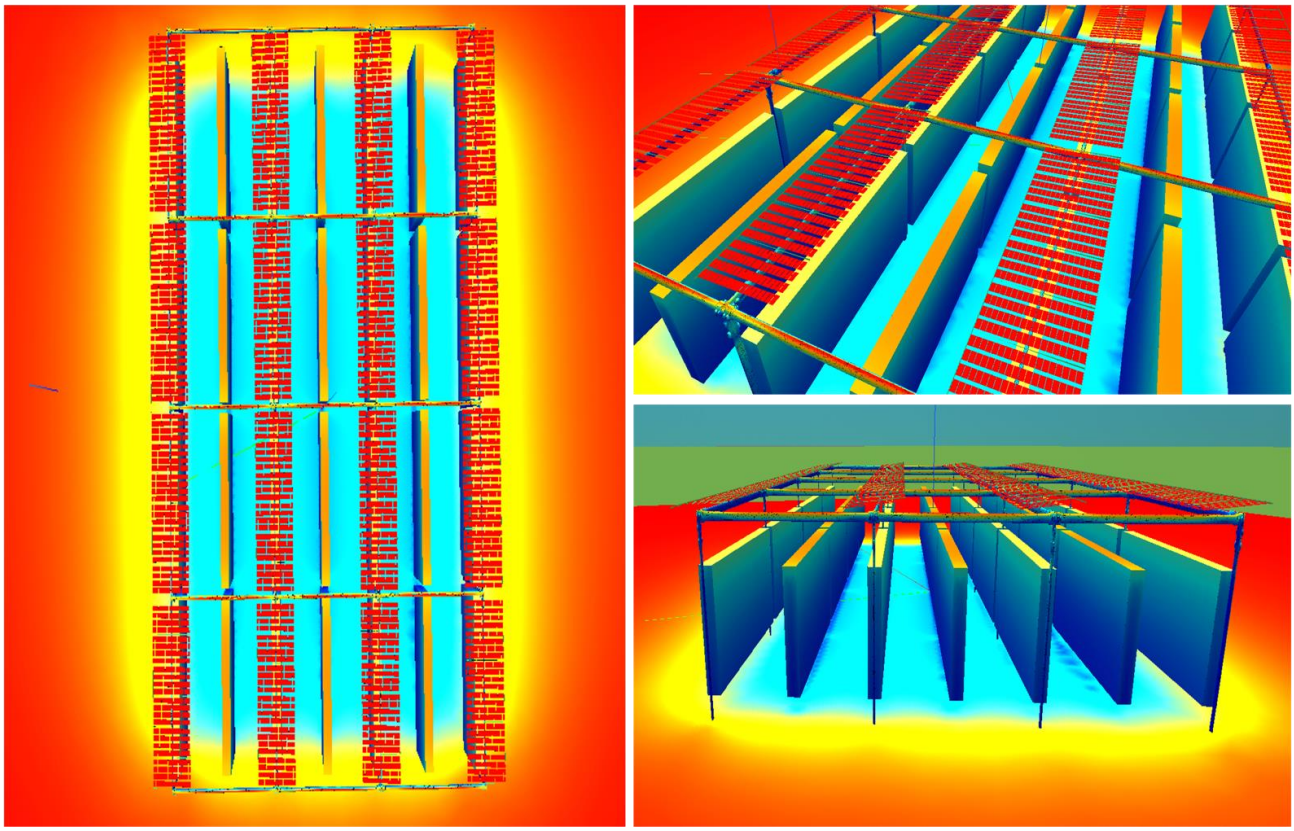

Figure 85: Heatmap of sky-visibility or diffuse irradiance applied to complete open Agri-PV scene in LuSim.

This visualization effectively demonstrates the interplay of the PV installation's geometry, crop arrangement, and the surrounding structures in modulating the diffuse component of solar irradiance.

For instance, the sky-facing zones closer to the PV modules exhibit colder tones due to restricted sky visibility caused by shading from the modules, while open areas away from the modules display warmer tones, reflecting higher sky visibility and enhanced diffuse irradiance.

In contrast, for the vertical sides, the bottom-west zone shows noticeably cooler tones, attributable to the decreased sky visibility caused by shading from the modules and surrounding structures. The ground areas, particularly beneath the crops, exhibit the least visibility, represented by the coldest tones, indicating minimal exposure to the sky.

The diffuse irradiance heatmap, or visibility mapping, as seen in Figure 85 above is applied comprehensively to the entire 3D environment, encompassing the crops, PV modules, frames, and ground. This holistic approach allows for a clear understanding of how the crop dimensions and arrangement, coupled with the PV modules, influence and interact with diffuse irradiance distribution.

Furthermore, the preliminary observations from the heatmap above are quantified by analysing the diffuse tilted irradiance reaching the different zones of both the targeted crops. This analysis enables a detailed comparison of the diffuse irradiance among the zones within each crop and between the two crops on a yearly basis. The results of this quantification are visualized in the bar plot shown in Figure 86.

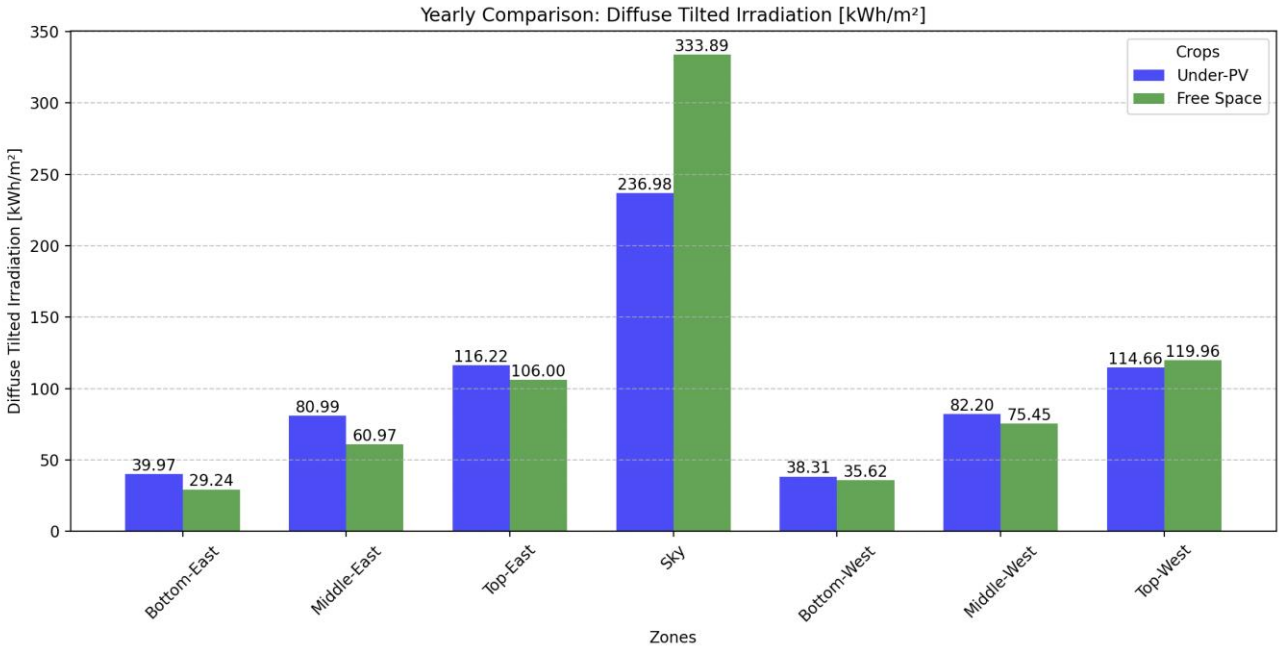

Figure 86: Yearly diffused tilted irradiation for all zones between crop in 'Free-Space' and crop 'Under-PV'.

As expected, the bar plot shows the sky-facing zones in both crops show significantly higher diffuse tilted irradiation compared to the vertical zones, primarily due to their greater exposure to the sky. The sky-facing zone in Free-Space exhibits significantly higher diffuse irradiation than its counterpart under PV modules, owing to the absence of shading structures like PV modules above it.

The expected trend for vertical sides of the crops is also clearly observed, where, as we move from the top zones to the bottom zones, the sky visibility decreases. This behaviour is attributed to the proximity of the bottom zones to the ground and the surrounding crop rows, which obstruct the view of the sky more significantly compared to the top zones.

Furthermore, similar to the trend observed for direct irradiance, the vertical sides of crops under PV modules receive more diffuse irradiance than their counterparts in free space.

This particular behaviour is visualised in Figure 87, where three heatmaps focused on the west facing part of the crops, are presented for three different instances of a summer day: 6:30 in the morning (left), 12:30 around noon (middle), and 16:30 in the evening (right). The targeted crops are distinctly marked along with the respective zones and orientation of the vertical face. Time of the day is also displayed at the top right corner of each snapshot.

Here, it is important to note that while the specific day is not critical, since sky visibility inherently remains constant for static structures, the inclusion of different times of day is relevant for PV installations with trackers. These trackers dynamically alter the sky visibility for the analysed zones by changing the module orientation, making the snapshots more informative. For fixed installations, such variations would be redundant, as sky visibility would not change throughout the day.

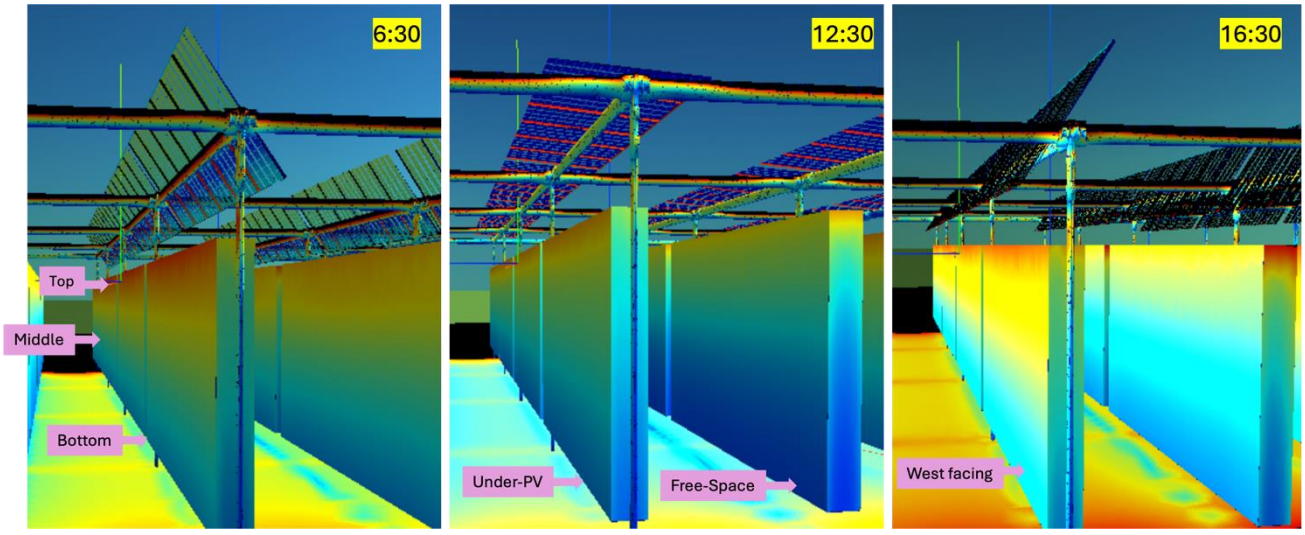

Figure 87: Sky visibility heatmap for three moments in May, 2023 at 6:30 in the morning (left), 12:30 around noon (middle), and 16:30 in the evening (right).

The heatmaps illustrate how vertical faces exhibit varying levels of sky visibility, with warmer tones for top zones and colder tones for bottom zones, regardless of their placement under or away from PV modules. Notably, crops under PV show warmer tones compared to those in free space, aligning with the yearly trend seen earlier. For instance, at 16:30 UTC (right), the top zone of the crop in free space is significantly obstructed by the PV module tilted vertically, whereas the corresponding zone under PV experiences minimal obstruction, showcasing better sky visibility.

Additionally, the dynamic variation of sky visibility throughout the day, due to the changing tilt of tracking PV modules, is evident. For example, the bottom zone of the free-space crop experiences reduced visibility at 12:30 UTC when the PV module above is horizontal, blocking the sky, but gains visibility again at 16:30 UTC as the module tilts vertically.

This dynamic visualization in 3D serves as a crucial tool for validating physical concepts and enhancing the understanding of system behaviour. The next section delves into the total global incident irradiance.

5.4.3. Reflected Irradiance

The results of the modelling of the reflected incident or tilted irradiance is primarily presented using 2D plots, complemented by realistic 3D renderings and corresponding 3D heatmap snapshots from the LuSim environment.

To gain an initial understanding of how different zones behave within a crop, the zones listed in the input section are analysed based on the coordinates of the points from the respective zones, as provided in Table 5. This analysis focuses on the zones for the crop in 'free space' under clear-sky conditions for the 17th of June.

As observed in Figure 88, different zones exhibit distinct behaviours, primarily influenced by their proximity to the ground and the environment corresponding to these zones, which are subjected to shading depending on the time of day. This is evident when following the curves over time. For instance, in terms of magnitude, 'Bottom-West' receives the highest reflected irradiance, closely followed by 'Bottom-East' and 'Middle-West'.

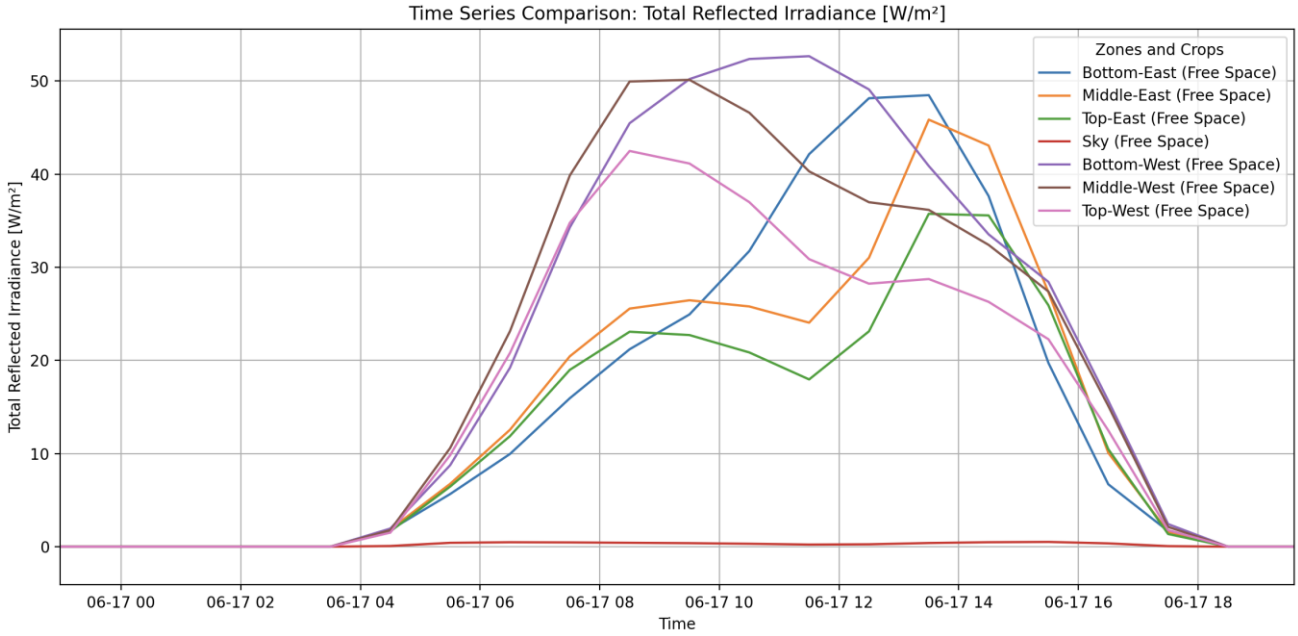

Figure 88: Hourly reflected irradiance for all the zones of the 'Free Space' crop on clear-sky day of 17th June, 2023.

The ‘Bottom-West’ zone receives the highest magnitude due to its closer proximity to the ground, which increases the reflection from the ground, additional to the influence of neighbouring crops at its front, an effect common across all zones. For the next two zones, ‘Bottom-East’ and ‘Middle-West’, peaks can be observed at distinct times of the day: afternoon for the East-facing zone and morning for the West-facing zone. Here, time-dependent shading effect plays a significant role, as it influences the reflected irradiance based on the sun’s position and the corresponding shading patterns in the 3D environment.

This time-dependent behaviour of reflected irradiance along with the depth observed for the Bottom-East zone during the morning and the peak for the Middle-West zone at the same time is shown in Figure 89, which illustrates the realistic shading rendering in 3D at the top and the corresponding heatmap at the bottom for direct tilted irradiance on the same clear sky day of 17th June, offering further insights into the shading dynamics. The East-West orientation is marked on the top-right corner, along with the targeted crop labelled as ‘Free Space’ and the three zones (Top, Middle, Bottom) for better understanding of the 3D structure. Additionally, in the bottom-left corner, the irradiance distribution values from the input file are displayed for the time 10:30 (UTC), along with the colour scale as the legend for the heatmap. At 10:30 UTC (morning time), the ‘Bottom-East’ zone of the ‘Free Space’ crop has both the ground and the crop face in front of it almost completely under shade. This significantly reduces the reflected irradiance observed in this zone, explaining the depth in the curve around this time. In contrast, for the ‘Middle-West’ and ‘Bottom-West’ zones, both the ground and the front crop are illuminated, resulting in higher magnitudes of reflected irradiance as seen from the respective curves. The ‘Bottom-West’ zone, being closer to the ground, exhibits the highest magnitude of reflected irradiance, which aligns logically with its position and proximity.

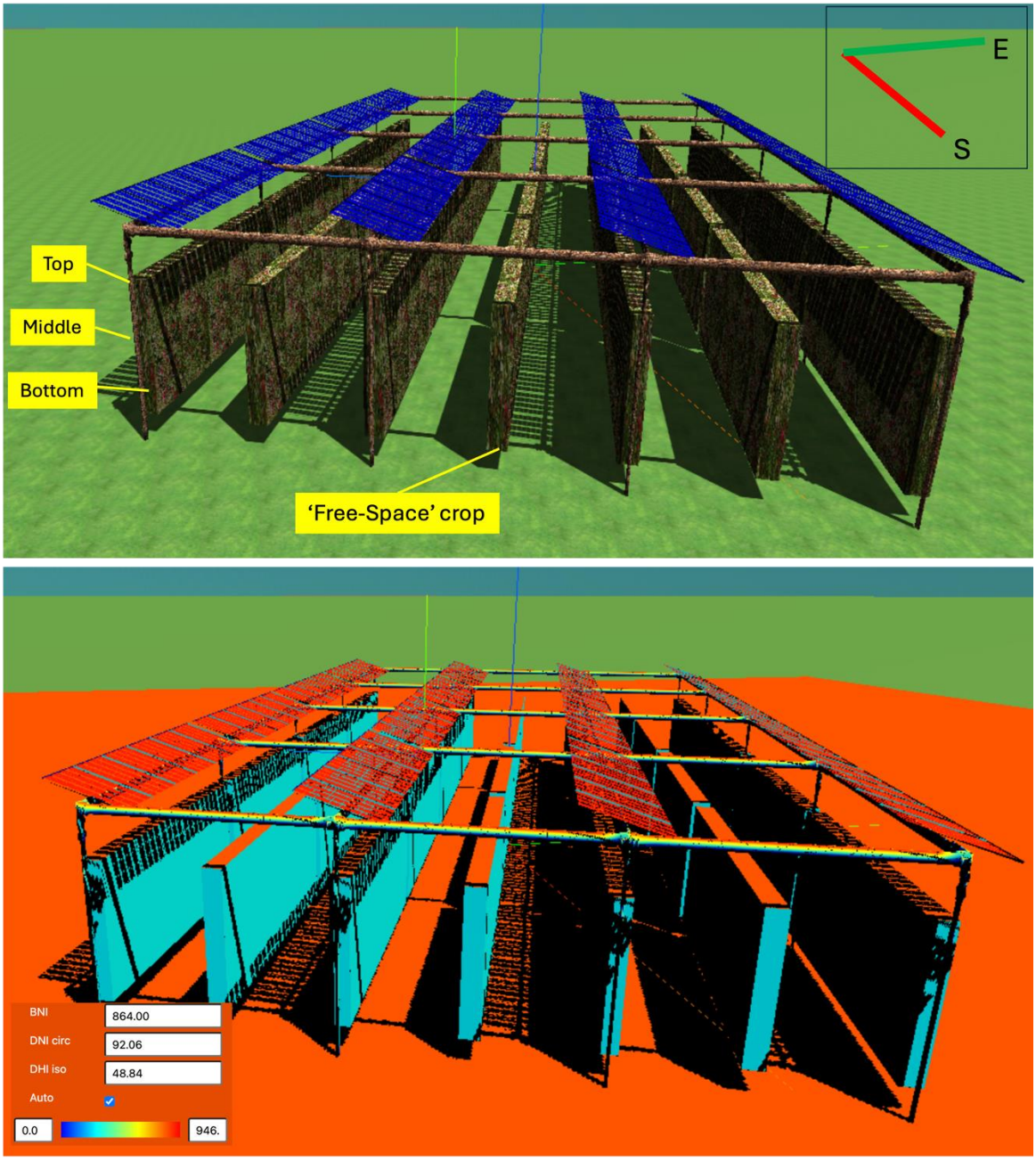

Figure 89: Realistic rendering of shading (top) and the corresponding direct tilted irradiance heatmap (bottom) at 10:30 (UTC) for the clear-sky day of 17th June, 2023.

To visualise the trend during the afternoon, Figure 90 presents the realistic 3D rendering (top) and the corresponding heatmap for direct tilted irradiance (bottom) for the same clear sky day of 17th June, but at a different time, 13:30 UTC (afternoon).

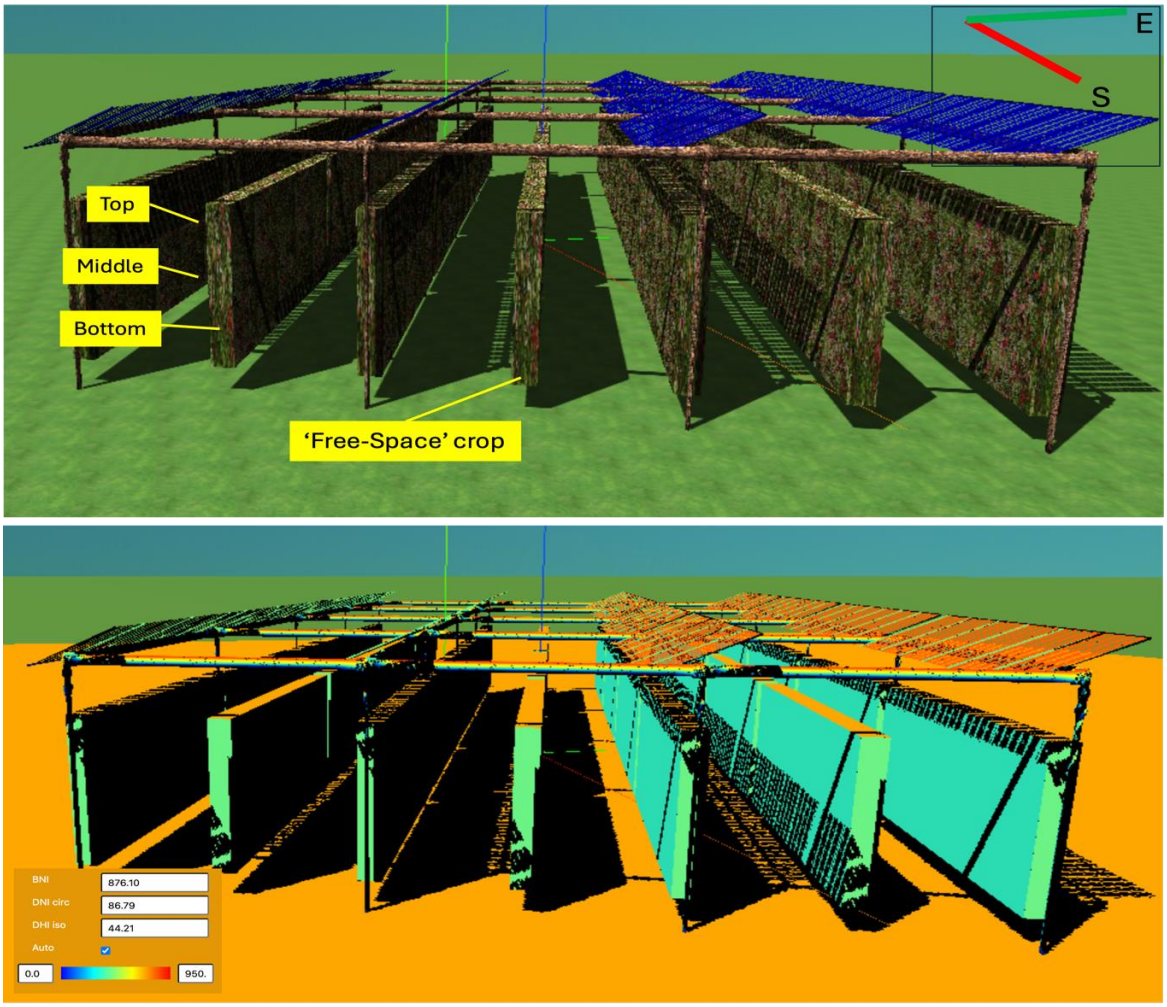

Figure 90: Realistic rendering of shading (top) and the corresponding direct tilted irradiance heatmap (bottom) at 13:30 (UTC) for the clear sky day of 17th June, 2023.

It can be observed that, in contrast to the trend seen in Figure 89, here the ground and crop in front responsible for reflecting light to the West zones, particularly the Middle-West and Bottom-West zones, are now under shade. On the other hand, the 'Middle-East' and 'Bottom-East' zones are exposed to illumination on the ground and crop in front of them, resulting in higher reflected irradiance values. The 'Bottom-East' zone, being in closer proximity to the ground, shows the highest magnitude, which aligns logically with its spatial positioning.

To observe and verify similar behaviour of varying levels of reflected irradiance across zones, a clear-sky day in a winter month, specifically the 24th of November, is chosen for analysis. Figure 91 presents the 2D hourly comparison plot for the reflected irradiance across zones for that day. The profiles are notably different from those observed for the clear sky day in the summer month of June, as shown in Figure 90. The middle regions on both sides exhibit higher magnitudes of reflected irradiance compared to the lowest zones, with the

'Middle-West' zone recording the highest overall magnitude. This behaviour can primarily be attributed to the system's orientation facing South-East and the lower sun elevation angle typical of winter months.

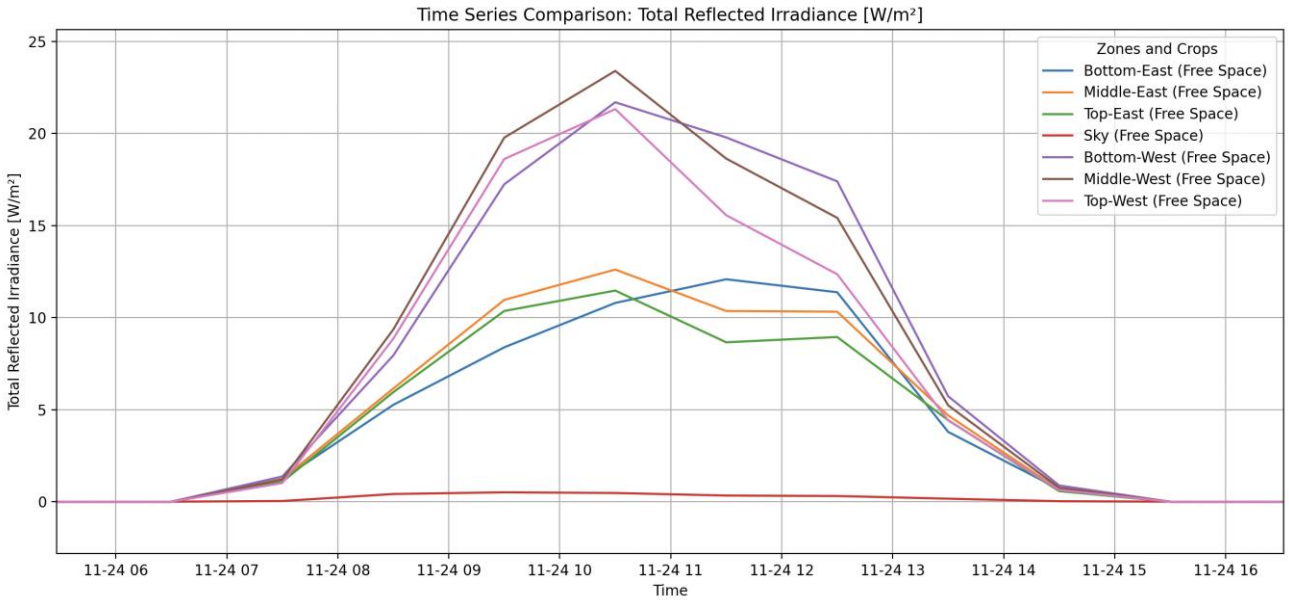

Figure 91: Hourly reflected irradiance for all zones of 'Free Space' crop on clear sky-day of 24th November,2023.

To further understand this behaviour, Figure 92 provides a realistic rendering of shading and the corresponding heatmap are presented for the same clear sky day of 24th November at 10:30 (UTC).

For the west side of the 'Free Space' crop, a comparison between the 'Middle-West' and 'Bottom-West' zones in the hourly plot in Figure 91 reveals an interesting interplay. It is evident from the shading visualised in Figure 92 that the ground contributing more to the 'Bottom-West' zone is predominantly shaded, while at the same time, the crop at the front of this zone is fully illuminated, thus causing the 'Middle-West' zone to receive more reflected irradiance.

This nuanced visualisation highlights the interplay between the sun's path and the shading effects created by the surrounding environment, emphasising how these factors impact the reflected irradiance.

Moreover, the comparison underscores how different regions within the crop respond to the time-dependent movement of shadows, influenced by the relative positioning of zones, the system's orientation, and the environmental geometry.

As it is well known, during winter months, at the latitude of Bolzano, Italy, the sun rises close to the South-East and maintains a low elevation throughout the day, creating distinct shadow patterns that influence the reflected irradiance across zones. The shadow effects supporting this behaviour can be observed, both in the realistic 3D shading rendering and the corresponding heatmap for the time 10:30 (UTC).

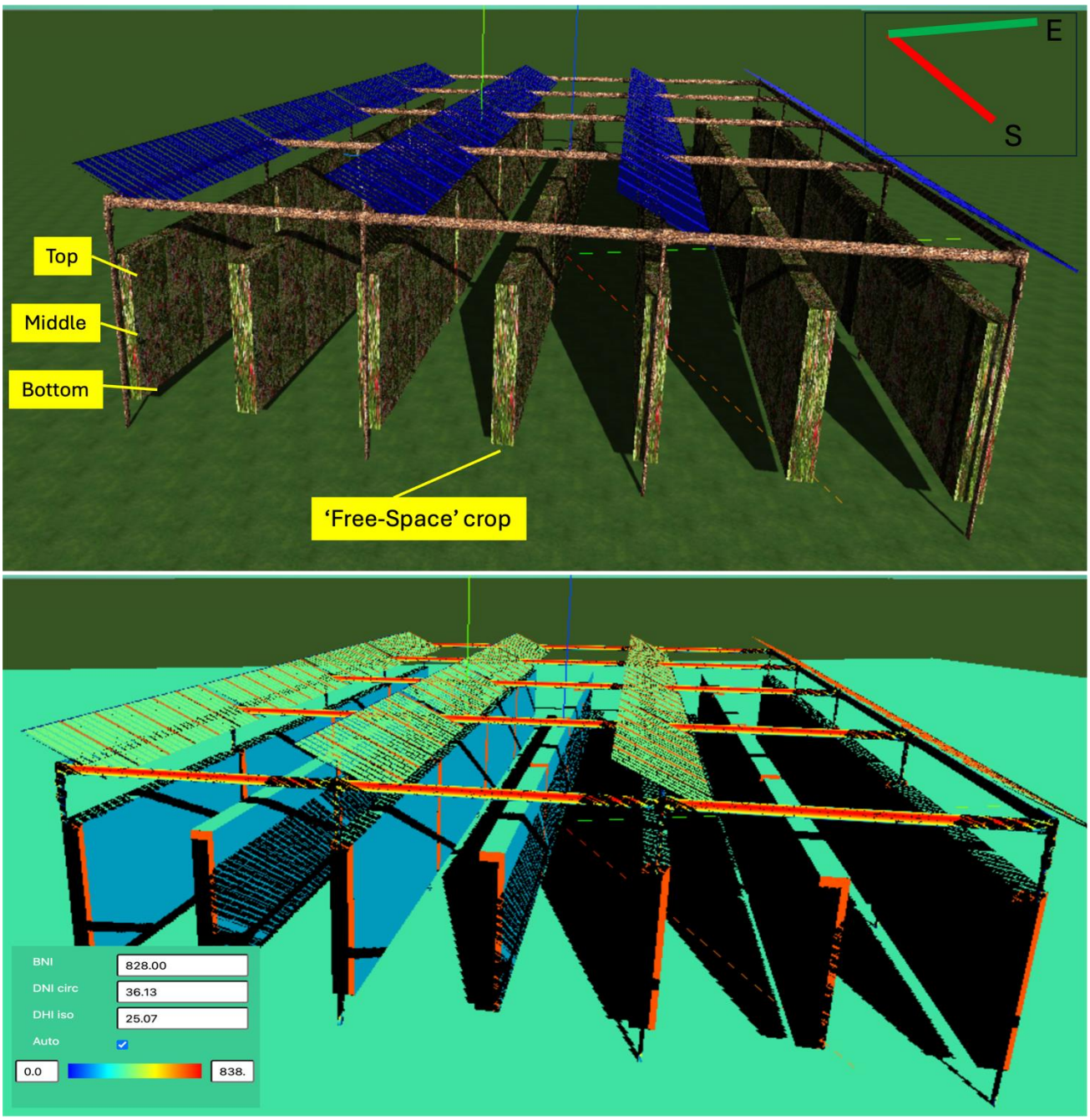

Figure 92: Realistic rendering of shading (top) and the corresponding direct tilted irradiance heatmap (bottom) at 10:30 (UTC) for the clear sky day of 24th November, 2023.

The impact of these varying behaviours is aggregated over the year for the different zones and compared with the crop 'Under-PV' in the yearly bar plot presented in Figure 93. The bar plot extends the hourly trends observed earlier for the respective crops. For each crop, the bottom-most zones receive the highest total reflected irradiance, followed by the middle zones, and finally, the top zones, with the sky-facing zones exhibiting the least due to the absence of reflective surfaces around them, except for the PV modules above, which have a negligible albedo value compared to the rest of the 3D environment. Additionally, the west-facing zones receive more reflected irradiation compared to the east-facing zones, primarily due to the system's orientation toward the south-east. This orientation exposes the east-facing zones to an environment that is more shaded compared to the relatively more illuminated exposure of the west-facing zones.

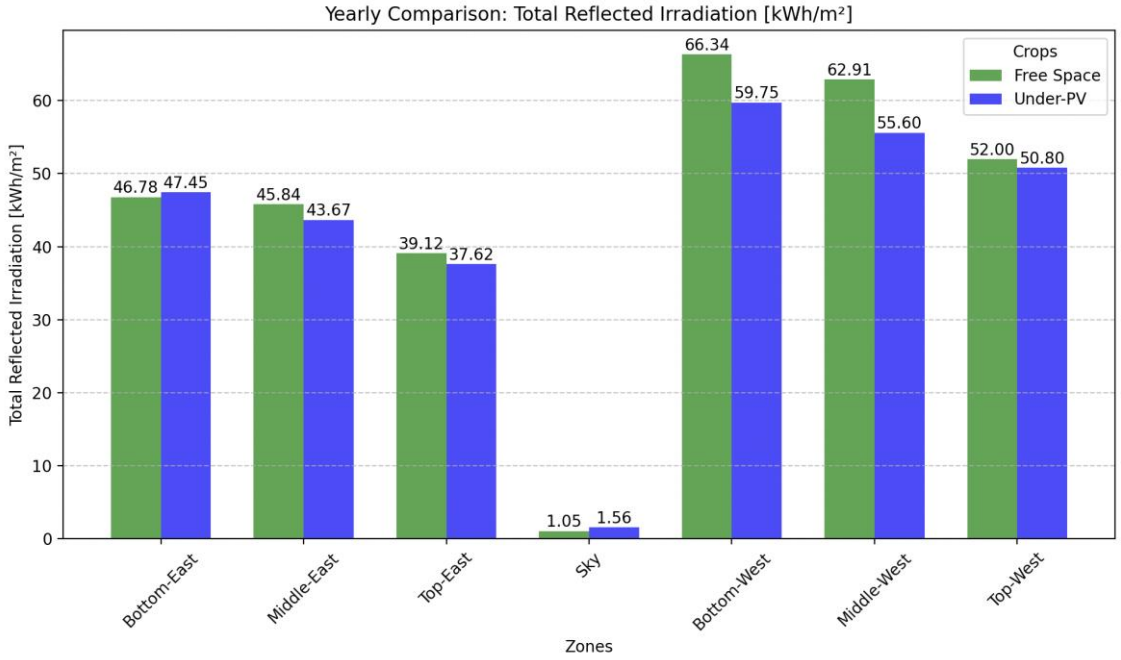

Figure 93: Yearly bar plot comparison of incident reflected irradiation across all the zones for the crop in 'Free-Space' and the crop 'Under-PV'.

Furthermore, the sky-facing zone under the PV module records slightly higher reflected irradiance than its counterpart in free space. This marginal difference is due to the PV module above the zone under the PV crop reflecting some irradiance, albeit to a small extent, compared to the free-space crop, which lacks such reflective surfaces above.

The annual comparison between the two crops does not entirely represent the accurate behaviour of all zones within the target crops as a whole. This is because the analysis is based on a single, randomly selected point in the middle of each zone, which may not fully capture the nuanced variability across the entirety of each zone.

This analysis, instead, focuses on the capability to export results for any desired point, which, following the comparison methodology outlined in the first exercise, makes it feasible to produce comparable results among

partners. This approach eliminates uncertainties arising from the spatial resolution of mesh points to represent irradiance at an object or zone level.

5.4.4. Global Irradiance

This component represents the summation of the three individual components analysed in the previous sections: direct tilted irradiance, diffuse tilted irradiance, and reflected tilted irradiance. With the understanding of zone-specific behaviour within and across crops for each of these components, the overall behaviour of their summation, total global tilted irradiance, can be logically deduced and is expected to align with the trends observed earlier.

To quantify this, Figure 94 presents the yearly comparison of total global tilted irradiation across all zones for the targeted crops.

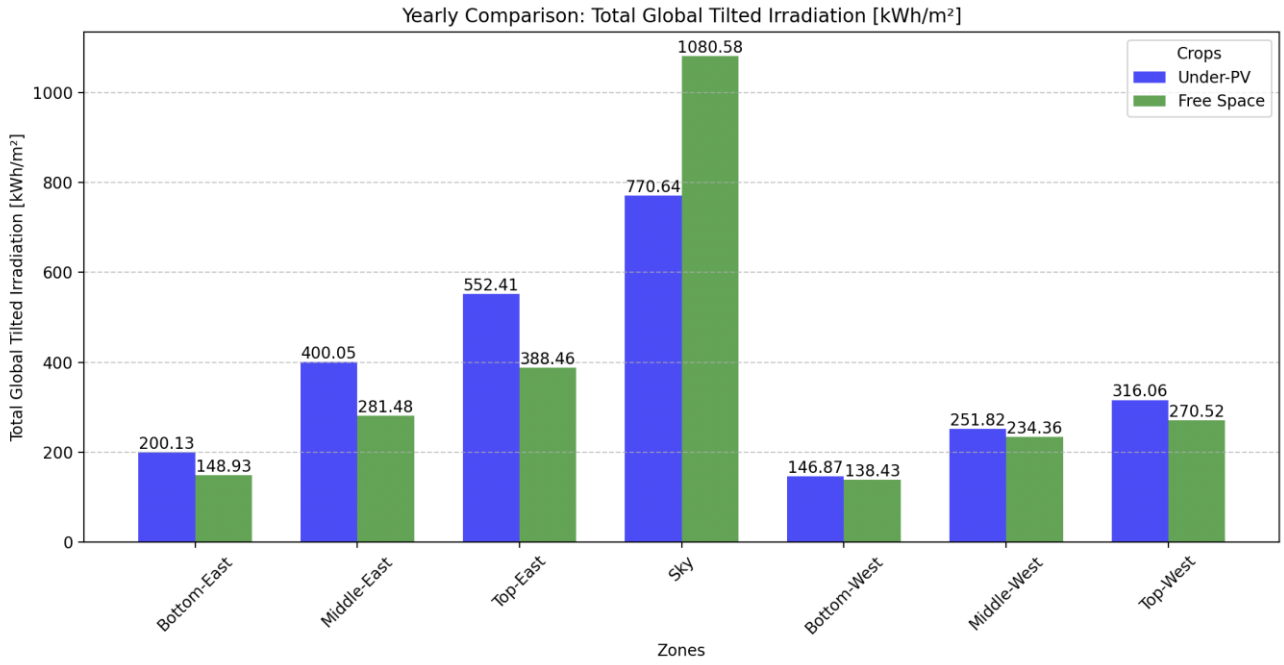

Figure 94: Yearly global tilted irradiation for all zones between crop in 'Free-Space' and crop 'Under-PV'.

The sky-facing zone of the crop in free space receives significantly more global tilted irradiation compared to its counterpart under PV, due to uninterrupted sky visibility. Conversely, the vertical zones of the crop under PV receive higher irradiation than those in free space. This aligns with the trends observed for individual irradiance components analysed earlier.

This study provides a comprehensive analysis of irradiance distribution in an open Agri-PV system in Bolzano, focusing on individual components, direct, diffuse, and reflected, and their summation into total global tilted irradiance. The results underscore the intricate interplay between crop placement, PV geometry, and shading dynamics, providing valuable insights into the behaviour of different zones within crops under varying conditions.

5.5. Imec

5.5.1. Agri-PV System Modelling Setup

Similarly to cases 1-3, Imec used SketchUp Pro 2023 to create the 3D model of the scene. The apple tree was modelled as a parallelepiped as shown in Figure 95.

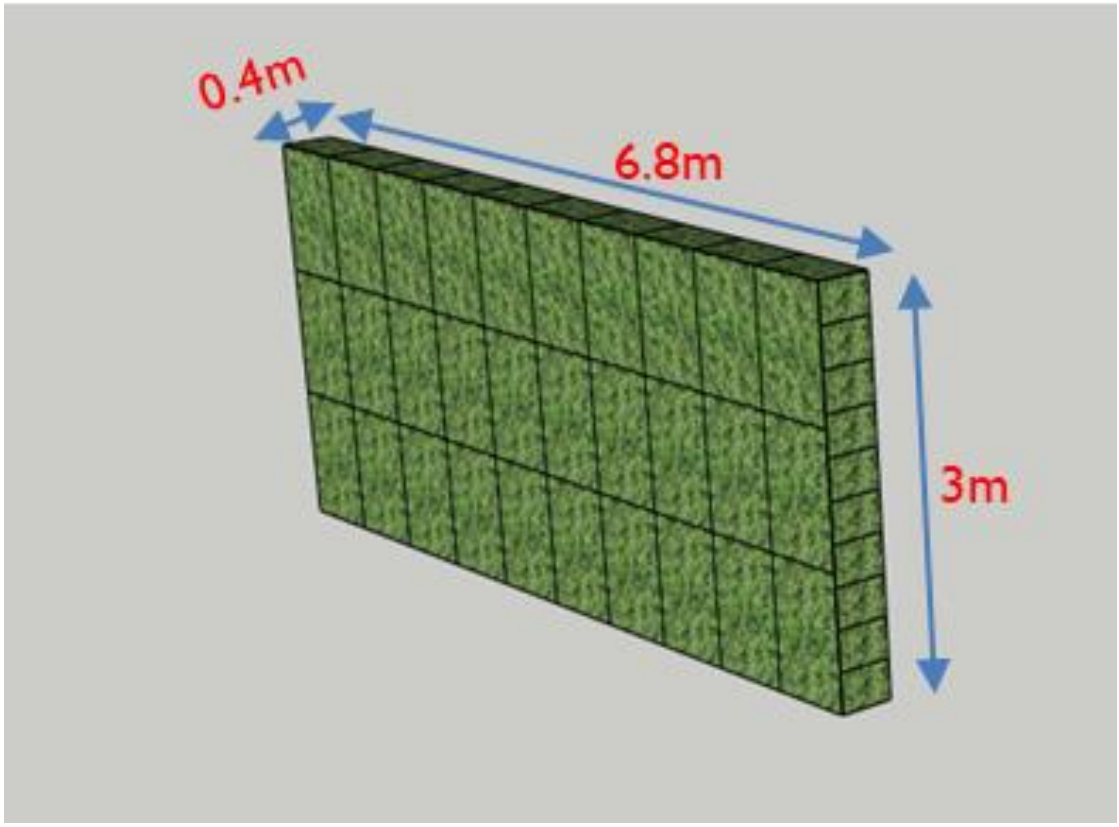

Figure 95: Model of apple tree.

Figure 96 shows the 3D scene of the apple orchard including the apple trees, the semi-transparent PV modules, the support structures and the grassland. Like in LuSim, the same orientation with a 20.3° clockwise deviation from the south was used. The mounting and support structures are modelled as steel poles and given a defined diffuse reflectance of 20% as described in the inputs. As the PV modules and the crop canopy are the main surfaces of interest, the sensors were placed on these regions to compute and assess the irradiance. As defined in the inputs, the crops were modelled as fully opaque with a diffuse reflectance of 20%. Similarly, the ground was given an albedo of 20%.

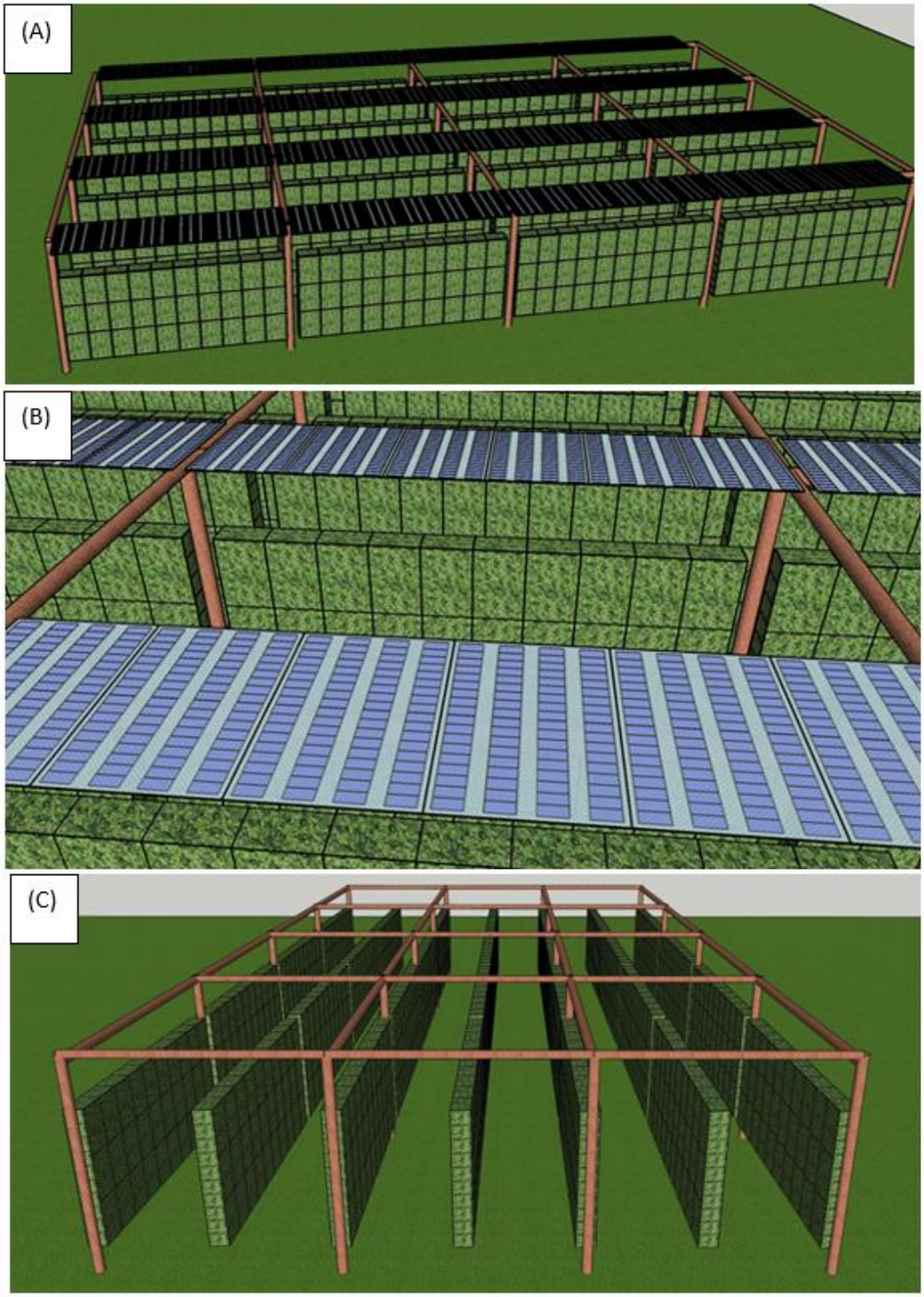

Figure 96: (A) Complete layout of the orchard field as modelled by Imec. (B) Close-up view of the orchard field showing the semi-transparent PV modules. (C) Layout of the open field as seen from the south side.

5.5.1. Irradiance evaluation on PV modules

The irradiance on distinct zones of the orchard trees were assessed. The yearly accumulated irradiation on the Agri-PV orchard system is shown in Figure 97 (Top view, front and back irradiation) and Figure 98 (Perspective view, back irradiation).

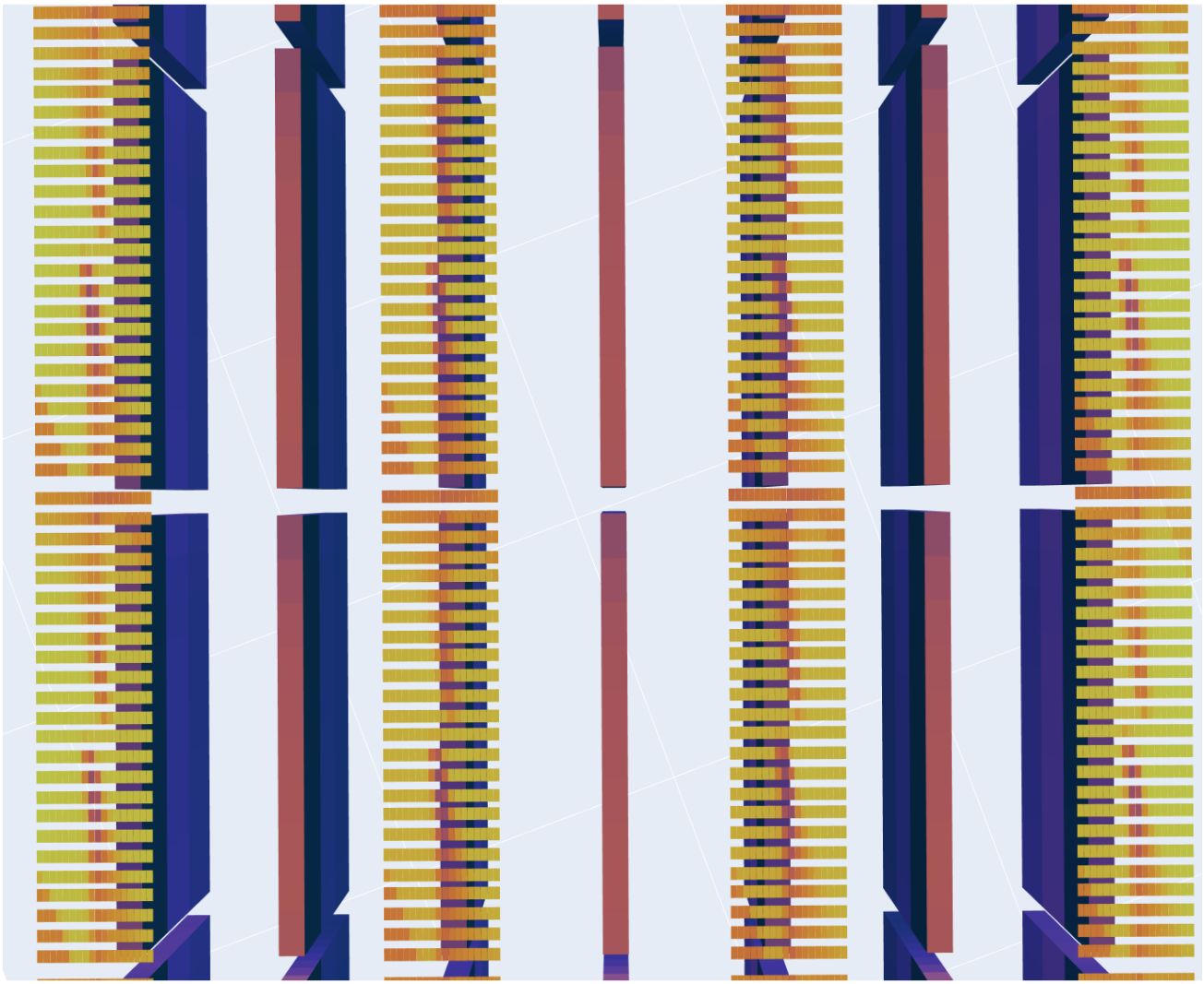

Figure 97: Yearly total (front and back) accumulated irradiation on the Agri-PV orchard system.

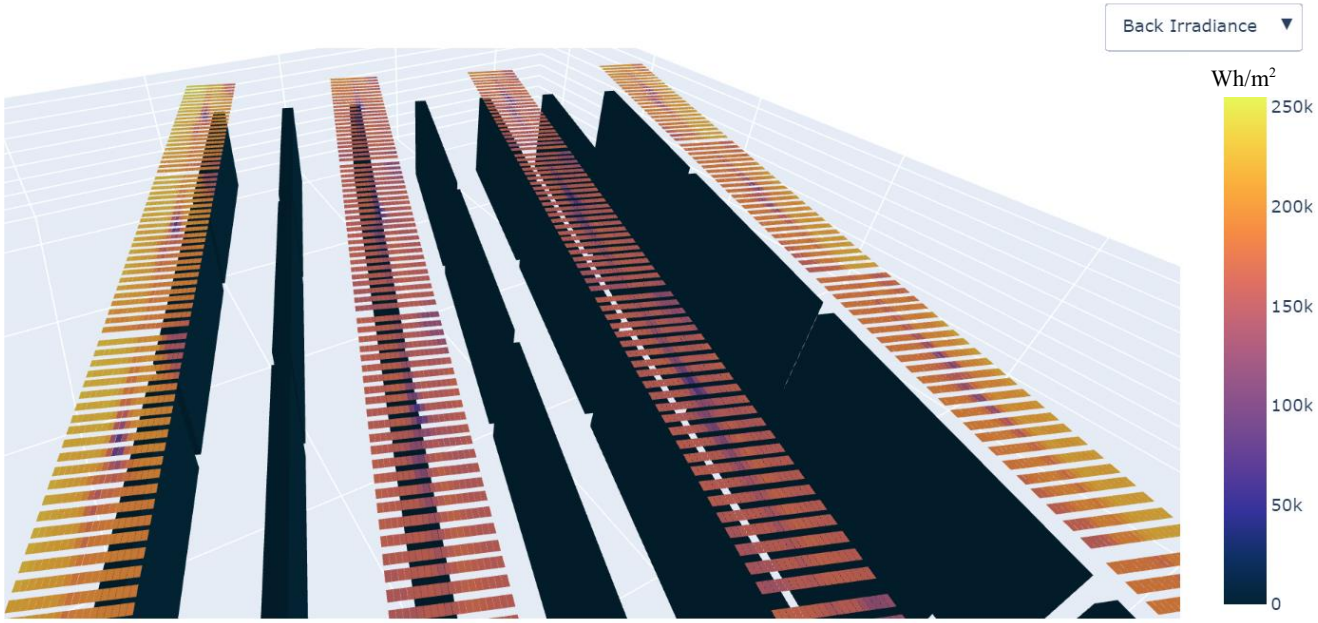

Figure 98: Yearly accumulated irradiation on the back side of the PV modules of the Agri-PV orchard system.

The back PV irradiance for selected times of the year including clear-sky and cloudy days is also presented in Figure 99 and Figure 100.

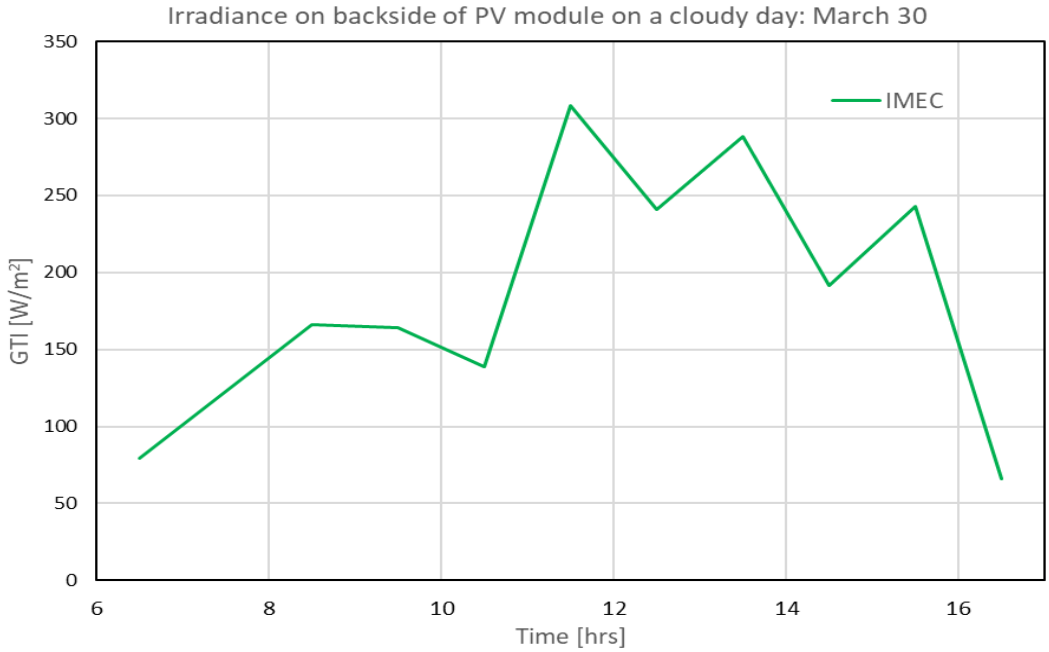

Figure 99: Hourly GTI for the cloudy day of 30th March (UTC) for Imec.

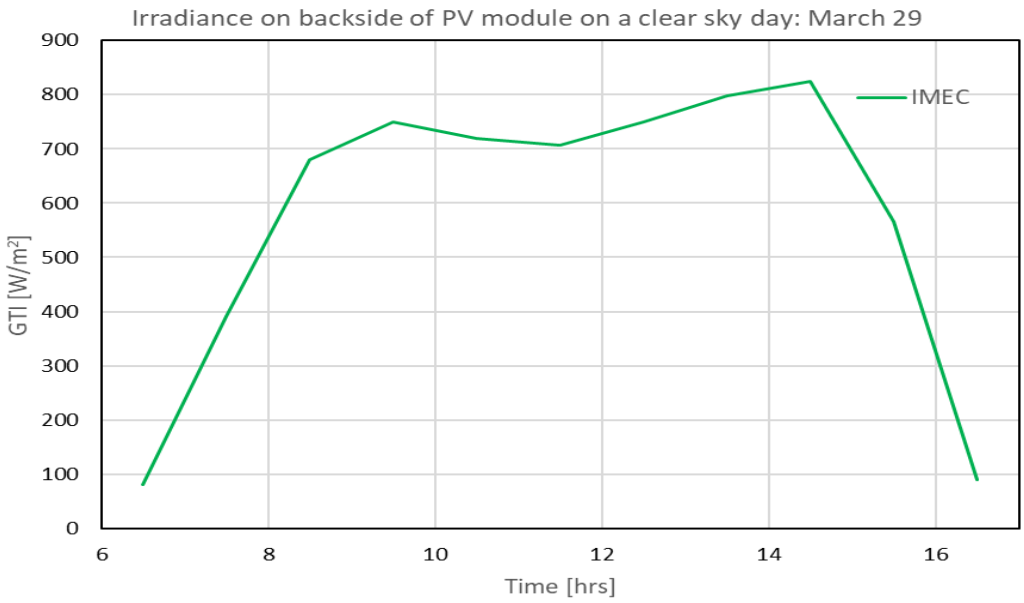

Figure 100: Hourly comparison for the clear-sky day of 29th March (UTC) for Imec.

5.5.2. Irradiance evaluation on sky-facing side of the crops

The flowering period of apples and pears which usually lasts between April and May is crucial for fruit production (in terms of number and quality). The irradiance on the sky-facing side during a clear sky day in April was assessed for both the free crop and crop under PV as shown in Figure 101. During sunrise and sunset periods, the irradiance on both crops is comparable in trend and magnitude. This is because the maximum and minimum tracker angles are respectively 55° and -55° and as such, the PV modules have little interference with the irradiance at the low solar elevations. However, as the solar elevation increases, the PV modules intercept most of the light reaching the crop under the PV module while the free crop continues to receive most of the irradiance.

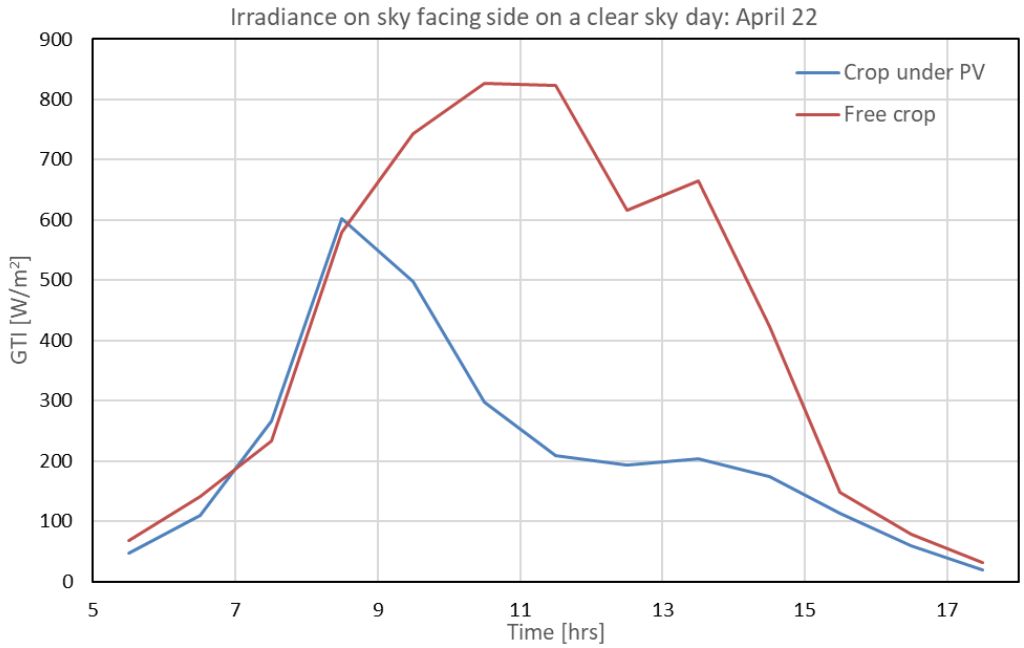

Figure 101: Hourly comparison of irradiance on sky facing side of free crop and crop under PV for a clear sky day (22nd April) during the flowering period for apple trees.

On a cloudy day (Figure 102), the irradiance profiles for the free crop and crop under PV are quite comparable. This is mainly due to the presence of more diffuse light under cloudy conditions which leads to similar irradiance on the two crops. However, the free crop receives more light due to less shading of the PV modules during tracking.

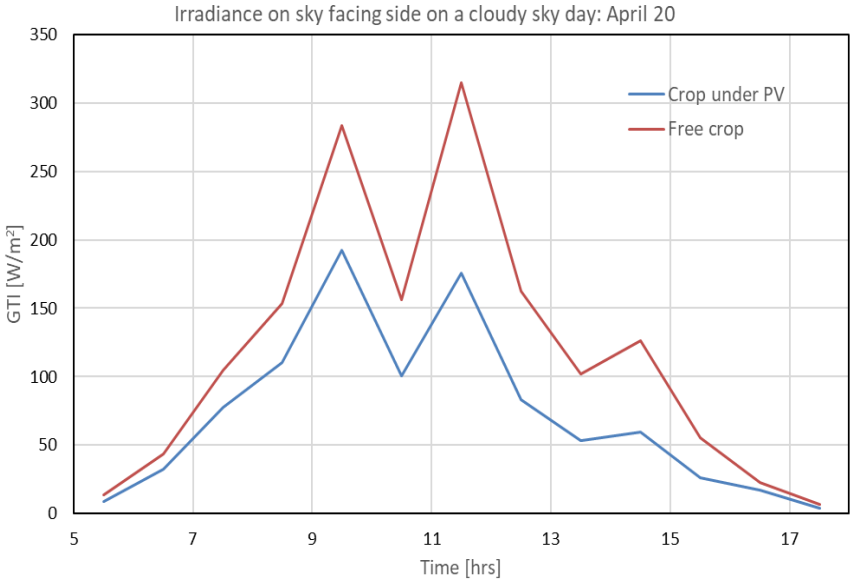

Figure 102: Hourly comparison of irradiance on sky facing side of free crop and crop under PV for a cloudy day (20th April) during the flowering period for apple trees.

5.6. TUD

The core architecture of TU Delft's irradiation model has already been outlined in Figure 3, at the beginning of this document. Building upon this foundation, the first subsection elaborates on two specialized developments that improve the tool's capabilities. These include spectral modelling, which benefits all types of PV systems, and detailed canopy modeling specifically tailored to Agri-PV. Subsequently, the second subsection utilizes the tool to simulate light levels of in a specific open Agri-PV setting: the apple orchard in Bolzano.

5.6.1 Modelling refinements

When using Radiance, a modeller can generate the sun and sky through the built-in command, *gendaylit*, that produces a description of these daylight sources based on the Perez All Weather model. The function computes solar radiance and creates a continuous, hourly sky irradiance distribution by inputting direct and diffuse components of irradiance. However, its current implementation does not produce spectral skies for various conditions, posing limitations in light modelling of any PV system. To address this, *gendaylit* was translated into Python, and customised to accept spectral direct and diffuse irradiance components. Given the rarity of such measurements, they are modelled with the method presented in Figure 103.

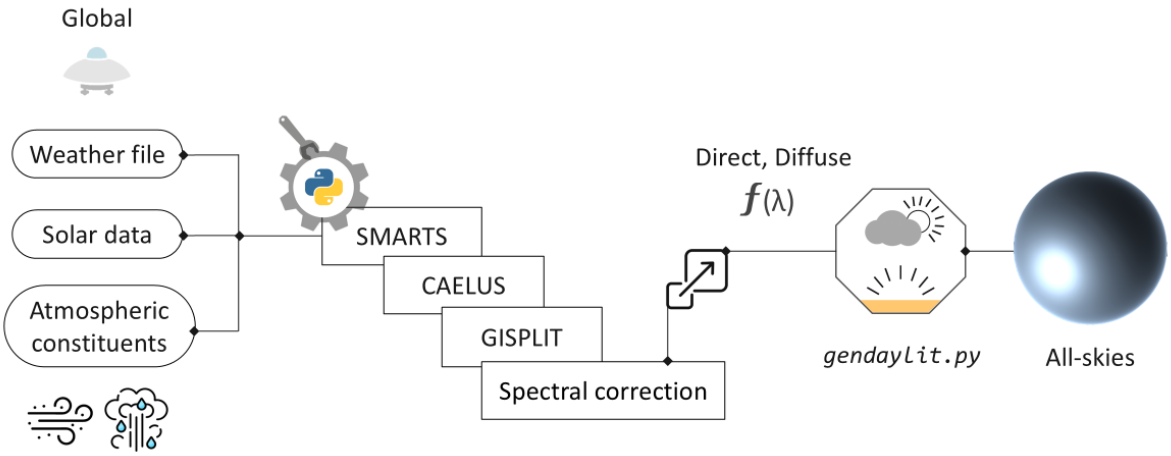

Figure 103: Overview of the spectral direct and diffuse irradiance reconstruction method. In addition to standard inputs, nearby atmospheric constituent data such as aerosol optical depth and precipitable water vapor are required. These inputs are processed by the atmospheric radiative transfer model, which outputs the spectral direct and diffuse irradiance for ideal skies. The sky classification algorithm then determines the sky type for each timestep, enabling the decomposition of broadband global irradiance. Finally, spectral correction factors based on semi-empirical formulations, and scaling are applied, resulting in the spectral direct and diffuse components for all sky conditions.

Weather stations are usually equipped with broadband pyranometers that measure global irradiance necessitating the use of decomposition models that extrapolate the direct and diffuse components. Unlike

most algorithms, the one adopted has integrated sky classification and is resilient to uncertainties caused by aerosols and water vapour. However, to utilize these models; CAELUS [15], and GISPLIT [16], an atmospheric radiative transfer model is required. One such renowned model is SMARTS [17]. To ensure a seamless modelling workflow, SMARTS has been translated into Python and customised for faster performance.

The workflow depicted in Figure 103 incorporate numerous substeps, many of which are not immediately apparent. Yet activating spectral modelling is straightforward once the number of wavebands and spectral range are passed. However, this simplicity assumes knowledge of spectral optical properties and nearby atmospheric constituent data. The latter often presents the main bottleneck preventing wider adoption of this method. Next, we will introduce the second major advancement in TUD's modelling approach.

Generating the plant architecture is the most challenging aspect of geometrical modelling in Agri-PV systems. This challenge is particularly troublesome for tall and porous tree canopies, which significantly alter light distribution, affecting both crop and PV performance. Creating exact replicas of tree canopies is neither practical nor desirable as simplified architectures can effectively reproduce key light interactions. If the simulation enhances our understanding of system behaviour, it is valuable, even if not exact.

The goal is to render a canopy that is porous and transient, capable of reproducing realistic and dynamic shading patterns. Capturing key phenological stages is crucial. In winter, the canopy is dormant, featuring only branches. Leaf growth begins in March, with the canopy updated daily until May. During this phase, self-shading within individual trees, becomes increasingly noticeable. Although leaf development is considered in our algorithm, it is assumed that the plant is mature without further branch development throughout the year. One such fully developed and mature canopy is displayed in Figure 104. The last stage is leaf drop which begins in October.

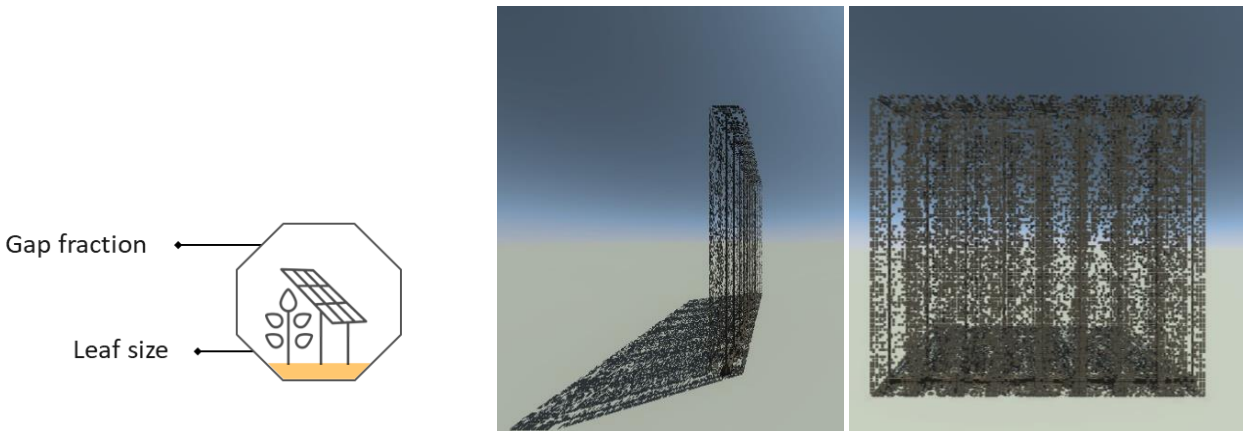

Figure 104: Rendering of the fully developed and mature canopy architecture. Given the specific tree training type, a minimum gap fraction of 50% was assumed and expected to vary linearly during leaf development or leaf drop. This informs the progressive leaf filling algorithm with the number of new leaves that must be spawned. The "size" of the leaves is determined by the grid's fineness, specifically by the dimension of each polygon (2.5 cm in this case).

Our leaf generation algorithm relies on two main inputs: the canopy's Gap Fraction (GF), which represents the percentage of open area, and grid size, which determines the spatial resolution of irradiance sampling. The leaves of the virtual canopy are modelled as opaque Lambertian polygons, which is reasonable given the arbitrary orientation of leaves leading to an overall diffuse effect.

Although the canopy geometry is relatively simple, it can quickly become a burden when converted into an orchard unless computational efficiency measures are taken. Specifically, the porous orchard scene, depicted in the right image of Figure 105, was rendered using instances due to its composition of over a million polygons. By "freezing" and instancing the tree geometry—where "freezing" refers to capturing a snapshot of the ever-changing canopy—we can effectively reproduce it to create an orchard. This technique allows for effective management of complex yet repetitive structures. As a result, modelling porosity incurs a computational overhead of 33% compared to an opaque orchard for an annual irradiance simulation with an hourly timestep.

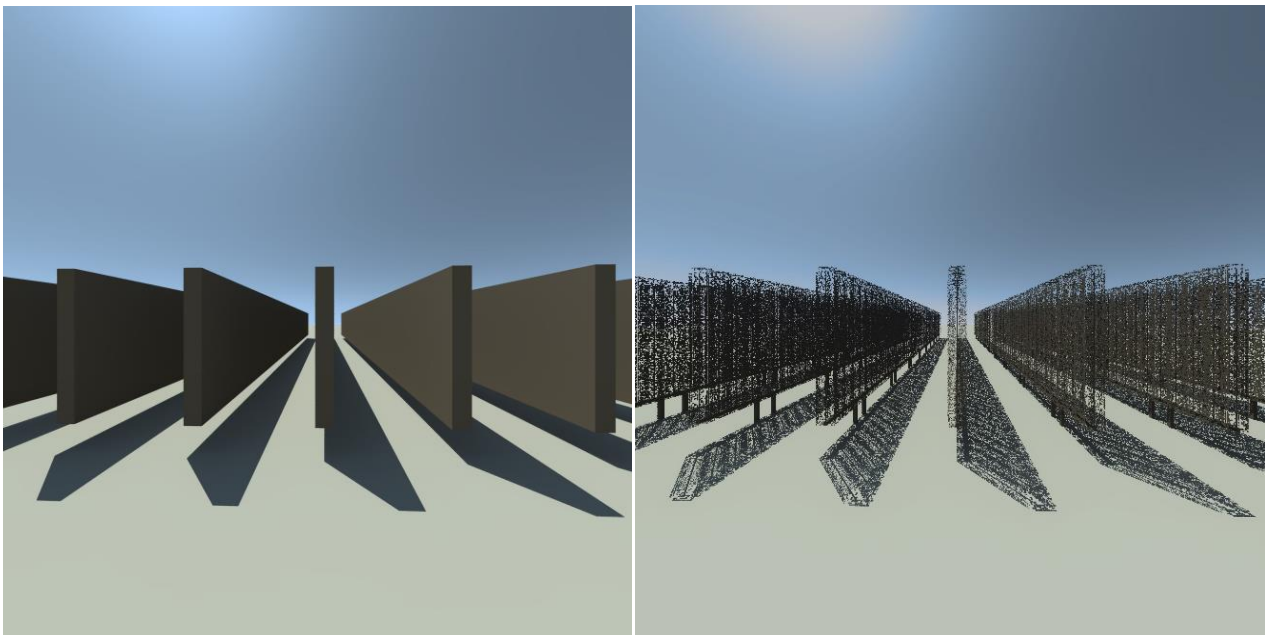

Figure 105: Rendering of an opaque (left) and porous (right) apple orchard, with a mature canopy trained using the 2D Guyot system.

5.6.2 Application and evaluation of light distribution

Raytracing was initiated using the *rtrace* command, which processed the final octree containing details about the spectral sky and orchard. Simulations were performed hourly throughout the growing season (March to October). Irradiance was sampled across the central tree of the orchard, ignoring edge effects, using 243 sensors spaced 2.5 cm apart along its height and on both sides. These virtual sensors, positioned horizontally, function like albedometers and "measure" incoming light from both sides. A spectral resolution of 20 nm was used to sample irradiance across the visible spectrum.

To evaluate the influence of tree porosity and phenological stage on shading dynamics, light penetration profiles were derived for both opaque and porous tree canopies across different timescales. These profiles demonstrate the gradient in Photosynthetically Active Radiation (PAR) levels across the canopy height, crucial for crop growth.

As illustrated in Figure 106 (a), when aggregating frontside irradiance throughout the season, both canopy geometries experienced increased light levels with height. The difference in PAR magnitude between the two remains relatively constant but diminishes towards the top. Additionally, the porous canopy leads to a high variability in light levels due to sun flecks—light penetrating through the gaps within the canopy. Importantly, leaves not only receive light on their frontside but also on their backside, significantly contributing to the overall light levels as displayed in Figure 106 (b).

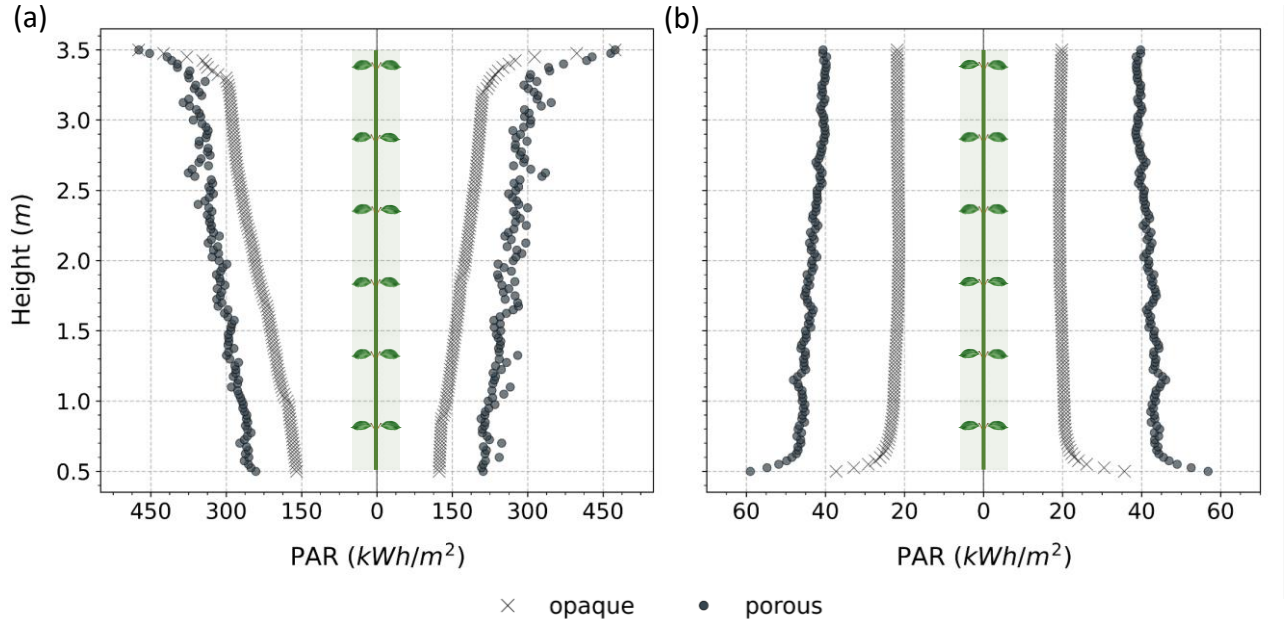

Figure 106: Seasonally aggregated light penetration profiles along the height of the tree canopy. Graph (a) displays PAR levels incident on the frontside of the virtual leaves, while graph (b) shows the levels on the backside. Each plot includes data for both east-facing (left) and west-facing (right) tree sides.

When aggregating PAR over the period of a month, as displayed in Figure 107, the differences between the two geometries vary with the phenological stage. During April, the canopy undergoes leaf development, resulting in more pronounced differences between the two geometries. In contrast, by June, the canopy has fully developed leading to similar shading conditions between the opaque and porous geometries. This offers insights into the seasonal variation of light transmission within apple tree orchards trained using the 2D Guyot system.

Analysing light penetration on an hourly timescale, as illustrated in Figure 108, shows that profiles can vary dramatically due to changing sky conditions. Two days in May were selected during which the canopy had fully

matured. Specifically, under clear skies, the highly heterogeneous nature of light within orchards becomes apparent: the east-facing side of the crop is well-illuminated, while the west-facing side remains in shadow. However, the porous geometry allows for sun flecks, which are otherwise not accounted for in opaque canopy models. In contrast, on cloudy days, light levels are homogenized, which minimizes the differences between the two geometries.

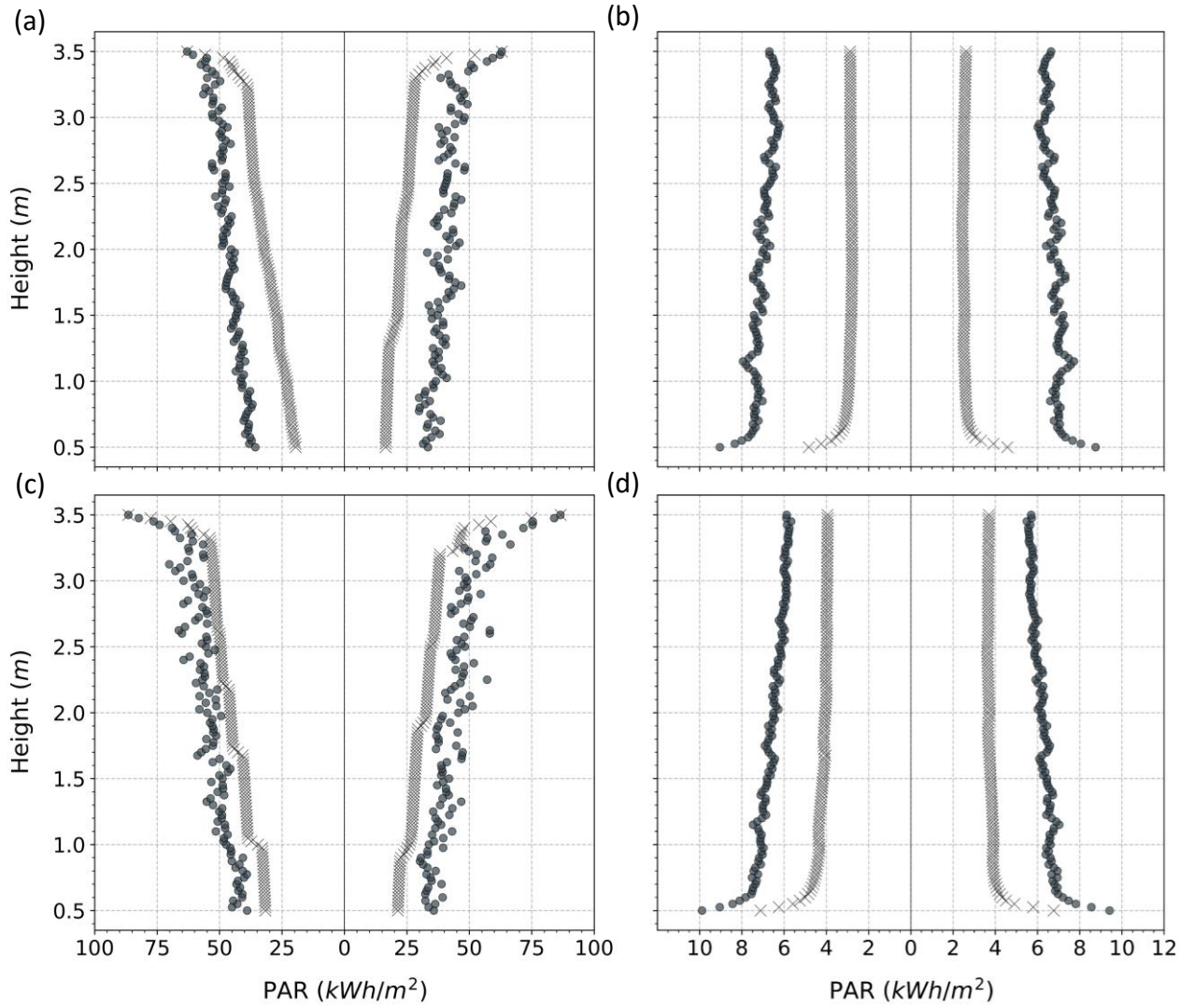

Figure 107: Monthly aggregated light penetration profiles along the height of the tree canopy. Graphs (a) and (b) correspond to April, while (c) and (d) to June. Graphs (a) and (c) display PAR levels incident on the frontside of the virtual leaves, while graphs (b) and (d) show the levels on the backside. Each plot includes data for both east-facing (left) and west-facing (right) tree sides.

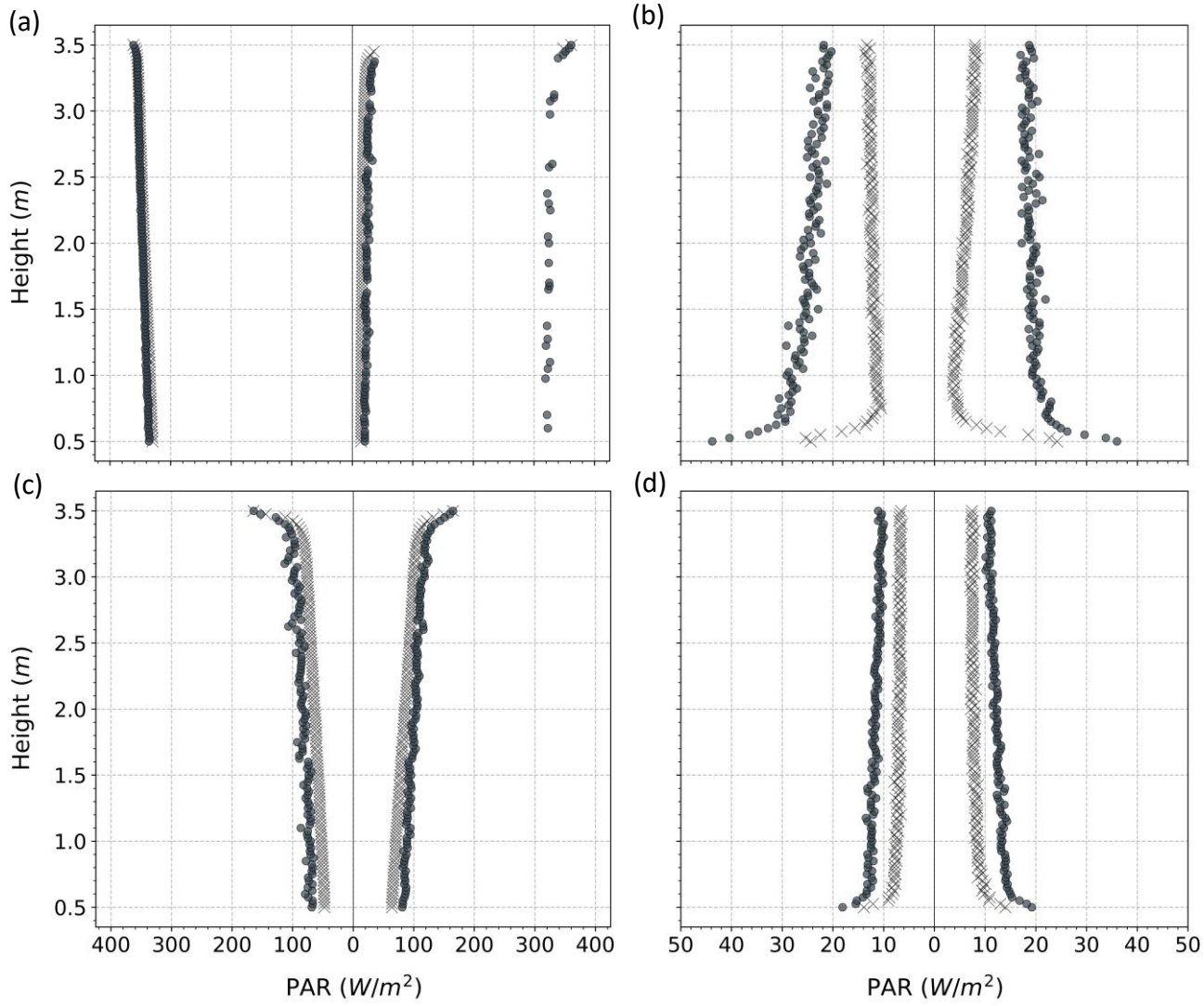

Figure 108: Hourly light penetration profiles along the height of the tree canopy. Graphs (a) and (b) illustrate clear-sky conditions, while (c) and (d) cloudy. Graphs (a) and (c) display PAR levels incident on the frontside of the virtual leaves, while graphs (b) and (d) show the levels on the backside. Each plot includes data for both east-facing (left) and west-facing (right) tree sides.

Having assessed light levels across the tree canopy, a similar evaluation was performed with an integrated PV array, as displayed in Figure 109. Specifications describing the orchard and PV array are largely the same with those in section 5.2, Input Data. The main differences include the implementation of spectral modelling and canopy porosity. To focus specifically on the shading effect of the PV array and orchard, the support structure and torque tube were omitted.

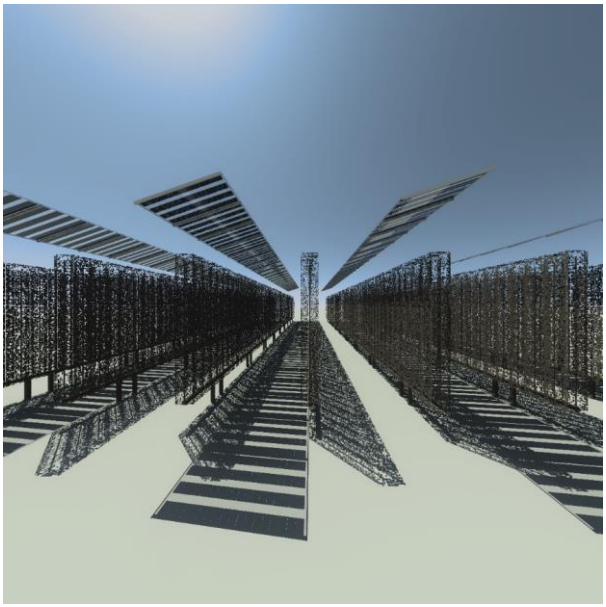

Figure 109: Digital replica of the Agri-PV demonstrator in Bolzano with a porous apple tree canopy.

The pitch of the PV array is twice that of the crop strips, necessitating irradiance sampling on two crops strips; one strip free of modules labelled as “open” and another directly beneath the PV modules labelled as “covered” in Figure 110.

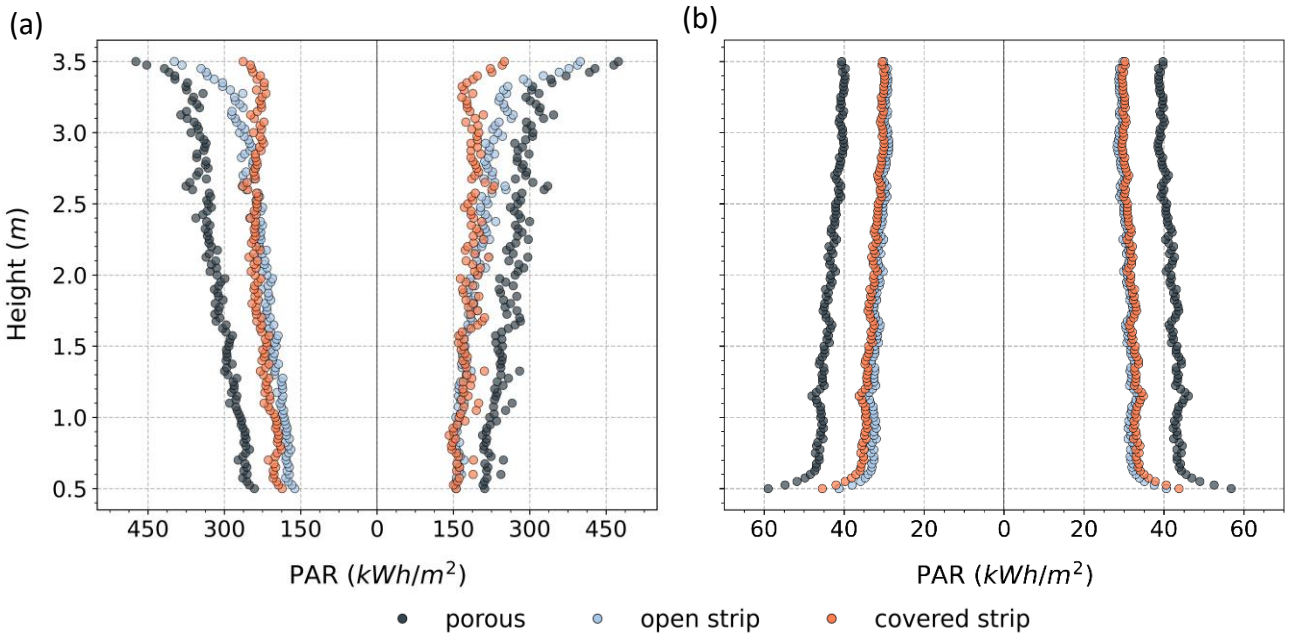

Figure 110: Seasonally aggregated light penetration profiles along the height of the tree canopy. Graph (a) displays PAR levels incident on the frontside of the virtual leaves, while graph (b) shows the levels on the backside. Each plot includes data for both east-facing (left) and west-facing (right) tree sides.

Comparison with the reference case—consisting of a porous orchard free of any PV modules—revealed similar patterns of light distribution. However, a more homogeneous vertical light distribution was observed for the crop strip covered with PV modules. This pattern persisted across both seasonal and monthly timescales, as shown in Figure 110, and Figure 111, respectively. Sensors positioned at a greater height had reduced sky views and experienced more frequent shading from the PV array. While light homogeneity generally benefits crop growth, it could pose challenges for crop pruning.

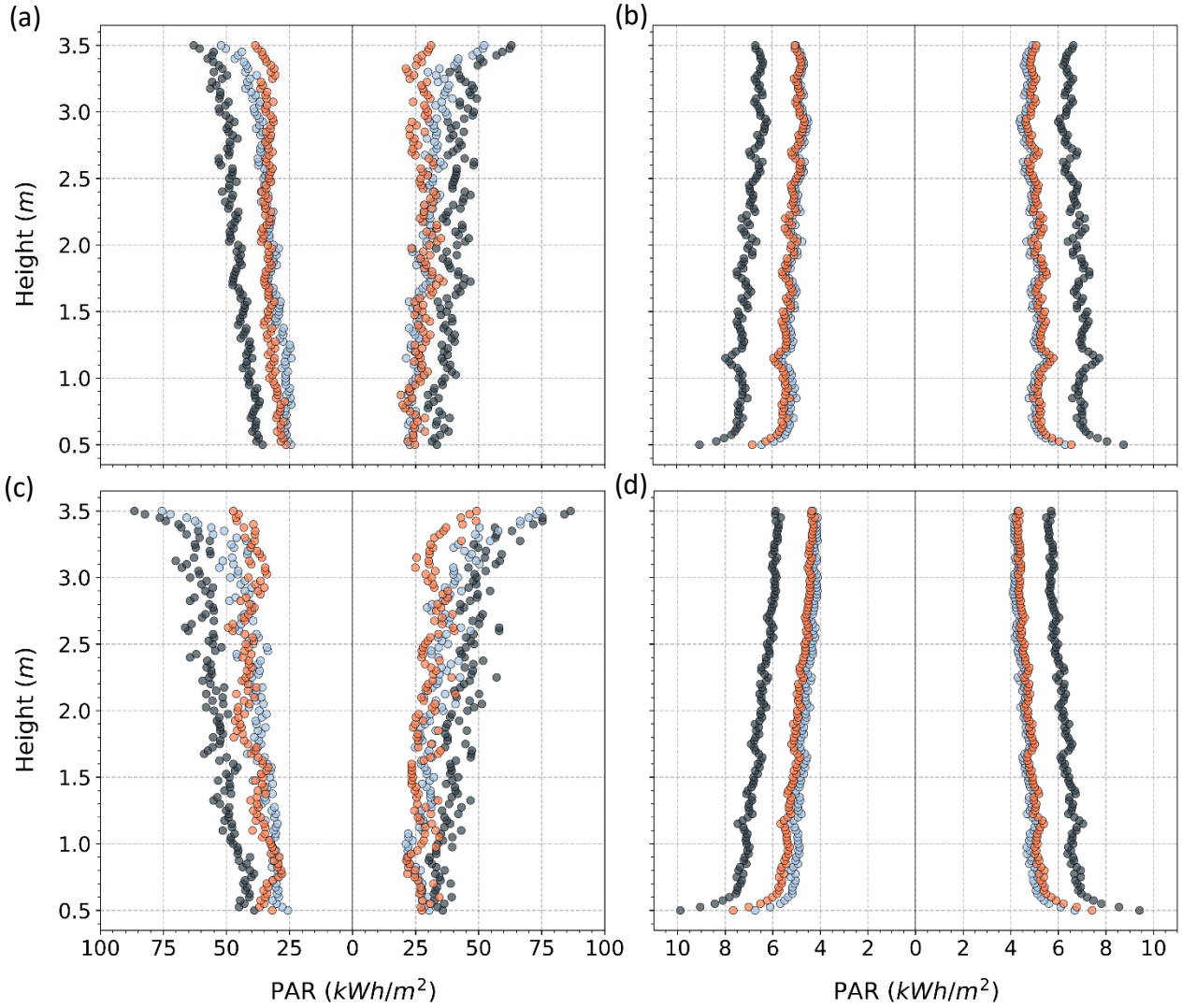

Figure 111: Monthly aggregated light penetration profiles along the height of the tree canopy. Graphs (a) and (b) correspond to April, while (c) and (d) to June. Graphs (a) and (c) display PAR levels incident on the frontside of the virtual leaves, while graphs (b) and (d) show the levels on the backside. Each plot includes data for both east-facing (left) and west-facing (right) tree sides.

The presence of the PV array and the stepwise like patterns under clear skies can be seen when shifting to an hourly timestep, as shown in Figure 112. Light penetrating in between the PV cells and through the glass can occur between PV cells and through the glass, with a noticeable reduction can also penetrate in between the cells and through the glass, leading to a noticeable reduction in comparison to the reference case. To accurately identify such effects, a high spatial resolution of irradiance sampling is essential. In other words, with decreasing timescale an increased number of virtual sensors is required to capture the heterogeneous nature of light.

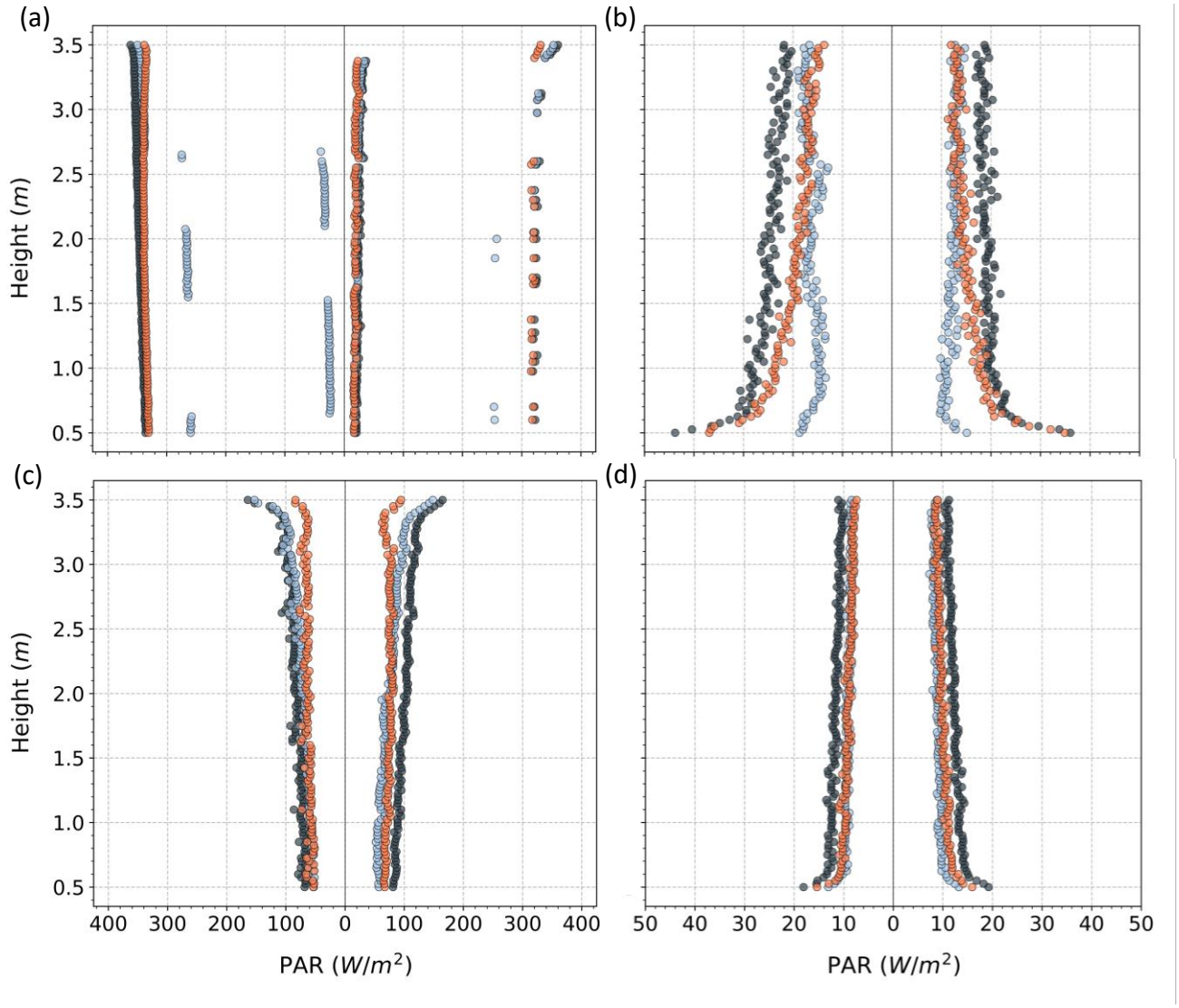

Figure 112: Hourly light penetration profiles along the height of the tree canopy. Graphs (a) and (b) illustrate clear-sky conditions, while (c) and (d) cloudy. Graphs (a) and (c) display PAR levels incident on the frontside of the virtual leaves, while graphs (b) and (d) show the levels on the backside. Each plot includes data for both east-facing (left) and west-facing (right) tree sides.

6. MODELLING OF CLOSED AGRI-PV SYSTEMS

6.1. Introduction

For the modelling case study in this exercise for the closed Agri-PV system, the greenhouse prototype located at Lotsweg 3, 2636 JH, in the municipality of Schipluiden (near Delft), Netherlands, has been selected. This demo driver features a typical greenhouse structure designed for growing various vegetables, including tomatoes, cucumbers, peppers, and lettuce. Currently, there is a growing demand for additional energy in such systems, which Agrivoltaic systems are expected to fulfil. However, the greenhouse market remains hesitant to install PV panels above vegetation areas due to concerns that sunlight availability, critical for crop yield maximization, might be reduced.

The primary aim of this demo is to measure how much energy is lost due to the presence of the glass and PV panels when installed in intervals on the glass gable roof above the growing area. The developed methodology for this work is applied in this context to explore such configurations, with a particular emphasis on the effect of glass. By modelling the light reaching the crops and analysing it over various temporal resolutions, valuable insights can be drawn regarding light availability.

The coordinates of the demo driver site are 51.997963, 4.313927. Figure 113 provides a satellite view of the site, showcasing the top view of the greenhouse.

Figure 113**:** Satellite of view of the greenhouse.

Figure 114 provides a closer view of the VENLO greenhouses at the specified location.

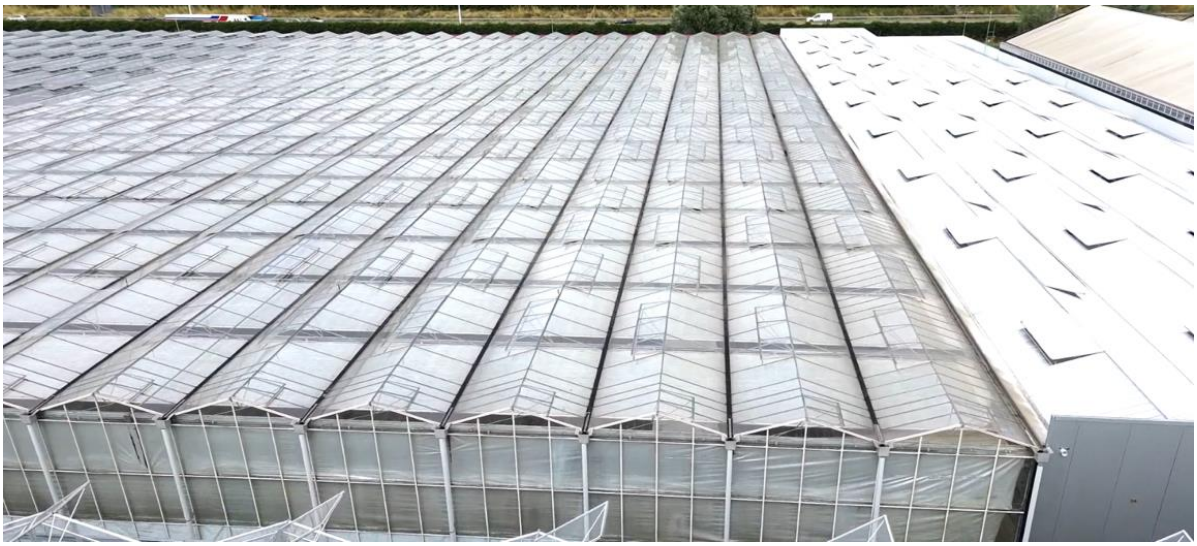

Figure 114**:** Closer view over the Venlo greenhouses.

From a modelling perspective, the closed Agri-PV plant is segmented into the following key components:

- Greenhouse Venlo support structures
- Glass layout encompassing the greenhouse
- Crop layout
- PV layout

Technical details including the details including the dimensions, layout configuration and other specification has been elaborated for each of the key component mentioned above.

6.2. Input Data

6.2.1. Greenhouse Venlo support structures

The Venlo greenhouse, being the most widely constructed greenhouse type globally, is known for its exceptional adaptability and functionality. This design is perfectly suited for a variety of agricultural purposes, such as cultivating vegetables and flowers, due to its modular nature and ease of customization.

The 3D model of the Venlo greenhouse structure in Figure 115 represents a single modular unit of this system in a top view of the Venlo structure. The model showcases a rectangular framework with vertical support poles, horizontal beams, and a triangular truss roof. The symmetrical truss design forms a gable roof, which enhances spatial utility while maintaining a clean and organized geometry. This modular unit acts as a basic building block that can be seamlessly replicated and connected to create larger structures.

The modularity of the 3D design also allows for easy scalability, making it adaptable to various spatial and operational requirements. The focus now remains on the geometric configuration and modular assembly of

the structure, facilitating precise visualization and understanding of the system's potential scalability and extensibility. The red axis represents the north-south line, with the downward direction indicating south, while the green axis denotes the east-west line, with the rightward direction representing east. The frame is oriented with a 30-degree tilt in an anti-clockwise direction from the south. This positioning results in the frame facing north-east. This layout establishes the reference orientation of the structure within the 3D space, allowing for accurate interpretation of subsequent dimensions and measurements. The tilt and alignment are critical for understanding the placement and interaction of this modular frame with its environment.

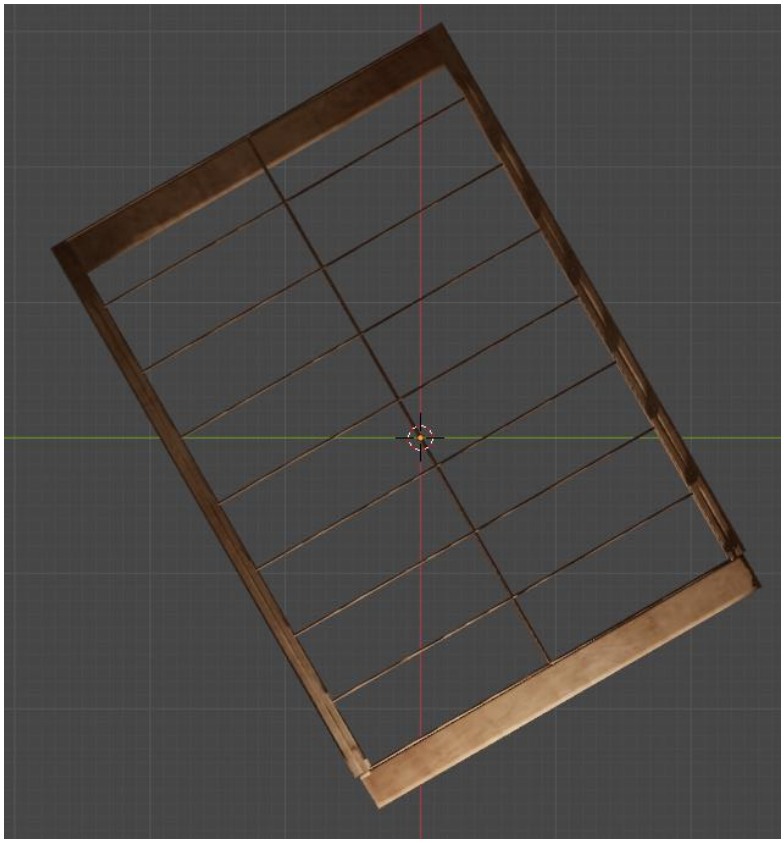

Figure 115: Top view of the Venlo frame structure.

The vertical support bars are placed 4.45 m, with width of each support bar being 0.05 m. The truss section consists of 0.21-m wide truss bars, spacing between alternate truss bars are 1.11 m, which defines the width of the photovoltaic (PV) module to be placed later. The height of the gutter is 0.12 m, and the total width of the horizontal truss is 0.30 m.

Figure 116 provides a view of the upper part of the Venlo greenhouse structure from the south side, where it can be observed that, the distance between two vertical support poles is 3.12 m. The upper horizontal truss bar and the lower horizontal beam are separated by 0.36 meters, with thicknesses of 0.039 m and 0.05 m, respectively. Each vertical support pole has a width of 0.079 m.

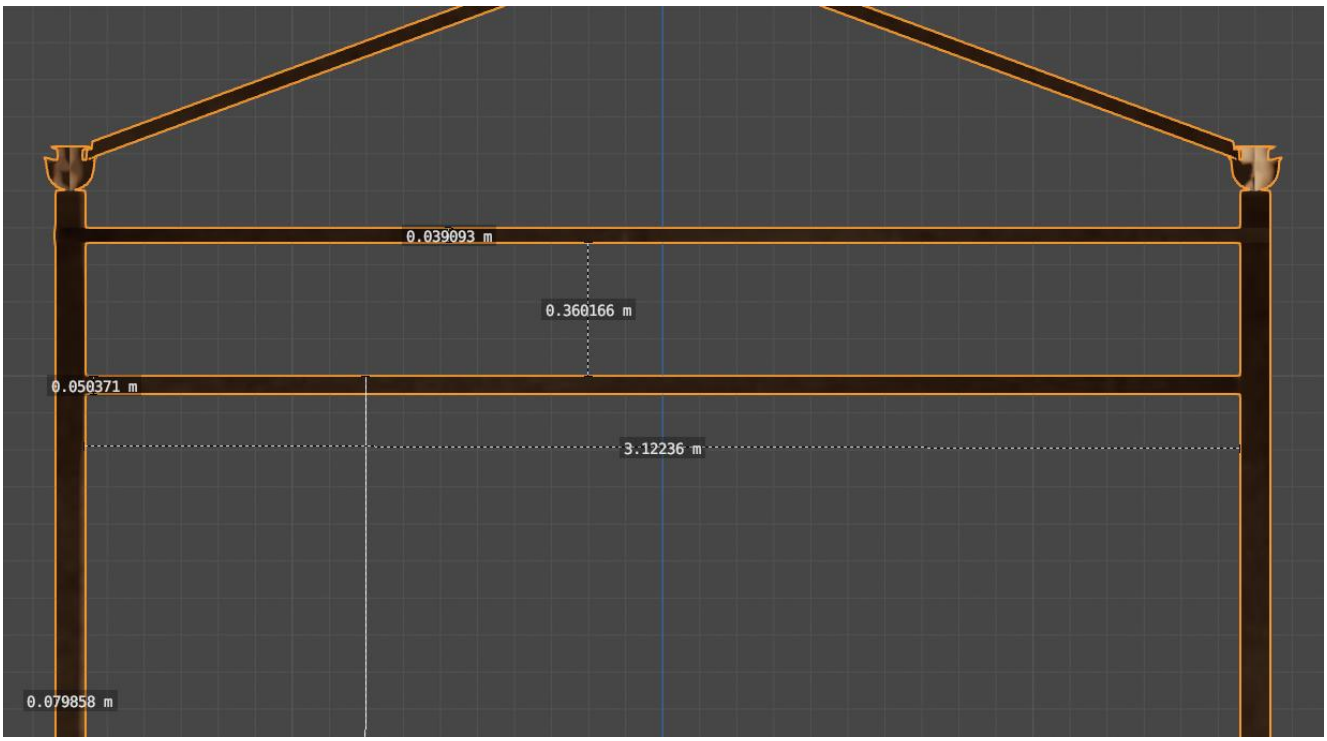

Figure 116: View of the upper part of the Venlo frame structure from the South side with dimensions.

Figure 117 shows the height measurements from the ground to key structural components, which are of 5.41 meters to the upper horizontal truss bar, and 5.01 meters to the lower horizontal beam. The midpoint of the truss bar is at 5.91 meters from the ground.

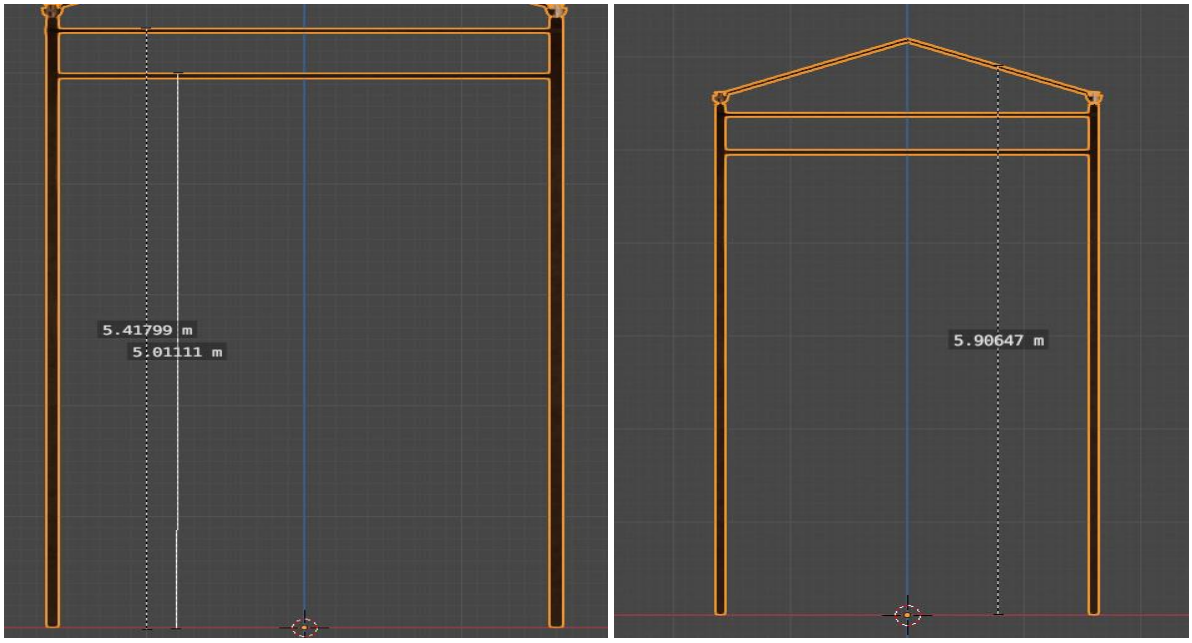

Figure 117: Bottom view of the Venlo frame structure from the South side with dimensions.

The frames are replicated as shown in Figure 118 with three point of views, and the direction marked at the top right corner. One frame is highlighted in white to indicate the building unit of the structure. There is a total of four frames arranged in the north-south direction and three frames in the east-west direction, making a total of 12 frames. These frames are placed without any spacing between them, creating a compact scenario. This configuration represents a smaller subset of a larger potential greenhouse scenario.

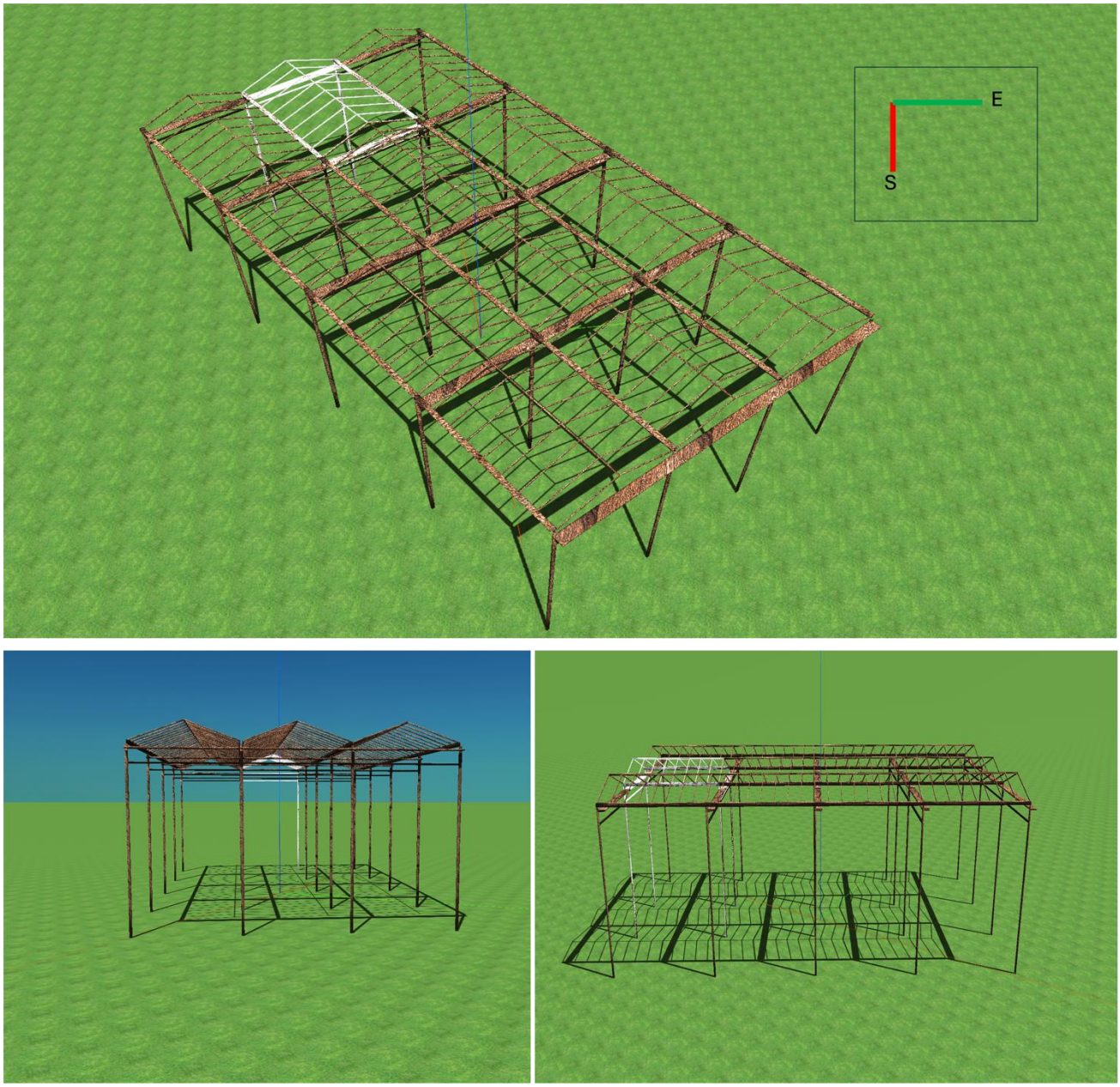

Figure 118: Frame layout for the greenhouse as seen from LuSim's 3D environment.

6.2.2. Glass

In this work, clear standard glass is considered as the primary material for enclosing the greenhouse. The glass covers all open areas defined by the structural frame, ensuring a fully enclosed environment. These areas are categorized into four distinct sections, as marked in the picture and described below:

- Front-Facing Region: This refers to the east-west facing area between the two vertical supporting poles.

- Side-Facing Region: This corresponds to the north-south facing area forming the vertical glass wall along the sides of the structure.
- Side-Facing Triangular Shed: This section refers to the north-south facing triangular region created by the truss bars as part of the gable roof. This triangular portion fills the gaps at the ends of the roof's structure in the east-west direction.
- Top Shed: This includes the top region of the greenhouse, covering the gable roof itself. The glass panels here provide a continuous covering across the roof while maintaining structural alignment with the truss system.

The dimensions of the glass panels are derived directly from the structural frame. The measurements presented earlier for the frame apply here to ensure that the glass fills the corresponding shapes and areas accurately.

The glass layout strictly follows the layout of the structural frame. As can be seen in Figure 119, the placement of the glass panels aligns with the modular structure, filling each open space seamlessly.

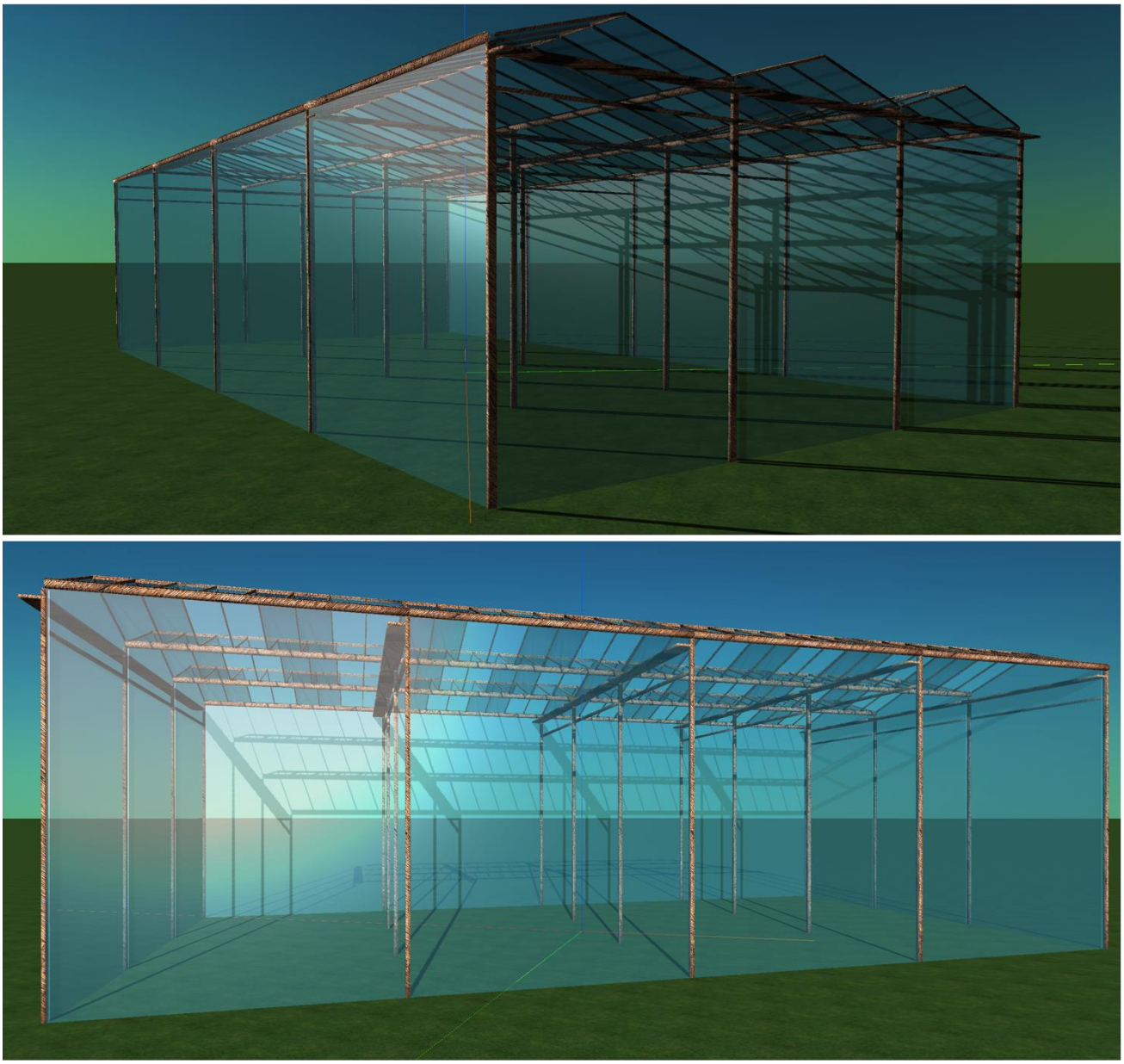

Figure 119: Inclusion of glass to fill the VENLO frame for the greenhouse.

6.2.3. Crops Modelling

The crop to be grown in this greenhouse from KUBO is a tomato plant, modelled as parallelepiped to represent its outer canopy. This approach simplifies the crop geometry for effective visualization and light modelling, following the crop modelling methodology described for Bolzano.

The model considers the complete vertical region from the gutter to the top of the canopy, reflecting the area where photosynthesis occurs and where light interception will be possibly studied with on-site sensors. The vertical walls facing east and west are divided into three equal zones, while the northern and southern sides

are not evaluated, as the rows of crops are considered long enough to render their contribution negligible. Additionally, the top horizontal surface is treated as a separate zone for light analysis.

This design is inspired by the research conducted at KU Leuven [18], where tomato plants were grown along crop wires at 4 m above a gutter positioned 0.8 m above the ground.

The vertical canopy, standing at a total height of 4 m, is divided into three equal zones along the east and west-facing walls. These zones are spaced at heights of 0 m, 1.33 m, 2.66 m, and 4.0 m, marking the boundaries for light analysis and distribution studies.

The length of the crop corresponds to the north-south length of the greenhouse, which is 18 m, ensuring complete coverage of each row. The width of the crop (east-west direction) is 0.4 m, matching the typical tomato crop canopy width.

The greenhouse structure consists of three frames along the east-west direction, with crops placed between these frames as follows:

- The first row of crops starts on the westernmost side, leaving a 0.4-m gap between the glass panel and the west-facing side of the first crop row.
- Consecutive rows are placed with 1.6 m of free space between each crop row
- A total of five rows of crops are arranged along the east-west direction within the greenhouse, following these spacing and alignment guidelines.

Figure 120 displays the crop layout along with the frame and the glass incorporated.

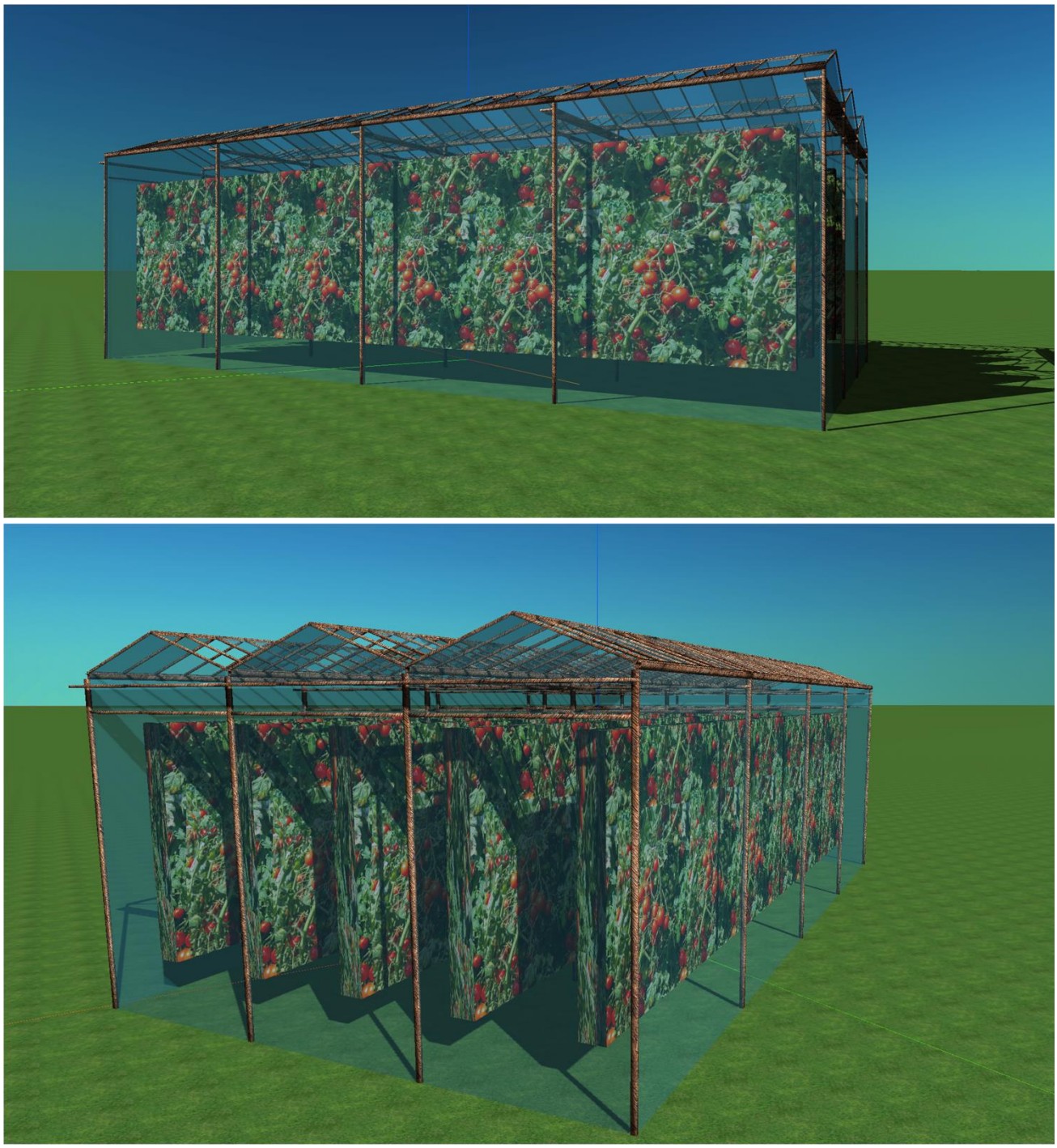

Figure 120: Crop layout for the greenhouse.

6.2.4. PV Array

Standard transparency PV modules are used in this design, chosen to fit seamlessly on the gable roof shed formed by the trusses of the frame. The dimensions of the module are designed to align perfectly with the structural layout. The width of the PV module corresponds to the free space between two alternating trusses, while the length of the PV module matches the length of the truss rod. This ensures precise coverage of the roof surface, optimizing both structural compatibility and functionality.

The width of each PV module corresponds to the 1.11 m of free space between two alternating trusses, as specified in the frame section, while the length of the module equals the 1.62 m length of the truss rod.

As observed in Figure 121, the PV modules are arranged in an alternating checkerboard pattern across the gable roof. This pattern combines semi-transparent glass of the 'top shed' and opaque modules, allowing for a balance of light penetration and shading. Each module is placed sequentially along the roof, aligning with the truss structure to ensure stability and proper spacing.

The roof features multiple rows of these alternating PV modules running along the length of the greenhouse in north-south direction. The picture illustrates the layout of the PV modules, with the bottom side corresponding to north and the right side corresponding to east.

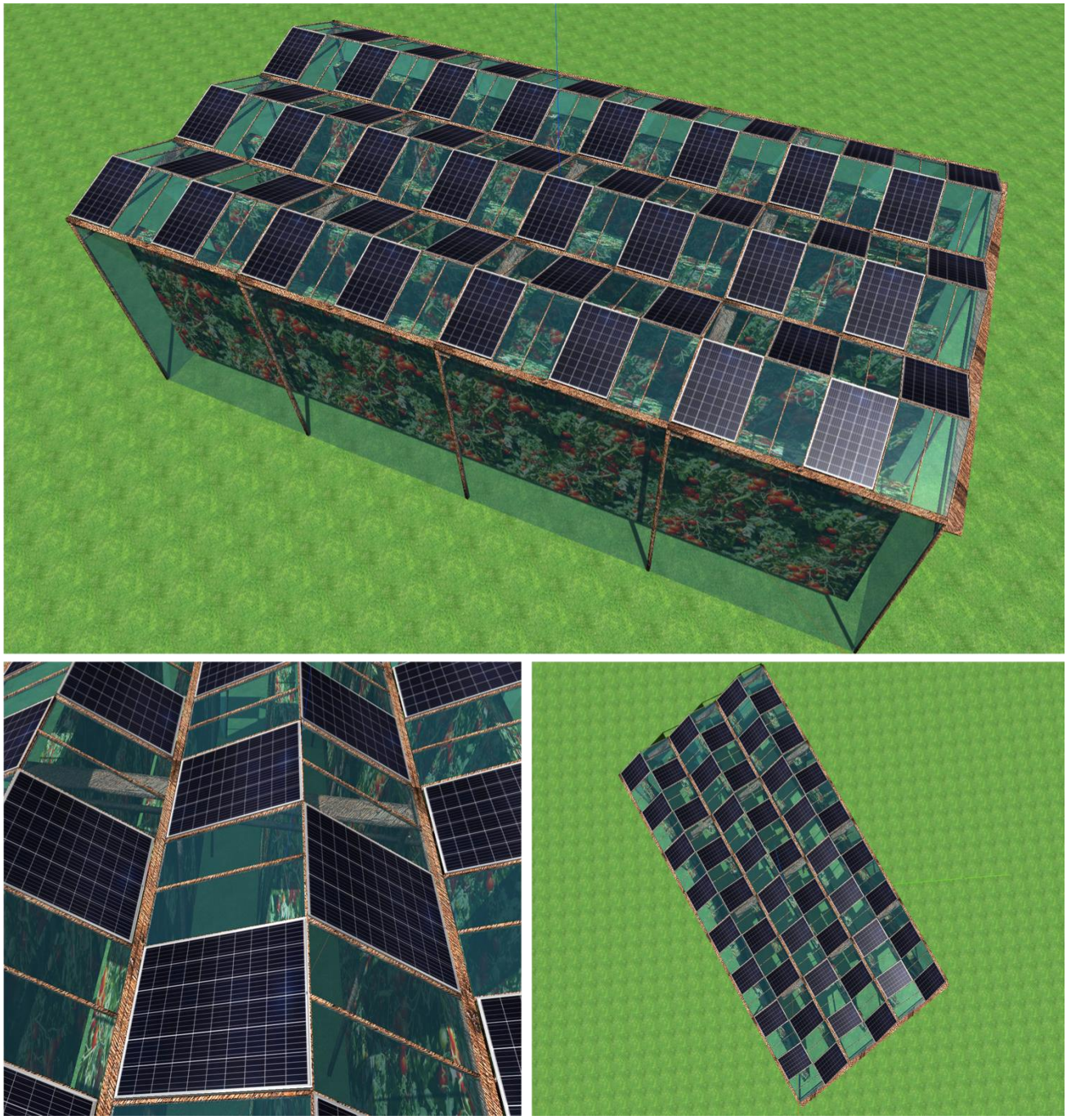

Figure 121: Module layout for the greenhouse.

6.2.5. Material Properties

Other than the glass of the greenhouse, the optical properties of all surfaces in the model are defined with a focus on consistency and simplicity, where Lambertian reflectance is assumed as the default for those reflecting surfaces, including the ground, crops, Venlo frame support structure, and the PV cells.

The albedo value is set to 0.2 for the ground, crops, and the frame, while the PV cells are assigned an albedo value of 0.05. The crop canopy reflectance is also modelled as Lambertian, with a transmittance of 0%.

The glass transmittance is modelled as specular with transmittance of 85% for Imec, while LuciSun assumes a diffusion factor of 60% for all the glass elements, in which case the Bidirectional Transmissivity Diffusion Factor (BTDF) considered is only dependent on the incident angle of the sun with the reference to the glass normal.

6.2.6. Solar Resource

The input solar resource for modelling is based on Typical Meteorological Year (TMY) irradiance data, obtained from SARAH2 for the coordinates 51.990 (latitude) and 4.310 (longitude).

For sky irradiance decomposition and transposition, each partner uses their preferred models tailored to their tools. LuciSun utilises the Erbs model for decomposition and the Hay-Davis transposition model, while Imec adopts the All-sky Perez model. Furthermore, the horizon profile is excluded from this study.

Table 7 shows a monthly summary of the solar resource data used in the modelling.

Table 7: Monthly summary of the most relevant solar resource and weather data used for modelling.

Month	GHI [kWh/m²]	DNI [kWh/m²]	DHI [kWh/m²]
Jan.	21.96	31.71	14.48
Feb.	32.37	29.31	22.14
Mar.	80.86	80.05	44.2
Apr.	131.5	117.11	67.22
May	146.88	113.61	76.78
June	171.82	142.18	80.45
July	154.81	109.77	87.82
Aug.	147.88	139.1	69.26
Sep.	87.92	84.55	48.15
Oct.	52.4	51.73	33.12
Nov.	24.61	31.01	16.56
Dec.	17.24	25.56	11.98
Year	1070.25	955.69	572.16

6.3. Methodology

The primary objective of this exercise is to enable each partner to independently simulate the scenario and showcase their respective simulation results. The focus of this analysis is on understanding the irradiance distribution across different zones of the crop canopy placed within a greenhouse environment. These developments specifically include the effects of greenhouse glass and the corresponding 3D environment, which are further detailed in the respective methodology sections from LuciSun and Imec.

A similar methodology to the case study conducted for Open Agri-PV in Bolzano has been applied in this exercise. This ensures compatibility and sets the groundwork for potential future studies that could build on the findings presented here.

6.3.1. Irradiance evaluation on crop envelopes: targets, zone and sensor creation

To ensure accurate comparisons, the entire system must be constructed with its centre aligned to the origin of the 3D coordinate system, adhering to the same layout and dimensions. This alignment ensures that the selected coordinates representing the point for evaluating irradiance will remain consistent across all modelling platforms.

This section details which crops are selected, how zones are allocated, and in what format results are exported to facilitate meaningful comparisons across different modelling tools.

Target Objects

To determine or obtain the coordinates for specific zones of the selected crop, the first step involves selecting a target object that is representative of similar objects within the 3D scene. In this study, the target object is the outer envelope of the tomato crop, as specified in the 'Inputs' section. It is essential to choose a specific envelope that accurately represent the behaviour of other crop envelopes in the scene. Thus, the middle row of the crop layout as seen from Figure 122 showcasing the closed Agri-PV system in the greenhouse with the target object highlighted in white and marked appropriately in the 3D scene.

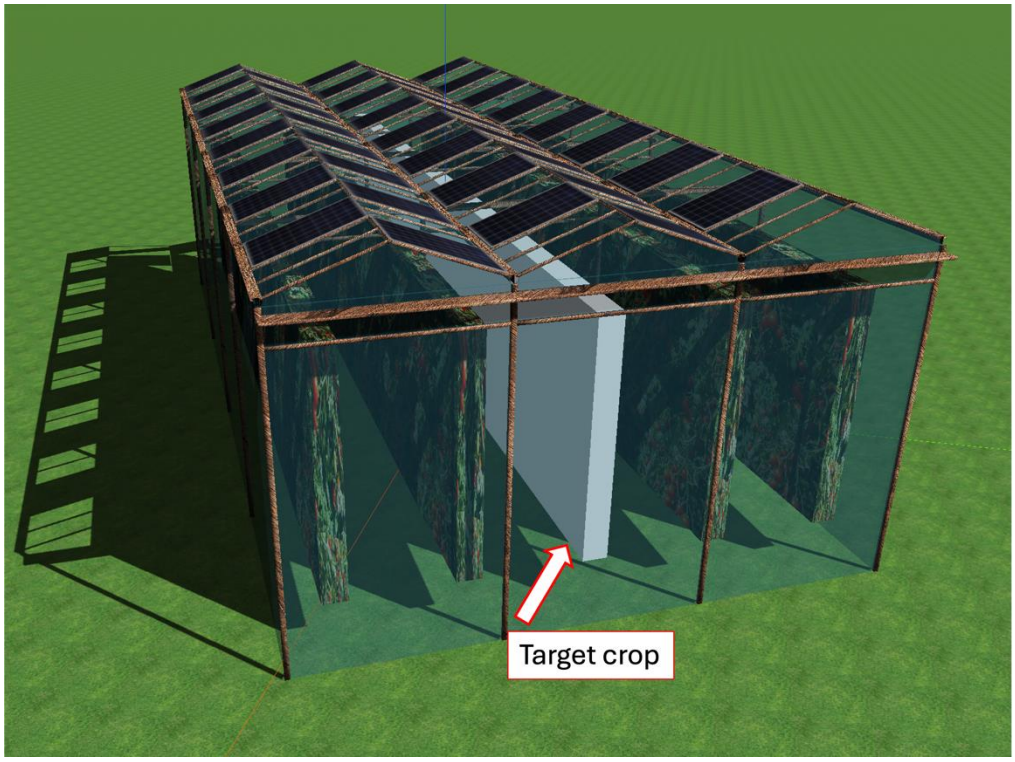

Figure 122: Greenhouse with middle crop indicated as target objects for the simulations.

Zone Creation

Like the zone split done for the apple crops in the case study of Bolzano, the vertical sides of the targeted object as seen in Figure 122 are divided into three equal zones based on their height and not relative to the ground:

- Bottom: Segment spanning from 0 to 1.33 meters
- Middle: Segment spanning from 1.33 meters to 2.66 meters
- Top: Segment spanning from 2.66 meters to 4 meters

The vertical faces are evenly divided into these three zones, while the top horizontal surface represents an additional zone for sky-facing light evaluation. Thus, there are 3 zones on the eastern side and 3 zones on the western side. In addition, there is a top horizontal zone, which represents the light incident on the upper surface of the crop canopy. This configuration results in a total of 7 distinct zones for evaluating solar irradiance on the crops. The southern and northern sides of the crop are not evaluated, as the length of the crop rows is considered long enough for the impact of these zones to be negligible.

Point Selection

Similar to the apple crops in Bolzano, here also, roughly midpoints are selected as representative points for each zone. These midpoints serve as the basis for calculating irradiance and shading loss, ensuring consistency

across the outputs of the modelling tools. Table 8 provides the 3D coordinates of the selected midpoints for each zone of the targeted crop.

Table 8: Coordinates corresponding to the selected zones of the targeted crop for the light analysis on the respective point.

Zone	Coordinates (x, y, z)
1-bottom-east	0.68, 0.63, 1.88
2-middle-east	0.7, 0.63, 2.84
3-top-east	0.67, 0.62, 4.38
4-bottom-west	0.27, -0.08, 1.46
5-middle-west	0.45, 0.03, 2.86
6-top-west	0.75, 0.2, 4.39
7-sky-facing	0.77, 0.45, 4.8

In this table:

- The Zone column describes the position of the zone, the corresponding number to identify it, and the direction it faces (east, west, or sky-facing).
- The Coordinates (X, Y, Z) column represents the 3D coordinates of the points on the targeted crop envelope.

6.3.2. Irradiance evaluation on PV modules

In addition to the crop evaluation, irradiance is also evaluated at one point on the front and back sides of the PV module, following the layout and other inputs. A roughly central PV module has been selected, and Table 9 provides the 3D coordinates of the selected points on its front and back sides. For better representation of the overall behaviour, a roughly midpoint location on the module is chosen for evaluation.

Table 9: Coordinates corresponding to the front and rear side of the targeted PV module for the light analysis on the respective point.

Side	Coordinates (x, y, z)
Front	0.6, - 0.56, 5.92
Back	0.63, - 0.55, 5.89

Simulations are performed on the complete timeseries dataset described in the input section. The GTI values from each modeler for the selected points (on the crop and PV module) are generated over the entire timeseries in hourly intervals.

6.4. LuciSun (LuSim)

This section focuses on validating the overall logical behaviour of the results obtained through both visual inspection, using heatmaps applied within LuSim's 3D environment, and quantitative assessment. The objective is to ensure that the results are consistent with expected physical and logical patterns within the defined scenario.

Figure 123 provides an example of the results obtained with and without greenhouse glass for midday on a clear-sky day (31st March). For clarity, the same colour scale is used in the visualisation.

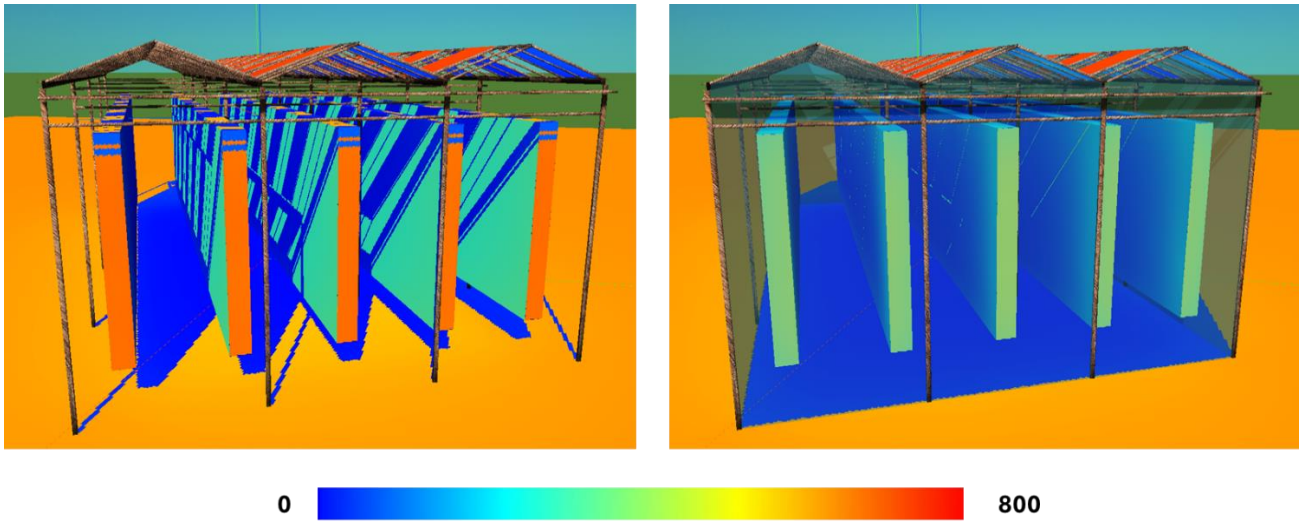

Figure 123: Irradiance heatmap for greenhouse (W/m^2) without glass (left) and with glass (right).

The diffuse effect of the glass can be observed across the different sections of the crops, creating a smoother irradiance distribution within the greenhouse. To examine this effect locally, dedicated comparisons are provided for each section, focusing on the reference points selected for the analysis. An adapted colour scale is used in each case to better highlight the impacts.

East side

Figure 124 shows the three reference points in the east side of the reference crop (1 – bottom, 2 – middle, 3 – top). The colour scales are adapted to highlight some effects. The pictures are taking in a clear sky day (31st March) close to noon time. As the crops present a deviation of 30º from the N/S line, that side is already under shade at that point of time. The point on the upper sector (3) receives more light over the day, as it has access to a more illuminated area during the day.

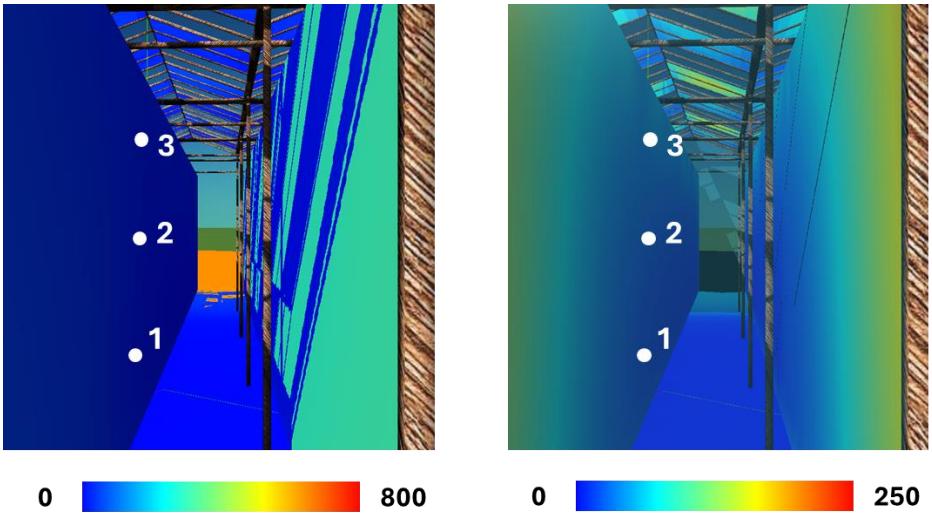

Figure 124: Irradiance for reference points on east side (W/m^2) without glass (left) and with glass (right).

The effect on hourly irradiance is illustrated in Figure 125 for two different days: 31st March (a clear-sky day) and 16th March (a cloudy day). The impact of the glass differs significantly between the two scenarios.

On the clear-sky day, the glass redistributes the irradiance. In the morning, rays receiving higher irradiance directly from the sun and those receiving it in the evening, primarily due to reflections from adjacent crop rows, are diffused. This redistribution aligns with the sun's trajectory, as the diffusion follows a Lambertian pattern, where the primary parameter is the cosine of the zenith angle.

On the cloudy day, the effect is primarily an attenuation of the irradiance entering from outside the greenhouse. This attenuation is more pronounced in the upper section of the crops compared to the middle and lower sections.

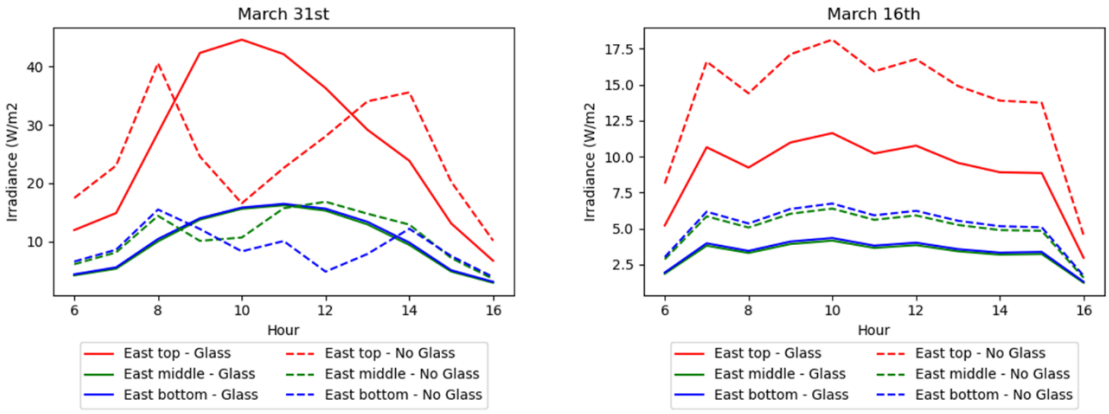

Figure 125: Irradiance for reference points on the east side (W/m^2), with or without glass, for 31st March (a clear-sky day) and 16th March (a cloudy day).

West side

The situation on the west side is similar to that on the east, but the effect of attenuation in the afternoon, when the sun's angle of incidence is higher due to the rotation of the crops, is more noticeable on clear-sky days. Figure 126 also shows that during this time of day, in the absence of glass, there is an alternation between shaded and illuminated areas. This alternation is not fully captured on an hourly basis, but when the glass is present, the diffusion effect eliminates these variations. Figure 127 shows the resulting irradiance for the reference points.

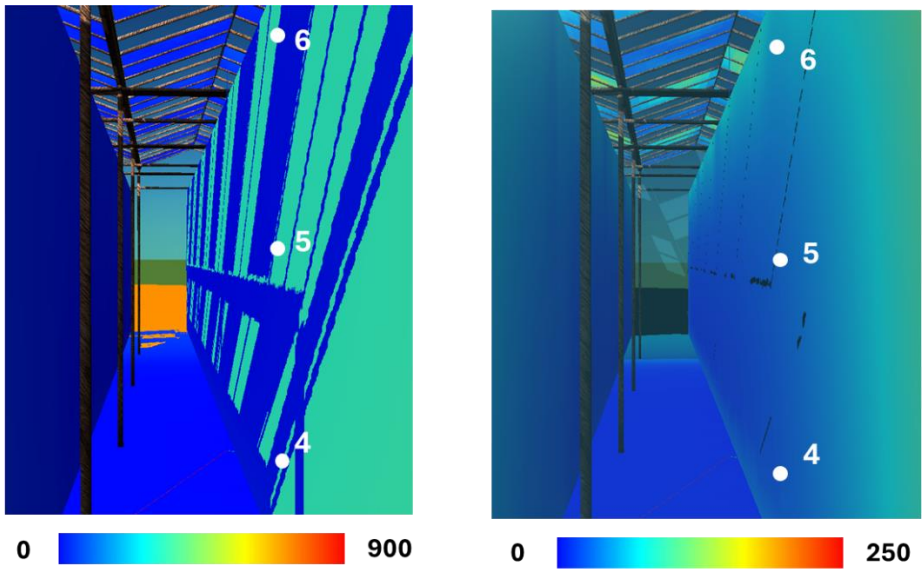

Figure 126: Irradiance for reference points on west side (W/m^2) without glass (left) and with glass (right).

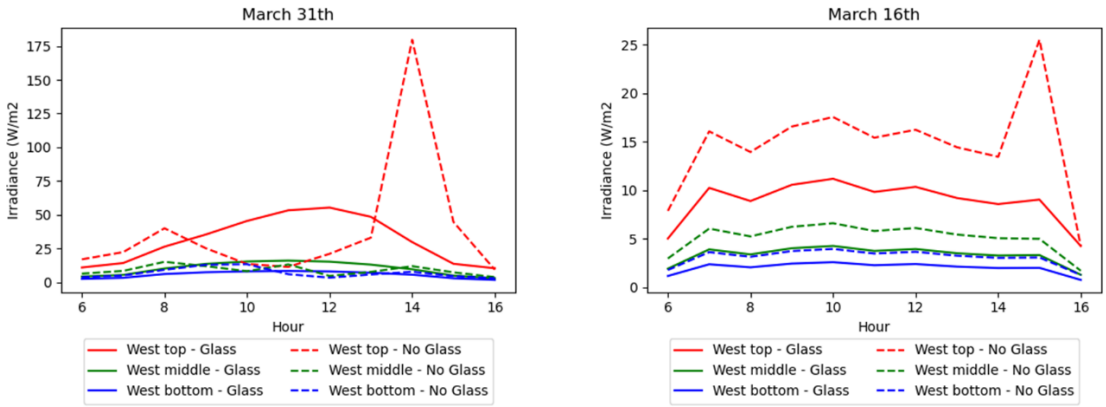

Figure 127: Irradiance for reference points on the west side (W/m^2), with or without glass, for 31st March (a clear-sky day) and 16th March (a cloudy day).

Top side

The upper side present the same effect as before, but in a more noticeable way as the surface is horizontal and the alternance of shading from the roof, where several opaque modules cast shadows, as shown in Figure 128. Figure 129 shows the resulting irradiance for the reference points.

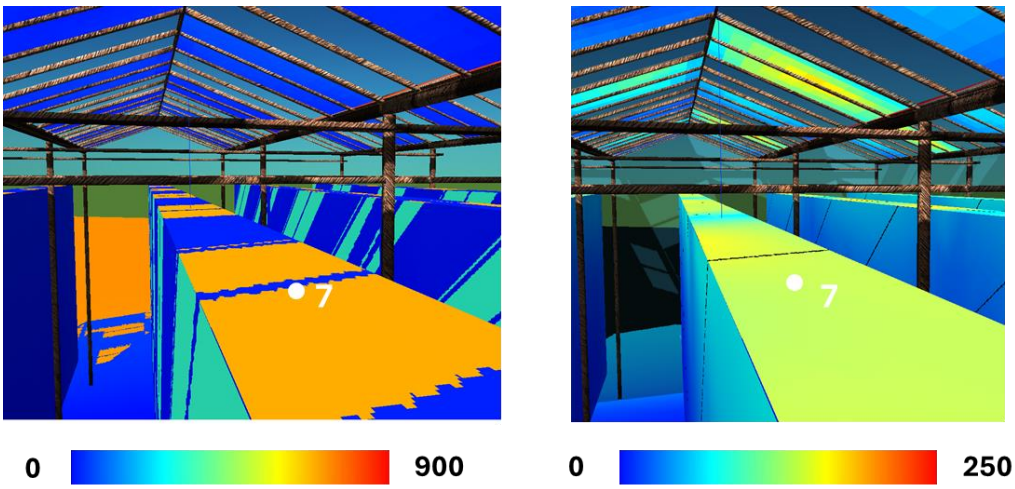

Figure 128: Irradiance for reference point on top of crops (W/m^2) without glass (left) and with glass (right).

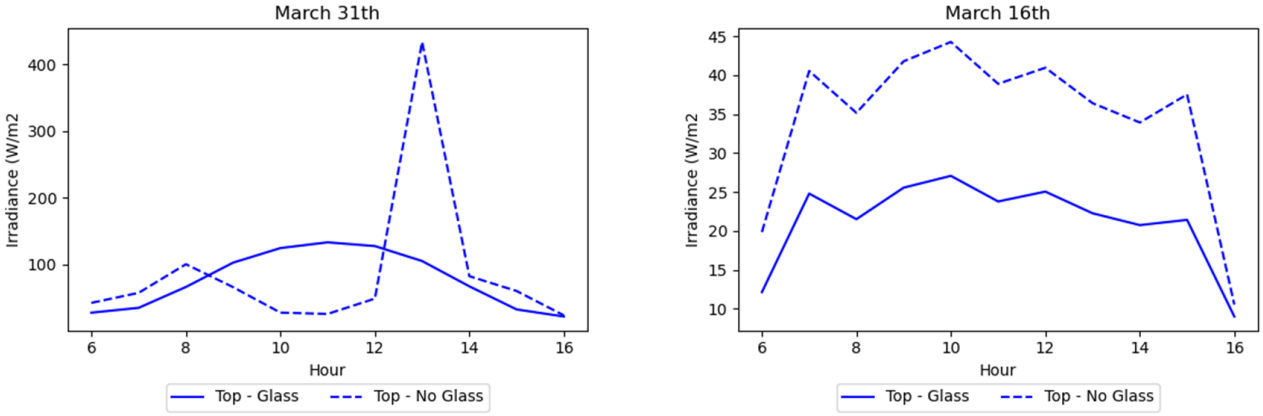

Figure 129: Irradiance for reference points on the top side (W/m^2), with or without glass, for 31st March (a clear-sky day) and 16th March (a cloudy day).

Yearly time integration

An analysis of the overall irradiation received on each of the reference points over the reference year is presented in Figure 130.

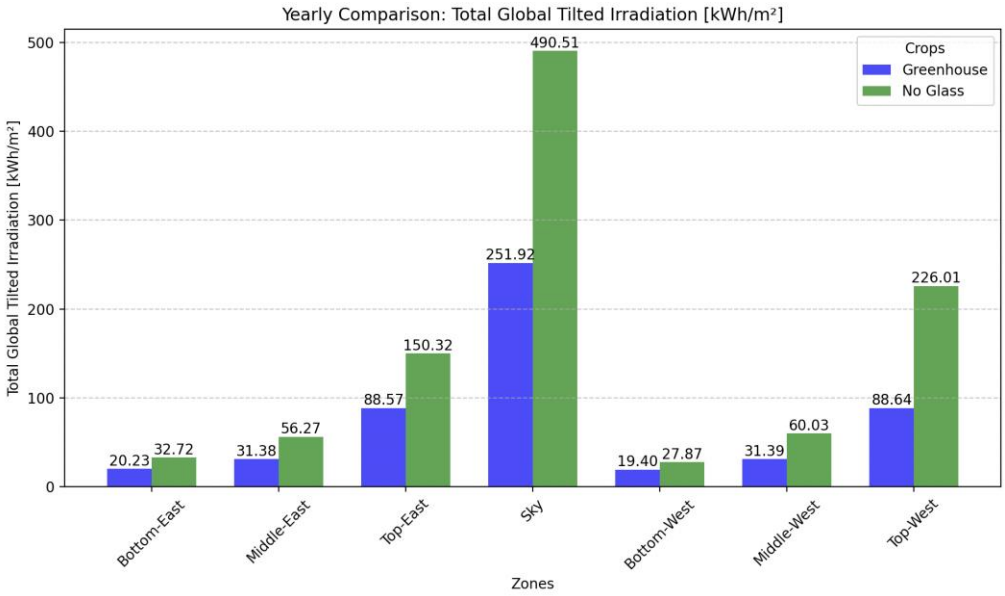

Figure 130: Yearly irradiation for reference points on crops (W/m^2) without glass (left) and with glass (right).

Based on the results obtained for each section and the accumulated yearly irradiation, the following conclusions can be drawn:

- The overall irradiation inside a greenhouse with glass is reduced compared to that received without glass.
- The irradiance is distributed more uniformly, particularly on clear-sky days. This uniformity is achieved by smoothing the alternation of peaks caused by fully illuminated and shaded areas associated with the direct component of irradiance.
- Due to the orientation of the greenhouse, this effect is more pronounced on the west side, which receives more direct irradiance throughout the day.

6.5. Imec

Figure 131 shows the 3D design of the EW greenhouse as described above. Figure 132 shows the layout and different view angles of the tomato greenhouse and PV modules.

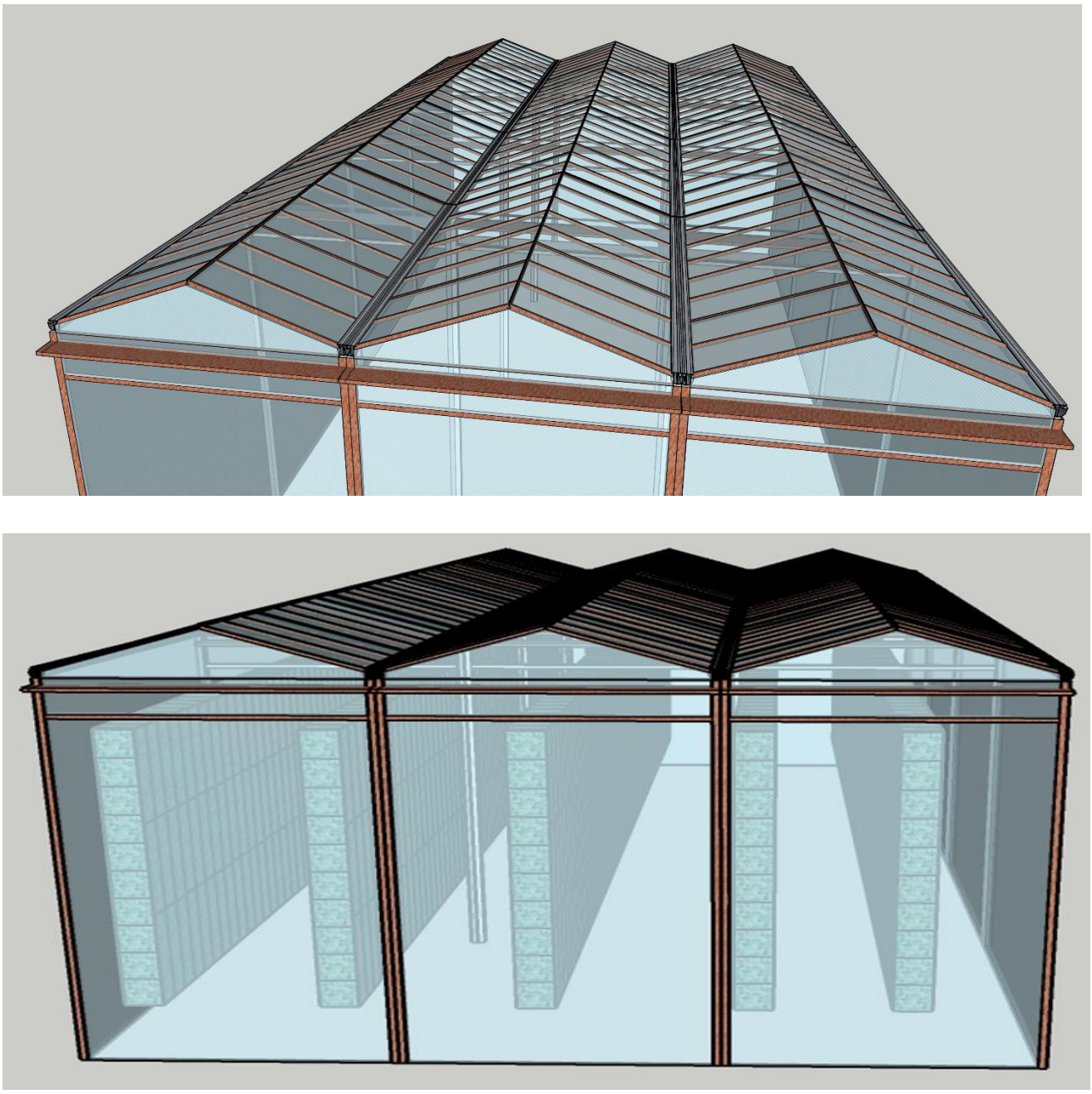

Figure 131: 3D design of the EW greenhouse.

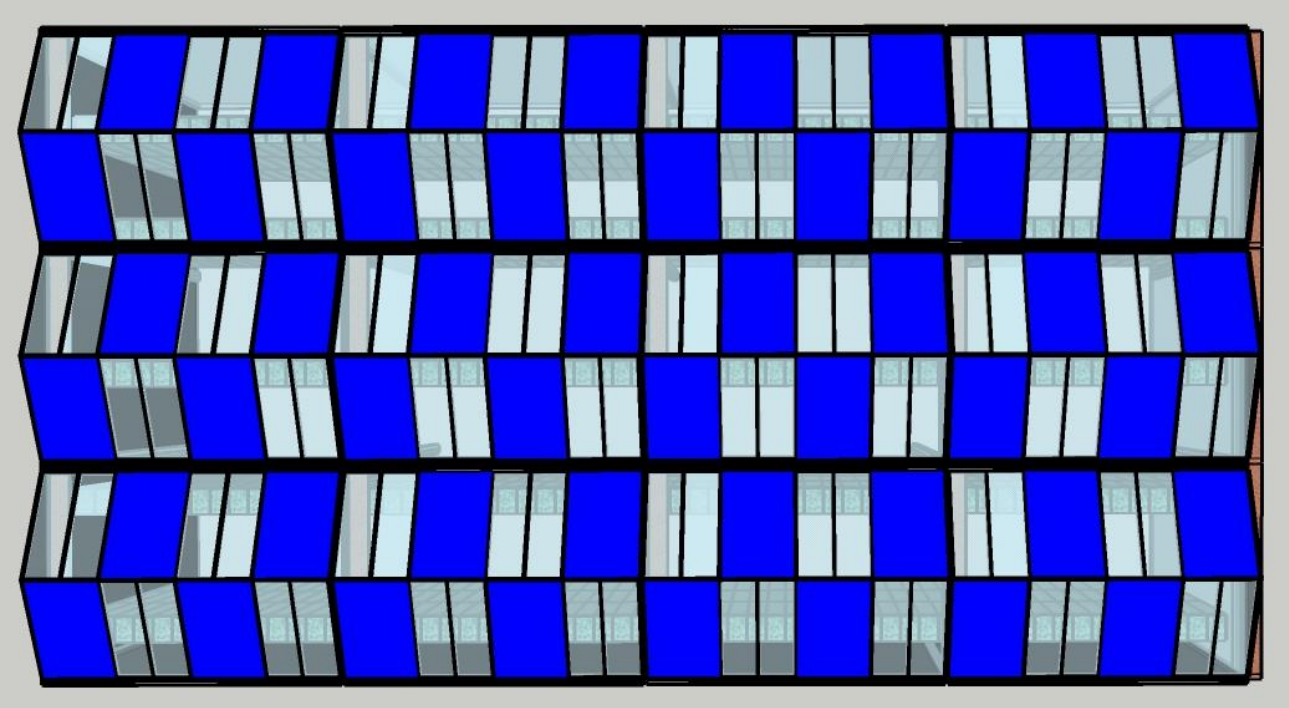

Figure 132: Layout and different view angles of the tomato greenhouse and PV modules.

The glass is modelled with a refractive index of 1.5 and a transmittance of 85%.

The irradiance on the seven zones of interest of the tomato plant and PV module are presented in this section. Figure 133 shows the yearly integrated irradiation on the greenhouse PV modules and plants.

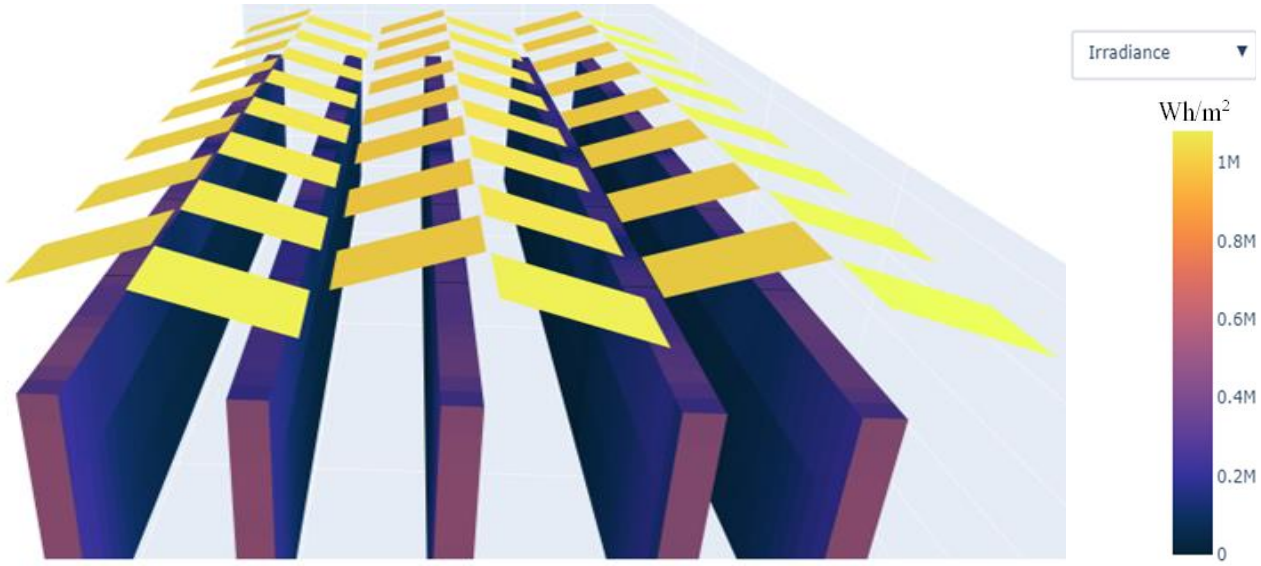

Figure 133: Illustration of yearly integrated irradiation on the PV modules and tomato plants.

Across the year, the east-facing PV modules receive more irradiation compared to the west facing ones. As the greenhouse is symmetrical, the difference in irradiation can be attributed to the location and available irradiance during the morning periods compared to the afternoon. This irradiation profile is very symmetrical across the east and west facing PV modules of the entire greenhouse (see Figure 134).

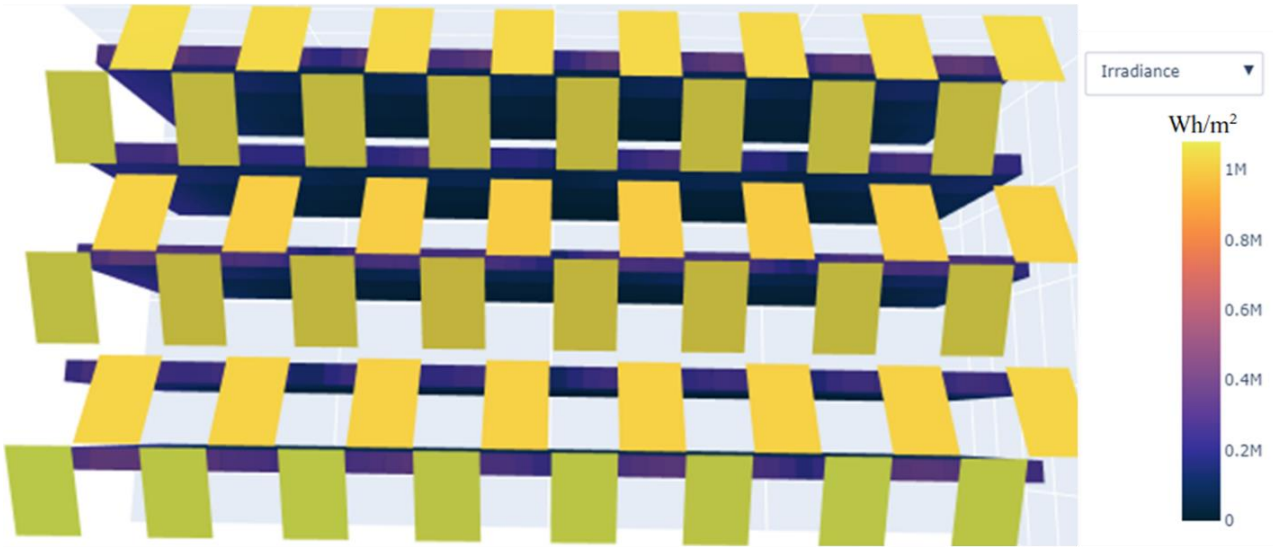

Figure 134: Top view of the total yearly irradiation across the greenhouse.

The yearly rear PV irradiation is also illustrated in Figure 135. It can be seen that the irradiance distribution on the rear side of the PV modules is very unsymmetrical across the greenhouse. This behaviour can be attributed to a non-uniform reflectance of light from the plants, ground and greenhouse structures, resulting in the observed irradiance distribution.

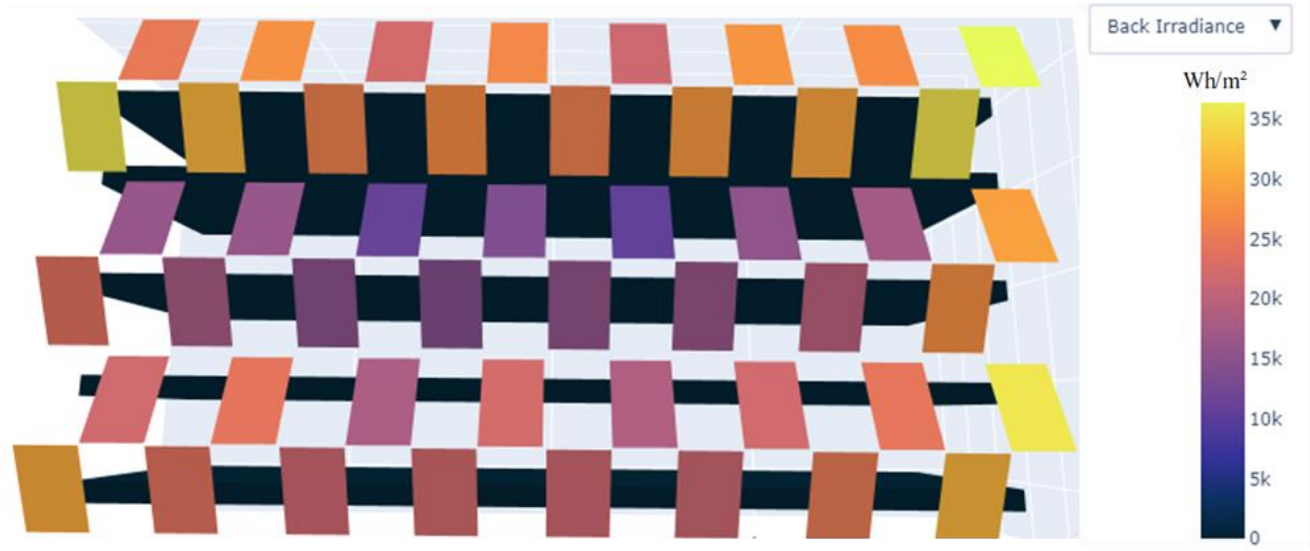

Figure 135: Top view of the total yearly rear side PV irradiation.

On a clear-sky day, the irradiance profile on the rear side follows the expected dome shape behaviour with peak irradiance around noon, as illustrated in Figure 136. The irradiance model uses the global horizontal irradiance (GHI) which is composed of the direct normal and diffuse horizontal irradiances. Under clear-sky, the rear PV irradiance is mainly composed of the grounds and crop reflected irradiance.

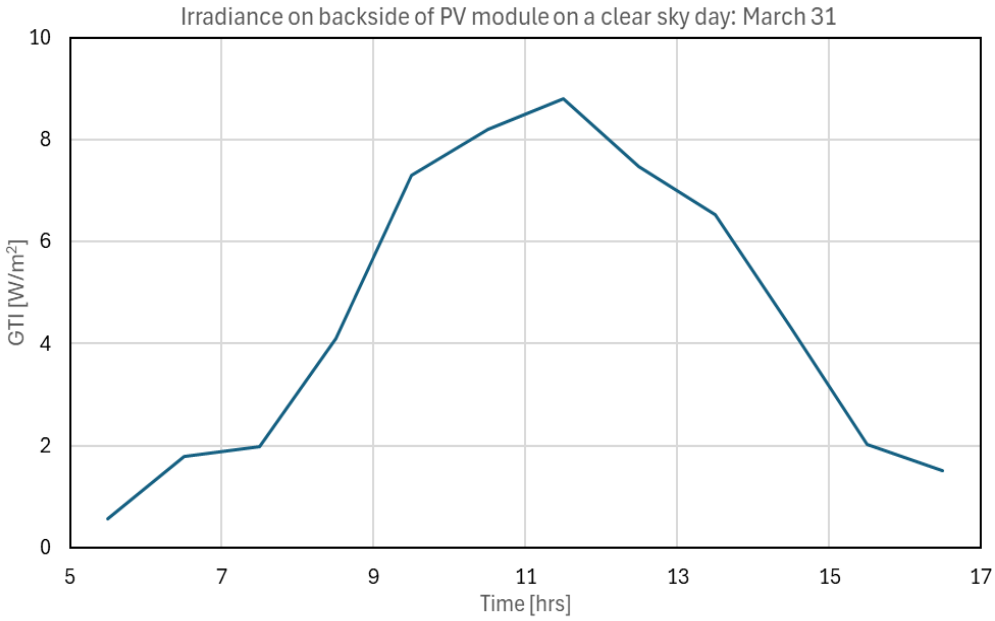

Figure 136: Rear PV irradiance on a clear-sky day.

On cloudy days, the evolution of the backside irradiance is illustrated in Figure 137.

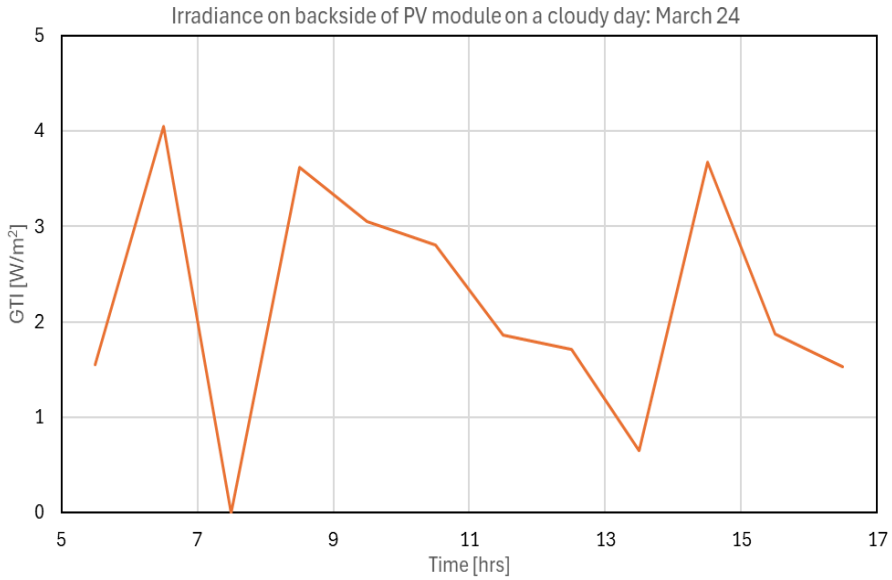

Figure 137: backside PV irradiance on a cloudy day.

The vertical walls (east and west zones) and sky-facing zones of the tomato canopy are considered to be more effective in the photosynthesis process, compared to the north and south sections. Hence, the yearly irradiance distribution on these zones were analysed. Figure 138 shows the yearly integrated irradiation on the different zones of the tomato canopy wall.

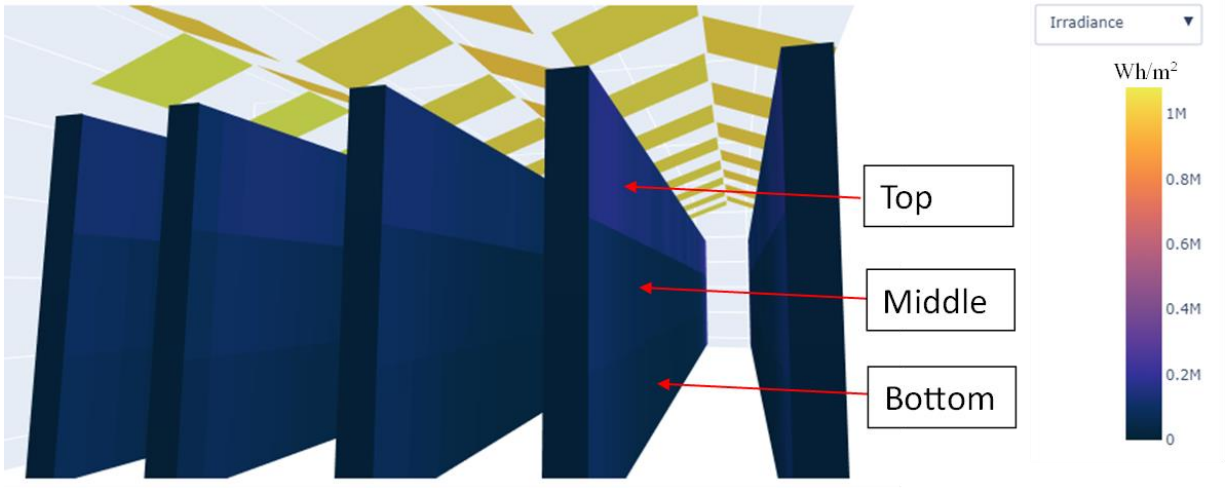

Figure 138: Illustration of yearly integrated irradiation on three sections of side walls of the tomato plants.

From Figure 138, the top zone receives more light followed by the middle and the bottom. The sky-facing zone receives the highest irradiation compared to the side walls as indicated in Figure 139 below. Also, the east sides of the plant canopy receive more irradiation than the west sides. Similar to the trend observed for the PV modules, this behaviour can be attributed to the weather profile of the location, where the irradiance in the morning periods is higher than later in the day.

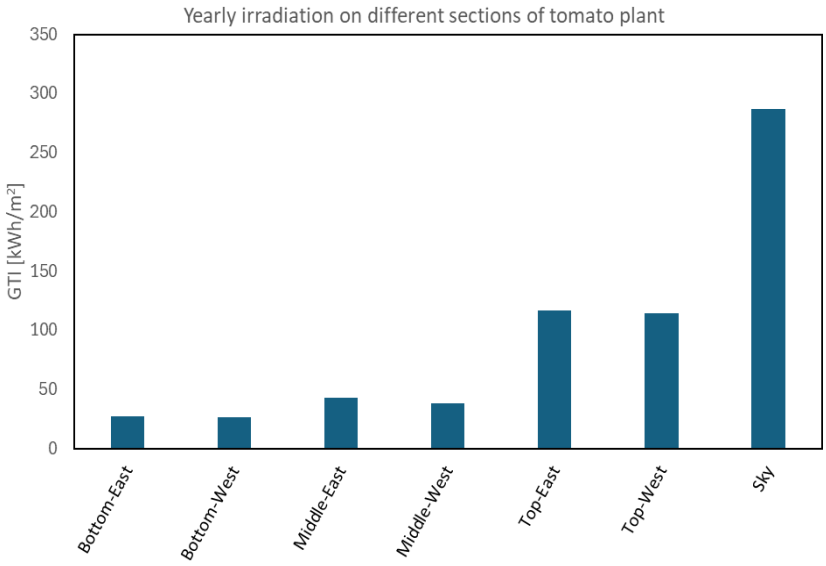

Figure 139: Calculated yearly integrated irradiation on the different sections of the tomato plant.

7. CONCLUSIONS

This work has provided a detailed analysis of the methodologies, tools, and validation processes used to evaluate the performance of agrivoltaic modelling systems within the SYMBIOSYST project. By combining the expertise of LuciSun, Imec, TUD and Fotoniq, and leveraging their respective modelling tools, it offers a comprehensive understanding of the strengths and limitations of current approaches in addressing the unique challenges of agrivoltaic systems. The validation framework developed in this study includes both simple and complex test cases. Simple cases allowed for analytical validation, ensuring consistency and reliability across the different tools, while complex scenarios, such as the Bolzano demonstrator, captured realistic challenges like shading effects, variations in albedo, and the role of module transparency.

One of the main findings is the significant influence of module height and shading on irradiance distribution. At lower module heights, discrepancies between the tools were more evident, primarily due to differences in how shading and ground reflectance were modelled. For example, Imec tended to slightly overestimate irradiance at low heights compared to LuciSun, which employs a high-resolution 3D view-factor methodology. However, as the module height increased, these discrepancies diminished, with results converging closely at heights of 50 meters. The modelling of greenhouse glass provided additional insights, revealing important trade-offs. While glass reduces the overall irradiance compared to open configurations, it creates more uniform light distribution, particularly on clear-sky days, by smoothing sharp transitions between shaded and illuminated areas. On cloudy days, the glass primarily attenuates incoming irradiance, with varying impacts across different crop sections.

The comparative performance of the tools showed that TUD and Imec, both using Radiance as their ray tracing core engine, produced closely aligned results. LuSim, which uses a GPU-accelerated 3D view-factor approach, also delivered consistent results, while all models showed slight differences between them. These findings underscore the importance of understanding the specific methodologies behind each tool when interpreting results. Despite the robust nature of this work, several limitations were identified. The complexity of real-world agrivoltaic systems, particularly the evolving nature of crop growth over time, poses challenges for static 3D models.

Future work should address these limitations to further advance agrivoltaic modelling. Incorporating dynamic crop growth models would allow for a more realistic representation of shading and light interactions over time. Expanding validation efforts with high-quality, long-term field measurements would enhance benchmarking and provide a stronger basis for real-world applications. Increasing the spatial and temporal resolution of simulations would enable the capture of finer details of light distribution in complex environments. Additionally, using these tools to iteratively optimise system design, including parameters such as module spacing, height, and transparency, could yield key insights for improving agrivoltaic efficiency. Further research into advanced materials, such as transparent PV modules and specialised coatings, could also enhance light-sharing capabilities while maintaining energy generation.

8. REFERENCES

[1] Anderson, K., Hansen, C., Holmgren, W., Jensen, A., Mikofski, M., and Driesse, A., pvlib python: 2023 project update, Journal of Open Source Software, 8(92), 5994, (2023). DOI: 10.21105/joss.05994.

[2] Robledo J. et al., From video games to solar energy: 3D shading simulation for PV using GPU, Solar Energy, https://doi.org/10.1016/j.solener.2019.09.041, 2019.

[3] Robledo J. et al., Dynamic and visual simulation of bifacial energy gain for photovoltaic plants, European Photovoltaic Solar Energy Conference and Exhibition (EUPVSEC), 2021.

[4] Robledo J. et al., Lessons learned from simulating the energy yield of an agrivoltaic project with vertical bifacial photovoltaic modules in France, European Photovoltaic Solar Energy Conference and Exhibition (EU PVSEC), 2021.

[5] Robledo J. et al., Key parameters for the simulation of agrivoltaics in greenhouses with bifacial PV modules,WCPEC-8, 2022.

[6] El Boujdaini I. et al., 3D modelling of light-sharing agrivoltaic systems for orchards, vineyards and berries, European Photovoltaic Solar Energy Conference and Exhibition (EU PVSEC), 2023.

[7] Goverde H. et al., Energy Yield Prediction Model for PV Modules Including Spatial and Temporal Effects, 29th European Photovoltaic Solar Energy Conference and Exhibition (EU PVSEC), 2014.

[8] Ayala Pelaez S., Deline C., (2020). bifacial_radiance: a python package for modeling bifacial solar photovoltaic systems. Journal of Open Source Software, 5(50), 1865, https://doi.org/10.21105/joss.01865.

[9] Tsubo, M., Walker, S. Relationships between photosynthetically active radiation and clearness index at Bloemfontein, South Africa. *Theor. Appl. Climatol.* 80, 17–25 (2005). https://doi.org/10.1007/s00704-004-0080-5.

[10] Roujean, J.-L., M. Leroy, and P.-Y. Deschamps (1992), A bidirectional reflectance model of the Earth's surface for the correction of remote sensing data, J. Geophys. Res., 97(D18), 20455–20468, doi:10.1029/92JD01411.

[11] Hay, J.E., Davies, J.A., 1980. Calculations of the solar radiation incident on an inclined surface. In: Hay, J.E., Won, T.K. (Eds.), Proc. of First Canadian Solar Radiation Data Workshop, 59. Ministry of Supply and Services, Canada.

[12] Pfeifroth, U., Kothe, S., Trentmann, J., Hollmann, R., Fuchs, P., Kaiser, J., & Werscheck, M. (2019). *Surface Radiation Data Set - Heliosat (SARAH)* - Edition 2.1. Satellite Application Facility on Climate Monitoring. DOI: 10.5676/EUM_SAF_CM/SARAH/V002_01.

[13] R. Perez, R. Seals, J. Michalsky, All-weather model for sky luminance distribution—Preliminary configuration and validation, Solar Energy, Volume 50, Issue 3, 1993, Pages 235-245, ISSN 0038-092X, https://doi.org/10.1016/0038-092X(93)90017-I.

[14] Rajan S.P. et al., Conceptual Design of the Agri-PV demonstrators, Deliverable D5.1, SYMBIOSYST, 2024, 10.13140/RG.2.2.26162.93124.

[15] Ruiz-Arias, J. A., Gueymard, C. A. (2023). CAELUS: Classification of sky conditions from 1-min time series of global solar irradiance using variability indices and dynamic thresholds. Solar Energy, 263, 111895. DOI: 10.1016/j.solener.2023.111895.

[16] Ruiz-Arias, J. A., Gueymard, C. A. (2024). GISPLIT: High-performance global solar irradiance component-separation model dynamically constrained by 1-min sky conditions. Solar Energy, 269, 112363. DOI: 10.1016/j.solener.2024.112363.

[17] Gueymard, C. A. (2019). The SMARTS spectral irradiance model after 25 years: New developments and validation of reference spectra. Solar Energy, 187, 233–253. DOI: 10.1016/j.solener.2019.05.048.

[18] Šalagović, J., Vanhees, D., Verboven, P., Holsteens, K., Verlinden, B., Huysmans, M., Van de Poel, B., Nicolai, B. (2024), Microclimate monitoring in commercial tomato (Solanum Lycopersicum L.) greenhouse production and its effect on plant growth, yield and fruit quality. Frontiers in Horticulture, 3. DOI: 10.3389/fhort.2024.1425285.